Carbon xerogels doped with silicon or tin oxide for lithium-ion battery anodes

Joseph CARABETTA

Supervisor

Pr. Nathalie JOB

UR Chemical Engineering ULiège – NCE, ULiège

Members of the Jury

Benoît Heinrichs	Professor, University of Liège, President
Nathalie Job	Professor, University of Liège, Supervisor
Cédric Gommes	F.R.S.-FNRS Research Associate, University of Liège
Alexandre Léonard	Logisticien de Recherche, University of Liège
Alexandru Vlad	Professor, Catholic University of Louvain
Diego Cazorla-Amorós	Professor, University of Alicante (Spain)

Acknowledgements

I would like to thank my promotor, Prof. Nathalie Job for her continued support and guidance. Over the course of my doctoral work, her attention to detail was invaluable as well as her ability to keep my on track when I needed it. Simply put, Prof. Job was a great promotor and I am extremely grateful that I had the pleasure of being her doctoral student.

I would like to thank Prof. Benoit Heinrichs, Dr. Cédric Gommes, and Dr. Alexandre Léonard from ULiège for agreeing to be a part of the jury for this thesis. I would also like to thank Prof. Alexandru Vlad from the Université Catholique de Louvain and Prof. Diego Cazorla-Amoros from the University of Alicante in Spain for agreeing to also be a part of the jury for this thesis. I appreciate not only the time and energy put into review my work, but for the criticism you are able to offer.

I would like to thank the F.R.S.-FNRS for the FRIA grant I was awarded for the last three years of my thesis. Their support has allowed me the ability to complete my doctoral work in a domain that had interested me. I am truly grateful for their confidence in me and the work that I planned to complete for my doctoral work.

I would also like to thank the School of Engineering at ULiège for the extra 3-months "COVID" financing that allowed me to complete my research that was delayed due to the COVID-19 pandemic.

I would also like to thank the other PhD students, researchers, and technicians in the NCE lab that I had the pleasure of meeting. Although I won’t name everyone personally here, the professional collaborations, brainstorming, and mutual learning during my thesis was key to the completion of my thesis and for me to grow as an engineer and scientist. I am glad that I am able to keep you all as not only colleagues, but as friends.

I would like to also thank the surrounding laboratories around the NCE group, including the Greenmat, CERM, and FOCUS research groups for graciously allowing us the use of their characterization tools. Notably, I would like to thank Prof. Philippe Compere, Dr. Catherine Henrist, Prof. Benedicte Vertruyen, and Dr. Abdelfattah Mahmoud for their help during my doctoral work.

I would finally like to thank my family and friends for making the last years so great. My time in Liege has been a great experience and I hope you understand how important your presence in my life has been.

Abstract

In this thesis, a carbon xerogel (CX) was used as an electrically-conductive 3D support matrix for either silicon, an alloying-type active material, or tin oxide, a conversion-type and alloying-type active material, for use as a negative electrode in a lithium-ion battery. This thesis aimed to understand not only the CX itself, but how the active material pulverization and excessive solid-electrolyte interphase (SEI) formation caused by the volumetric change of the Si and SnO_2 during cycling can be mitigated. The mitigation techniques consisted of (i) reducing the domain size of the silicon and tin oxide dopants to limit their pulverization, (ii) using a protective coating or binder to improve the SEI, and (iii) optimizing the inclusion of the silicon or tin oxide in the CX. The thesis is thus organized into three main sections: (i) the synthesis and characterization of the CX, and the modeling of its electrochemical behavior, (ii) the synthesis and characterization of a Si-doped CX, and (iii) the synthesis and characterization of a SnO_2-doped CX.

First, electrodes composed of a CX with either poly(vinylidene difluoride) (PVDF) or poly(sodium 4-styrene sulfonate) (PSS) as a binder were synthesized and assembled into a symmetric supercapacitor cell in order to more fully understand how the electrochemical properties are affected by the binder, the microstructure of the CX, and other extrinsic properties of the active layer such as its thickness and density. Additionally, a unique consideration of the total capacitance of these CX-based supercapacitors was formulated and a new model for disordered mesoporous carbon with internal microporosity was developed. This model showed that, although the specific capacitance of a pore increases with decreasing diameter, the addition of a secondary diffuse region outside of the pore causes a net decrease in the specific capacitance per unit surface area, which corresponded with experimental results.

In the second section, a CX was doped with Si with either pre-formed nanoparticles (SiNPs) or with a Si precursor, such as silica nanoparticles or tetraethyl orthosilicate (TEOS)-derived silica, which was subsequently *in situ* transformed into silicon *via* magnesiothermal reduction. The latter synthesis procedure was thought to further increase the cycling stability of the CX-based electrodes given the more homogenous and intimate inclusion of the Si dopant. Furthermore, the use of PSS as a protective coating or binder was explored. The synthesis of both the CX doped with SiNPs or *via* a Si precursor was successful; however, cycling instability still remained, albeit to a lesser extent than in the case of SiNPs alone. Finally, using PSS as a protective coating or binder yielded composite electrodes that were up to 10 times more stable during cycling than the same electrodes with only conventional PVDF as a binder.

In the third section, a CX was doped with SnO_2 using either pre-formed nanoparticles (SnONPs) or a precursor that was subsequently *in situ* transformed into tin oxide *via* a simple sol-gel process. Both procedures were successful: SnO_2 was included within the porosity of the CX. The latter synthesis additionally seemed to deposit SnO_2 at least partially within the microporosity of the CX. The electrodes were relatively stable upon cycling for both synthesis techniques, yielding a material that maintained 80% of the initial capacity after 50 cycles. The use of PSS as a protective coating or binder only yielded a moderate increase in the cycling as compared to the same electrodes with only conventional PVDF as a binder. Overall, the effects of the volumetric change these dopants exhibited during cycling were at least partially mitigated through the use of a CX as a support structure, PSS as a protective coating or binder, and the more intimate inclusion of Si or SnO_2 *via* liquid precursors.

Résumé

Dans cette thèse, un xérogel de carbone (CX) a été utilisé comme matrice support 3D électriquement conductrice pour soit du silicium, un matériau actif de type alliage, soit de l'oxyde d'étain, un matériau actif de type conversion et alliage ; ces matériaux étaient destinés à une utilisation comme électrode négative dans une batterie lithium-ion. Cette thèse visait à comprendre non seulement le CX lui-même, mais aussi comment la pulvérisation de matière active et la formation excessive d'interphase électrolyte solide (SEI) causées par le changement volumétrique du Si et du SnO_2 pendant le cyclage peuvent être atténuées. Les techniques d'atténuation ont consisté à (i) réduire la taille des domaines cristallins du silicium et de l'oxyde d'étain pour limiter leur pulvérisation, (ii) utiliser un revêtement protecteur ou un liant spécifique pour améliorer la SEI, et (iii) optimiser l'inclusion du silicium ou de l'oxyde d'étain dans la matrice carbonée. La thèse est ainsi organisée en trois sections principales : (i) la synthèse et la caractérisation du CX, et la modélisation de son comportement électrochimique, (ii) la synthèse et la caractérisation d'un CX dopé au Si, et (iii) la synthèse et caractérisation d'un CX dopé au SnO_2.

Tout d'abord, des électrodes composées d'un CX avec soit du poly(difluorure de vinylidène) (PVDF) soit du poly(sodium 4-styrène sulfonate) (PSS) comme liant ont été synthétisées et assemblées dans une cellule de supercondensateur symétrique afin de mieux comprendre comment les propriétés électrochimiques sont affectées par le liant, la microstructure du CX et d'autres propriétés extrinsèques de la couche active telles que son épaisseur et sa densité. De plus, une considération unique de la capacité totale de ces supercondensateurs à base de CX a été formulée et un nouveau modèle pour le carbone mésoporeux désordonné avec une microporosité interne a été développé. Ce modèle a montré que, bien que la capacité spécifique d'un pore augmente lorsque son diamètre diminue, l'ajout d'une région diffuse secondaire à l'extérieur du pore provoque une diminution nette de la capacité spécifique par unité de surface, ce qui correspond aux résultats expérimentaux.

Dans la deuxième section, un CX a été dopé au Si avec des nanoparticules préformées (SiNPs) ou avec un précurseur de Si, tel que des nanoparticules de silice ou de la silice dérivée de tetraethyl orthosilicate (TEOS), qui a ensuite été transformé *in situ* en silicium par réduction magnésiothermique. Cette dernière procédure de synthèse visait à augmenter la stabilité de cyclage des électrodes à base de CX étant donné l'inclusion plus homogène et intime du Si dans la matrice carbonée. En outre, l'utilisation du PSS comme revêtement protecteur ou liant a été explorée. La synthèse à la fois du CX dopé avec des SiNPs ou *via* un précurseur de Si a été un succès ; cependant, l'instabilité des électrodes au cyclage persistait, bien que dans une moindre mesure que dans le cas des SiNPs seules. Enfin, l'utilisation du PSS comme revêtement protecteur ou liant a conduit à des électrodes composites jusqu'à 10 fois plus stables pendant le cyclage que les mêmes électrodes avec uniquement du PVDF conventionnel comme liant.

Dans la troisième section, un CX a été dopé avec du SnO_2 en utilisant soit des nanoparticules préformées (SnONP) soit un précurseur qui a ensuite été transformé *in situ* en oxyde d'étain *via* un procédé sol-gel simple. Les deux procédures ont été couronnées de succès : de particules de SnO_2 ont été incluses dans la porosité du CX. Le dernier type de synthèse semblait en outre déposer du SnO_2 au moins partiellement dans la microporosité du CX. Les électrodes étaient relativement stables lors du cyclage pour les deux techniques de synthèse ; en effet, le matériau obtenu a pu maintenir 80% de la capacité initiale après 50 cycles. L'utilisation de PSS comme revêtement protecteur ou liant n'a donné qu'une augmentation modérée de la stabilité au cyclage par rapport aux mêmes électrodes avec uniquement du PVDF conventionnel comme liant. Dans l'ensemble, les effets du changement volumétrique que ces dopants présentaient pendant le cyclage ont été au moins partiellement atténués grâce à l'utilisation d'un CX comme structure de support, de PSS comme revêtement protecteur ou liant, et de l'inclusion plus intime de Si ou de SnO_2 *via* des précurseurs liquides.

Table of Contents

Introduction

Context

Cheap, clean, and widely available energy is one of the most important tools for a civilization to grow and prosper. Prior to industrial revolution in the 20th century, technological progress was slow and incremental [1-3]. Most people lived in rural areas rather than urban centers where the standard of living was relatively low and unchanging [1-3]. However, with the advent of widely available energy during the industrial revolution, the well-being and standard of living for the common person increased exponentially [1-3]. As people began to move away from the rural farmland and into urban centers, the availability of public infrastructure, centralized energy production, and access to healthcare and education, among other amenities and opportunities, could be utilized more efficiently [3, 4]. For those living in these industrialized areas, the democratization of energy and resources decreased inequality and increased the standard of living and well-being of the otherwise impoverished [3, 4]. As shown in Figure 1, there is a strong correlation between global energy consumption and the rate of global poverty. In this chart, poverty is considered as "living-in-poverty", which is living with less than $2 per day (adjusted for inflation with respect to the year 2002) [4]. The energy consumption in this figure considers all forms of direct energy consumption, including coal, oil, gas, hydroelectric, nuclear, renewables, and traditional biofuels [5]. From this figure, it can likely be said that the higher consumption of energy, generally, is related to an increase in the standard of living.

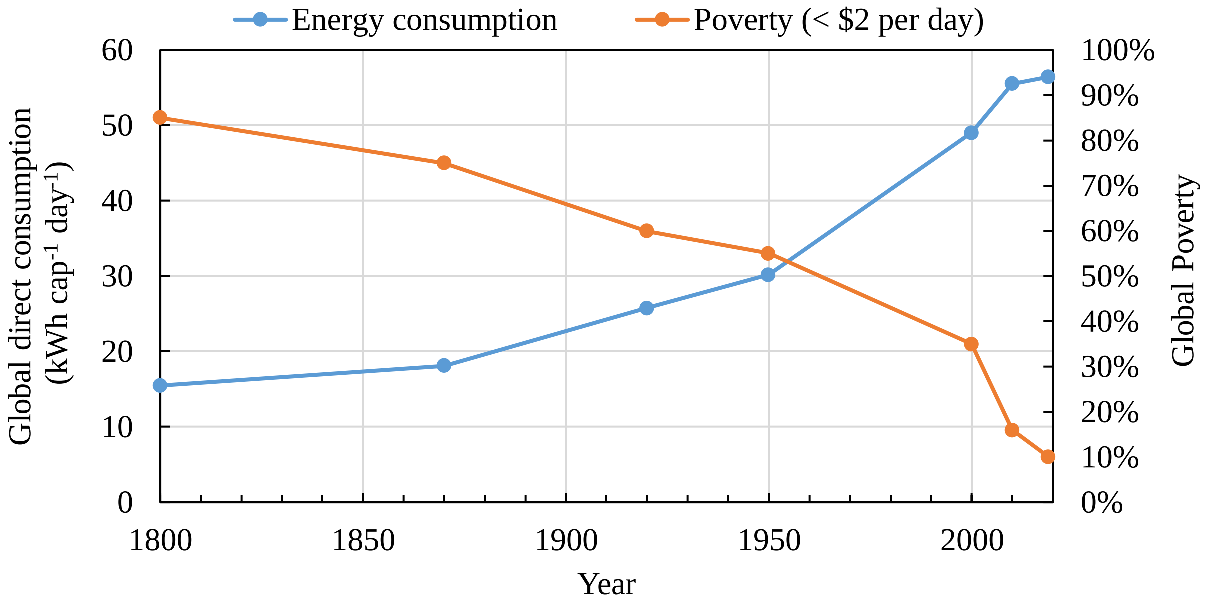

Figure 1 – Energy consumption per capita per day and global poverty rate from the year 1800 to 2000. Poverty is considered as "living-in-poverty", which is living with less than $2 per day (adjusted for inflation with respect to the year 2002) [4]. Direct primary energy consumption does not take account of inefficiencies in fossil fuel production [5].

In the 20th century, however, it has become evident that this rapid industrialization and increase in energy use, especially from fossil fuel sources, has come at a cost that was not foreseen. This cost is, of course, the pollution of our oceans and atmosphere and the resulting global crisis of climate change [6, 7]. Given that it is likely that the use of energy will continue to increase as more and more people are pulled out of poverty and increase their living standard, we must find better solutions to how we produce and consume energy in light of this crisis [6, 7]. In order to combat global climate change, the scientific consensus seems to be that we must reduce the global human-sourced output of greenhouse gases (*i.e.* CO_2, N_2O, CH_4, and water vapor) that we release into the oceans and atmosphere. We must both (i) reduce our per capita energy use and (ii) change our sources of energy from highly polluting non-renewable sources (such as coal, oil, and natural gas) to renewable, carbon-neutral sources, such as wind, solar, hydroelectric, geothermal, and nuclear [6-8].

Reducing our per capita energy use, especially in highly industrialized countries, would require a fundamental shift in how individuals and families choose to live. Modern, yet wasteful, amenities such as home air conditioning, which is fairly common in the US and Canada, contribute a significant amount to the total household energy consumption (~12%) [9]. Other life choices, such families choosing to live in suburbs or rural areas, require significantly more driving, and therefore more fuel, than would otherwise be necessary. Both of these examples are not necessarily a result of necessity in most cases, but rather a product of bad urban design, poor planning, and the life choices our society incentivizes. The way a city, state, or government decides how to incentivize certain energy inefficient choices, such as where and how to live and work, seems to be necessary to help slow down the energy and climate crisis.

Anyone who considers the global climate crisis a significant threat to our current society and way of life would also agree that the conversion away from greenhouse gas producing energy sources is not only important, but necessary. Despite recent advances to convert our energy system to a renewable or carbon-neutral source, the global fossil fuel consumption rate continues to rise at a disturbingly fast rate [5]. Global energy consumption shows that about 85% of the total primary energy consumption is in the form of fossil fuels or up to 97% when correcting for inefficiencies in the conversion process from the source fuel to electrical energy (Figure 2) [5, 8, 9].

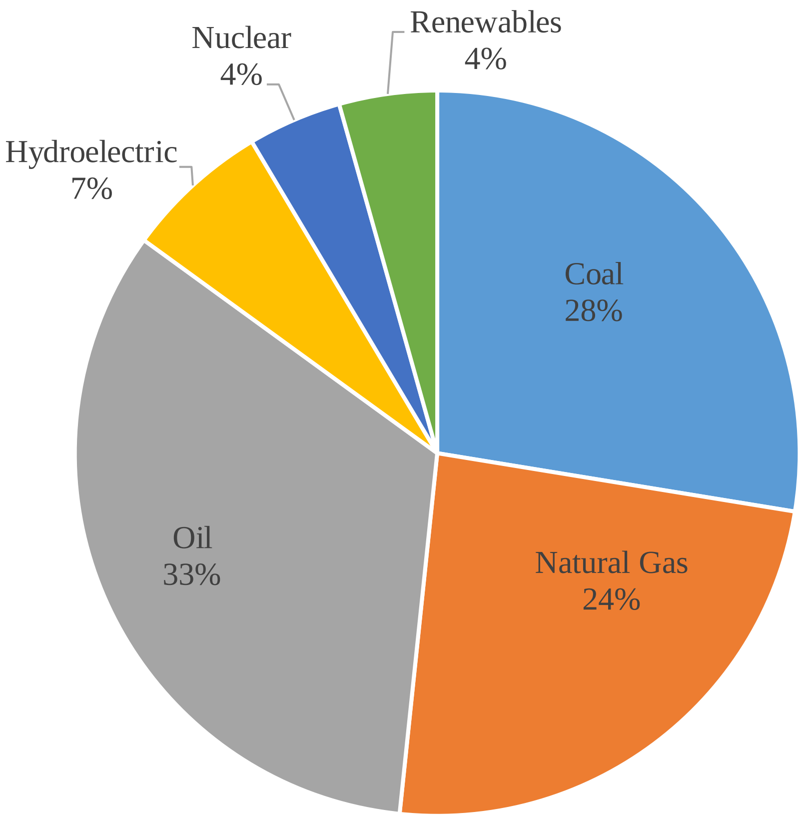

Figure 2 – Worldwide primary energy consumption by source in 2020 [5, 9].

There are a few promising solutions to convert the world energy production from non-renewable to renewable sources. As you may know, renewable resources such as wind, hydrothermal, solar and geothermal, are all fantastic technologies that offer very little waste over the life cycle of their use [10, 11]. Despite the energy needed and CO_2 inevitably emitted to build, transport, and maintain these new technologies, the long-term reduction of CO_2 emitted more than compensates for these emissions [10, 11]. Coal and natural gas emit between 200 g_{CO2eq} kWh^{-1} to more than 1000 g_{CO2eq} kWh^{-1} over their entire life cycle, depending on whether carbon capture and storage is used or not, respectively [10, 11]. Renewable energy sources, on the other hand, emit at most 100 g_{CO2eq} kWh^{-1} in the worst case and on average below 50 g_{CO2eq} kWh^{-1} over their entire life cycle [10, 11].

Unfortunately, these renewable energy sources are inherently intermittent and would require some type of storage mechanism (*i.e.* smart-grid technology) to meet energy demands at times the renewable energy sources are not producing energy [12, 13]. Nuclear energy, which is another low-carbon energy source, offers continuous, stable, and geographically dense energy while offering similarly little waste relative to fossil fuels over the life of their use [14]. Albeit nuclear power has had quite a bad reputation in media and pop culture since its invention in the mid-20th century, innovations in Generation IV nuclear reactors have the possibility to completely revolutionize energy generation with unparalleled safety and minimal waste, even compared to other renewable technologies [15]. However, even considering we re-invest into the development of nuclear energy, it is unlikely that nuclear power will be the sole source for energy production, especially in the near future. Therefore, if we intend to increase the use of renewable energy sources, like wind and solar, there is a need to develop a stable, efficient, fast, safe, and easily producible energy storage mechanism.

Why are batteries the best choice as an energy storage mechanism?

In this section, the case will be made as to why batteries are not only the best choice in terms of performance for consumer electronics and other small applications, but also for grid level storage and transportation (*i.e.* cars, trains, airplanes, *etc.*). Now, without making too many assumptions, the most straightforward way to practically store electrical energy would be with a battery. After all, most people are relatively familiar with the devices since they appear frequently in our everyday life. We use batteries in most, if not all, portable electronics from the remote control for our TV, to the cellphone in our pockets, to, more recently, in the cars that we drive. However, this is by far not the only way we could imagine of storing energy.

The most common large scale energy storage device is, surprisingly, gravity. Pumped hydroelectric storage stores up to 9000 GWh globally, which accounts for 94% of the energy stored, and produces 121 GW globally [16, 17]. This mechanism consists mainly by pumping water to a higher altitude, effectively increasing the gravitational potential energy of the water, similar to running a hydroelectric dam in reverse. This water can then be run through the dam turbines later to produce electricity. Another technology, such as flywheels, have been used as an energy storage mechanism famously in Formula 1 racing with the advent of the Kinetic Energy Recovery System (KERS) [18]. This device was comprised of a small, dense wheel that stores kinetic energy from the car's inertia during braking by speeding up, then was released during acceleration by reducing the speed of the flywheel by connecting it to the output of the car.

However, as should be apparent from these examples, they have their own set of pros and cons, especially in the use case as a grid-level energy storage. Other storage mechanisms, such as hydrogen storage, compressed gas storage, or other chemical reactions offer similar set of pros and cons. The most pertinent characteristics of large-scale energy storage devices or mechanisms can be reduced to their (i) response time, (ii) energy and power density, and (iii) production feasibility and cost. These characteristics will now be discussed and compared with battery-based storage devices.

Response time

In 2017, the government of South Australia decided, after years of blackouts that culminated in many severe blackouts in 2016, to transition their energy system to renewable sources. The first project intended to support this goal would end up being the largest battery-powered energy storage device in the world [19]. The battery farm, named the Hornsdale Power Reserve (HPR), was constructed by Tesla Inc. in 2017 and consisted of 129 MWh of battery reserve with the capability of supplying up to 100 MW of power (Figure 3) [20, 21]. The real value of this battery reserve, however, was exemplified by not only the ability to supply and store energy over the normal load demand of an average day, but also in the ability to supply power extremely fast and reliably in emergency situations.

Figure 3 – Hornsdale Power Reserve in South Australia, built in 2017. The 127 MWh of batteries, supplied by Tesla Inc., are capable of supplying up to 100 MW of power essentially instantly in case of emergencies [22].

Normally, when a power station is tripped and supply is lost, fast emergency backup generators quickly turn on to maintain a sufficiently high power. Unfortunately, the speed of these backup generators is too often not fast enough, requiring between 6 s to 60 s to reach maximum power [23]. In the case of a major trip, like what happened on August 25th, 2018 in South Australia, this delay would have been simply not fast enough to avoid an underfrequency event, which can cause higher strain on the electrical grid system, loss in revenue for the energy company, and potentially a loss of service to customers [19, 23]. However with the construction of the HPR, given the incredible speed of battery-powered backup systems to ramp up to maximum power, underfrequency load shedding, which is the cutting off of certain customers' electricity in order to lower demand, was avoided [23]. Experiments and reports from this event showed that the battery backup system was able to deliver an additional power within 134 ms, safely maintaining the frequency above the underfrequency cutoff value [23]. This type of system not only maintains the stability of grid systems and makes renewable energy production feasible, but saves the utility company, and therefore the customers, money by avoiding lost revenue from a loss of service to their customers [23]. Adding more capacity in the form of lithium ions (Li^+ ion) batteries would lead to even more stability in the electrical grid system and make the need for emergency generators all but obsolete.

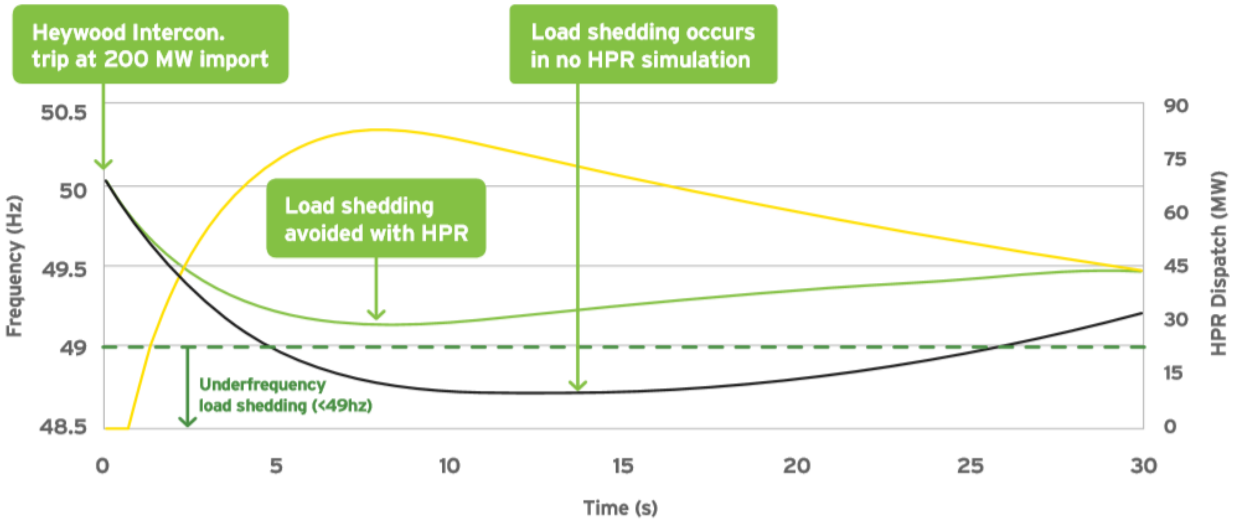

Figure 4 – Tesla Powerpack at the Hornsdale Power Reserve (HPR) in South Australia. The fast Frequency Control Ancillary Services (FCAS) response time of the HPR stopped the underfrequency load shedding from being necessary and saves power companies millions of dollars in lost revenue by avoiding power outages. Reprinted from [23].

Energy density and power density

Since the first commercialization of the modern Li^+ ion battery in the early 1990's, the energy and power density of batteries have had the ability to power cars, trucks, and other land-based vehicles. Only recently, with the advent of companies like Tesla Motors and the motivation of legacy carmakers like BMW and Nissan, have the economies-of-scale been developed sufficiently in order to make a compelling electric vehicle at a low cost. Before the unveiling of the first Tesla roadster in 2007-2008, the prevailing sentiment among legacy car manufacturers as well as the media was that a completely battery-powered car would not be feasible or be able to compete with the contemporary fossil fuel powered vehicles of the time. We have all heard the main objections against electric cars: they are too slow, too expensive, impractical, and do not go far enough on a charge (*a.k.a.* range anxiety). The first commercial electric car by a major automaker, the 1996 General Motors EV1, didn't do too much to disprove those fears. Although the car was known for being fairly quick, thanks to the instantaneous torque available from its electric motor, the car was, among other things, unattractive. Furthermore, the range was limited by its lead acid battery and the top speed was electronically limited to 80 mi h^{-1} (128 km h^{-1}). The second generation of the EV1 utilized nickel-metal hydride (NiMH) batteries, which improved the performance characteristics; however, it was not until the Tesla Roadster in 2008, with its Li^+ ion battery, that people began to be convinced of the practicality and potential of the technology.

The Tesla Roadster was, in my opinion, a monumental event in the automotive industry. It was able to convince the experts in the industry, such as GM VP Bob Lutz and automotive engineer Sandy Munro, as well as the public at large that not only could electric vehicles match the abilities of their fossil-fueled counterparts, but that it could actually outperform them in almost every respect [24, 25].

Figure 5 – (a) The GM EV 1 was the first practical and commerically available all-electric vehicle [26]. (b) The 2008 Tesla Roadster, the car that changed the perception of electric vehicles in the industry and media [27].

Batteries offer one of the highest energy and power densities out of all other clean storage mechanisms. As shown in Figure 6, Li$^+$ ion batteries exhibit a specific energy density of between 100-300 Wh kg^{-1} while the only other technology with a higher specific energy density are fuel cells. The specific power density of batteries is, however, generally greater than fuel cells, which in combination with its good specific energy density, high efficiency, and fast response time, makes batteries one of the best choices as an energy storage mechanism.

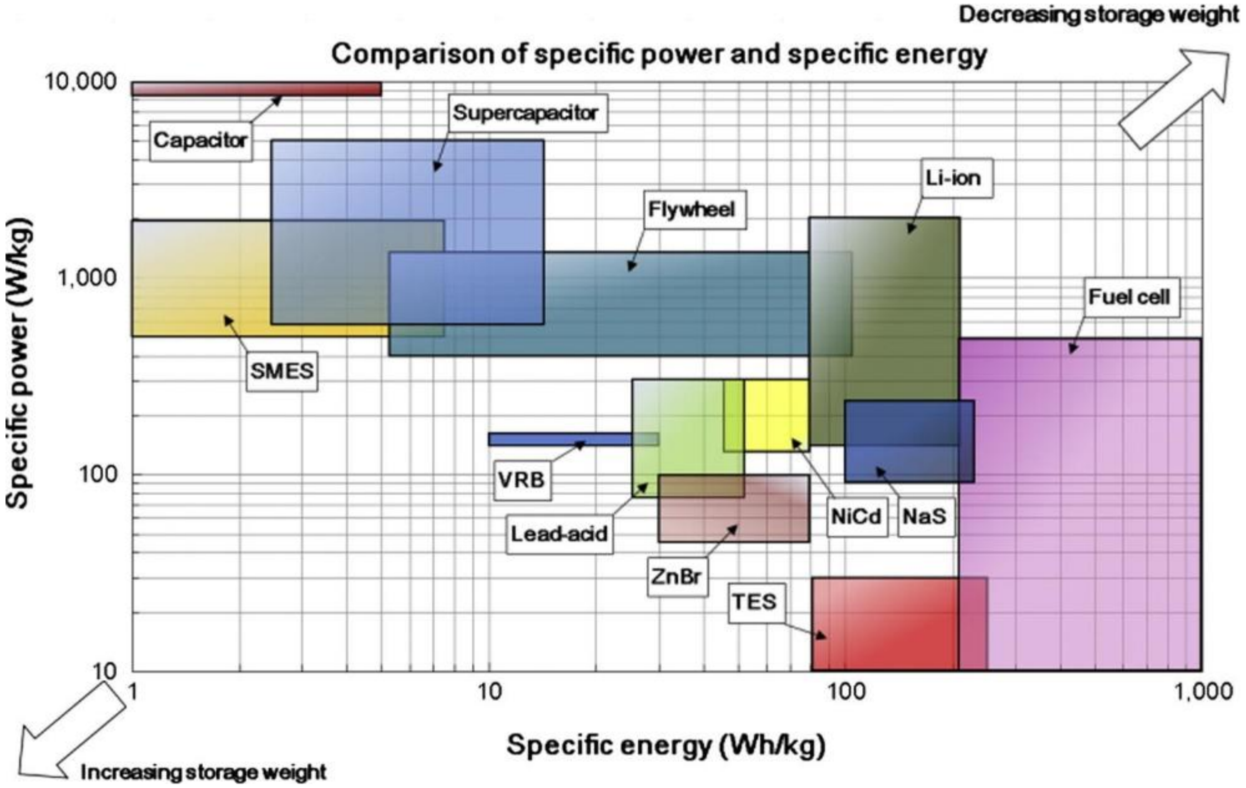

Figure 6 – Comparison of specific energy and specific power of various energy storage mechanisms. Reprinted from [28].

Efficiency

Many of the same advantages that batteries offer for grid-level energy storage also translate for their use in electric vehicles. A main argument for battery-powered electric vehicles is that it is one of the few technologies that becomes cleaner as the source of electricity evolves away from fossil fuels. Although other technologies for electric vehicles, like fuel cells, also have this property, the "extra steps" required to convert that energy into electricity in the first place make them less desirable. Even assuming that the power source comes from a clean renewable source, extra steps are necessary for fuels cells given that the hydrogen must be stored in the vehicle at high pressure, converted into electricity *via* a fuel cell, store the produced electricity in an on-board battery, and then finally convert the electrically energy in the battery into usable motion *via* an electric motor. It should be obvious that this process is significantly more complex than simply using a large battery and the overall cycle efficiency is consequently negatively impacted.

Batteries, on the other hand, have the advantage of delivering energy with high efficiency (> 85%) when considering losses incurred during charging, storage, and use [28-31]. Other storage mechanisms, such as hydrogen storage or compressed gas storage, will necessarily be lower efficiency given the more steps required to convert the energy stored into usable electrical energy [28-31]. For example, compressed gas storage requires compression, *via* a pump, to be "charged", then "discharged" *via* a turbine and generator. This process reaches a total efficiency of approximately 50%-70%. Similarly, hydrogen storage requires these steps as well, but also the reaction to produce hydrogen, *via* steam reforming or water electrolysis, then run through a proton-exchange membrane to convert the stored energy into electricity [28-31]. Using electrolysis (from renewables) to produce hydrogen, the full process yields a total cycle efficiency between 20% and 40% [30]. Comparatively, batteries are charged directly with incoming electricity and can directly output electricity. The reduction in the number of "steps" yields a storage device that has a roundtrip efficiency between 85% and 97%.

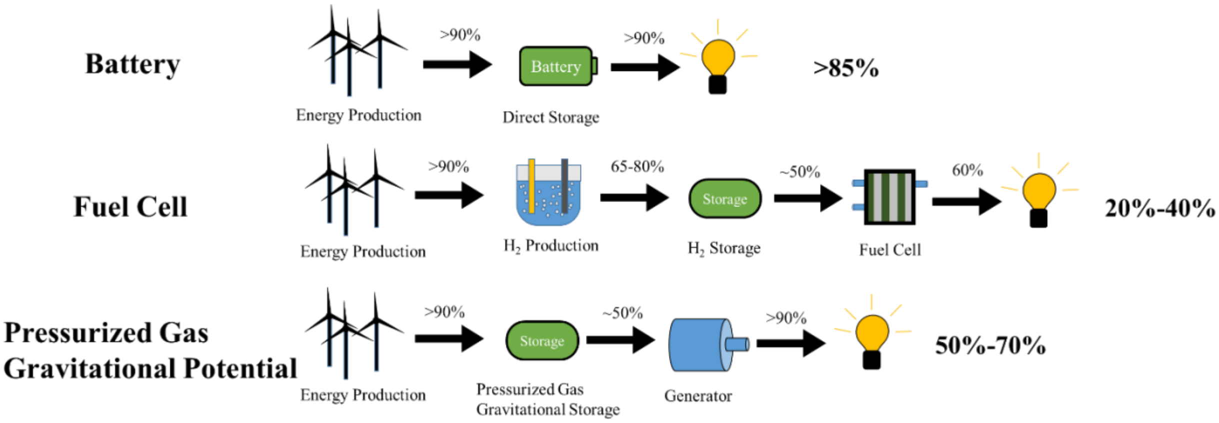

Figure 7 – A pictogram showing how the number of steps reduces the overall efficiency of a grid-level storage technology. Each arrow in the pictogram represents a process where energy loss could occur due to inefficiencies.

Production feasibility and cost

Finally, thanks to the already large market for battery-powered devices, batteries can be produced relatively cheaply and on a large scale. For example, the Tesla Gigafactory, located in the Nevada desert, is slated to produce more battery capacity than all other battery manufacturers combined, with a total of up to 35 GWh yr^{-1} [32]. According to Bloomberg, battery cell production cost across the entire market has dropped below 200 \$ kWh^{-1} in 2018 down from over 1000 \$ kWh^{-1} in 2010 [33]. Tesla, the market leader, has had costs below 200 \$ kWh^{-1} since 2016 and some estimates claim that it has reduced costs down to 158.27 \$ kWh^{-1} [32, 33]. As manufacturers ramp up production and reach the necessary economy-of-scale to offer batteries at a reasonable cost, the availability of not only the production but the recycling of batteries should increase accordingly. Companies like Tesla and BMW are already offering deals to customers to recycle used batteries [34, 35].

As for the cost of battery-powered vehicles, the main cost is of course the battery itself, with up to half of the cost coming from the battery and its management systems. But amazingly, companies have enabled the use of Li$^+$ ion batteries for electric vehicles by dramatically reducing the cost.

Given the previous estimates of 114 \$ kW h^{-1} for Tesla's batteries, and a battery pack size between 50 kWh and 62 kWh for their Model 3 Sedan, the total cost of the battery can be estimated to be about 8,000 \$ and 10,000 \$ with a driving range between 220 miles and 300 miles, respectively [36]. This enables Tesla to sell their premium Sedan between \$30,000 and \$40,000 with a 20% gross margin [36, 37]. Similarly BMWs i3 sedan, the Chevy Bolt, and the Nissan Leaf have been frontrunners in the electric vehicle market, where the industry average of battery cost is approximately 150 \$ kW h^{-1} [37]. The ability of manufacturers to make a profit at a reasonable cost to consumers is what will ultimately drive the mass conversion away from fossil fuels for transportation.

Problems and future research

At the moment, Li^+ ion batteries still have problems that need to be solved. For example, the mining, recycling, and disposal of current Li^+ ion batteries are not a standardized process and is fairly difficult due to their complex internal structure [38]. Some technologies, such as "green" or solid-state electrolytes, non-transition metal active materials, and sodium-ion batteries aim to address the environmental and safety issues that are currently plaguing the technology today. Other technologies, such as high specific energy density materials, like the use of tin oxide and silicon, aim to also increase the specific energy density of Li^+ ion batteries, but may be plagued by other technological considerations, such as thermal runaway or electrochemical stability. These new technologies should not only improve production and post-use environmental impact but should further reduce the cost and weight of batteries for all modes of transportation. Therefore, in the following section, the state of the art in Li^+ ion battery technology will be discussed in order to get a better understanding of the technology that currently exists and the problems that need to be solved for future Li^+ ion battery technology.

Batteries: State of the art

The first primary (non-rechargeable) electrochemical battery was the voltaic pile invented in 1800 by Alessandro Volta [39]. Although at the time he did not understand the exact mechanism by which his invention actually produced electricity, it opened up the opportunity for others to build upon his groundbreaking discovery. Years later, in 1859, French physicist Gaston Planté invented the first modern secondary (rechargeable) battery, the lead-acid battery [40]. This invention was truly a turning point for the use of electrical energy for a wide range of applications. It made possible the ability to store electrical energy directly without the need to convert the energy back and forth into some other form for storage. Throughout the 20th century, many other chemistries were developed that expanded the energy density, power density, and safety of both primary and secondary batteries [41, 42]. It was not until the discovery of the $LiCoO_2$ cathode, and therefore the modern Li^+ ion battery, in the early 1980's by physicist John B. Goodenough that a sufficiently high specific energy density could be achieved that had the potential to revolutionize how we use energy [43].

Mechanism of a secondary Li$^+$ ion cell

A Li$^+$ ion battery produces electrical energy *via* two electrochemical reactions connected ionically *via* an electrolyte. When these two reactions are subsequently connected through an external electrically-conducting circuit, a current flows, producing usable electrical energy. Within a Li$^+$ ion battery, there are three major components: (i) a positive electrode, (ii) a negative electrode, (iii) and the electrolyte. The electrode active materials undergo reversible reduction-oxidation (redox) reactions while Li$^+$ ions are transferred back and forth between the two electrodes *via* the electrolyte. During charging, Li$^+$ ions in the positive electrode active material move to the negative electrode active material, *via* the electrolyte. During discharging the reverse reaction occurs, where Li$^+$ ions are transferred from the negative electrode to the positive electrode, similarly *via* the electrolyte. During both charging and discharging, electrons are transferred between the two active materials *via* the current collector and an external electrical circuit. A Li$^+$ ion battery with $LiCoO_2$ and graphite as the positive and negative electrode active material, respectively, is shown in Figure 8. During charging, the oxidation state of cobalt in the positive electrode is changed from Co(III) to Co(IV) as Li$^+$ ions are deintercalated. Likewise, Li$^+$ ions intercalate into the graphite between graphitic sheets on the negative electrode, where the charge of one Li$^+$ ion is shared among six carbon atoms. Then during discharging, the reverse reaction occurs. Figure 8 shows the movement of the Li$^+$ ions and electrons during charging and discharging as well as the state of both electrodes when the battery is charged and discharged.

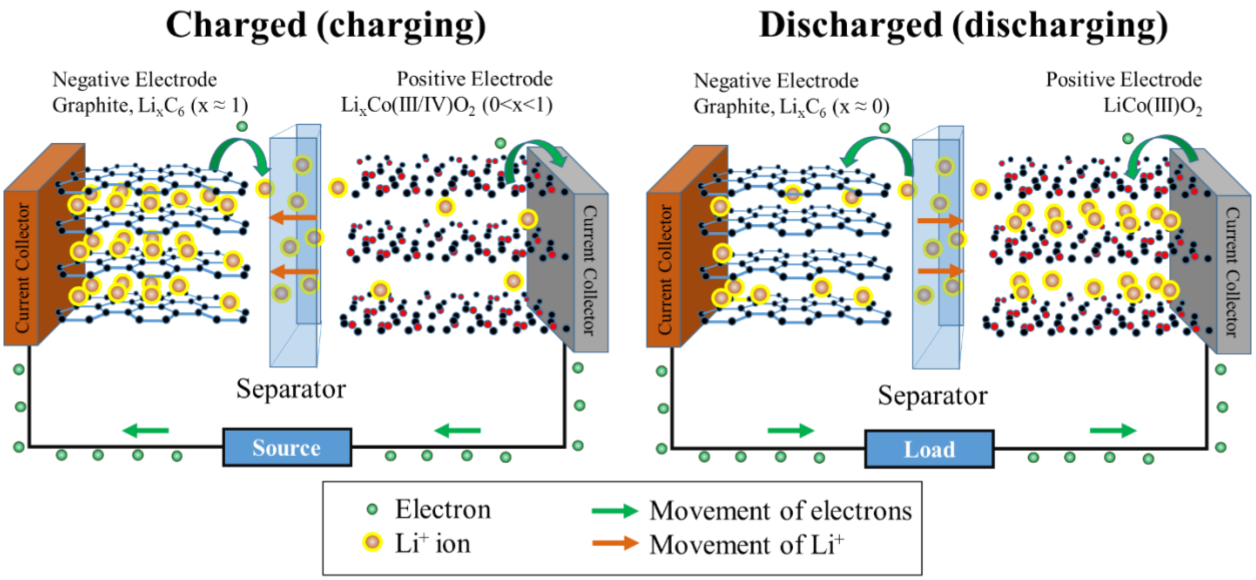

Figure 8 – Schematic showing the movement and location of Li$^+$ ions and electrons during discharging and charging of a Li$^+$ ion battery using two intercalation-type active materials were used for this representation, namely graphite for the negative electrode and $LiCoO_2$ for the positive electrode.

The electrolyte is an ionically-conducting and electrically-insulating medium that allows the Li^+ ions to move between the negative and positive electrode. The electrolyte usually contains a salt of lithium, such as $LiPF_6$ or LiTFSI, dissolved in an organic solvent, such as ethylene carbonate, dimethyl carbonate, diethylene carbonate, or a mixture of these three compounds [44-46]. Additives can be used to improve the chemical stability, conductivity, and other characteristics specific to the chemistry of a given cell [46]. But apart from lithium salts in organic solvents, other formulations such as ionic liquids, solid or gel electrolytes, and composite polymer electrolytes are being explored due to their unique electrochemical properties [47, 48]. These properties usually include larger stable potential windows, safer operation in high or low temperatures, higher energy density, and safer operation due to the less flammable nature as compared to a liquid electrolyte [47, 48]. Other solvents, Li-salts, and additives are currently being explored to improve the performance characteristics of the electrolyte [46].

As for the active material of a battery, the three most important qualities are: (i) the ability to store as many Li^+ ions as possible, (ii) the insertion/deinsertion of Li^+ ions at each respective electrode should occur at different potentials, and (iii) the process of Li^+ ion insertion and deinsertion should be reversible. The product of the first two qualities, *i.e.* the number of Li^+ ions that are able to be stored within the material, *i.e.* the sum of the charge of all the Li^+ ions transferred, and the potential difference between the two intercalation/deintercalation reactions, ultimately determines the specific energy density of the battery cell. Practically, the total charge of a battery is just the product of the applied current, I_{applied}, over the total time this current is applied, t, ignoring of course other inefficiencies. By then, dividing this product by the total mass of the active materials, m, the specific charge density, Q_{total}, commonly expressed in mAh g^{-1}, can be determined (as shown in Equation 1.1).

$$Q_{total} = \frac{I_{applied} \times t}{m} \tag{1.1}$$

However, the specific charge density is only half of the battle. To truly quantify the value of a given battery system, the specific energy density should be known. Therefore, one must then take the product between the specific charge density and the difference between the redox potentials of the positive and negative electrodes, ΔV, to determine the specific energy density, commonly expressed in Wh kg^{-1}, as shown in Equation 1.2.

$$E_{total} = \Delta V \times Q_{total} \tag{1.2}$$

It should be noted that throughout literature, however, the specific charge density and the specific energy density are both referred to as the specific energy density. This is usually the case since the redox potential, when comparing active materials in a half-cell, are similar and the specific charge density is a more meaningful quantity for comparisons. Nevertheless, as the reader may have already guessed, it would be advantageous to maximize both the potential difference between the positive and negative electrodes and the total charge stored/transferred between the electrodes during charging and discharging.

Other components of the Li^+ ion battery, such as the current collectors, separator, and battery casing also play an important role in the performance characteristics of a battery and ultimately determine the energy density, power density, and thermal characteristics of the battery. Minimizing the weight of the "inactive components" and extrinsic properties of the "active components" is the ultimate goal to fully optimize a given chemistry. For example, the relative mass percent of the current collector to active material is an important "extrinsic" characteristic of a commercial Li^+ ion battery that helps maximize the specific energy density of a given cell. Therefore, in commercial cells, the active material layer, that is the layer that actually participates in the electrochemical reaction, is coated on both sides of the current collector with the highest possible thickness and density. However, limitations of electrical and ionic conductivity, and mechanical stability ultimately limit the thickness and density of the active layer. The active layer thickness of commercial Li^+ ion batteries usually is around 100 µm. Contrarily, the current collector material, which is usually made of copper and aluminum for the negative and positive electrodes, respectively, is manufactured as thin as possible while maintaining sufficient electrical conductivity and mechanical strength. In commercial batteries, the current collector is usually less than 10 µm thick.

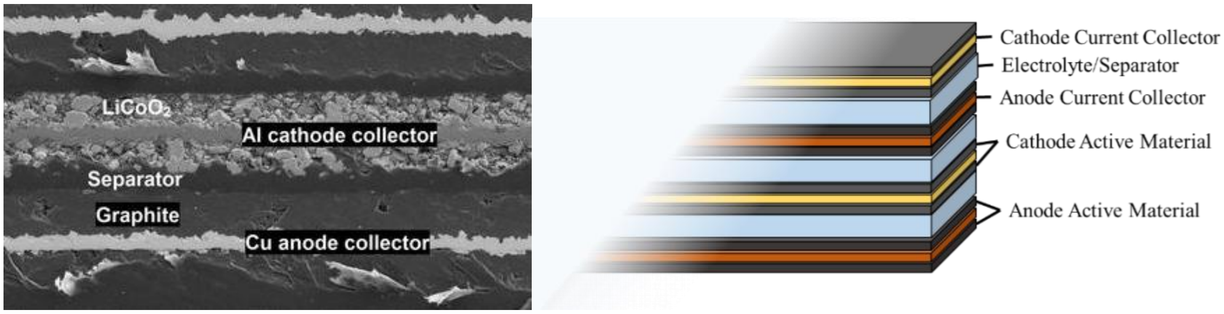

Figure 9 – (a) Cross-section of an iPhone 6 battery, reprinted from [49] and (b) a schematic representation of the construction of the positive electrode, negative electrode, electrolyte, and separator of a commercial Li^+ ion battery. In prismatic cells, the layers of each respective electrode would be connected in parallel with tabs that are soldered together on the exterior. In cylindrical cells, a single layer of positive electrode, negative electrode, and separator are rolled together until the desired diameter is attained.

The active layer of a positive or negative electrode is usually composed of three main components: (i) the active material, (ii) a conductive additive, and (iii) and binder. The active material in a conventional negative electrode usually consists of graphite, given its relatively good specific capacity (350 mAh g^{-1}), electrochemical stability, reversibility, and low cost [50]. The most common active materials for the positive electrode are $LiCoO_2$ and $LiFePO_4$, given their relatively good specific capacity (> 110 mAh g^{-1}), electrochemical stability and electrochemical reversibility [51]. $LiFePO_4$ also has the advantage of being low cost as compared to $LiCoO_2$, albeit with a slightly lower specific capacity [51]. The conductive additive in conventional batteries is typically also a carbon material, like carbon black, which increases the electrical conductivity of the layer without adding too much weight. Finally, the binder is commonly a polymer, like poly(vinylidene difluoride) (PVDF) or carboxymethylcellulose/styrene-butadiene rubber (CMC/SBR), whose purpose is to bind these two other components together and attach them to the current collector [52, 53].

There are three main types of active materials used for Li^+ ion battery electrodes: intercalation-type, alloying-type, and conversion-type. Most conventional Li^+ ion batteries utilize intercalation-type materials; however, alloying and conversion-type batteries offer higher performance characteristics over intercalation-type materials, although there remains some unsolved issues with these new types of materials.

Intercalation-type active material

In a conventional Li^+ ion battery, the negative and positive electrodes are both made of an intercalation-type active material. The negative electrode is typically composed of a graphitic carbon while the positive electrode is usually composed of a lithiated oxide of transition metals, like cobalt, iron, or manganese [51]. $LiCoO_2$ is one of the most common positive electrode active materials given its high electrode potential and relative physicochemical stability [51]. The corresponding reversible half-reactions for the positive electrode and negative electrode, respectively, in a Li^+ ion battery composed of $LiCoO_2$ and graphite can then be written as follows:

Positive electrode: $\mathrm{LiCo(III)O_2} \rightleftharpoons \mathrm{Li_{1-x}Co(III/IV)O_2} + x\mathrm{Li^+} + e^- \quad 0 < x < 1$

Negative electrode: $\mathrm{C_6} + \mathrm{Li^+} + \mathrm{e^-} \rightleftharpoons \mathrm{LiC_6}$

Graphite, which is an intercalation-type active material, stores Li^+ ions by inserting Li^+ ions in between graphitic sheets. This reaction is a relatively “easy” reaction and only requires a small overpotential of about 0.1 V *vs.* Li^+/Li [50]. The low redox potential of graphite has been attributed to the similar size of the graphitic layer spacing to the Li^+ ion radius as well as the high electron mobility resulting from the out-of-plane conjugated pi-bonds of the graphitic sheet. Graphite also forms a passivation layer during the 1st lithiation called the solid-electrolyte interphase (SEI). During the 1st lithiation, the low potential of the negative electrode causes the electrolyte to decompose. This layer is thought be composed of mostly lithium carbonates but also lithium fluorides, lithium oxides, and other related species [44]. Although this layer consumes electrolyte, it acts a good interphase between the electrolyte and graphite which prevents further electrolyte decomposition and allows for better cyclability, temperature dependence, power density, and safety [44]. Graphite has a maximum theoretical charge density of 372 mAh g^{-1} with practical values generally reaching 350 mAh g^{-1} [50]. The maximum theoretical specific charge density of the most energy dense positive electrode material, $LiCoO_2$, is 274 mAh g^{-1}, but practically only reaches 150 mAh g^{-1} due to the inability of all the Li^+ ions to be removed from the CoO_2 lattice without irreversibly damaging the material structure [43, 50].

These types of materials are generally electrochemically and physically stable mainly due to the low volumetric change of only a few percent between the lithiated and delithiated states. Their main downside is that they offer relatively low specific energy density per unit mass or volume compared to other active material types. Modern Li^+ ion batteries offer up to 250 Wh kg^{-1} for the most energy dense chemistries while others excel in longevity, safety, or other aspects [54, 55]. The following tables give a brief overview of these chemistries that all function on the intercalation method for storing Li^+ ions. Table 1 shows some common positive electrode intercalation materials that are used in commercial batteries. Table 2 shows the two most common negative electrode intercalation-type materials, although graphite is used by most commercial batteries.

Table 1 – Intercalation-type positive electrode chemistries.

Chemistry	**Potential** V *vs*. Li^+/Li	**Charge Density** mAh g^{-1}	**Cycle Life**[a]	**Safety**	**Environmental Impact**	**Cost**
$LiFePO_4$	~ 3.5	120	> 2000	Safe	Good	Low
$LiNi_yMn_xCo_zO_2$	~ 4.2	160	> 500	Poor	Fair	High
$LiNi_xCo_yO_2$	~ 4.2	200	> 500	Poor	Fair	High
$LiCoO_2$	~ 4.2	200	> 500	Poor	Fair	High
$LiMn_2O_4$	~ 4.2	150	> 200	Moderate	Fair	Med

[a] *cycles until capacity reaches 80% of initial capacity.*

Table 2 – Intercalation-type negative electrode chemistries.

Chemistry	**Potential** V *vs*. Li^+/Li	**Charge Density** mAh g^{-1}	**Cycle Life**	**Safety**	**Environmental Impact**	**Cost**
$Li_4Ti_5O_{12}$	~ 1.5	~ 160	> 5000	Safe	Good	Medium
Graphite	~ 0.1	~ 350	> 1000	Safe	Good	Low

In addition to the properties listed in Table 2, lithium titanate, $Li_4Ti_5O_{12}$, is also able to discharge at relatively high rates as compared to graphite due to its resistance to lithium metal plating during fast charging [56]. It also has the properties of close to zero volumetric expansion during lithiation and no solid-electrolyte interphase (SEI) formation due to its high redox potential.

Alloying-type material

Another way to increase the total charge stored in a Li^+ ion battery active material is by using an alloying-type material. These materials are commonly metals, such as tin, silicon, and antimony, which form an alloy with lithium rather than inserting into interstitial sites within the material. These materials are commonly used as a negative electrode due to low potential at which lithium interacts. Furthermore, they generally offer a higher specific energy density when compared to the more conventional intercalation-type material. The most common alloying-type material used in recent research is silicon. Silicon has an incredible theoretical specific charge density of up to 4200 mAh g^{-1} and a very low redox potential of between around 0.1 to 0.5 V *vs.* Li^+/Li [57-59].

$$\mathrm{Li}_x\mathrm{Si} \rightleftharpoons \mathrm{Si} + x\mathrm{Li}^+ + \mathrm{e}^- \ (0 < x < 3.75) \tag{1.3}$$

Unfortunately, silicon undergoes a large volumetric change between the lithiated and delithiated states, of up to 300%, that leads to a quick decrease in specific capacity after only a few cycles [57-59].

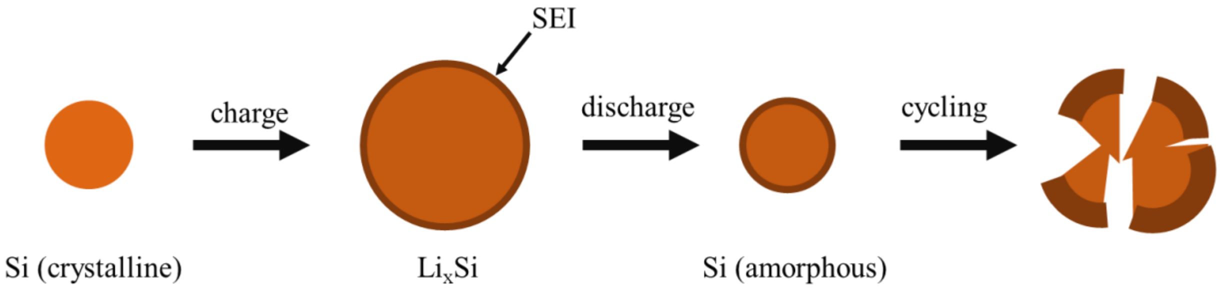

Figure 10 – Schematic of silicon lithiation and delithiation. A solid electrolyte interphase (SEI) forms on the surface of the silicon during lithiation. Then, during cycling, the volume change causes unstable SEI formation and cracking of the silicon due to internal stresses within the silicon. This leads to both the pulverization of the silicon and/or a thick SEI layer that inhibits further lithiation, which prevents further cycling.

Other alloying materials, such as tin and antimony, undergo this volumetric change to a lesser extent, however, they in turn generally offer a lower specific charge density. The review by X. Zuo *et al.* [57] is a great source for information on alloying-type negative electrodes for Li^+ ion batteries. This review article not only covers the various types of alloying-type materials, but also the mechanisms, phase diagrams, stability, and implementation of these materials in commercial cells. Table 3 shows the properties of just a few alloying-type materials that are currently being researched [58].

Table 3 – Alloying-type negative electrode chemistries.

Chemistry	**Li-ions per atom,** x	**Potential** V *vs.* Li^+/Li	**Charge Density** mAh g^{-1}	**Volume expansion** %
Li_xSi	3.75	~ 0.400	3500 – 4200	> 280
Li_xSn	4.40	~ 0.500	993	~ 240
Li_xSb	3.00	~ 0.900	660	~ 147
a-Li_xC	0 - 0.5	0 - 3	1115	30

The majority of research on these types of materials focus on mitigating the negative consequences of this volumetric change. Recent studies have shown that, generally, controlling the microstructure of the silicon and protecting the interface between the silicon and the electrolyte significantly reduce the negative effects of the volume change. These effects such as pulverization of the silicon, excessive SEI instability, and loss of electronic conductivity seem to be mitigated. Y. Cui *et al.* [60] have devised an interesting solution in which a silicon nanoparticle is supported within a hollow carbon sphere in a "yolk-like" morphology. This design, they claim, allows the silicon particle to expand and contract during cycling into a void volume while isolating the silicon surface from the electrolyte. Other silicon nanostructures, such as nanowires and films both aim to reduce the dimensions of the silicon in order to reduce strain inside the material, although these materials generally still suffer from SEI instability problems [57-59]. The inclusion of silicon nanowires and nanoparticles in composites of other carbon structures, such as 3D mesoporous carbon, graphene, or nanotubes, have aimed to further mitigate the SEI instability, with varying degrees of success [54-60]. In any case, there have been a lot of research in this area given that the potential benefits of alloying-type materials are so great [54-60].

Conversion-type material

Conversion-type materials work not by making an alloying with lithium or by intercalating lithium into some crystallographic structure, but by breaking and forming chemical bonds, effectively transforming the active material molecules into other, lithiated molecules. Some materials that can undergo conversion-type reactions include transition metal oxides, sulfides, fluorides, phosphides, nitrides, and hydrides among others [61, 62]. For the positive electrode, one of the most promising active materials is the lithium-sulfur chemistry [63]. Lithium-sulfur is promising not only for its high specific energy density, but for its relative abundance in nature, benign environmental impact, and low cost. Unfortunately, the major problem with this chemistry is that of the polysulfide shuttle effect, as shown in Figure 11 [63]. The conversion reaction of sulfur includes the progressive transformation of rings of sulfur, S_8, into lithiated polysulfide species of various lengths. These species are unfortunately soluble to varying degrees in most electrolytes, which leads to the subsequent shuttling of the polysulfide species away from the positive electrode and toward the negative electrode through the electrolyte. Although positive electrode chemistries are not the focus of this doctoral work, it is still an interesting area of research when considering high energy density chemistries.

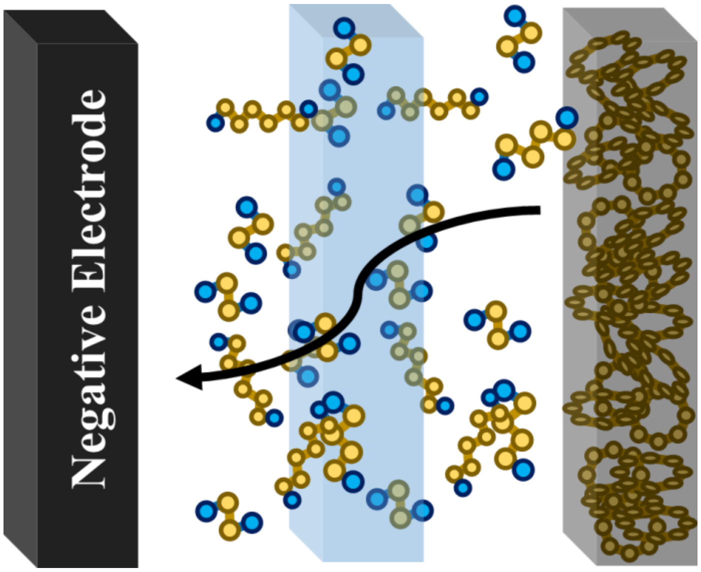

Figure 11 – Sulfur undergoes a conversion reaction that converts S_8 rings into Li_2S *via* intermediate polysulfide species of the form, Li_2S_x ($2 < x < 6$). These intermediate polysulfide species are soluble in most electrolytes and lead to the polysulfide shuttle effect that decreases the cycling performance.

More relevant to the work presented in this thesis, there are a wide range of conversion type compounds for the negative electrode. The aforementioned groups, *i.e.* oxides, hydrides, *etc.*, are widely studied in this field of research. Monoxides, dioxides, trioxides, and tetroxides of transition metals, such as manganese, cobalt, nickel, zinc, and tin have been studied for as a conversion-type negative electrode material [64, 65].

Tin oxide, SnO_2, is an interesting candidate as an active material for Li^+ ion batteries given its relatively low standard redox potential, lower volumetric change between lithiated and delithiated states compared to other conversion-type or allowing-type materials, and its wide range of synthesis possibilities [64, 65]. The conversion reaction of tin oxide differs from the sulfur-based positive electrode reaction previously discussed by that the lithium is stored in another compound, Li_2O, with tin monoxide, another conversion-type material, and then finally tin metal [64, 65]. Interestingly, tin is also an alloying-type material. So, after the two conversion processes are completed, an alloying-type reaction occurs that further increases the specific capacity of the material. The conversion reactions of SnO_2 and subsequent alloying reaction of Sn are given as the following:

$$\mathrm{SnO_2 + 2Li^+ + 2e^- \rightarrow SnO + Li_2O} \tag{1.1}$$

$$\mathrm{SnO + 2Li^+ + 2e^- \rightarrow Sn + Li_2O} \tag{1.2}$$

$$\mathrm{Sn} + x\mathrm{Li^+} + x\mathrm{e^-} \rightarrow \mathrm{Li_xSn} \quad (0 < x < 4.4) \tag{1.3}$$

The theoretical specific capacity of the two first conversion reactions combined is 711 mAh g^{-1}. This reaction, however, seems to be only partially reversible given that the reaction between Li_2O and tin metal into tin oxide is itself not fully reversible; the reasons are not clearly understood [64, 65]. The tin alloying reaction has a theoretical specific capacity of 993 mAh g^{-1} and is more reversible, but also suffers from similar volumetric changes as other alloying-type materials, such as silicon and antimony. The dual behavior of SnO_2, however, makes it an interesting candidate for a negative electrode active material. These two reactions can be used together or isolated, which opens up some interesting synthesis and use considerations.

Main goal of this thesis

In this work, a carbon xerogel (CX) was used as an electrically-conductive 3D support matrix for high specific energy density active materials. The two materials explored are silicon, an alloying-type active material, and tin oxide, a conversion-type and alloying-type active material. The goal was to determine if the use of a CX can mitigate the negative effects associated with the volumetric difference between the lithiated and delithiated states of these high energy density active materials.

A CX is an amorphous hard carbon with an interconnected 3D meso-macroporous structure. These meso-macropores are formed by spherical nodules connected in a rigid “string of pearls”-like structure [66-70]. The tunable meso-macropores are useful to support dopant materials as the CX can be tuned to fit the dopant particle size. The CX is prepared *via* a simple and cheap resorcinol-formaldehyde (RF) sol-gel synthesis where the average meso/macropore size of the CX can be easily increased or decreased by respectively decreasing or increasing the pH of the precursor solution during synthesis [66]. Additionally, a CX has a nominal intrinsic reversible capacity of approximately 200 mAh g^{-1}, albeit this capacity is achieved *via* a linear lithium insertion/deinsertion potential between 0.005 V and 1.5 V *vs.* Li^+/Li [67, 68]. This material should be able to act as a support structure for the dopant materials and offer good electrical conductivity that, in effect, combines the properties of a conductive additive, active material, and a support structure. A schematic of the synthesis procedure of a CX is shown below in Figure 12.

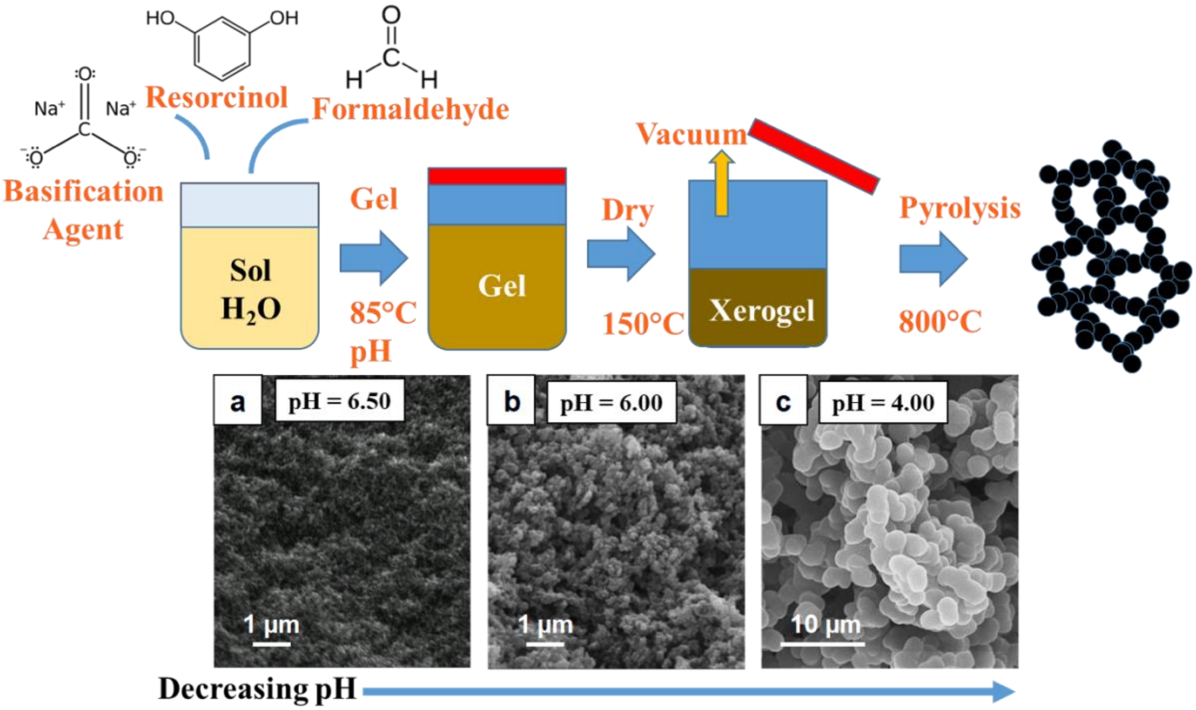

Figure 12 – Synthesis procedure for a resorcinol-formaldehyde carbon xerogel using Na_2CO_3 as a basification agent. Corresponding SEM images of the carbon xerogel morphology are shown when the pH of the precursor solution is changed [71].

Secondly, poly(sodium 4-styrenesulfonate) (PSS) was used as an ionically-conductive binder or coating to further improve the cycling stability of these CX-based alloying-type and conversion-type active materials. The ionic conductivity of this polymer arises from the sulfonate functional groups that are attached to the polymer backbone, as pictured in Figure 13. Additionally, PSS is a water-soluble polymer and, therefore, allows for the synthesis of electrode active materials in an aqueous environment. Water soluble binders have been shown in a previous work [67] to change how the binder forms a composite material with the CX-based active materials and, therefore, likely changes its electrochemical characteristics.

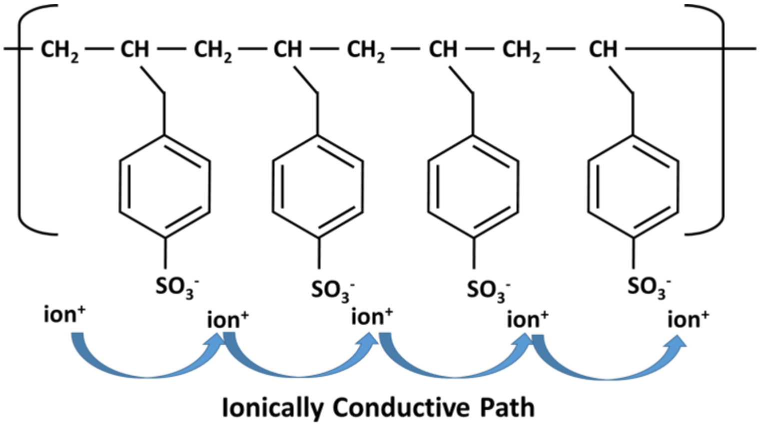

Figure 13 – Molecular schematic of poly(styrene sulfonate) and its proposed mechanism for ionic conduction.

Therefore, in this thesis, the synthesis and characterization of a CX doped with either silicon or tin oxide as an active material for high specific capacity Li^+ ion battery negative electrodes will be explored. PSS will also be used as a protective element, either as a coating or binder, to determine if this material can improve the cycling stability of the Si-CX and SnO_2-CX-based composite electrodes.

Chapter overview

The thesis is divided into 6 chapters, which can be regrouped in 3 sections. The first section is comprised of the characterization of the CX, the second section studies doping the CX with silicon, and the third section studies doping the CX with tin oxide.

Section 1 - Electrochemical model of a carbon xerogel

- In the **first chapter**, the preliminary synthesis, physico-chemical characterization, and electrochemical characterization of the CX are explored. The physico-chemical characterizations include the determination of the pore size distribution, density, and surface area among other properties. The synthesized CX was then processed into an electrode with either PVDF or PSS as a binder. PVDF was used as a reference material to compare the electrochemical performance of the electrodes synthesized with PSS. Electrochemical characterization techniques, such as electrochemical impedance spectroscopy (EIS), cyclic voltammetry (CV), and galvanostatic cycling, are used in conjunction with the physical characterization of the CX to support a proposed model. The proposed electrochemical model for a porous electrode consists of a 3D disordered carbon, such as the CX-based electrodes synthesized in this work. This model, along with the other characterizations in this chapter, can be used to further understand how the CX can best support the high energy density dopants used in the following chapters.

Section 2 – Silicon-doped carbon xerogel

- In **Chapter 2**, the doping of a CX with silicon nanoparticles (SiNPs) *via* impregnation is studied. The three types of impregnations considered in this chapter include introducing the SiNPs into the CX (i) in the resorcinol-formaldehyde (RF) precursor solution, (ii) in the unpyrolyzed resorcinol-formaldehyde condensate, and (iii) in the pyrolyzed CX. The doping of the precursor solution involves including the SiNPs into the precursor RF solution before the gelation of the RF gel. The other two doping strategies, on the other hand, involves relying on the ability of SiNPs to either diffuse or infiltrate into the already formed 3D structure of the RF gel or CX matrix. Although all three types of impregnations could have been tried, only the doping of the precursor solution and the doping of the unpyrolyzed RF condensate were finally studied in this chapter. Physico-chemical and electrochemical characterizations were conducted on both the synthesized active material and composite electrodes with PVDF as a binder. The main results of this chapter were the galvanostatic cycling stability.

- **Chapter 3** explores the use of poly(sodium 4-styrenesulfonate) (PSS) as a protective coating or binder for the CX-SiNPs composite electrodes. The impregnation of the unpyrolyzed resorcinol-formaldehyde condensate was used to prepare the active material. Electrodes were prepared using PSS as a binder or PSS as a coating with PVDF as a binder. These formulations were compared to the composite electrodes that used PVDF as a binder only. This unique binder in combination with the carbon xerogel support matrix seems to offer a unique and promising material for use in a high-capacity Li^+ ion battery negative electrode. A rationale for the improved capacity retention and possible improvement is discussed in a recently published peer-reviewed paper [72]. Similar physico-chemical and electrochemical characterizations were conducted on both the synthesized active material and composite electrodes as in Chapter two.

- In **Chapter 4**, an interesting new synthesis technique based on the magnesiothermal reduction of silica in silicon within the CX is studied. The conversion of silica into silicon has conventionally been achieved by the high temperature carbothermal reaction of silica with carbon, usually well above the melting point of silicon (1410°C). This process, although well-known, is not particularly interesting since the nanostructure of the silicon particles would be lost due to the high reaction temperature. Therefore, the magnesiothermal reduction reaction, which proceeds at about 700°C, is much more interesting since the silica nanoparticles can maintain their nanostructure when they are reduced into silicon. Similar physico-chemical and electrochemical characterizations as in Chapters two and three were conducted on both the synthesized active material and composite electrodes with either PVDF or PSS as a binder.

Section 3 - Tin oxide-doped carbon xerogel

- In **Chapter 5**, the doping of the CX *via* impregnation with tin oxide nanoparticles (SnONPs) is studied. Similar to chapter three, the same three major types of impregnations can be used: including the SnONPs (i) in the resorcinol-formaldehyde precursor solution, (ii) in the unpyrolyzed resorcinol-formaldehyde condensate, and (iii) in the pyrolyzed CX. However, since a reaction between SnO_2 and carbon that forms tin metal occurs at the temperatures within the pyrolysis oven, only the doping of the already pyrolyzed CX was studied in this chapter. Similar physico-chemical and electrochemical characterizations were conducted on both the synthesized active material and composite electrodes as with the Si-doped CX active material and composite electrodes with either PVDF or PSS as a binder. Additional *in situ* XRD measurements were also conducted on the CX doped SnONPs active material (without a binder) in order to see how the SnO_2 species evolve during cycling.

- Finally, **Chapter 6** considers the doping of a carbon xerogel with tin oxide by impregnation with a solution containing the tin oxide precursor compound, sodium stannate trihydrate. This liquid compound can be easily reduced within the CX by controlling the pH of the solution. By this method, it may be possible to more homogenously distribute tin oxide throughout the CX support matrix without depending on the diffusion of solid SnONPs into the CX particles. As in Chapter five, similar physico-chemical and electrochemical characterizations were conducted on both the synthesized active material and composite electrodes with either PVDF or PSS as a binder.

References

[1] Sustainable Development, UN, United Nations Development Programme (UNDP) and University of Bergen. Accelerating SDG 7 achievement policy briefs in support of the first SDG 7 review at the UN high-level political forum 2018. Available: https://sustainabledevelopment.un.org/content/documents/17480PB8.pdf. Accessed on: Mar. 3, 2021.

[2] Britannica, The emergence of western technology (1500–1750). Available: https://www.britannica.com/technology/history-of-technology/The-emergence-of-Western-technology-1500-1750. Accessed on Mar 3, 2021.

[3] M. Ravallion, S. Chen, and P. Angraula, New evidence on the urbanization of global Poverty. Popul. Dev. Rev. 33, 4 (2007) 667–701.

[4] M. Roser and E. Ortiz-Ospina, Global extreme poverty. OurWorldInData.org. Available: https://ourworldindata.org/extreme-poverty. Accessed on: April 4, 2021.

[5] H. Ritchie, Our World in Data. Energy production and consumption. Available: https://ourworldindata.org/energy-production-consumption. Accessed on: April 4, 2021.

[6] NASA, Causes. Available: https://climate.nasa.gov/causes/. Accessed on: Mar 3, 2021.

[7] IPCC, O. Edenhofer, R. Pichs-Madruga, Y. Sokona, E. Farahani, S. Kadner, K. Seyboth, A. Adler, I. Baum, S. Brunner, P. Eickemeier, B. Kriemann, J. Savolainen, S. Schlömer, C. von Stechow, T. Zwickel and J.C. Minx., editors, Summary for policymakers. In: climate change 2014: mitigation of climate change. Contribution of working group III to the fifth assessment report of the intergovernmental panel on climate change. Cambridge University Press, Cambridge, United Kingdom and New York, NY, USA

[8] NASA, Is it too late to prevent climate change? Available: https://climate.nasa.gov/faq/16/is-it-too-late-to-prevent-climate-change/. Accessed on: Mar. 3, 2021.

[9] D. Mayclin. Today in energy. U.S. Energy Information Administration. Available: https://www.eia.gov/todayinenergy/detail.php?id=36692. Accessed on: April 4, 2021.

[10] N.Y. Amponsah, M. Troldborg, B. Kington, I. Aalders, and R.L. Hough, Greenhouse gas emissions from renewable energy sources: A review of life cycle considerations. Renew. Sust. Energ. Rev. 39 (2014) 461-475.

[11] The Parliamentary Office of Science and Technology, Carbon footprint of electricity generation. Available: https://www.parliament.uk/globalassets/documents/post/postpn_383-carbon-footprint-electricity-generation.pdf. Accessed: April 4, 2021.

[12] S. S. Bhalshankar and C. S. Thorat, Integration of smart grid with renewable energy for energy demand management: Puducherry case study. 2016 International Conference on Signal Processing, Communication, Power and Embedded System (SCOPES), Paralakhemundi, India (2016) 1-5.

[13] I. Alotaibi, M.A. Abido, M. Khalid, and A.V. Savkin, A comprehensive review of recent advances in smart grids: A sustainable future with renewable energy resources. Energies 13 (2020) 6269-6311.

[14] M. Lenzen, Life cycle energy and greenhouse gas emissions of nuclear energy: A review. Energ. Convers. Manage. 49,8 (2008) 2178-2199.

[15] G. Locatelli, M. Mancini, and N. Todeschini, Generation IV nuclear reactors: Current status and future prospects. Energ. Policy 61 (2013) 1503-1520.

[16] International Hydropower Association, Pumped storage hydropower. Available: https://www.hydropower.org/factsheets/pumped-storage. Accessed on: April 4 2021.

[17] International Renewable Energy Agency (IRENA). Renewable energy capacity 2019. Available: https://www.irena.org/publications/2019/Mar/Renewable-Capacity-Statistics-2019. Accessed on: April 4, 2021.

[18] FIA Formula 1. Re-writing the F1 rulebook - Part 4: 'cleaner' cars, KERS and the return of slicks. Available: https://www.formula1.com/en/latest/article.re-writing-the-f1-rulebook-part-4-cleaner-cars-kers-and-return-of-slicks.1NUrjfG83a6aE0QSuAkGK8.html. Accessed on: April 4, 2021.

[19] Australian Energy Regulator, Investigation report into South Australia's 2016 state-wide blackout. Available: https://www.aer.gov.au/wholesale-markets/compliance-reporting/investigation-report-into-south-australias-2016-state-wide-blackout. Accessed on: April 4, 2021.

[20] Australian Energy Market Operator Limited, Guide to ancillary services in the national electricity market. (2015). Available: https://www.aemo.com.au/-/media/Files/PDF/Guide-to-Ancillary-Services-in-the-National-Electricity-Market.ashx. Accessed on: April 4, 2021.

[21] Hornsdale Power Reserve, Our vision. Available: https://hornsdalepowerreserve.com.au/learn/. Accessed on: April 4, 2021.

[22] S. Alvarez, Tesla's Powerpack farm in South Australia is about to get 50% larger. Teslarati (2019). Available: https://www.teslarati.com/tesla-powerpack-farm-south-australia-50-percent-expansion/. Accessed on: April 4, 2021.

[23] Aurecon Group, Hornsdale power reserve, year 1 technical and market impact case study (2018). Available: https://www.aurecongroup.com › downloads-library. Accessed on: April 4 2021.

[24] K. Naughton, Bob Lutz: The man who revived the electric car. (2007) Available: https://www.newsweek.com/bob-lutz-man-who-revived-electric-car-94987. Accessed on: April 8, 2021.

[25] B. Schmidt, Auto expert Sandy Munro reveals Tesla Model Y battery pack cost reductions. Available: https://thedriven.io/2020/04/23/auto-expert-sandy-munro-reveals-tesla-model-y-battery-pack-cost-reductions/. Accessed on: April 8, 2021.

[26] Wikipedia. General Motors EV1. Accessed on: April 4, 2021. Available: https://en.wikipedia.org/wiki/General_Motors_EV1

[27] Road & Track, Elon Musk admits to shareholders that the Tesla Roadster was a disaster. Available: https://www.roadandtrack.com/new-cars/news/a29378/elon-musk-admits-to-shareholders-that-the-tesla-roadster-was-a-disaster/. Accessed on: April 4, 2021.

[28] X. Luo, J. Wang, M. Dooner, and J. Clarke, Overview of current development in electrical energy storage technologies and the application potential in power system operation. Appl. Energ. 137 (2015) 511-536.

[29] O. Gröger, H.A. Gasteiger, and J.P. Suchsland, Review—Electromobility: Batteries or fuel cells? J. Electrochem. Soc. 162 (2015) A2605-A2622.

[30] M.A. Pellow, C.J.M. Emmott, C.J. Barnhart, and S.M. Benson, Hydrogen or batteries for grid storage? A net energy analysis. Energy Environ. Sci. 8 (2015) 1938-1952.

[31] InsideEVS, Battery Electric vs. hydrogen fuel cell: Efficiency comparison. Available: https://insideevs.com/news/406676/battery-electric-hydrogen-fuel-cell-efficiency-comparison/. Accessed on: April 4, 2021.

[32] Tesla Inc. Gigafactory (2020) Available: https://www.tesla.com/sites/default/files/blog_attachments/gigafactory.pdf. Accessed on April 8, 2021.

[33] C. Martin, Better batteries. Bloomberg (2019) Available: https://www.bloomberg.com/quicktake/batteries. Accessed on: April 4, 2021.

[34] A. Dellinger. BMW will give EV batteries new life with recycling program. (2018) Available: https://www.engadget.com/2018-10-15-bmw-ev-battery-recycling-program.html?guccounter=1&guce_referrer=aHR0cHM6Ly93d3cuZ29vZ2xlLmNvbS91cmw_c2E9dCZyY3Q9aiZxP. Accessed on: April 8, 2021.

[35] J. Forfar. Tesla's approach to recycling is the way of the future for sustainable production. Available: https://medium.com/tradr/teslas-approach-to-recycling-is-the-way-of-the-future-for-sustainable-production-5af99b62aa0e. Accessed on: April 8, 2021.

[36] Tesla Inc. Investor relations. Quarterly disclosure Q4 2020. Available: https://ir.tesla.com. Accessed on: April 8, 2021.

[37] Trefis Team, Forbes, How battery costs impact Tesla's margins: An interactive analysis, Available: https://www.forbes.com/sites/greatspeculations/2020/01/13/how-battery-costs-impact-teslas-margins-an-interactive-analysis/. Accessed on: April 12, 2021.

[38] A. Katwala. Forbes. The spiralling environmental cost of our lithium battery addiction. Available: https://www.wired.co.uk/article/lithium-batteries-environment-impact! Accessed on: May 4, 2021.

[39] Britannica, The Editors of Encyclopaedia. Alessandro Volta. Encyclopedia Britannica, Available: https://www.britannica.com/biography/Alessandro-Volta. Accessed on: April 8 2021.

[40] Britannica, The Editors of Encyclopaedia. Gaston Planté. Encyclopedia Britannica, Available: https://www.britannica.com/biography/Gaston-Plante. Accessed on: April 8, 2021.

[41] J. Alarco and P Talbot. The history and development of batteries. Available: https://phys.org/news/2015-04-history-batteries.html. Accessed on: April 8, 2021

[42] B. Schumm, Battery. Encyclopedia Britannica. Available: https://www.britannica.com/technology/battery-electronics. Accessed on: April 8 2021

[43] K. Mizushima, P.C. Jones, P.J. Wiseman, and J.B. Goodenough, Li_xCoO_2 (0<x<-1): A new cathode material for batteries of high energy density. Mater. Res. Bull. 15, 6 (1980) 783-789.

[44] R. Jow, K. Xu, O. Borodin, M. Ue, Electrolytes for lithium and lithium-ion batteries. Mod. Aspect Electroc. (2014) 58T.

[45] C.L. Campion, W. Li, and B.L. Lucht, Thermal decomposition of $LiPF_6$-based electrolytes for lithium-ion batteries. J. Electrochem. Soc. 152 (2005) A2327.

[46] V. Sharova, A. Moretti, T. Diemant, A. Varzi, R. Jürgen Behm, and S. Passerini, Comparative study of imide-based Li salts as electrolyte additives for Li-ion batteries. J. Power Sources 375 (2018) 43-52.

[47] W.H. Meyer, Polymer electrolytes for lithium-ion batteries. Adv. Mat. 10, 6 (1998) 439-448.

[48] J.W. Fergus, Ceramic and polymeric solid electrolytes for lithium-ion batteries. J. Power Sources 195, 15 (2010) 4554-4569.

[49] iPhone 6 battery cross section. Available: www.techinsights.com. Accessed on: May 5, 2021.

[50] J. Asenbauer, T. Eisenmann, M. Kuenzel, A. Kazzazi, Z. Chen, and D. Bresser, The success story of graphite as a lithium-ion anode material – fundamentals, remaining challenges, and recent developments including silicon (oxide) composites. Sustainable Energy and Fuels 4 (2020) 5387-5416.

[51] Z. Chen, W. Zhang, and Z. Yang, A review on cathode materials for advanced lithium ion batteries: microstructure designs and performance regulations. Nanotechnology 31,1 (2019) 012001.

[52] X. Zhao, S. Niketic, C.H. Yim, J. Zhou, J. Wang, and Y. Abu-Lebdeh, Revealing the role of poly(vinylidene fluoride) binder in Si/Graphite composite anode for Li-ion batteries. ACS Omega 3, 9 (2018) 11684–11690.

[53] R. Wang, L. Feng, Y. Zhang, Y. Zhang, W. Bai, B. Liu, W. Zhang, Y. Chuan, Z. Zheng, H. Guan, and W. Yang, Effect of different binders on the electrochemical performance of metal oxide anode for lithium-ion batteries. Nanoscale Res. Lett. 12 (2017) 575-586.

[54] A.K. Shukla and T.P. Kumar, Materials for next-generation lithium batteries. Curr. Sci., 94, 3 (2008) 314–331.

[55] M.S. Whittingham, Materials challenges facing electrical energy storage. MRS Bulletin, 33, 4 (2008) 411–419.

[56] S. Chauquea, F.Y. Olivaa, A. Visintind, D. Barracob, E.P.M. Leivac, and O.R. Cámara, Lithium titanate as anode material for lithium ion batteries: Synthesis, post-treatment and its electrochemical response. J. Electroanal. Chem. 799 (2017) 142–155.

[57] X. Zuo, J. Zhu, P. Müller-Buschbaum, and Y.J. Cheng, Silicon based lithium-ion battery anodes: A chronicle perspective review, Nano Energy 31 (2017) 113-143.

[58] M. N. Obrovac and V. L. Chevrier, Alloy negative electrodes for Li-ion batteries. Chem. Rev. 2014, 114, 11444−11502.

[59] D. Ma, Z. Cao, and A. Hu, Si-based electrode materials for Li-ion batteries: A mini review, Nano-Micro Lett. 6 (2014) 347–358.

[60] Y. Cui, N. Liu, H. Wu, M.T. McDowell, Y. Yao, and C. Wang, A yolk-shell design for stabilized and scalable Li-ion battery alloy electrodes. Nano Lett. 12 (2012) 3315-3321.

[61] S.H. Yu, X. Feng, N. Zhang, J. Seok, and H.D. Abruña, Understanding conversion-type electrodes for lithium rechargeable batteries. Acc. Chem. Res. 2018, 51, 2, 273–281.

[62] T.Brousse, R.Retoux, U.Herterich, and D.M.Schleich. Metal oxide anodes for Li-ion batteries. Ionics 3 (1997) 332–337.

[63] W. Kang, N. Deng, J. Ju, Q. Li, D. Wu, X. Ma, L. Li, M. Naebe, and B. Cheng, A review of recent developments in rechargeable lithium–sulfur batteries. Nanoscale 6, 8 (2016) 16541-16588.

[64] Y. Idota, T. Kubota, A. Matsufuji, Y. Maekawa, T. Miyasaka. Tin-based amorphous oxide: A high-capacity lithium-ion-storage material. Science 276, 5317 (1997) 1395-1397.

[65] F. Zoller, D. Bohm, T. Bein, and D. Fattakhova-Rohlfing. Tin oxide based nanomaterials and their application as anodes in lithium-ion batteries and beyond. ChemSusChem 12 (2019) 4140-4159.

[66] N. Job, R. Pirard, J. Marien, and J.P. Pirard, Porous carbon xerogels with texture tailored by pH control during sol–gel process, Carbon 42 (2004) 619-628.

[67] N. Rey-Raap, M.L.C. Piedboeuf, A. Arenillas, J.A. Menéndez, A.F. Léonard, and N. Job, Aqueous and organic inks of carbon xerogels as models for studying the role of porosity in lithium-ion battery electrodes, Mater. Design 109 (2016) 282–288.

[68] X. Yuan, Y.J. Chao, Z.F. Ma, and M. Deng, Preparation and characterization of carbon xerogel (cx) and CX-SiO composite as anode material for lithium-ion battery, Electrochem. Commun. 9 (2007) 2591-2595.

[69] J.P. Lewicki, C.A. Fox, and M.A. Worsley, On the synthesis and structure of resorcinol-formaldehyde polymeric networks-precursors to 3D carbon macroassemblies, Technical report, Lawrence Livermore National Laboratory (2015).

[70] M.-L. Piedboeuf, A.F. Léonard, K. Traina, and N. Job, Influence of the textural parameters of resorcinol–formaldehyde dry polymers and carbon xerogels on particle sizes upon mechanical milling, Colloid Surface A 471 (2015) 124-132.

[71] N. Job, S. Berthon-Fabry, M. Chatenet, J. Marie, M. Brigaudet, J.-P. Pirard. Nanostructured carbons as catalyst supports for PEM fuel cell electrodes. Top. Catal. 52 (2009) 2117-2122

[72] J. Carabetta and N. Job, Silicon-doped carbon xerogel with poly(sodium 4-styrenesulfonate) as a novel protective coating and binder. Micropor. Mesopor. Mat. 310 (2021) 110622-110630.

Chapter 1

Physico-chemical and electrochemical characterization of a porous carbon xerogel electrode

Abstract

In this chapter, the physico-chemical and electrochemical characterization of a porous carbon xerogel (CX) as well as composite electrodes with either poly(vinylidene difluoride) (PVDF) or poly(sodium 4-stryrenesulfonate) (PSS) as a binder was performed. An electrochemical model (ECM) to determine resistive, capacitive, and diffusive characteristics for a CX-based electrode has been developed. In the next chapters, a CX will be used as a support structure for high energy density dopant materials for lithium-ion batteries, such as tin oxide and silicon. PSS will also be used as a protective coating or binder to help improve the cycling performance of these dopant materials. Therefore, a thorough characterization of this material as well as the development of an ECM of a carbon xerogel-binder composite is necessary in order to understand the electrochemical and physico-chemical characteristics of both the CX itself as well as the active layer formed from this material with the binder and electrolyte.

Physico-chemical characterization showed that the CX is amorphous in nature and is comprised of nodules connected in a “string-of-pearls”-type structure, as expected. The composite active layer with PSS as a binder showed significantly higher apparent density than the composite active layer with PVDF as a binder. N_2 adsorption analysis indicated that, unlike the CX with PVDF as a binder, the CX with PSS as a binder maintained the microporosity of the CX. These differences in morphology between the CX with PVDF or PSS as a binder have a significant effect on the ionic and electronic conductivity of the active layer as well as on the capacitance.

The proposed ECM and equivalent circuit in this work is comprised of a transmission line model, where each element includes a pore resistance, charge transfer resistance and capacitance, double layer capacitance, and CX resistance. This model, however, can be reduced down into an equivalent series resistance (ESR), and a single value for charge transfer resistance (R_{ct}) and capacitance (C_d), and double layer capacitance. A parametric study was performed to determine how the thickness, type of binder, and average pore size of the CX active layer affect these electrochemical characteristics. Increasing the thickness of the active layer increased the ESR and R_{ct} but decreased the C_d. The use of PSS as a binder increased the ESR but decreased the R_{ct} and C_d. Notably, the double layer capacitance decreased substantially when PSS was used as a binder. In order to understand this phenomenon, a pseudo-2D model of the double layer capacitance was developed by considering the total capacitive energy of pores connected to the bulk electrolyte. The developed model suggests that decreasing the average pore size beyond a critical diameter, as occurs with the CX with PSS as a binder since the microporosity is retained, does not increase the specific capacitance of the active material, as one might expect, but rather reduces the specific capacitance due to a change in the diffuse region capacitance.

1.1 Introduction

Future electrically-powered applications will undoubtedly benefit from storage devices with higher energy density, power density, and cycling stability. Such applications, like electrically powered airplanes or long-distance electric vehicles, require higher energy density storage devices to be commercially or even practically viable. Generally, portable storage devices with higher energy density are the result of either (i) reducing the weight of the packaging and secondary components of the storage device, (ii) optimizing the active mechanism by which the storage device operates, or (iii) by developing a fundamentally new chemistry, material, or mechanism with a higher intrinsic energy density [1-3]. The latter has been widely shown to offer potentially large improvements and is usually the most popular route of research. For example, the development and synthesis of alloying-type materials like silicon have been shown to be a good candidate to improve the specific energy density of lithium-ion batteries [1-5]. Likewise, in supercapacitor research, materials with high specific surface areas, such as graphene, aim to increase the specific capacitance [6-9]. Other than new materials, however, other optimizations of the storage device should not be neglected and can offer great insights into other properties of the electrodes that are not intrinsic to the active material itself. Secondary extrinsic properties, such as the active layer thickness, density, and morphology can be explored to determine how these extrinsic properties affect the electrochemical characteristics of the active material, such as the ionic and electronic conductivity, capacitance, and charge transfer characteristics between the electrodes and the electrolyte.

Conventional supercapacitors and batteries are usually composed of two electrodes separated by an electrically insulating separator soaked in an ionically-conducting electrolyte. The electrodes are usually comprised of (i) the current collector, which conducts the electrons to/from an external circuit, (ii) the active layer, which is composed of a powdery active material usually bound together with an inactive polymeric binder, and (iii) the electrolyte, which infiltrates into the free spaces within the active layer and ionically connects the two electrodes. The main difference between the electrodes of supercapacitors and batteries is that the latter exploits two redox reactions to store charge, usually *via* lithium ions (Li^+ ions), within the active material while the former stores charges as a layer of ionic charges within the electrolyte and electric charges at the surface of the active material. Although the work in this chapter consists of constructing and analyzing the electrodes in a supercapacitor, the aim is to use the electrochemical properties observed in this chapter and apply them for use as a negative electrode in a battery. Given this aim, a Li-containing electrolyte that is suited for batteries will be used instead of a typical supercapacitor electrolyte in order to minimize differences between the supercapacitors in this study and the battery-type half cells synthesized in the following chapters.

One parameter of interest for a porous electrode is the thickness of the deposited active layer. A way to increase the energy density of a battery or supercapacitor without changing the nature of the active materials of the electrodes would be to minimize the total mass of inactive materials (*i.e.* the current collector, separator, electrolyte, and casing) while maximizing the mass loading of active material (*i.e.* the material that participates in storing the electrical charge). This is accomplished, naturally, by forming the thickest and most dense layer of active material possible while minimizing the amount of binder and other inactive components. However, as one might expect, as the thickness and density of the active layer is increase, the electronic and ionic conductivities may be adversely affected. Therefore, it would be useful to study how the electrochemical properties of an electrode change with the thickness and density of the active layer.

Another parameter that can be explored is the type of the binder used in the active layer. An interesting comparison to make would be between two polymers that are either soluble in water or an organic solvent. On the one hand, poly(vinylidene difluoride) (PVDF) is a conventional binder that is soluble in an organic solvent and used in current commercial Li^+ ion batteries and supercapacitors. This binder offers good mechanical stability; however, it is not ionically or electronically conductive. Poly(sodium 4-stryrene sulfonate) (PSS), on the other hand, is a water-soluble, ionically conductive polymer recently utilized in our lab as a binder due to its unique physico-chemical properties [10-12]. Chapter 3 in this thesis covers how the use of PSS as a protective coating or binder improves the cycling performance of a battery electrode containing silicon nanoparticles. Therefore, in this work a comparison was made between composite electrodes that used either PSS or PVDF as a binder.

The last parameter of interest would be the average pore size of the material composing the active layer. A carbon xerogel (CX) is a great choice for this purpose given that the average pore size of the material can be easily tuned without changing other physico-chemical properties of the material. A CX is an amorphous hard carbon with meso/macro-pores that are formed by the connection of spherical microporous nodules in a rigid “string of pearls”-like structure [13-16]. A simple and cheap sol-gel synthesis allows one to easily tune the average meso/macro-pore size by decreasing or increasing the pH of a precursor solution [13-16]. Also, in the following chapters of this thesis, a CX will be used as the active material to support high-energy density dopants for Li^+ ions batteries, such as tin oxide and silicon. Therefore, a CX will be used to explore the effect the average pore size on the physico-chemical and electrochemical properties of the active layer.

In this chapter, a parametric study of the thickness, type of binder, and average meso-macropore size of the active layer was conducted to determine how the electrochemical properties, such as ionic and electronic conductivity, diffusion characteristics, and other capacitive, resistive, and inductive properties, of the CX-based active layer are affected. An electrochemical model and a corresponding equivalent circuit were then developed to determine how the equivalent series resistance, charge transfer resistance and capacitance, and total double layer capacitance are affected by these parameters. Results will be used in the next chapters to understand the behavior of Li-ion battery electrodes using Si- and SnO_2-doped CX materials as active material with either PVDF or PSS as a binder.

1.2 Experimental

Materials: Resorcinol (R, 99%), formaldehyde (F, 37 wt% in H_2O), sodium carbonate (C, 99.5%), and poly(sodium 4-styrenesulfonate) (PSS, M_w= 70,000 g mol^{-1}) were purchased from Sigma-Aldrich. Poly(vinylidene difluoride) (PVDF), and N-methyl-2-pyrrolidone (NMP, ≥ 99%) were purchased from Alfa Aesar.

1.2.1 Carbon xerogel synthesis

Three carbon xerogels (CXs) were synthesized *via* the sol-gel polycondensation of resorcinol and formaldehyde in water, as outlined in previous works [10, 13-17]. For the three samples, the precursor solution was first prepared and magnetically stirred at room temperature for about 30 min until the resorcinol, formaldehyde, and basification agent (sodium carbonate) had thoroughly mixed. The three precursor solutions were synthesized using an *R/C* molar ratio of either 2000, 1375, or 750. An *R/F* molar ratio of 0.5, and a dilution ratio (*D* = total solvent/reactants molar ratio) of 5.7 were used in all cases. The solutions were then placed in a Binder VD-53 oven at atmospheric pressure in closed synthesis vials and underwent gelation for 3 days at 85°C. After gelation, the synthesis vials were opened, and the solvent was removed by progressively reducing the pressure every 45 min from atmospheric pressure to 2.5 kPa at 60°C using a Vacuubrand CVC 3000 pump connected to the oven. The pressure was then held at 2.5 kPa for 8 h. After 8 h, the temperature was increased to 150°C while maintaining a pressure of 2.5 kPa for 24 h.

The organic xerogels (OXs) were recovered as monoliths from the synthesis vials. The monoliths were then pulverized following a method described in a previous work in order to obtain particles with an average size of 10 µm [17]. The monolith was first crushed in a crucible and sifted by hand through a 1-mm mesh. The 1 mm powder was then ball-milled in a Fritsch Pulverisette ball mill at 400 rpm for 60 min. The ball mill consisted of twenty agate balls (diameter = 1 cm) in an agate-lined stainless-steel crucible (volume = 80 mL) with approximately 3 g of dried xerogel per batch. Some monoliths were conserved and pyrolyzed similar to the powder in order to accurately determine the bulk density of the CX.

The OXs were then pyrolyzed at 800°C under a gentle nitrogen flow in a horizontal tubular furnace. The carbonization process was performed in three successive steps: (i) heating up to 150°C at a rate of 1.7°C min^{-1}, (ii) heating up to 400°C at a rate of 5°C min^{-1} and (iii) heating up to 800°C at a rate of 5°C min^{-1}. The residence time for each step was 15 min, 60 min and 120 min, respectively. After the last step, the obtained material was left to cool down to room temperature within the furnace under nitrogen flow. The three recovered CXs (CX2000, CX1375, and CX750) were black in color and the mass had reduced by half, likely due to the conversion of the OXs to CXs, which is in line with previous syntheses [10, 13-17].

1.2.2 Preparation of CX inks and electrodes

The CX2000, CX1375, and CX750 powders were processed into electrodes by airbrush coating with either (i) PVDF as a binder (conventional) or (ii) PSS as a binder. Ink slurries were prepared for subsequent electrode preparation and electrochemical characterization. The PVDF-based inks were prepared by mixing 80 wt% of CX and 20 wt% of PVDF in NMP under magnetic stirring at 1000 rpm. The PSS-based inks were prepared by mixing 80 wt% of CX and 20 wt% of PSS in high purity water (*via* MilliQ process until R > 18 MΩ). A solvent-to-solid mass ratio of 20:1 was used in both cases to ensure that the prepared inks flowed easily through the airbrush in order to form a homogeneous coating on the current collector. The PVDF or PSS-based inks were spray-coated onto pre-weighed 15.5 mm diameter stainless steel disks. These disks were fixed on a 70°C heated surface. The coating was performed using a Harder & Steenbeck Evolution Silverline 2 airbrush. After spray-coating, the electrodes were dried at 60°C for 2 h and then at 120°C under vacuum overnight. The electrodes were then weighed to determine the mass of the deposited material prior to their electrochemical characterization. Excess dried material surrounding the electrodes, which was deposited around the disks during the spray-coating process, was collected for further characterization. Thus, a total of six different types of electrode samples were produced, consisting of CX2000, CX1375, and CX750, each with either PSS or PVDF as a binder. Electrodes of each of these six samples were also synthesized with varying active layer thicknesses.

1.2.3 Physico-chemical characterization

CX powders were analyzed by mercury porosimetry and nitrogen adsorption-desorption in order to determine the total (S_{BET}), microporous (S_{micro}), and meso/micro-porous (S_{ext}) surface areas, as well as the average pore size (d_{pore}) and pore size distribution, following methods described in Annex 1. In addition to these physico-chemical characterizations, the bulk density of the CX2000, CX1375, and CX750 particles, ρ_{bulk}, was determined by conducting Hg porosimetry on monoliths of the CX samples in order to reduce error caused by the packing efficiency of the particles in the powder. The bulk density was calculated using the following equation:

$$\rho_{\mathrm{bulk}} = \frac{m}{V_{\mathrm{Hg}} + \frac{m}{\rho_{\mathrm{nodule}}}} \tag{1.1}$$

where m is the mass of the sample (g), V_{Hg} is the total intrusion volume (cm^3), and ρ_{nodule} is the density of a carbon nodules without meso/macro-porosity (g cm^{-3}). The density of the carbon nodules, ρ_{nodule}, has been determined to be approximately 1.5 g cm^{-3} [18, 19], which is significantly lower than that of dense hard carbon due to the existence of microporosity in the CX nodules.

The apparent density of the deposited active layer is the effective density of the CX/binder composite on the current collector as a result of the density of the CX particles, density of the binder, and the packing efficiency of the deposited CX particles. The apparent density of the deposited active layer was evaluated by determining the mass of the CX/binder composite deposited on the current collector and measuring the thickness of the active layer, t_{layer} (cm), *via* SEM to determine the volume occupied by the active layer. Then the following equation was used to calculate the apparent density (g cm^{-3}):

$$\rho_{\text{apparent}} = \frac{m_{\text{layer}}}{t_{\text{layer}} \pi r_{\text{electrode}}^2} \tag{1.2}$$

where m_{layer} is the mass of the active layer (g) on the current collector and $r_{\text{electrode}}$ is the radius of the current collector (cm).

1.2.4 Electrochemical characterization

Symmetric supercapacitors were assembled in CR2032-type coin cells. Two CX electrodes, with approximately equal mass, were assembled with two porous polyethylene/polypropylene separators (Celgard®, 25 µm thickness, MTI Corporation) soaked with 80 µL of electrolyte (1 M $LiPF_6$ in a 1:1:1 ratio of ethylene carbonate: diethylene carbonate: dimethyl carbonate, Selectilyte LP71 Merck) placed between the electrodes. Note again that the electrolyte used here is a conventional Li-ion battery electrolyte. This choice was motivated by the fact that future chapters of this thesis will focus on the use of these CX-based electrodes as electrodes in Li-ion batteries. The supercapacitors were assembled in an argon-filled glovebox (MBraun, MB200B). Electrochemical measurements were conducted on the assembled CR2032 coin-cells. The coin-cells were kept inside a climate-controlled chamber at 25°C to ensure temperature stability. At least two coin-cells of each sample were tested in identical conditions in order to ensure repeatability of the results. Results shown below were thus checked for reproducibility.

Electrochemical impedance spectra (EIS) measurements were conducted between 1 MHz and 10 mHz with a voltage amplitude of 10 mV and 10 data points per decade at open circuit voltage in the discharged state. These measurements were conducted in order to determine other electrochemical characteristics, such as the equivalent series resistance (ESR), polarization resistance, and polarization capacitance of each formulation.

Cyclic voltammetry (CV) measurements were performed on each sample over a voltage window of -2 V to +2 V at scan rates of 1 mV s^{-1}, 5 mV s^{-1}, 20 mV s^{-1}, and 50 mV s^{-1} in order to determine the total capacitance, which was calculated using the following equation:

$$C_{\text{total}}(F\ m^{-2}) = \frac{\int i(v)dv}{\frac{dV}{dt}\Delta V S_{\text{BET}} m} \tag{1.3}$$

where $i(v)$ is the instantaneous current (A), V is the voltage (V), $\frac{\mathrm{dV}}{\mathrm{dt}}$ is the scan rate (V s^{-1}), ΔV is the voltage window over which the integral is calculated (V), S_{BET} is the total surface area (m^2 g^{-1}) determined by applying the BET method to the N_2 adsorption isotherm, and m is the mass of the active material on the electrode (g). The measurements were recorded in the discharged state (*i.e.* when there was no charge built up on either electrode).

1.3 Results and discussion

1.3.1 Physico-chemical characterization

Transmission electron microscopy

Figure 1.1 shows TEM micrographs of the CX2000 powder at various magnifications. The lowest magnification micrograph (Figure 1.1a) shows the overall structure and shape of a single CX2000 particle. The CX2000 particle is in fact a cluster of nodules linked together in a “string-of-pearls” type fashion, as expected from literature [10, 13-17]. The meso/macro-porosity is also partially visible at this magnification given that the average meso/macro-pore size is approximately 120 nm, as observed below using Hg porosimetry. The higher magnification images in Figure 1.1b and 1.1c show the surface roughness and shape of these nodules in more detail. Furthermore, the highest magnification micrograph in Figure 1.1d gives evidence that the CX is an amorphous hard carbon given the lack of any apparent graphitic planes that would be visible at this magnification. The spotted and rough texture of the CX surface seen at this magnification suggests that these materials could contain some additional structure, such as microporosity. The presence of microporosity in the CX was further confirmed *via* N_2 adsorption (see below), as is usual in carbon xerogels reported in the literature [10, 13-17]. The other samples (CX1375 and CX750) look the same, but the nodule size decreases as the *R/C* value decreases, as expected from the above-mentioned previous studies as well.

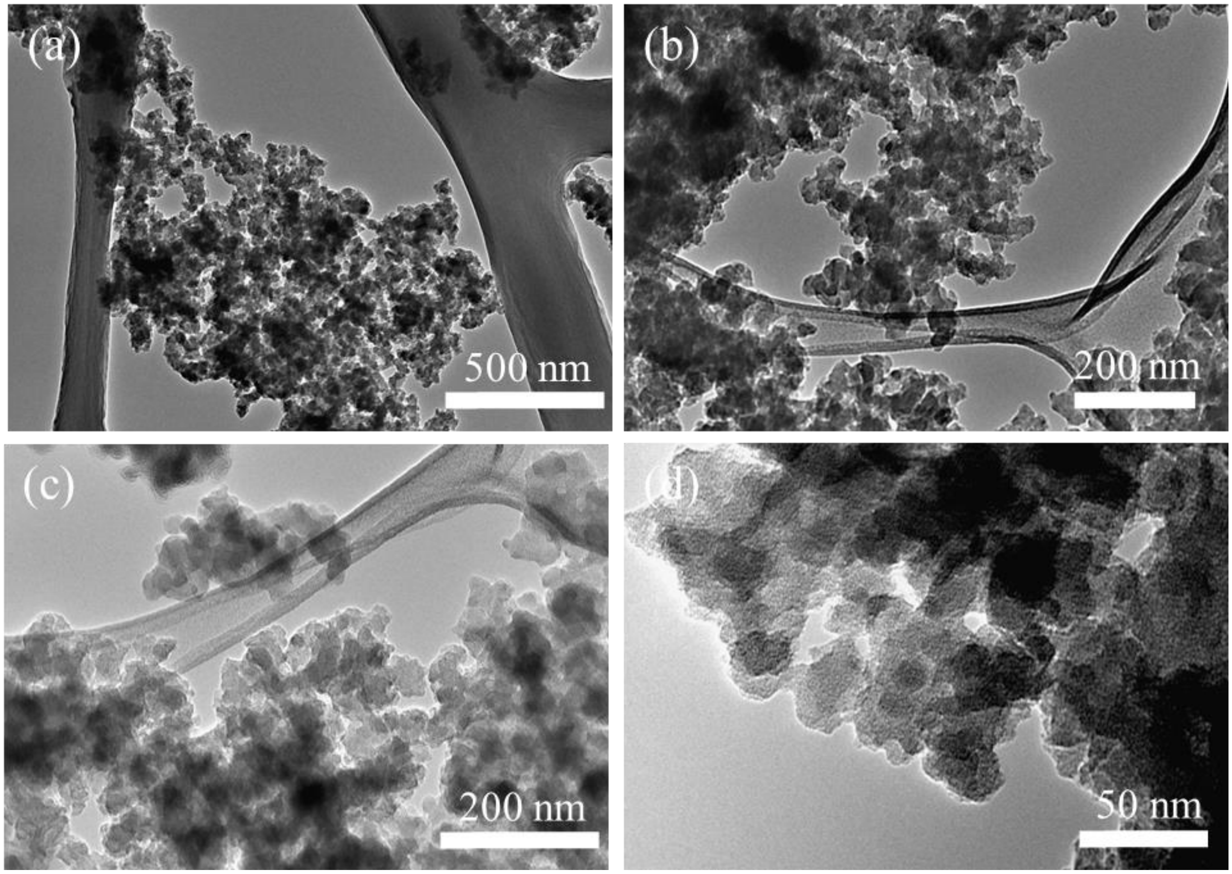

Figure 1.1 – TEM micrographs of sample CX2000 at various magnifications.

X-ray diffraction

XRD patterns were collected for samples CX2000, CX1375, and CX750 and are shown in Figure 1.2. The XRD pattern of all three CXs exhibits three very wide peaks at 2θ angles of approximately 15°, 30°, and 42 corresponding to interplanar spacing, *via* Bragg's Law, of 0.261 nm, 0.517 nm, and 0.765 nm, respectively. The first two peaks are likely related to the interplanar spacing of the graphitic sheets of the carbon xerogel, *i.e.* the C(002) planar direction [18, 19]. Normally, in a graphitic material, the (002) diffraction peak is located at a 2θ angle of 26°. Interestingly, however, the CX exhibits two (002) diffraction peaks. This suggests that there is roughly two populations of C(002) interplanar spacing in the material. The peak at 15° may be related to oxygenate graphitic sheets, similar to graphene oxide or graphite oxide, while the peak at 30° may be just related to the amorphous nature of the CX [20, 21]. The peak at a 2θ angle of 42° likely corresponds to C(001). These three peaks are not well-defined, which suggests that the CX is, indeed, an amorphous carbon with no well-defined crystallographic plane spacing between graphitic layers.

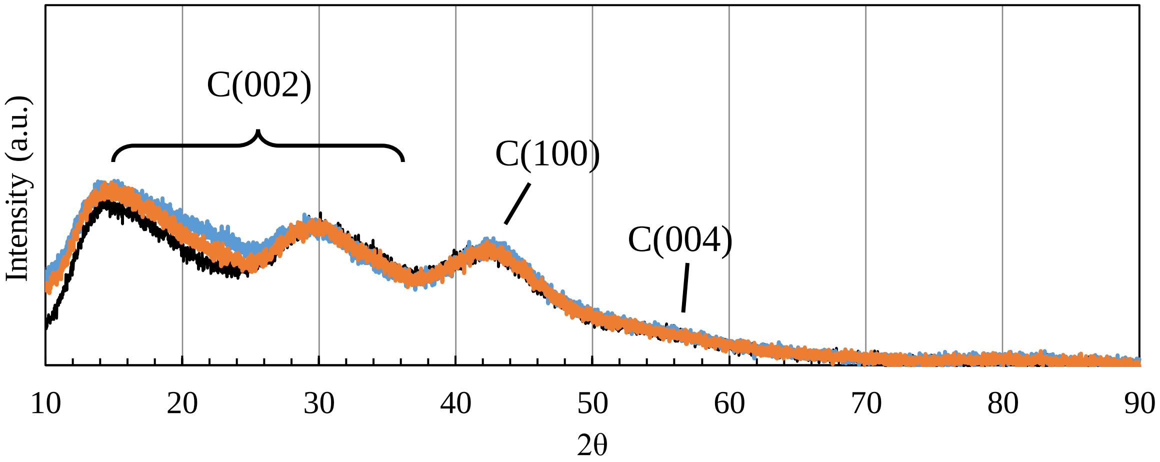

Figure 1.2 – XRD patterns of the (—) CX2000, (—) CX1375, and (—) CX750 samples.

Mercury porosimetry

Mercury porosimetry was conducted on the CX2000, CX1375, and CX750 powder and monolith samples in order to determine the particle size and pore size, and pore size distribution of the CX powders. The Hg intrusion volume and the corresponding pore size distributions are displayed in Figure 1.3. In Figure 1.3a, each mercury intrusion volume curve shows two inflection points: the first one, at approximately 1 MPa, corresponds to the pressure at which Hg infiltrates between the CX particles while the second one, which range between 10-50 MPa depending on the *R/C* ratio, corresponds to the pressure at which mercury enters within the meso/macro-pores. The average pore diameters of the CX2000, CX1375, and CX750 samples have been calculated to be 130 nm, 70 nm, and 20 nm, respectively, using the second inflection point between 10 MPa and 150 MPa and Equation A1.. The pore size distributions, shown in Figure 1.3b, were calculated by differentiating the Hg intrusion volume with respect to the pore diameter. The full width half maximum (FWHM), which corresponds to the dispersion of pore sizes around the average pore size in the sample, decreased as the average pore size decreased. The values of the FWHM, for the CX2000, CX1375, and CX750 samples were calculated to be 15 nm, 8 nm, and 2 nm, respectively. Note that the true dispersion of pore sizes may be wider than measured given that the constituent pores in the CXs may have constriction to the intrusion of Hg; as a result, the pressure must be increased to that corresponding to the intrusion within these constrictions to reach larger pores inside the material. This would cause larger pores to appear as smaller pores in the curves. The average particle size of all three CXs were calculated to be approximately 10 µm, using the first inflection point at around 1 MPa and Equation A1.2.

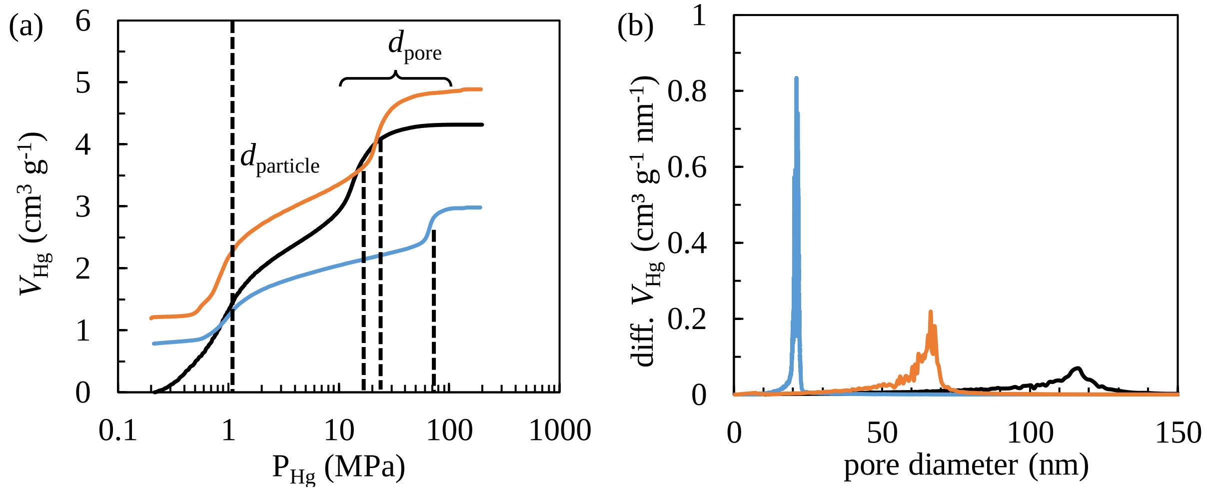

Figure 1.3 – Mercury porosimetry measurements performed on (▬) CX2000, (▬) CX1375, and (▬) CX750 powders. (a) Intrusion volume *vs.* applied pressure with the average pore diameter, d_{pore}, and particle size, $d_{particle}$, labeled with dotted lines. (b) Corresponding pore size distribution calculated in the pressure range of 0.01 MPa to 200 MPa, in order to exclude inter-particle voids.

Hg porosimetry measurements were also performed on monoliths of each CX, as shown in Figure 1.4, to determine the bulk density of each CX material, at the particle level. Performing these measurements on monoliths of the CX rather than on powders should eliminate the effect of the packaging efficiency of the CX particles. These measurements showed that, as the *R/C* ratio decreased, the average pore size decreased and the bulk density of the CX particle increased. Table 1.1 gives a summary of the average particle size, pore size, FWHM of the pore size, and bulk density of each respective CX.

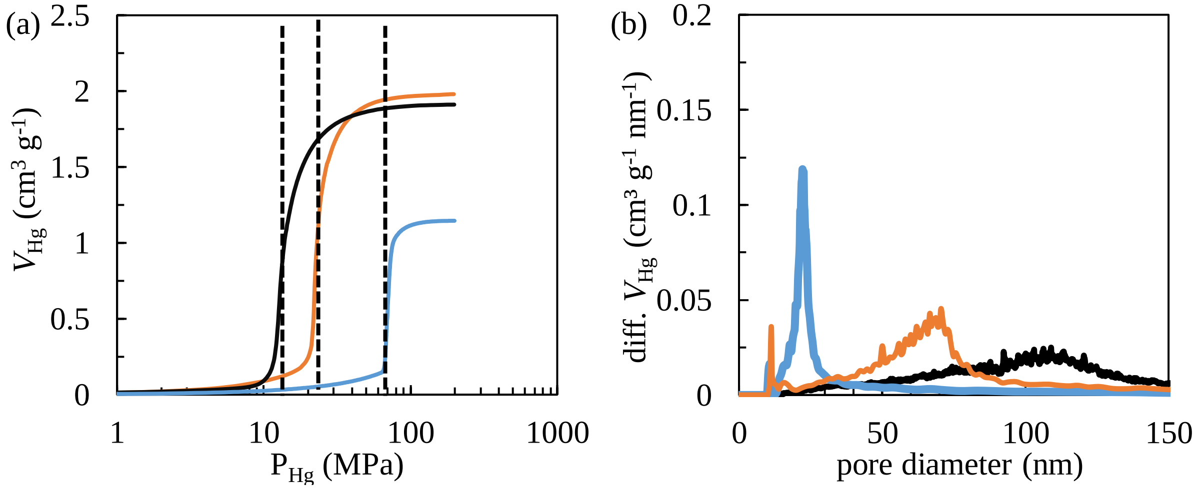

Figure 1.4 – Mercury porosimetry measurements performed on (▬) CX2000, (▬) CX1375, and (▬) CX750 monoliths. (a) Intrusion volume *vs.* applied pressure with the average pore diameter, d_{pore}, labeled with dotted lines. (b) Corresponding pore size distribution calculated using Eq. 1.

Table 1.1 – Particle, pore size, and CX bulk density determined *via* Hg porosimetry analysis.

Sample	d_{particle} **± FWHM**[a] **(µm)**	d_{pore} **± FWHM**[b] **(nm)**	ρ_{bulk}[b] **(g cm^{-3})**
CX2000	10 ± 4.3	120 ± 15	0.388
CX1375	10 ± 2.8	70 ± 8	0.378
CX750	10 ± 2.5	20 ± 2	0.552

[a] Measurement performed on powder.

[b] Measurement performed on monolith.

Scanning electron microscopy

The thickness and therefore the apparent density of each composite electrode was determined *via* Equation 1.2 using SEM micrographs of the profile of the electrodes. These measurements showed that the apparent density was higher for the CX active layers synthesized with PSS as a binder (CX2000: 0.080 g cm^{-3}, CX1375: 0.261 g cm^{-3}, CX750: 0.400 g cm^{-3}) as compared to the CX active layers synthesized with PVDF as a binder (CX2000: 0.070 g cm^{-3}, CX1375: 0.142 g cm^{-3}, CX750: 0.183 g cm^{-3}). This would suggest that the packing efficiency, *i.e.* the amount of void space between CX particles, is dependent on the binder type and seems to be reduced with PSS as a binder. The apparent density also increased as the *R/C* ratio decreased, likely related to the fact that the bulk density of the CX particles themselves increased as the *R/C* ratio decreases, as shown in Table 1.2. Therefore, the increase in the apparent density of the CX composite electrodes is a function of the binder type and *R/C* ratio of the CX.

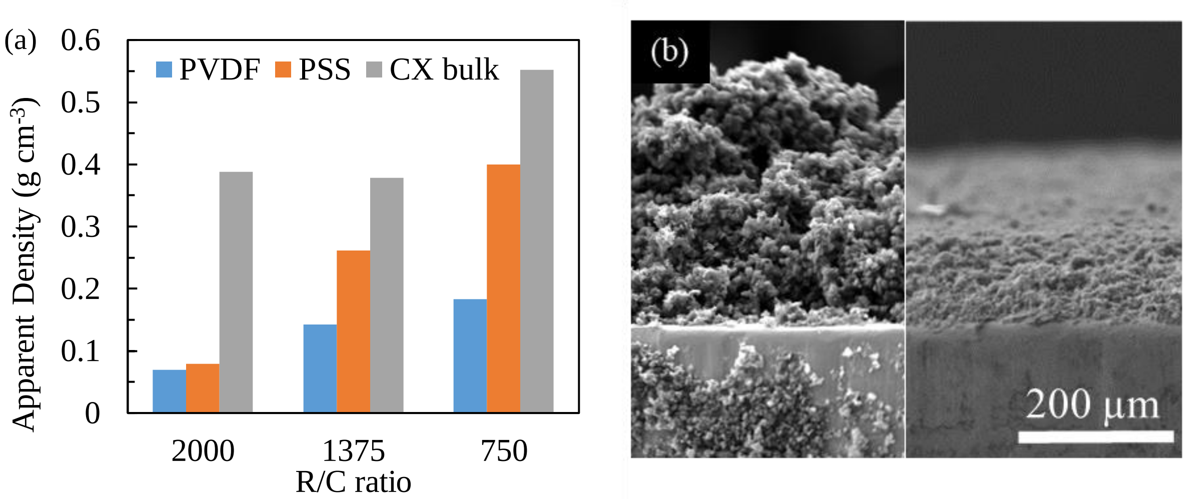

Figure 1.5 – (a) Comparison of the apparent densities of the deposited active layers for the CX2000, CX1375, and CX750 composite electrodes with either PVDF or PSS as a binder compared with the bulk density of the CX. (b) SEM micrograph of the active layer profile thickness consisting of a CX (*R/C* = 2000) with either PVDF (left) or PSS (right) as a binder.

Nitrogen adsorption-desorption analysis

In order to further understand the interaction and effect the binder has with the textural properties of the CX, nitrogen adsorption-desorption analysis was performed (i) on the three CX powders without any binder, (ii) on the CX composites with PVDF as binder, and (iii) on the CX composites with PSS as a binder. The N_2 isotherms of the CX2000, CX1375, and CX750 powders are shown in Figure 1.6a, b, and c, respectively. The CX2000 and CX1375 powders resemble a type I/II isotherm, corresponding to a material that includes micropores as well as a distribution of meso/macropores whereas the CX750 powder more resembles a type I/IV isotherm, given the small hysteresis loop present in the measurement; this is in line with usual results obtained with CXs.

Specific surface areas were calculated per mass unit of carbon, the binders being considered to be non-porous. Figure 1.6d and Table 1.2 show that all CX samples with either PVDF or PSS as a binder exhibited a decrease in the micropore surface area, S_{micro}. The composites with PVDF as a binder lost more of the micropore surface area than the composites with PSS as a binder. The composite material with PSS as a binder retained approximately half of the micropore surface area with respect to the CX without any binder. All composites with either PVDF or PSS as a binder also show a similar reduction of the external area, S_{ext}, which corresponds to the meso/macropore surface area. The decrease in accessibility of both the micropore and meso/macropore surface area measured in this analysis is an indication that these surfaces would not be accessible to the electrolyte when the CX/binder composite is assembled in the supercapacitor. An in-depth analysis of the difference of the specific surface area of the composites with PVDF as a binder as compared to the composite with PSS as a binder are given in Chapter 3. In short, it seems that PSS is able to partially infiltrate the micropores of the CX. The aqueous nature of the PSS and the hydrophilic nature of the CX surface would allow the PSS to coat the surfaces of the micropores while the PVDF seems to simply cover the openings to the micropores, which makes them inaccessible to the N_2 adsorption analysis and likely the electrolyte when used assembled in the supercapacitor.

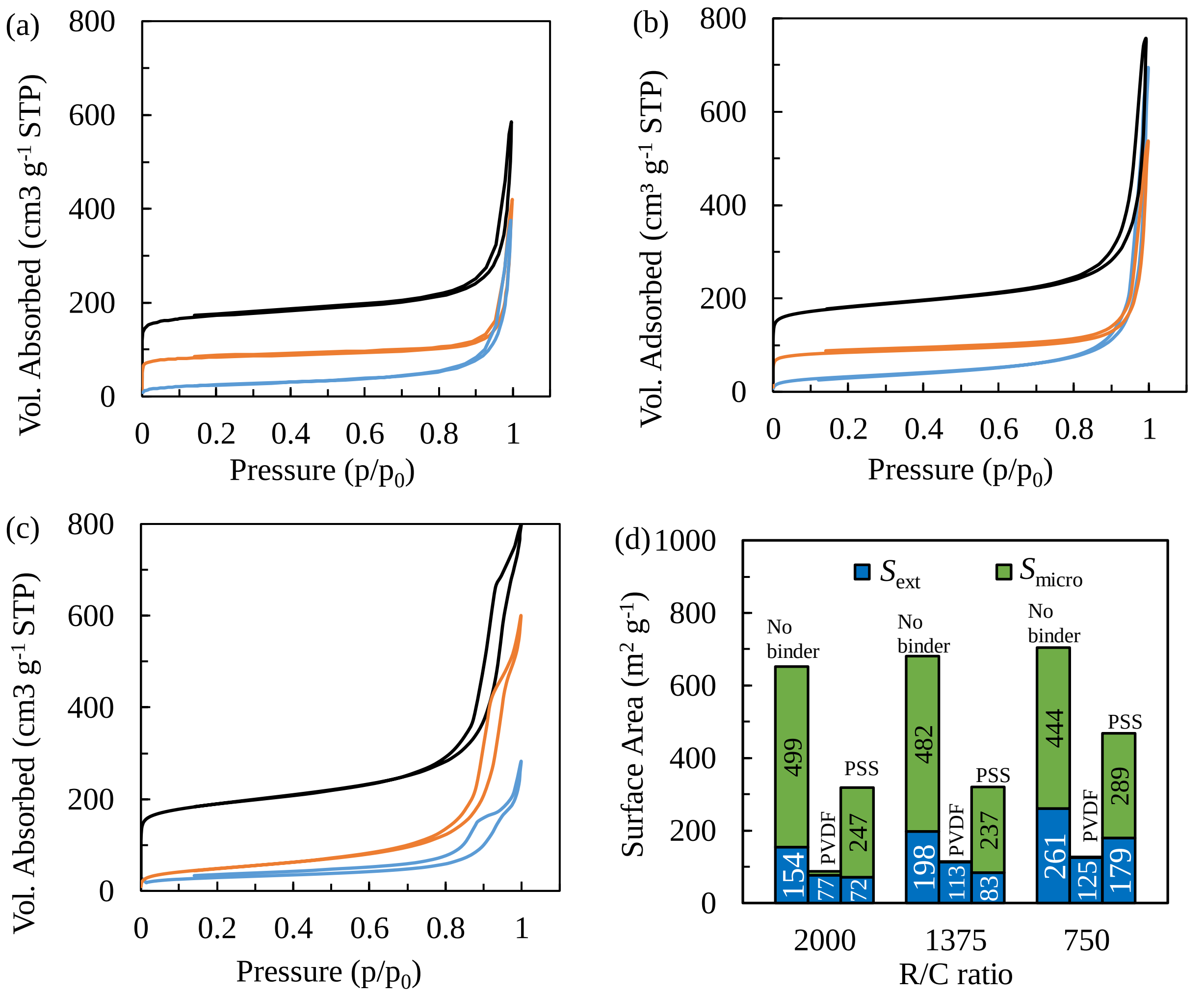

Figure 1.6 – Nitrogen adsorption-desorption isotherms of the (a) CX2000 (b) CX1375 and (c) CX750 samples; (—) pristine CX, (—) CX composite with PVDF as a binder, and (—) CX composite with PSS as a binder. (d) Meso/macropore (S_{ext}) and micropore (S_{micro}) surface areas of the CXs without binder, with PVDF as a binder, or with PSS as a binder. Specific surface areas are reported per mass unit of carbon.

Table 1.2 – Specific surface area from nitrogen adsorption-desorption analysis, reported per mass unit of CX.

	S_{BET} (m^2 g^{-1})			**S_{ext} (m^2 g^{-1})**			**S_{micro} (m^2 g^{-1})**		
	No Binder	PVDF Binder	PSS Binder	No Binder	PVDF Binder	PSS Binder	No Binder	PVDF Binder	PSS Binder
CX2000	653	87	319	154	77	72	499	10	247
CX1375	680	114	320	198	113	83	482	1	237
CX750	705	125	468	261	125	179	444	< 0.1	289

1.3.2 Electrochemical characterization and equivalent circuit model of CX electrode

The formulation of an equivalent circuit model (ECM) for porous electrodes is a widely researched area in surface electrochemistry given the possibly complicated interactions at the electrolyte/electrode interface. The most complicated, yet interesting, aspect of this interface is the so-called double layer and the corresponding measured capacitance. Gouy, Chapman, Helmholtz, and Stern, among others, has provided a fairly accurate and predictive model for the behavior of this double layer for flat electrode surfaces [22-26]. However, as the surfaces of the electrodes become more complex, as is the case for porous materials like in the present work, the expected behavior predicted by these models differs from what is observed.

The aim of this part of the work was to develop a model that more accurately resembles the true electrochemical phenomena that are occurring within the active layer. Other models, such as a Randles cell, rely on an equivalent circuit model with a loosely defined Warburg element connected in series with the charge transfer resistance to describe the diffusion characteristics of a cell [27, 28]. This model, which gives fairly accurate results, still can be improved to more accurately model the true nature of the movement of charge within the active layer. The ECM proposed in this work aims to model these interactions within the active material and at the surface of the material explicitly and more accurately.

The purposed ECM has been based on a previous model by Fletcher *et al.* [29], where the inhomogeneities of a disordered porous carbon-based material are accounted for by an asynchronous transmission line. This asynchronous transmission line is composed of a parallel array of series RC circuits with an array of different time constants. The array of RC circuits attempts to capture the inhomogeneities of the disordered carbon pore structure arising from the range of pore diameters and shapes present in the material. Although this model seems to work well in many cases, the effect of micropores on the total real capacitance of the carbon-based electrode is neither sufficiently explained nor understood by this model.

Therefore, in this work, another ECM is proposed that attempts to explain the effect of the microporosity on the total capacitance by considering a transmission line of identical RC-circuit elements. The proposed transmission line model for a disordered carbon electrode is shown in Figure 1.7:

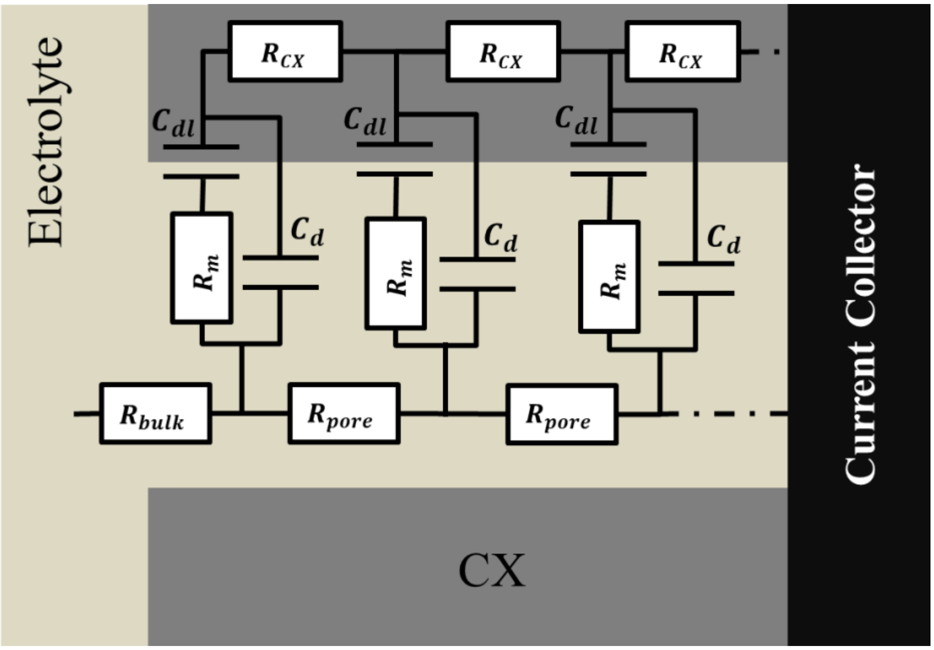

Figure 1.7 – Proposed transmission line model for a microporous CX with identical transmission line elements consisting of a series migration resistance, R_m, and double layer capacitance, $C_{dl,}$ in parallel with a displacement capacitance, C_d. Each of these transmission line elements is separated from the next one by a pore resistance, R_{pore}, and a carbon resistance, R_{CX}.

The resistive element, R_{bulk}, is the ionic resistance of the bulk electrolyte in the separator far away from the electrode surface; therefore, this quantity should be relatively independent of the nature of the electrode. The resistive elements R_{CX} and R_{pore} represent the electrical resistance of the CX and the ionic resistance of the electrolyte within the CX pores, respectively. The elements C_d and R_m represent the displacement capacitance and migration resistance, respectively, at the CX/electrolyte interface. Finally, the capacitive element, $C_{DL,}$ is the total capacitance resulting from the double layer formed at the CX/electrolyte interface at steady state. The asynchronous response shown in the model proposed by Fletcher *et al.* [29] would also be exhibited by this model given the extra pore resistance elements and CX resistance elements between each transmission line group. This model, however, can be reduced down into an equivalent series resistance (ESR), charge transfer resistance (R_{ct}) and capacitance (C_d), and double layer capacitance when considering the responses observed from the EIS measurements: see

Figure S1.1 and Figure S1.2 for the EIS spectra of the CX electrodes with either PVDF or PSS as a binder, respectively. Annex 2 gives an explanation of these quantities, except for the double layer capacitance, which will be explored later in this chapter.

Equivalent series resistance

The equivalent series resistance (ESR) is a measure of the resistive components in the electrochemical model, while considering all capacitive elements as short-circuits. This value is easily determined *via* EIS by probing the electrochemical cell at a sufficiently high frequency and finding where the EIS spectra intersects the abscissa of the Nyquist plot (see Annex 2). In this model, the ESR can then be expressed as the series resistance of (i) the bulk electrolyte resistance, R_{bulk}, and (ii) the resistance of the active layer, R_{layer}:

$$R_{\text{ESR}} = R_{\text{bulk}} + R_{\text{layer}} \tag{1.4}$$

The bulk electrolyte/separator resistance, R_{bulk}, was measured to be approximately 1.4 Ω (5.6 Ω m) *via* the impedance spectra performed on two lithium foils separated by the electrolyte-soaked separators (see Figure S1.3 for the EIS spectrum). Given that the resistance of the bulk electrolyte should be constant for all samples formulated in this work, the ESR values obtained from these measurements can be used to compare the resistance of CX active layers.

A model of the resistance of the CX active layer, R_{layer}, was formulated by considering a random model of a two-phase porous material [30, 31]. In this model, the conductivity of the entire layer is the product of the two phases raised to their respective volume fraction in the total material [28, 29]. Then, by multiplying this product by geometrical surface area of the electrode and dividing by the thickness of the layer, the conductivity, and therefore the total resistance of the active layer can be predicted. In this model the two phases are (i) the CX nodules phase that forms the meso/macro-porosity of the CX particles and contains microporosity and (ii) the electrolyte phase. Then, the resistance of the active layer can be expressed as:

$$R_{layer} = \left[\left[(\sigma_{nodule})^{V_{nodule}}(\sigma_{electrolyte})^{V_{electrolyte}}\right]\left(\frac{A_{electrode}}{t_{layer}}\right)\right]^{-1} \tag{1.5}$$

where σ_{nodule} and $\sigma_{\text{electrolyte}}$ are the CX nodule phase and electrolyte phase conductivity (mS cm^{-1}), respectively, and V_{nodule} and $V_{\text{electrolyte}}$ are the volume fractions of each respective phase, $A_{\text{electrode}}$ is the geometric surface area of the current collector (cm^2), and t_{layer} is the thickness of the deposited active layer (cm) [30, 31]. The volume fraction of the CX nodule and electrolyte phases can be calculated by comparing the apparent density measurements of the active layer, shown in Figure 1.5a, with the known density of CX nodules:

$$V_{\text{nodule}} = \frac{\rho_{\text{active layer}}}{\rho_{\text{nodule}}} \tag{1.6}$$

$$V_{\text{electrolyte}} = 1 - V_{\text{nodule}} \tag{1.7}$$

where ρ_{nodule} is approximately 1.5 g cm^{-3} and $\rho_{\text{active layer}}$ is the active layer apparent density values, shown in Figure 1.5a. The conductivity of the electrolyte is given by the manufacturer as 9.5 mS cm^{-1} while the conductivity of the CX nodules is unknown. The conductivity of the CX skeleton, which consists of the pure amorphous carbon phase, has been determined in literature to be approximately 16,000 mS cm^{-1} [13]. However, the low contact surface between the CX particles as well as the presence of microporosity is expected to severely inhibit the conductivity of the CX nodule phase. Then by measuring the resistance across a short-circuited electrode with a deposited active layer without any electrolyte, the conductivity of the CX nodule phase was estimated, at least to within an order of magnitude, to be ~1.2 mS cm^{-1} (8 Ω m) (see Figure S1.4 in the supplemental information for the EIS spectrum).

Figure 1.8 compares the ESR of CXs with different pore sizes against the thickness of the deposited active layer. The series resistance increased for all pore sizes as the thickness of the CX active layer increased. Given that, in general, the absolute resistance of any material increases as a function of its length, the increase in resistance with increasing active layer thickness comes as no surprise. However, the series resistance decreased as the average pore size of the CX increased. This phenomenon may be attributed to a combination of the electrical conductivity of the CX and the ionic conductivity in the electrolyte changing with the effective volumes of each in the active layer, respectively [23].

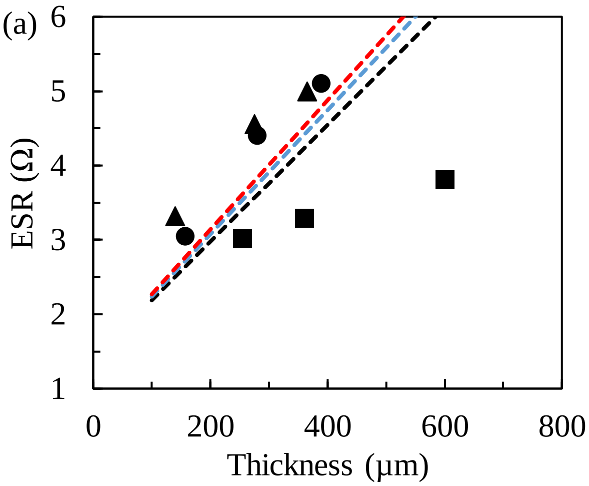

Figure 1.8 – Comparison of electrolyte/electrode total resistance of carbon xerogels using PVDF as a binder against the active layer thickness. (■) CX2000, (●) CX1375, and (▲) CX750. The dotted lines represent the fitting of the random two-phase porous model consisting of the CX and electrolyte as the two phases. Fit for the composite electrodes containing the (---) CX2000, (---) CX1375, and (---) CX750 samples.

Figure 1.9 compares the measured ESR of CX2000 composite electrodes with either PSS or PVDF as a binder against the thickness of the deposited CX active layer. The same trend was observed for the CX1375 and CX750 composite electrodes (results not shown). PSS seems to lead to a more resistive active layer of CX than PVDF, especially for a thicker deposited active layer. Although one may expect the CX with PSS as a binder to have a lower equivalent series resistance, given the ionic conductivity of PSS, it may be the case that the PSS binder reduces the amount electrolyte in the active layer given that the active layer is more dense, as shown in Figure 1.5, and therefore there is less room for the electrolyte in the active layer. This would therefore decrease the total conductivity of the active layer since the CX phase has a lower conductivity than the electrolyte as a result of the low contact surface area between CX particles.

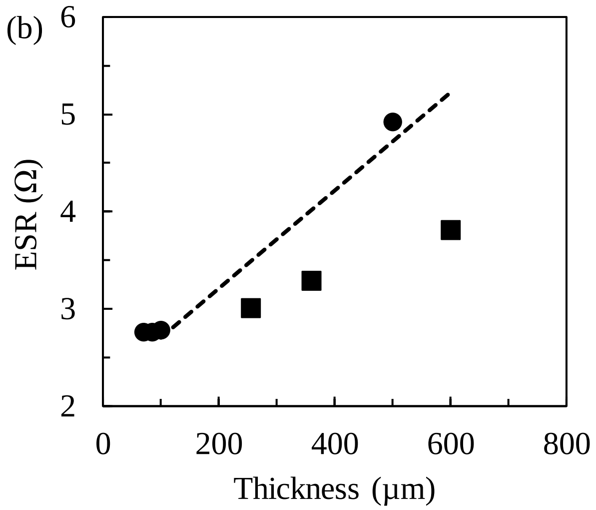

Figure 1.9 – Comparison of electrolyte/electrode total resistance of electrodes prepared from a chosen CX (CX2000) using (■) PVDF as a binder or (●) PSS as a binder as a function of the active layer thickness. The dotted line represents the fitting of the random two-phase porous model consisting of the CX2000 sample and electrolyte as the two phases.

Migration resistance and displacement capacitance

Near the interface between the CX and electrolyte, two currents can be measured: (i) a migration current, j_m, which is proportional to the motion of charges in the electrolyte and (ii) a charging current, or displacement current, j_d, related to the varying electric field caused by the formation of an electrical double layer at this interface [32-34]. The migration current can be related to the motion of charges in the electrolyte as a result of the applied external voltage [32-34]. The resulting external field formed due to the polarization of the CX electrodes causes charges in the electrolyte to migrate towards each respective electrode. The migration current can be modelled as a resistor, R_{ct}, with a current, j_m, since the motion of charges is solely dictated by the ionic species in the electrolyte [32-34].

These moving charges ultimately result in a separation between the charges in the CX and the electrolyte, which necessarily results in a changing electric field. The electric field at the CX/electrolyte interface is dictated by the difference in charge density between the CX and the electrolyte, which is constantly changing as the charges move in the electrolyte towards the CX. As was shown by Maxwell's addition to Ampere's Law, a changing electric field must also result in a current, *i.e.* displacement current, proportional to the rate of change of the electric field [32-34]. The evolution of the current should then be dictated by the rate at which the charges near the CX/electrolyte interface form this charge separation, given that the charge density dictates the local electric field. Since the displacement current is proportional solely to the change in the electric field, and the current through a capacitor is also proportional to the change in the electric field between its electrodes, one can model the displacement current measured at the CX/electrolyte interface as a capacitor. For example, as the local charge density approaches a steady-state, *i.e.* the capacitance of this layer has been fully charged and the double layer forms, the electric field approaches a steady-state as well and, therefore, the displacement current approaches zero, similar to how a charged capacitor acts as an open circuit. Furthermore, given that the migration current and displacement current occur simultaneously and are dependent on each other, they can be modeled by two discrete elements, *i.e.* a resistor and capacitor, respectively, in parallel with each other. The relative dielectric permittivity surrounding the interface, the nature of the charged species and the electrolyte, and the pore texture of the CX are the properties that should likely affect the resistance and capacitance of these two elements, respectively.

Figure 1.10 compares the values measured for the migration resistance, R_{ct}, as a function of the porosity of the CX, the type of binder, and the thickness of the CX active layer. In Figure 1.10a, the migration resistance slightly decreases as the average pore size of the CX increases. Likewise, the migration resistance decreases as the thickness of the active layer increases, except for the CX750 sample with high thickness, which exhibited a higher resistance. The ability of charges to move from the bulk electrolyte into the electrolyte within the CX active layer is hindered non-linearly with respect to the thickness and average pore size of the CX active layer. The non-linear evolution of the migration resistance is not clearly understood but seems to be linked to the porosity and tortuosity of the CX matrix. In any case, a CX with larger pores and thinner active layers seem to allow the most facile migration of charges from the bulk electrolyte to the electrolyte within the active layer, and ultimately to the CX/electrolyte interface.

In Figure 1.10b, the migration resistance for the CX2000 composite electrodes was decreased when PSS is used as a binder instead of PVDF as a binder. The same trend was observed for the CX1375 and CX750 composite electrodes as well. The decrease in migration resistance with the CX2000 composite electrode with PSS as a binder as compared to PVDF may be attributed to either the higher ionic conductivity of PSS, the lower relative permittivity of PSS, or the enhanced wetting properties of the PSS with the CX given the hydrophilic nature of the CX and the aqueous nature of the PSS-based ink.

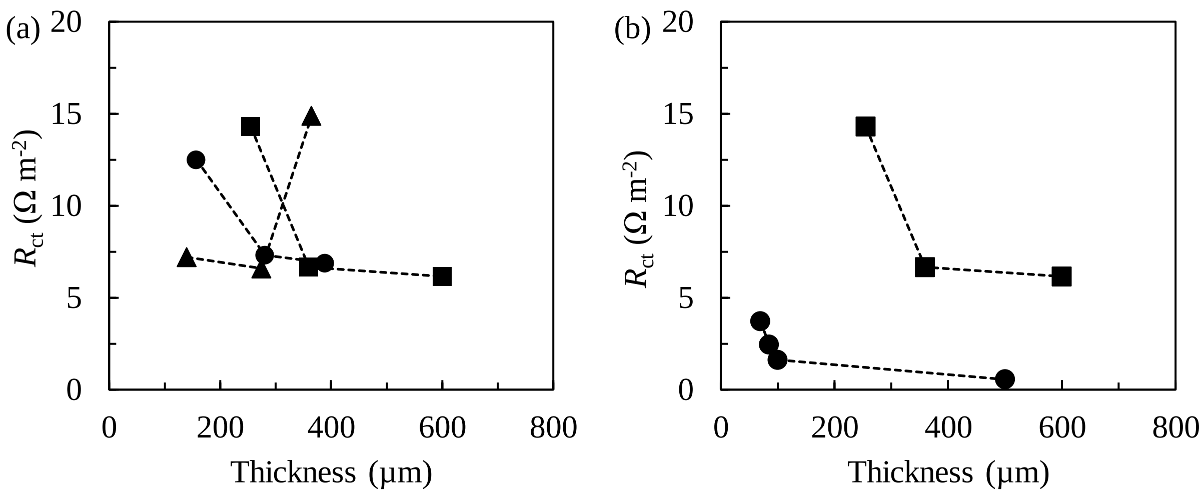

Figure 1.10 – (a) Comparison of migration resistance, R_{ct}, per BET surface area for electrodes prepared with various carbon xerogels and using PVDF as a binder against the active layer thickness; (■) R/C = 2000, (●) R/C = 1375, (▲) R/C = 750. (b) Comparison of the migration resistance, R_{ct}, per BET surface area as a function of the active layer thickness for electrodes prepared with the same CX (R/C = 2000), using either (■) PVDF or (●) PSS as a binder.

Figure 1.11 compares the measured values for the displacement capacitance, C_d, per unit area of CX as a function of the CX active layer thickness. Figure 1.11a compares how the displacement capacitance changes with the pore texture of the CX, using the three different CXs. The displacement capacitance decreases non-linearly with respect to the thickness and average pore size of the CX active layer (Figure 1.11a). The displacement capacitance responds similarly for the active layers that used PSS as a binder (Figure 1.11b).

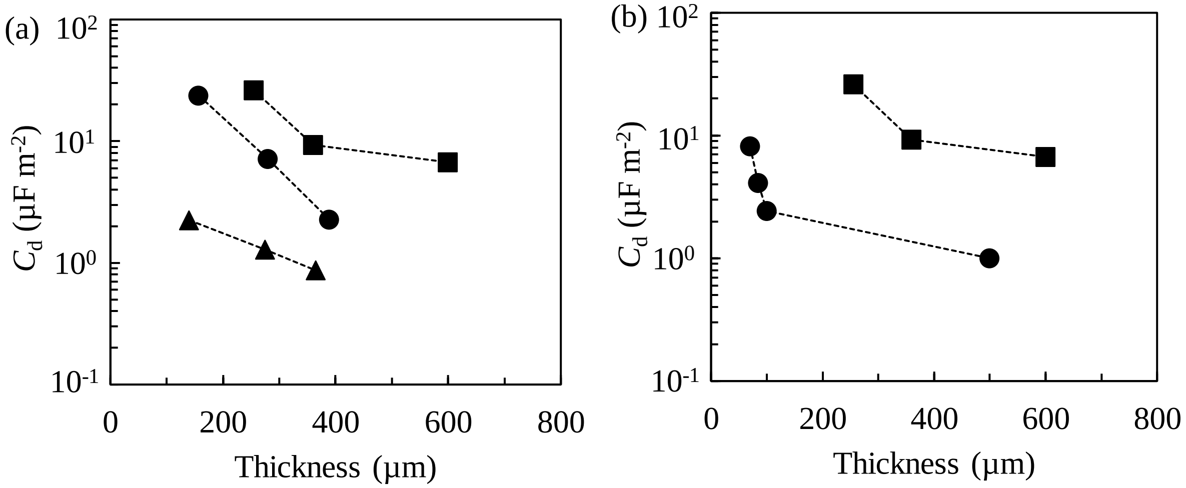

Figure 1.11 – (a) Comparison of the displacement capacitance per surface area of the active material; (■) CX2000, (●) CX1375, (▲) CX750. (b) Comparison of the displacement capacitance per unit area of active material, C_d, as a function of the active layer thickness for CX2000 composite electrode; (■) PVDF as a binder or (●) PSS as a binder.

Since the displacement capacitance decreases with increased total surface area of the electrode, *i.e.* thicker layers or smaller average pore diameter, the displacement current is likely independent of the total surface area of the active layer and dependent only on the geometric surface area of the electrode. A recalculation of the displacement capacitance per unit area of electrode (Figure 1.12) shows that the capacitance remains relatively constant as compared to the displacement capacitance per unit surface area of active material as a function of the thickness of the active layer. Only small differences seem to arise as a function of the average pore size, but may be due to other affects, such as restricted diffusional characteristics or imperfect wetting of the surface.

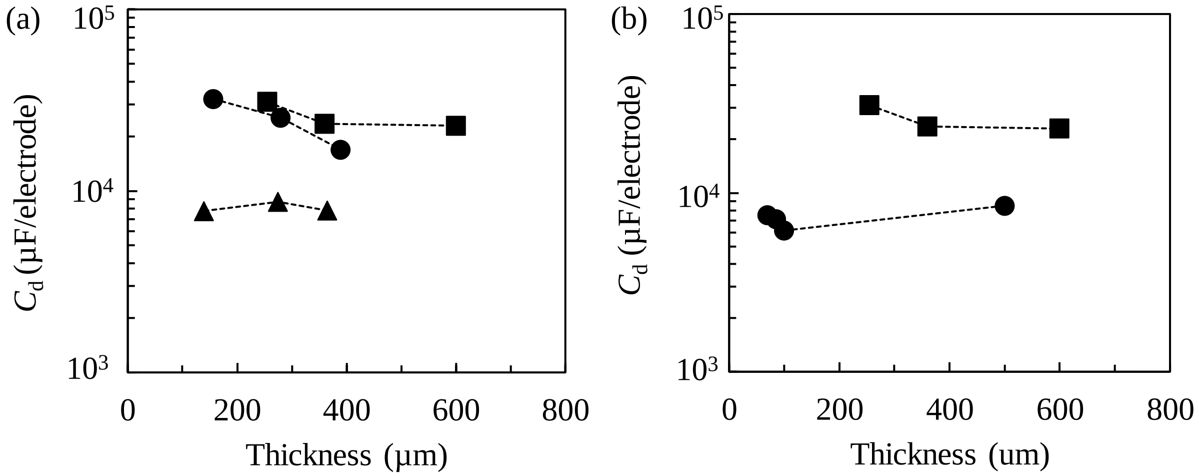

Figure 1.12 – Comparison of the displacement capacitance per geometric area of the electrode; (a) (■) CX2000, (●) CX1375, (▲) CX750. (b) Comparison of the displacement capacitance per geometric area of the CX2000 composite electrode; (■) PVDF as a binder or (●) PSS as a binder.

Double layer capacitance

The specific double layer capacitance of the supercapacitors per unit surface area of the CX was calculated by applying Equation 1.3 to the CV measurements of each sample (see supplemental information for CV measurements in Figure S1.5 (PVDF) and Figure S1.6 (PSS)). All values are reported per surface area of the carbon/binder composite, *i.e.* total surface area measured on the composite layer. Figure 1.13a compares the specific double layer capacitance against the thickness of the active layer of the CX2000, CX1375, and CX750 composite electrodes with PVDF as a binder. For each CX, only a minor decrease in the specific double layer capacitance as the active layer thickness increased was observed for each respective composite electrode. Both the CX2000 and CX1375 composite electrodes in Figure 1.13a showed similar specific double layer capacitance of about 100 mF m^{-2} while the CX750 composite electrode, which has the smallest average pore size, exhibited a higher specific total capacitance of around 120 mF m^{-2}. In Figure 1.13b a large difference in the specific double layer capacitance can be seen between the CX2000 with either PVDF or PSS as a binder. The trend for the CX1375 and CX750 composite electrodes were similar to the CX2000 composite electrode. The specific double layer capacitance was reduced from 100 mF m^{-2} for the CX2000 with PVDF as a binder as compared to 15 mF m^{-2} for the CX2000 composite electrode with PSS as a binder. One would expect the specific double layer capacitance of the composite electrodes with PSS as a binder to be reduced as compared to the same electrodes with PVDF given the ratio of the permittivity of the PSS and PVDF ($\varepsilon_{PVDF}/\varepsilon_{PSS} = 3$). However, if the specific double layer capacitance of the CX2000 composite electrode with PSS as a binder is corrected for the difference in permittivity, the specific double layer capacitance would be approximately 45 mF m^{-2}. Therefore, there must be some other phenomenon occurring that causes the specific double layer capacitance to decrease.

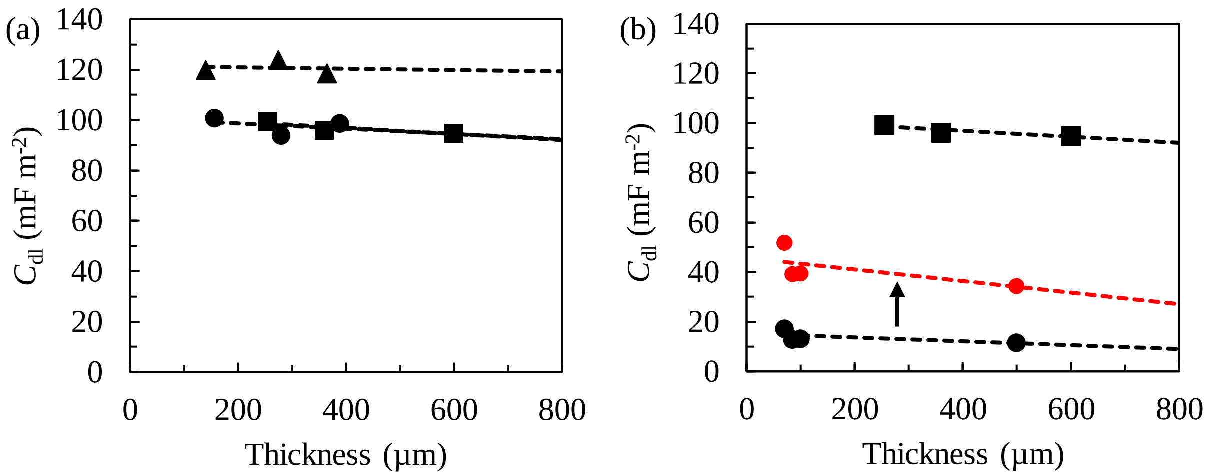

Figure 1.13 – (a) Comparison of specific double layer capacitance, C_{dl}, as a function of the active layer thickness for electrodes with PVDF as a binder: (■) CX2000, d_{pore} = 120 nm, (●) CX1375, d_{pore} = 60 nm, (▲) CX750, d_{pore} = 20 nm. (b) Comparison of the specific double layer capacitance, C_{dl}, as a function of the active layer thickness for electrodes prepared with the same carbon xerogel (CX2000, d_{pore} = 120 nm) using either (■) PVDF as a binder, (●) PSS as a binder, (●) PSS as a binder with the permittivity of PVDF ($\varepsilon_{PVDF}/\varepsilon_{PSS}$ = 3). Dotted lines represent a least squares regression fit of each material. All capacitance values are reported per BET surface area of the carbon/binder composite.

An important difference between the composite electrodes with either PVDF or PSS as a binder is that the composite electrodes with PSS as a binder retain some of the microporosity of the parent CX powder, as shown by the N_2 adsorption analysis in Figure 1.6d. These remaining micropores should be accessible to the electrolyte and be able to form a capacitive double layer. Consequently, the loss in capacitance for the composite electrodes with PSS as a binder may be related to some phenomenon that reduces the specific capacitance of a surface when the surface is partly made of sufficiently small pores. The following electrochemical model for the specific double layer capacitance aims to prove that sufficiently small pores would effectively decrease the specific double layer capacitance of a given surface.

The electrochemical model for the specific double layer capacitance developed in this work is based on the Stern model [22-26]. The Stern model was used given its relative simplicity, ease of calculation, and broad applicability [22-26]. Other phenomena related to the effects of de-solvated ionic species or pseudocapacitance are not considered since the active material and electrolyte remain constant [37]. Although it is possible that some type of electron-transfer reaction may be taking place, the effects, if present, should not vary greatly between each formulation in this work.

The Stern model states that the distribution of ionic species in an electrolyte near a charged surface consists of two distinct layers: (i) a close-packed outer Helmholtz plane (OHP) and (ii) a diffuse layer [22, 23]. The OHP forms near the charged surface at a distance approximately equal to the solvated radius of the ions, $r_{\mathrm{ion,solvated}}$. Grahame [37] showed that unsolvated ions are also able to form an additional layer closer to the surface, the inner Helmholtz plane (IHP), which has a separation distance approximately equal to the radius of the ionic species [22, 23]. However, as previously stated, for the purposes of the present work, a simplification was chosen to consider that the solvated ions only are present in the OHP. The specific double layer capacitance of these two layers can then be considered as two capacitors in series:

$$C_{\mathrm{DL}} = \left(\frac{1}{C_{\mathrm{OHP}}} + \frac{1}{C_{\mathrm{diffuse}}}\right)^{-1} \tag{1.8}$$

where C_{OHP} and C_{diffuse} are the specific capacitances per unit surface area of the CX of the charge in the OHP and diffuse region, respectively (F m^{-2}). In the OHP, there is no distribution of charge between the OHP and the CX surface given that the ionic species are very closely packed to the charged CX surface [21-25, 38]. Therefore, the variation in potential between the CX surface and the layer of ionic species in the OHP can be considered as linear and the specific capacitance per unit area of CX for the OHP reduces to the following equation:

$$C_{\mathrm{OHP}} = \frac{\varepsilon_0 \varepsilon_{\mathrm{r}}}{r_{\mathrm{ion,solvated}}} \tag{1.9}$$

where ε_{r} is the relative dielectric permittivity of the solvent, ε_0 is the dielectric permittivity constant (8.8×10^{-12} F m^{-1}), and $r_{\mathrm{ion,solvated}}$ is the radius of the solvated ions in the electrolyte (m) [37, 38]. The diffuse layer, first proposed by Gouy and Chapman, extends from the OHP to the bulk of the electrolyte [24, 25]. This layer consists of a distribution of charges as a result of the varying concentration of ionic species in the electrolyte moving away from the OHP. Thus, the capacitance of this layer should be solved by considering the following differential capacitance equation:

$$C_{\mathrm{diffuse}} = \frac{\mathrm{d}\sigma}{\mathrm{d}\varphi} \tag{1.10}$$

where $\mathrm{d}\sigma$ is the differential surface charge density and $\mathrm{d}\varphi$ is the differential potential. The integral form of Equation 1.10 (shown in Equation S2.4 in the Supplemental Information) is derived by considering Gauss's law. The potential distribution and its corresponding derivatives necessary to calculate the diffuse capacitance was explicitly determined for a cylindrical pore geometry by considering a linearized Poisson-Boltzmann equation, shown in Equation S2.8, which relates how the potential evolves with the local charge density. This explicit solution was implemented within a Matlab® script to calculate the total double layer capacitance for various pore sizes and geometries. A complete derivation of the equations used in this script can be found in the supplementary information [39].

The unique aspect of the model used in this work is how the micropores interact with the meso/macro-pores of the CX. Although Equation 1.10 applies for sufficiently large pores where the potential within the pore is able to reach the potential of the bulk electrolyte, this is not necessarily the case for pores with smaller radii. For pores with sufficiently small radii, such as the case for the small mesopores or micropores present within the nodules of a CX, the potential distribution would look similar to Figure 1.14. In this case, the potential within smaller pores does not reach the potential of the bulk electrolyte and therefore, the total capacitance per unit surface area of the CX would change.

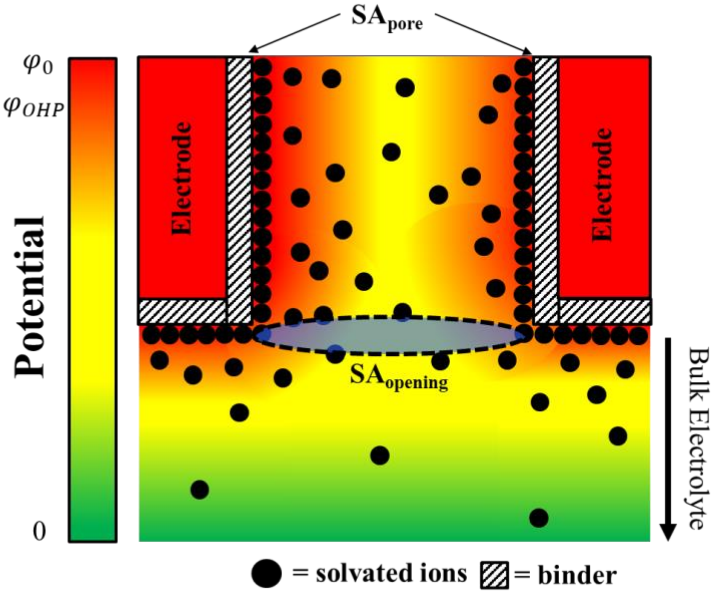

Figure 1.14 – Schematic diagram of the potential profile within a theoretical pore of the carbon xerogel. φ_0 is the potential at the electrode/electrolyte interface, φ_{OHP} is the potential at the outer Helmholtz plane (OHP), SA_{pore} is the surface are within the pore, and SA_{opening} is the surface area of the opening of the pore. When this pore is sufficiently small, the potential within the pore does not approach the potential within the bulk electrolyte. Therefore, two diffuse region capacitances will develop that are dependent on each other; one diffuse region within the pore and one extending from the entrance of the pore into the bulk electrolyte.

In this case, one can consider two diffuse capacitances: (i) the diffuse capacitance within a sufficiently small pore and (ii) the diffuse capacitance that forms at the opening of the sufficiently small pore and extends into the bulk electrolyte. Although the exact diffuse capacitance would require some higher dimensional terms to consider all the phenomena, such as edge effects around the entrance of the pore, the two-capacitance model outlined here should be a good approximation of the total diffuse capacitance.

Since the potential difference across these two capacitances are dependent on each other, the total capacitance cannot be calculated by just considering the capacitance as a series of two discrete capacitors. The total capacitance per unit surface area can be calculated by considering the total capacitive energy of the layer from the potential at the charged surface to the potential in the bulk electrolyte:

$$U_{diffuse} = U_{pore,diff} + U_{out,diff} \tag{1.11}$$

where $U_{\text{pore,diff}}$ is the capacitive energy within the sufficiently small pore and $U_{\text{out,diff}}$ is the capacitive energy held in the diffuse region outside the sufficiently small pore (J). These energy terms can be expanded into the following:

$$\frac{1}{2}C_{\text{diffuse}}\varphi_{\text{OHP}}^{2}(S_{\text{pore}}) = \frac{1}{2}C_{\text{pore,diff}}(\varphi_{\text{OHP}} - \varphi_{min})^{2}(S_{\text{pore}}) + \frac{1}{2}C_{\text{out,diff}}(\varphi_{min})^{2}(S_{\text{opening}}) \tag{1.12}$$

where the CX surface area inside the pore and at the surface area of the pore opening are SA_{pore} and SA_{opening}, respectively (m^2). The terms φ_{min} and φ_{OHP} represent the minimum potential within the sufficiently small pore and the potential at the OHP, respectively (V). The term $C_{\text{pore,diff}}$ is the specific capacitance per unit surface area of CX within the sufficiently small pore and $C_{\text{out,diff}}$ is the specific capacitance outside the sufficiently small pore per unit surface area of the sufficiently small pore opening (F m^{-2}). The values for the specific capacitance inside and outside the sufficiently small pore were calculated numerically using Equation S2.4 and the explicit solutions for either a cylindrical (Equations S1.10, 11, and 12) or a planar surface (Equations S1.13, 14, and 15), respectively. Rearranging Equation 1.12, the total diffuse capacitance can be expressed as the following:

$$C_{\text{diffuse}} = \left[C_{\text{pore,diffuse}}\frac{(\varphi_{\text{OHP}}-\varphi_{min})^{2}}{\varphi_{\text{OHP}}^{2}}\right] + \left[\frac{S_{\text{opening}}}{S_{\text{pore}}}C_{out,diffuse}\left(\frac{\varphi_{min}}{\varphi_{\text{OHP}}}\right)^{2}\right] \tag{1.13}$$

The surface area ratio was held constant as, $\frac{\pi r^2}{3\pi r^2} = 0.34$, by considering the pore as a blind cylinder with length, r. This ratio should be a good approximation of the morphology of the CX surface. Note that longer pores in this model, *i.e.* a lower surface area ratio, mostly reduce the total capacitance for a material with a small pore diameter.

Figure 1.15 shows how the experimental data points of the total capacitance match the electrochemical model for a porous CX electrode shown in Figure 1.14 and the diffuse capacitance expressed in Equation 1.13. The addition of the specific capacitance outside the pore, $C_{\mathrm{out,diffuse}}$, which extends into the bulk electrolyte and is approximately equal to the value shown for sufficiently large radii pores, generally acts to reduce the total specific capacitance of a CX with sufficiently small pores. Since the diffuse capacitance in the pores can be considered to be connected in series with the diffuse capacitance in bulk electrolyte, the more that the potential drop occurs within the bulk electrolyte region, the more the specific capacitance of the CX electrode is reduced. Although the specific capacitance inside the pore increases exponentially as the pore diameter decreases, as shown by the dotted line in Figure 1.15, the fraction of the potential difference within the pore decreases as the average pore size is reduced.

These results and analysis indicate that sufficiently small pores have a lower specific capacitance than a surface that is in contact with the bulk electrolyte directly. Although the specific capacitance per unit area of a confined surface is increased as compared to an unconfined surface, the addition of a secondary diffuse region outside of these confined surfaces causes a net decrease in the specific capacitance of a surface within a sufficiently small pore.

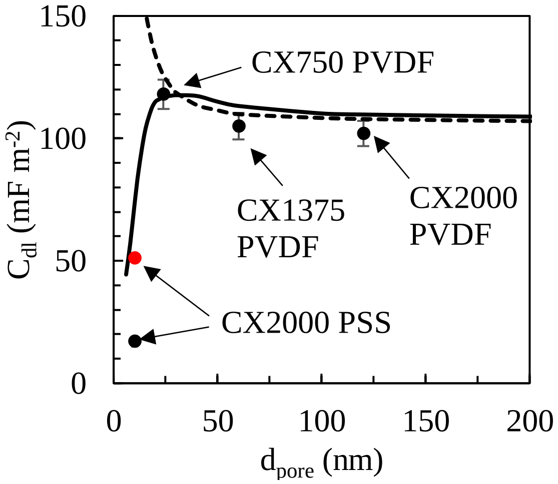

Figure 1.15 – Specific capacitance per unit area calculated for a CX with cylindrical pores as well as corresponding experimental results. The dotted curve (---) represents the specific capacitance resulting from the pore itself only. The solid curve (▬) considers how the capacitance of these pores are affected by the fact that the pores must necessarily be in contact with a bulk electrolyte solution, which decreases the total capacitance as the pores become sufficiently small. The red data point (●) represents the CX2000 with PSS as a binder but with the permittivity of PVDF ($\varepsilon_{PSS}/\varepsilon_{PVDF} = 3$).

1.4 Conclusion

Electrodes composed of a carbon xerogel (CX) with either PVDF or PSS as a binder were synthesized and assembled into a symmetric supercapacitor cell in order to more fully understand how the electrochemical properties, such as the equivalent series resistance (ESR), charge transfer resistance (R_{ct}) and capacitance (C_d), and total capacitance, are affected by the binder, the microstructure of the CX, and other extrinsic properties of the active layer such as the thickness and density of the active layer. The ESR increased more rapidly with respect to the active layer thickness with PSS as a binder as compared to PVDF as a binder. Similarly, the ESR of a CX with smaller pores increased more rapidly with respect to the active layer thickness. Both of these phenomena can be attributed to the fact that the CX in the active layer exhibits a lower conductivity than the electrolyte due to the low contact surface area between the constituent CX particles. The R_{ct} increased with decreasing average pore size and increasing active layer thickness while the use of PSS as a binder decreased the migration resistance. The C_d decreased with decreasing pore size and while using PSS as a binder.

A unique consideration of the total capacitance of these CX-based supercapacitors was formulated. A new model for disordered mesoporous carbon with internal microporosity was developed. The model consisted of cylindrical pores connected to a bulk electrolyte. Then, the diffuse capacitance in the pores was considered to be connected in series with the diffuse capacitance in bulk electrolyte. However, since the potential drop across these two capacitances are dependent on each other, the total capacitance of the diffuse region was calculated by considering the total capacitive energy of these two diffuse region capacitances. This model showed that, although the specific capacitance of a pore increases with decreasing diameter, the addition of a secondary diffuse region outside of the pore causes a net decrease in the specific capacitance per unit surface area, which corresponded with experimental results. These experimental results and corresponding model can be used for the analysis of other carbonaceous materials in similar electrode configuration.

1.5 References

[1] D. Ma, Z. Cao, and A. Hu, Si-based electrode materials for li-ion batteries: A mini review, Nano-Micro Lett. 6 (2014) 347–358.

[2] T. Kim, W. Song, D.Y. Son, L. K. Ono, and Y. Qi. Lithium-ion batteries: outlook on present, future, and hybridized technologies J. Mater. Chem. A, 2019,7, 2942-2964

[3] Y. Kuang, C. Chen, D. Kirsch, and L. Hu. Thick Electrode Batteries: Principles, Opportunities, and Challenges. Adv. Energy Mater. 2019, 9, 1901457.

[4] J. Sakabe, N. Ohta, T. Ohnishi, K. Mitsuishi, and K. Takada, Porous amorphous silicon film anodes for high capacity and stable all-solid-state lithium batteries, Comm. Chem. 1 (2018) 1 – 24.

[5] R. A. Huggins, Lithium alloy negative electrodes, J. Power Sources 81 (1999) 13–19.

[6] C. Zhong, Y. Deng,W. Hu, J.Qiao, J. Zhang, and J. Zhang, A review of electrolyte materials and compositions for electrochemical supercapacitors, Chem. Soc. Rev. 44 (2015) 7484.

[7] H. Wang, H. Yi, C. Zhu, X. Wang, H.J. Fan, Functionalized highly porous graphitic carbon fibers for high-rate supercapacitive electrodes, Nano Energy 13 (2015) 658-669.

[8] S.W. Hwang and S.H. Hyun, Synthesis and characterization of tin oxide/carbon aerogel composite electrodes for electrochemical supercapacitors, J. Power Sources 172 (2007) 451-459.

[9] Q. Ke and J. Wang, Graphene-based materials for supercapacitor electrodes - A review, J. Materiomics 2 (2016) 37-54.

[10] J. Carabetta and N. Job, Silicon-doped carbon xerogel with poly(sodium 4-styrenesulfonate) as a novel protective coating and binder. Micropor. Mesopor. Mater. 310 (2021) 110622.

[11] J.E. Coughlin, A. Reisch, M.Z. Markarian, J.B. Schlenoff, Sulfonation of Polystyrene: Toward the “Ideal” Polyelectrolyte J. of Polymer Science, Part A: Polymer Chemistry 51 (2013) 2416-2424.

[12] W.B. Ying, J.U. Jang, M.W. Lee, T.S. Hwang, K.J. Lee, B. Lee, Novel flexible styrenic elastomer cation-exchange material based on phenyl functionalized polystyrene-butadiene copolymer. J. of Industrial and Engineering Chemistry 47 (2017) 128-140.

[13] N. Job, Pirard, J. Marien, and J.P. Pirard, Porous carbon xerogels with texture tailored by pH control during sol–gel process, Carbon 42 (2004) 618–628.

[14] X. Yuan, Y.J. Chao, Z.F. Ma, and M. Deng, Preparation and characterization of carbon xerogel (CX) and CX–SiO composite as anode material for lithium-ion battery, Electrochem. Commun. 9 (2007) 2591–2595.

[15] J.P. Lewicki, C.A. Fox, and M.A. Worsley, On the Synthesis and Structure of Resorcinol-Formaldehyde Polymeric Networks-Precursors to 3D Carbon Macroassemblies, Technical Report, Lawrence Livermore National Laboratory (2015).

[16] K. Tokumitsu, A. Mabuchi, H. Fujimoto, and T. Kasuh. Electrochemical Insertion of Lithium into Carbon Synthesized from Condensed Aromatic. J. Electrochem. Soc., 143 (1996) 2235-2239.

[17] K. Gotoh, M. Maeda, A. Nagai, A. Goto, M. Tansho, K. Hashi, Tadashi Shimizu, Hiroyuki Ishida. Properties of a novel hard-carbon optimized to large size Lion secondary battery studied by 7Li NMR. Chemistry Physical & Theoretical Chemistry fields. Okayama University Digital Information Repository (2006).

[18] R. Siburian, H. Sihotang, S. Lumban Raja, M. Supeno, and C. Simanjuntak, New Route to Synthesize of Graphene Nano Sheets. Orient. J. Chem. 34, 1 (2018) 182-187.

[19] G. Wang, J. Yang, J. Park, X. Gou, B. Wang, H. Liu, and J. Yao, Facile Synthesis and Characterization of Graphene Nanosheets. J. Phys. Chem. C112 (2008) 8192-8195.

[20] M. Winter, J. O. Besenhard, M. E. Spahr, and P. Novµk, Insertion Electrode Materials for Rechargeable Lithium Batteries. Adv. Mater. 10 (1998) 725-763.

[21] A. N. Popova, Crystallographic analysis of graphite by X-Ray diffraction. Coke Chem. 60, (2017) 361–365.

[22] K.B. Oldham, A Gouy–Chapman–Stern model of the double layer at a (metal)/(ionic liquid) interface. J. of Electroanalytical Chem. 613 (2008) 131–138.

[23] O. Stern, Zur Theorie der Elektrolytischen Doppelschicht. Z Elektrochem 30 (1924) 508-16.

[24] M. Gouy, Sur la constitution de la charge électrique à la surface d'un électrolyte. J. Phys. Theor.Appl. 9, (1910) 457-468.

[25] D.L. Chapman, A contribution to the theory of electrocapillarity. Philos. Mag. 25 (1913) 475.

[26] A. Velikonja, E. Gongadze, V. Kralj-Iglič, and A. Iglič, Charge dependent capacitance of stern layer and capacitance of electrode/electrolyte interface. Int. J. Electrochem. Sci., 9 (2014) 5885 – 5894

[27] J. E. B. Randles, Discussions of the faraday society. Kinetics of rapid electrode reactions Vol. 1 (1947).

[28] Gamry. Common Equivalent Circuit Models. Available: https://www.gamry.com/assets/White-Papers/Gamry-Common-Equivalent-Circuit-Models.pdf. Accessed on: February 22, 2021.

[29] S. Fletcher, V.J. Black, and I. Kirkpatrick, A Universal equivalent circuit for carbon-based supercapacitors. J. Solid State Electrochem. (2014) 18:1377–1387.

[30] J. Caia, W. Weia, X. Hua, and D. A. Wood. Electrical conductivity models in saturated porous media: A review. Earth-Science Reviews 171 (2017) 419–433.

[31] Y. Gueguen and V. Palciauskas. Introduction to the Physics of Rocks. Princeton University Press (1994).

[32] D. Harrington, Electrochemical impedance spectroscopy, Chapter 2: Simple Electrochemical Systems. (2004).

[33] J. C. Maxwell. A dynamical theory of the electromagnetic field. Philosophical transactions of the Royal Society of London 155 (1865) 459–512.

[34] A.-M. Ampere, Exposé méthodique des phénomènes électro-dynamiques, et des lois de ces phénomènes. Bachelier (1823).

[35] Y. Jiang and J. Liu. Definitions of Pseudocapacitive Materials: A Brief Review. Energy Environ. Mater. 2 (2019) 30–37.

[36] P. Leroy and A. Maineult. Exploring the electrical potential inside cylinders beyond the Debye–Huckel approximation: a computer code to solve the ¨ Poisson–Boltzmann equation for multivalent electrolytes. Geophys. J. Int. 214 (2018) 58–69.

[37] D.C. Grahame, The Electrical Double Layer and the Theory of Electrocapillarity. Chemical Reviews 41 (3) (1947) 441–501.

[38] E. Gongadze, S. Petersen, U. Beck, and U. van Rienen. Classical Models of the Interface between an Electrode and an Electrolyte. Excerpt from the Proceedings of the COMSOL Conference (2009) Milan.

[39] P. Leroy and A. Maineult, Exploring the electrical potential inside cylinders beyond the Debye–Huckel approximation: a computer code to solve the ¨ Poisson–Boltzmann equation for multivalent electrolytes. Geophys. J. Int. 214 (2018) 58–69.

1.6 Supplemental information

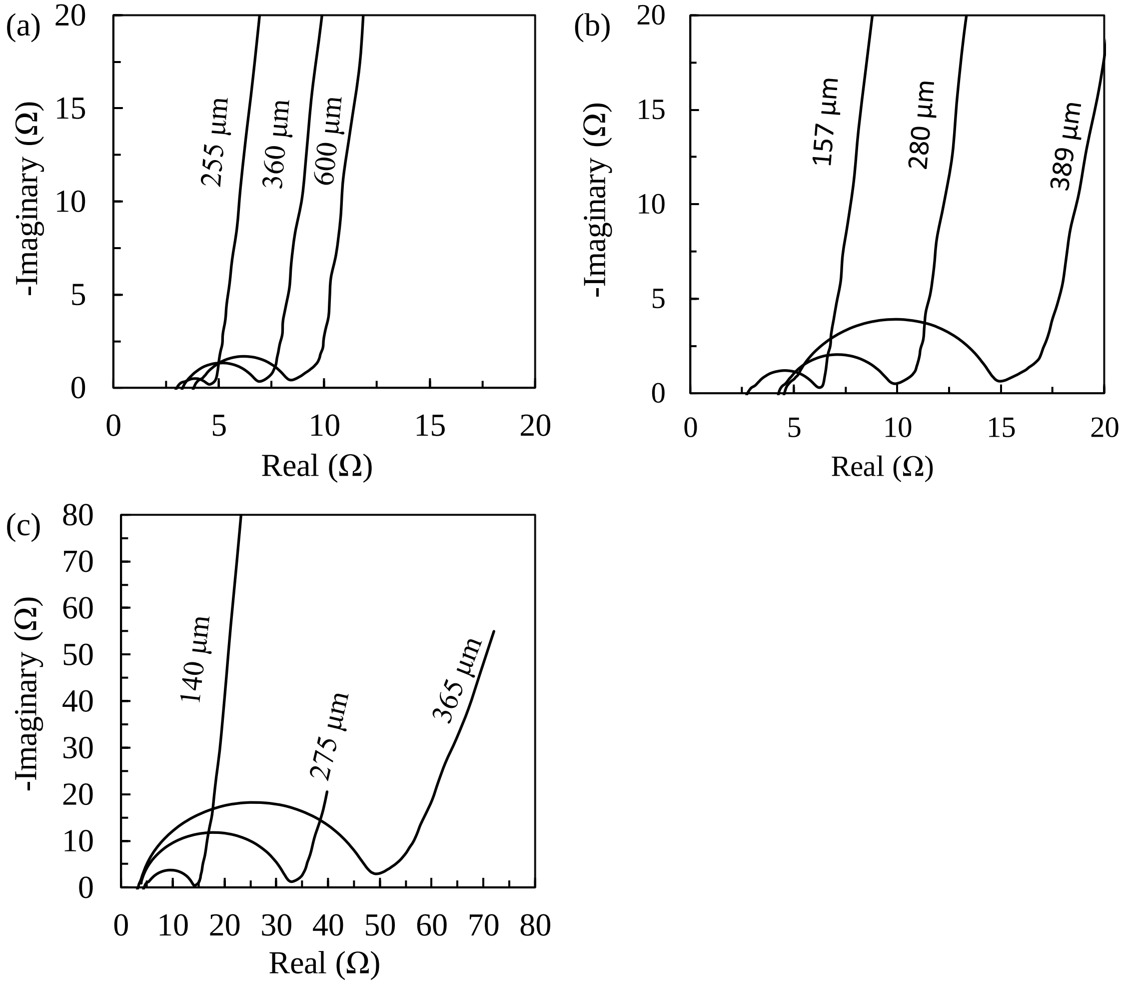

Figure S1.1 – CX with PVDF as a binder. (a) *R/C* = 2000 (b) *R/C* = 1375 (c) *R/C* = 750. The thickness of the layer is displayed next to the curve. Scan between 1 MHz and 100 mHz with 10 points per decade. Voltage amplitude of 10 mV.

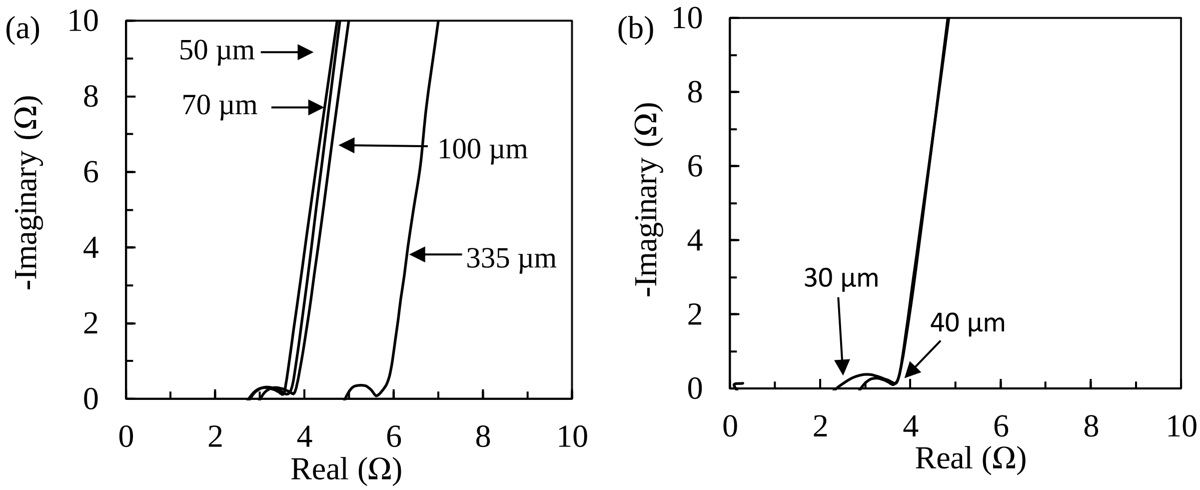

Figure S1.2 – CX with PSS as a binder with a R/C ratio of (a) 2000 and (b) 1375. The thickness of the layer is displayed next to the curve. Scan between 1 MHz and 100 mHz with 10 points per decade. Voltage amplitude of 10 mV.

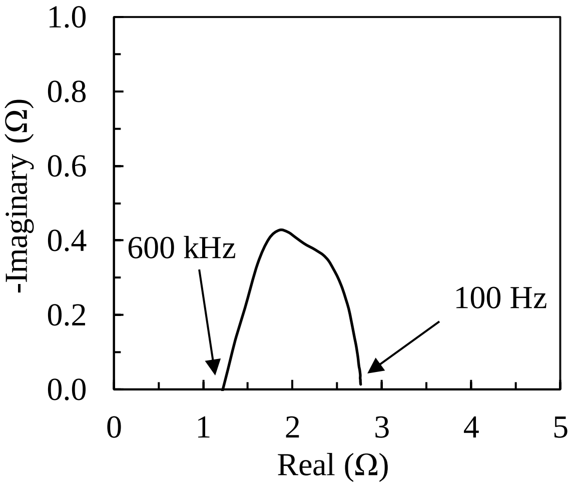

Figure S1.3 – EIS spectrum of the electrolyte and 2 sheets of Celgard 2400 separator. Scan between 600 kHz and 100 Hz with 10 points per decade. Voltage amplitude of 10 mV. The electrolyte-soaked Celgard sheets were sandwiched in between two lithium foils. This measurement was used to determine the conductivity of the bulk electrolyte with the separator. The arrow pointing to the 600 kHz measurement likely corresponds to the conductivity electrolyte while the half circle between the 600 kHz and 100 Hz arrows likely corresponds to the charge transfer resistance between the lithium foils and the electrolyte.

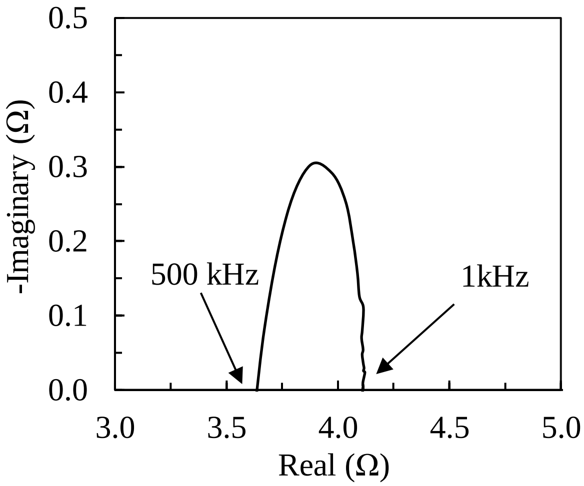

Figure S1.4 – EIS spectrum of the CX2000 composite electrode with PSS as a binder without electrolyte or separator. Scan between 1 MHz and 1 kHz with 10 points per decade. Voltage amplitude of 10 mV. The CX composite was sandwiched in between two stainless steel current collectors. This measurement was used to determine the conductivity of the CX active layer without the contribution of the electrolyte. The arrow pointing to the 500 kHz measurement likely corresponds to the conductivity of the CX2000 active material while the half circle between the 500 kHz and 1 kHz arrows likely corresponds to the charge transfer resistance between the CX2000 and the stainless steel electrodes.

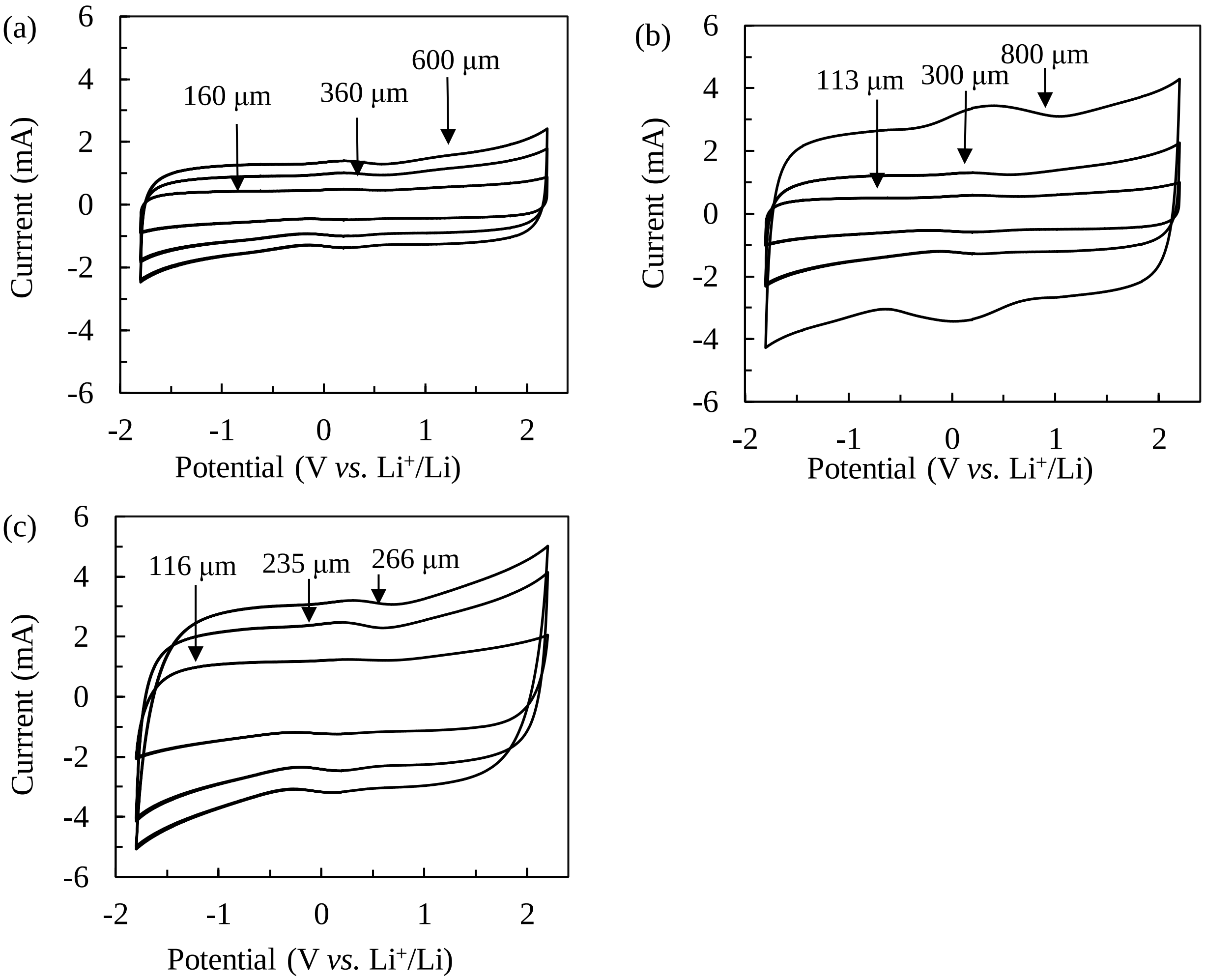

Figure S1.5 – Cyclic Voltammetry of CX electrodes with PVDF as a binder. (a) CX2000, (b) CX1375, (c) CX750. The scan rate was 50 μV s^{-1} between -2 V and 2 V *vs.* Li$^+$/Li.

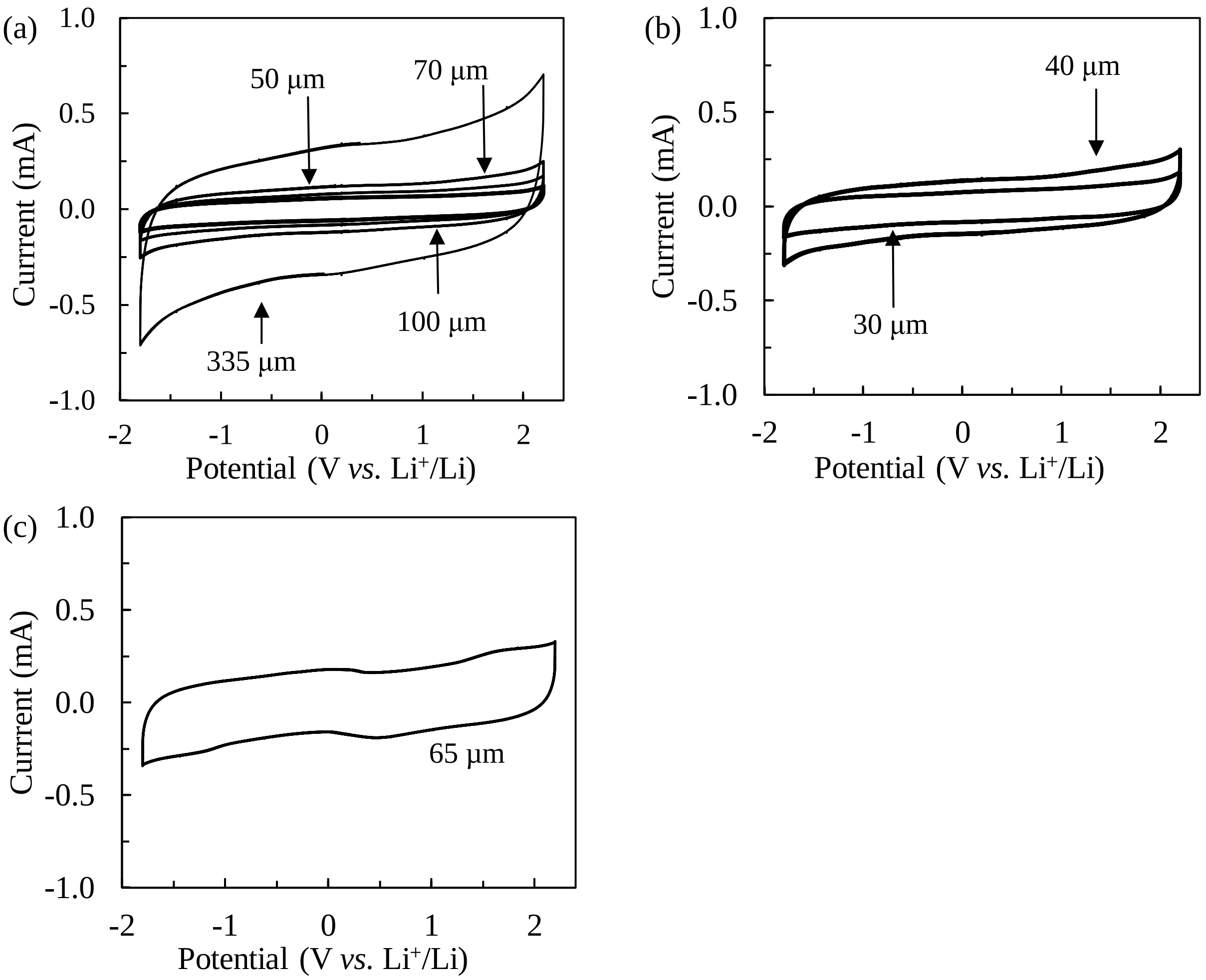

Figure S1.6 – Cyclic Voltammetry of CX electrodes with PSS as a binder. (a) CX2000, (b) CX1375, (c) CX750. The scan rate was 50 µV s^{-1} between -2 V and 2 V *vs.* Li^+/Li.

1.6.1 Matlab® calculation of the diffuse layer capacitance for confined surfaces

The diffuse layer, first proposed by Gouy and Chapman, extends from the OHP into the bulk of the electrolyte. This layer consists of a distribution of charge as a result of the varying concentration of ionic species within the electrolyte around the charged surface. Thus, the capacitance of this layer can be found by considering the differential capacitance (Equation 6), where the integral form of this equation is derived by considering Gauss's law:

$$\varphi'' = -\frac{\rho_e}{\varepsilon} \tag{S1.1}$$

where ρ_e is the volumetric charge density, φ'' is the second derivative of the potential, and ε is the dielectric permittivity of the electrolyte. Then by considering a 1-D case, where there is a dimension, x, normal to the charged surface, the differential surface charge density can be expressed by multiplying by a differential distance, dx, on both sides:

$$d\sigma = \rho_e dx = \varepsilon\varphi'' dx \tag{S1.2}$$

Finally, by plugging Equation S1.2 into Equation 1.10 and multiplying by dx on both sides and integrating, the diffuse capacitance can be expressed as:

$$C_{diffuse} = \varepsilon \frac{\int \varphi'' dx}{\int \varphi' dx} \tag{S1.4}$$

In order to calculate this capacitance, a solution to the Poisson-Boltzmann (PB) equation must be found either explicitly or numerically. First, the 1-D volumetric charge density can then be expressed as the following:

$$\rho_e = N_A q C_0 \exp\left(-\frac{q_i\varphi}{kT}\right) \tag{S1.6}$$

where q and C_0 is the charge and concentration, respectively, of each ionic species in the electrolyte (mol m^{-3}), N_A is Avogadro's number, k is the Boltzmann constant, and T is the temperature. Then, by plugging in this volumetric charge density into the PB equation:

$$\nabla^2\varphi = -\frac{N_A q C_0}{\varepsilon} \exp\left(-\frac{q_i\varphi}{kT}\right) \tag{S1.7}$$

However, given that the PB equation expressed in Equation S1.7 is non-linear and can be difficult to solve explicitly or numerically, a linearization of the PB equation, given the Debye-Hückel approximation, can be made by only considering the first two terms of the power expansion of the exponential term. This then reduces Equation S1.7 into the following equation:

$$\nabla^2\varphi = \frac{N_A q^2 C_0}{\varepsilon kT}\varphi \tag{S1.8}$$

where a characteristic length, the Debye length (λ_{debye}), can then be defined as the following:

$$\lambda_{debye}^{-2} = \left(\frac{N_A q^2 C_0}{\varepsilon kT}\right) \tag{S1.9}$$

An explicit 1-D solution to the Equation S1.8 is given in cylindrical coordinates where a radius, *r*, is defined from the center of a cylinder to the charged surface. The solutions for this geometry and the respective boundary conditions are given below:

$$\varphi(r) = C\,\mathrm{I}_0\left(i\frac{r}{\lambda_{debye}}\right)\begin{cases}\varphi\left(r_{pore}\right) = \varphi_0 \\ \varphi'(0) = 0\end{cases},\; C = \frac{\varphi_0}{\mathrm{I}_0\left(\frac{r_{pore}}{\lambda_{debye}}\right)} \tag{S1.10}$$

where φ_0 is the potential of the charged surfaces and I_0 is the zero-order modified Bessel functions of the first kind where the first and second derivatives are trivially known. This explicit solution can then be implemented in a short Matlab® script which can calculate Equation S1.4 using the first and second derivatives of Equation S1.10:

$$\varphi'(r) = \frac{C\,\mathrm{I}_1\left(i\frac{r}{\lambda_{debye}}\right)}{\lambda_{debye}} \tag{S1.11}$$

$$\varphi''(r) = \frac{\frac{C}{2}\left(\mathrm{I}_0\left(i\frac{r}{\lambda_{debye}}\right)+\mathrm{I}_2\left(i\frac{r}{\lambda_{debye}}\right)\right)}{\lambda_{debye}^2} \tag{S1.12}$$

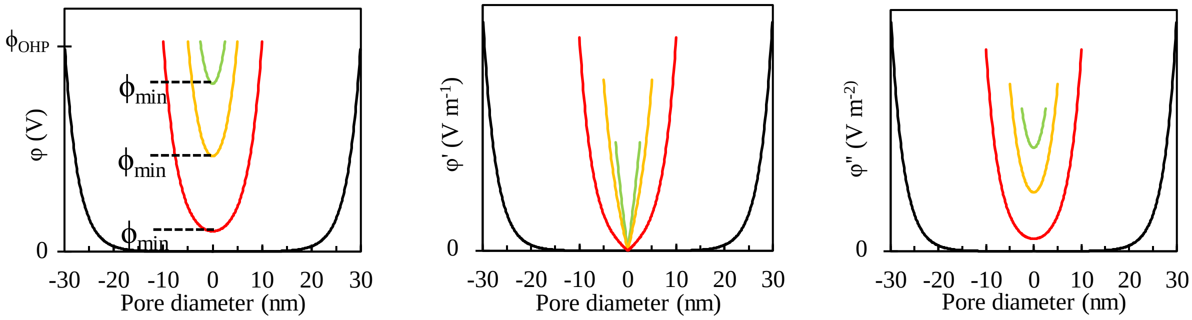

Figure S1.7 – (a) Potential vs. pore diameter, (b) first derivative of potential *vs.* pore diameter, and (c) second derivative of potential *vs.* pore diameter.

An explicit 1-D solution to the Equation S1.8 is given in planar coordinates where a distance, x, is defined for the diffuse capacitance in the bulk electrolyte. The solution for this geometry and the respective boundary conditions are given below:

$$\varphi(x) = C_1 e^{-\frac{x}{\lambda_{debye}}} \begin{cases} \varphi(0) = \varphi_{min} \\ \varphi'(\infty) = 0 \end{cases}, C_1 = \varphi_{min} \tag{S1.13}$$

where φ_{min} is the potential at the entrance of the pores. This explicit solution can then be implemented in a short Matlab® script which can calculate Equation S1.4 using the first and second derivatives of Equation S1.10:

$$\varphi'(x) = -\frac{C_1}{\lambda_{debye}} e^{-\frac{x}{\lambda_{debye}}} \tag{S1.14}$$

$$\varphi''(x) = \frac{C_1}{\lambda_{debye}^2} e^{-\frac{x}{\lambda_{debye}}} \tag{S1.15}$$

Chapter 2

Carbon xerogel doped with silicon nanoparticles

Abstract

Silicon can be used as a high capacity lithium-ion (Li^+ ion) battery anode given its high theoretical capacity (4200 mAh g^{-1}) and low lithium redox potential (< 0.5 V *vs.* Li^+/Li). However, the volume change of silicon that causes solid-electrolyte interphase (SEI) instability and pulverization of the active material during cycling should be avoided to obtain long-cycling electrodes. The aim of this chapter is therefore to use a carbon xerogel (CX) as a support matrix for silicon nanoparticles (SiNPs) in order to mitigate some of these negative characteristics. SiNPs were incorporated into the CX either (i) in the resorcinol-formaldehyde precursor solution before gelation (RF-SiNPs) or (ii) in the xerogel after gelation process but before pyrolysis (OX-SiNPs) with 15 wt% SiNPs. Physico-chemical characterization of the SiNPs-doped CX obtained after pyrolysis were conducted *via* TEM, XRD, and N_2 adsorption. Composite electrodes with PVDF as a binder were synthesized and assembled into half-cells. The RF-SiNPs exhibited a low capacity (250 mAh g^{-1}) with a relatively stable cycling while the OX-SiNPs exhibited a high capacity (> 600 mAh g^{-1}) but with poor cycling stability, albeit better than SiNPs by themselves. The cause of the low capacity of the RF-SiNPs composite electrode may be due to the inaccessibility of the Li^+ ions to the silicon surface. The inclusion of the SiNPs into the CX precursor solution may also have caused a change in the silicon surface or made lithiation of the silicon difficult for some other reason. The poor cycling stability of the RF-SiNPs composite electrode is likely due to the volumetric change of the silicon during cycling. Cyclic voltammetry and electrochemical impedance spectroscopy were used to further electrochemically characterize these composite electrodes.

2.1 Introduction

A primary area of research in lithium-ion (Li^+ ion) batteries is focused on improving their energy density, power density, and lifespan while maintaining safety and minimizing environmental impact. As has been discussed in the previous chapter, developing a fundamentally new chemistry or material with a higher intrinsic energy density is one way to accomplish these goals. An interesting group of materials are alloying-type active materials, which can be used in place of conventional graphite or other carbon material as the negative electrode [1, 2]. Alloying-type materials offer significantly higher energy densities than graphite by forming an alloy with lithium instead of intercalating Li^+ ion between the graphitic layers, thus increasing the number of Li^+ ions stored per mass of active material [1, 2]. Silicon has been shown to be an interesting alloying-type material for a Li^+ ion battery negative electrode given (i) its low electrochemical lithiation/delithiation potential (< 0.5 V *vs.* Li^+/Li) and (i) its high theoretical energy density of up to 4200 mAh g^{-1} as compared to ~350 mAh g^{-1} for a conventional graphite electrode [1, 2]. Silicon is also a relatively abundant element in the Earth's crust and a large silicon-based economy currently supports the mining and synthesis of high purity silicon metal [3].

Unfortunately, the use of silicon as a Li^+ ion battery negative electrode has been limited due to instability arising from the large difference in volume (up to 300%) between the lithiated and delithiated silicon [4-6]. This change in volume causes (i) an unstable solid electrolyte interphase (SEI) to form and (ii) pulverization of the silicon and the other electrode layer materials, such as graphite or other conductive additives, which leads to a shorten lifespan of the battery [4–6]. Additionally, silicon is an inherently poor electrical conductor; therefore, some type of conductive element is usually required to attain sufficient power density.

Some recent studies have shown promising results that address some of the problems related to silicon as a negative electrode material. One such study showed that silicon nanoparticles (SiNPs) with a diameter of less than 150 nm can significantly reduce pulverization of the silicon by decreasing the internal stresses caused by the large volume changes; however, the problems of SEI instability and poor electrical conductivity persist [5]. Other studies have found that coating the SiNPs with some type of carbon improves the SEI stability [6-8]. Other studies also worked with a "yolk-shell"-type of morphology that is comprised of a void space between the silicon and the carbon coating. This morphology would allow for the expansion of the silicon during lithiation while maintaining electrical contact throughout the layer and with the current collector [9, 10]. In conventional batteries, given the low conductivity of transition metal oxides, conductive additives, such as carbon black, are added to increase the conductivity of the active layer without adding too much weight [11, 12]. These two properties are highly desirable in order to offer both high power density and energy density. However, since carbon black does not cover the silicon surface, it can neither act as a support for the silicon nanoparticles to accommodate their volume expansion nor does it protect their surface from SEI instability. Additionally, the high specific surface area of carbon black would lead to large losses in the pristine cycle due to excessive SEI formation.

In the previous chapter, a carbon xerogel (CX) was introduced as an interesting candidate material to support high energy density dopants, such as tin oxide or silicon. A CX is an amorphous hard carbon with an interconnected 3D meso-macroporous structure. These meso-macropores are formed by spherical microporous nodules connected in a rigid "string of pearls"-like structure [13-17]. CXs are usually prepared *via* a simple and cheap sol-gel synthesis where the average meso/macro-pore size of the CX can be easily increased or decreased by respectively decreasing or increasing the pH of the precursor solution (most often a resorcinol-formaldehyde (RF) aqueous solution) during synthesis [13-17]. Additionally, a CX has a nominal intrinsic reversible capacity of approximately 200 mAh g^{-1}, albeit this capacity is achieved *via* a linear Li^+ ion insertion/deinsertion potential between 0.005 V and 1.5 V *vs*. Li^+/Li [14, 15]. This material should be able to act as a support structure for the SiNPs and offer good electrical conductivity.

Therefore, in this work, an electrode comprised of SiNPs supported by a CX is proposed as negative electrode material. The silicon that was used as the dopant in this work was composed of commercial SiNPs synthesized *via* the well-known PVD method of pulsed-laser ablation. In this process, a silicon target is placed in a vacuum chamber and an intense pulsed laser ablates the silicon surface, which leads to the formation of a plume of silicon particles [18]. These particles are then collected *via* a pump or deposited on a surface. Less common synthesis techniques include other laser-ablation techniques, such as the ablation of a silicon target in a liquid media, or mechanical milling of silicon [19-21].

The inclusion of SiNPs into a CX was carried out at two different points during the CX synthesis procedure: SiNPs were either incorporated (i) in the resorcinol-formaldehyde (RF) precursor solution before gelation (RF-SiNPs) or (ii) in the organic xerogel (OX) after gelation and drying processes but before pyrolysis (OX-SiNPs). The latter procedure consisted of preparing an aqueous suspension of the OX powder and SiNPs and allowing the SiNPs to diffuse into the OX particles. The former procedure would potentially allow the SiNPs to be more even distributed in the gelled OX since the SiNPs are included in the precursor solution.

The two SiNPs-doped samples were then pyrolyzed and assembled into electrodes by spray coating a slurry of the composite material with a binder onto a current collector. The binder that was used in these syntheses was poly(vinylidene difluoride) (PVDF), which is a conventional binder used to prepare Li^+ ion battery electrodes. These electrodes were then assembled into half-cells for electrochemical characterization. The active materials were also physico-chemically characterized, with and without a binder, to determine pertinent textural properties *via* TEM imaging, N_2 adsorption, Hg porosimetry, and X-ray diffraction. In a similar manner, the SiNPs used in this synthesis were separately physico-chemically and electrochemically characterized for a baseline comparison. Electrochemical characterization of all half-cells included galvanostatic cycling, electrochemical impedance spectroscopy (EIS), and cyclic voltammetry (CV).

2.2 Experimental

Materials: Resorcinol (R, 99%), formaldehyde (F, 37 wt% in H_2O), sodium carbonate (C, 99.5%), and polyvinylpyrrolidone (PVP, M_w = 40,000 g mol^{-1}) were purchased from Sigma-Aldrich. N-methyl-2-pyrrolidone (NMP, ~99%), poly(vinylidene difluoride) (PVDF), and silicon nanoparticles (SiNPs, laser-synthesized, average particle size (APS) ≤ 50 nm) were purchased from Alfa Aesar.

2.2.1 CX sample: carbon xerogel synthesis

A carbon xerogel (CX) with an *R/C* ratio of 2000 was synthesized *via* the sol-gel polycondensation of resorcinol and formaldehyde in high purity water (*via* MilliQ process until R > 18 MΩ) [6-8]: see section 1.2.1 in Chapter 1 for the solution preparation, gelation, drying, ball-milling, and pyrolysis procedures). The recovered OX powder from this synthesis was used later in the preparation of the OX-SiNPs sample shown in section 2.2.3.

2.2.2 RF-SiNPs sample: Doping with SiNPs before gelation step

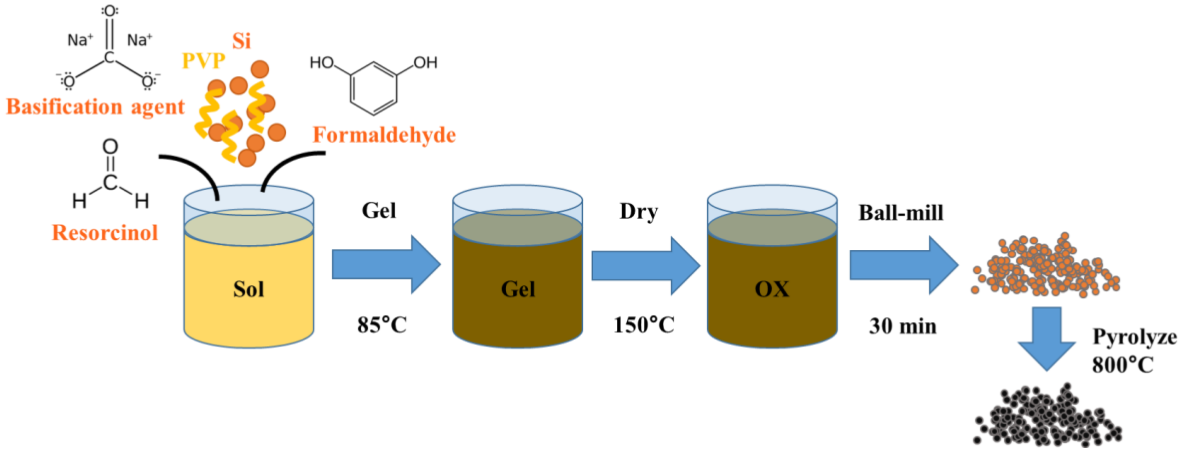

Figure 2.1 – Schematic diagram of the preparation of the RF-SiNPs sample: silicon nanoparticles are introduced in the xerogel precursor solution.

A CX doped with SiNPs was synthesized *via* the direct inclusion of commercial silicon nanoparticles into a xerogel precursor solution. The precursor solution was the same as in the case of CX sample (*R/C* = 2000, *R/F* = 0.5, *D* = 5.7). First, the precursor solution was prepared and magnetically stirred at room temperature for about 30 min until the resorcinol, formaldehyde, and basification agent had thoroughly dissolved. Once a stable solution was obtained, PVP was dispersed into the solution to act as a surfactant for the SiNPs. Finally, the SiNPs were dispersed into the solution to a mass ratio of 10:1 between the surfactant and SiNPs and a 12:1 mass ratio of (R+F):SiNPs. The amounts of each component are indicated in Table 2.1. The suspension was mixed for 10 min and then treated in an ultrasonic bath for 30 min to ensure a good dispersion of the silicon. The solution was then placed in a Binder VD-53 oven at atmospheric pressure in a closed synthesis bottle and underwent gelation for 3 days at 85°C.

Table 2.1 – Mass of reactants for RF-SiNPs composite synthesis.

Component	**Quantity** g (mL)	**Mass % on dry basis** %
Resorcinol	5.77	63.3
Formaldehyde (37 wt%)	2.66 (7.85)	29.2[a]
Sodium carbonate	0.0042	< 0.5
SiNPs	0.670	7.3
Water (solvent)	50 (50)	-

[a] Calculated considering the amount of undiluted formaldehyde.

Gelation, ball-milling, and pyrolysis were carried out in a similar manner as the CX. The recovered carbonized material, referred to as RF-SiNPs, was dark gray in color and the mass had reduced by approximately half, likely due to the carbonization process. Given the loss of mass of the xerogel during pyrolysis, the final mass percent of silicon was expected to be approximately 15 wt% SiNPs (which was confirmed *via* thermogravimetric analysis, see Figure S2.1a).

2.2.3 OX-SiNPs sample: Organic xerogel doped with SiNPs by impregnation

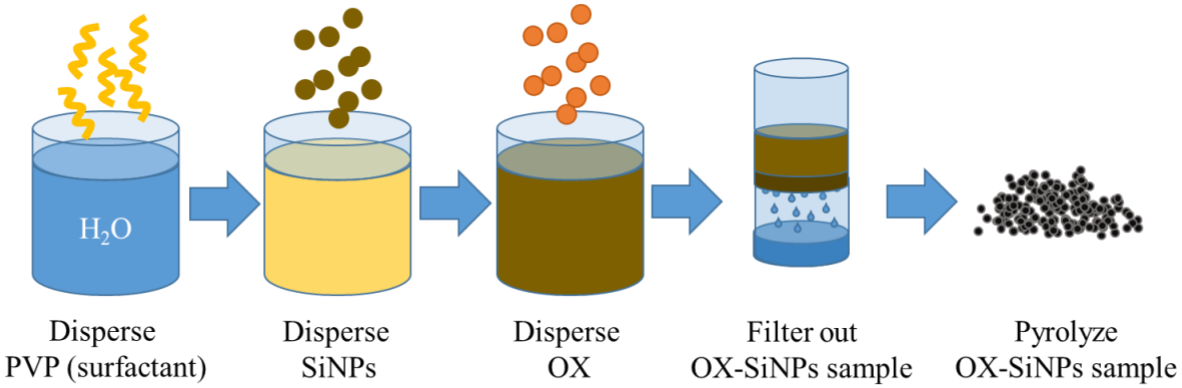

Figure 2.2 – Schematic diagram of the preparation of the OX-SiNPs sample: the SiNPs were impregnated into the xerogel after the gelation and drying steps.

A carbon xerogel doped with silicon nanoparticles was synthesized *via* the impregnation of commercial SiNPs into a xerogel after gelation, drying, and grinding. First, the preparation, gelation and ball-milling of an unpyrolyzed xerogel (OX) was carried out in a similar manner as with the CX sample. The OX was doped with SiNPs by first dispersing a surfactant, PVP, in high purity water (*via* MilliQ process until $R > 18$ MΩ) to a concentration of 20 $\mathrm{mg_{PVP}}$/mL to aid in the suspension of the SiNPs. The SiNPs were then added to the solution with a surfactant/SiNPs mass ratio of 10:1. The amounts of each component are indicated in Table 2.2. The resultant suspension was ultrasonicated for 1 h in a Branson 2510 ultrasonic bath to obtain a well-dispersed suspension of the SiNPs. Then the unpyrolyzed xerogel was added to the suspension with a xerogel-SiNPs mass ratio of 10:1. The suspension was then ultrasonicated for 1 h and mixed for 4 h with a magnetic stirrer at 500 rpm at 25°C. The solvent was then removed by vacuum filtration through a 0.024 µm PVDF microporous filter. The collected sample was subsequently dried for 24 h at 80°C and 2.5 kPa in a vacuum oven.

Table 2.2 – Mass of reactants for OX-SiNPs sample synthesis.

Component	**Mass**	**Mass % on dry basis**
	g	%
OX	1.0	47.6
PVP	1.0	47.6
SiNPs	0.1	4.8

The sample was then pyrolyzed in a similar manner as the CX and RF-SiNPs samples. The recovered pyrolyzed material, referred to as OX-SiNPs, was black in color and the mass had reduced by approximately two-thirds, likely due to the carbonization process that causes some mass loss of the xerogel and complete loss of the PVP surfactant. Given these mass losses during pyrolysis, the final silicon mass percent was expected to be approximately 15 wt% SiNPs (which was confirmed *via* thermogravimetric analysis, see Figure S2.1b).

2.2.4 Preparation of inks and electrodes

Electrodes were prepared using the CX, SiNPs, RF-SiNPs, or OX-SiNPs powder as the active material with PVDF as a binder. First, ink slurries were prepared for subsequent electrode preparation and electrochemical characterization. The inks were prepared by mixing 90 wt% of the active material and 10 wt% of PVDF in NMP under magnetic stirring at 1000 rpm for 4 h. The inks were spray-coated onto pre-weighed 15.5 mm diameter stainless steel disks. These disks were fixed on a 70°C heated surface. The coatings were deposited using a Harder & Steenbeck Evolution Silverline 2 airbrush. A solvent-to-solids ratio of 20:1 was used in all cases to ensure that the prepared inks flowed easily through the airbrush. After spray-coating, the electrodes were dried at 70°C for 2 h and then at 120°C under vacuum for 24 h. The electrodes were then weighed to determine the mass of the deposited material prior to their electrochemical characterization. Excess dried material surrounding the electrodes, which was deposited around the disks during the spray-coating process, was collected for further characterization.

2.2.5 Physico-chemical and electrochemical characterization

Physico-chemical and electrochemical characterizations carried out in this chapter are outlined in Annex 1. The physico-chemical characterizations included transmission electron spectroscopy, nitrogen adsorption-desorption, and X-ray diffraction. N_2 adsorption was used to determine the BET surface area (S_{BET}) and the corresponding microporous (S_{micro}) and meso/macroporous (S_{ext}) surface areas. XRD and TEM with EDS analysis was used to determine the SiNPs crystallite size, particle size and distribution, elemental characterization, and crystallographic microstrain of the dopant silicon nanoparticles. Electrochemical characterization consisted of cyclic voltammetry (CV), galvanostatic cycling, and electrochemical impedance spectroscopy (EIS). CV characterizations show the redox potentials of the electrochemically active components as well as how these reactions evolve during cycling, cycling gives the specific capacity and stability of the prepared composite electrodes. EIS analysis was used to determine how the equivalent series resistance (ESR), charge transfer resistance (R_{ct}), charge transfer capacitance (C_d) and the diffusive properties of the composite electrodes evolves during cycling. An overview of these parameters and the electrochemical model for these electrodes can be found in Annex 2.

2.3 Results and discussion

2.3.1 Physico-chemical characterization

Transmission electron microscopy

TEM micrographs were obtained on CX, SiNPs, RF-SiNPs, and OX-SiNPs samples. Figure 1.1 shows the CX at various magnifications. The TEM micrographs and discussion have been given previously in section 1.3.1 in Chapter 1. Figure 2.3 shows TEM micrographs of the SiNPs as-received from the supplier. The silicon nanoparticles appear as fairly round with a smooth texture. They seem to cluster together on the macroscopic scale when viewed in a TEM; however, this clustering may be just an effect of the SiNPs layering on top of each other. It does seem, however, that the particles have fused together into larger macrostructures, which may require some additional treatment, such as ultrasonication, surfactants, or some other type of process, to break the nanoparticles apart. The higher magnification micrographs in Figure 2.3c and d further show the size and shape of these SiNPs and the extent of how much these nodules have agglomerated.

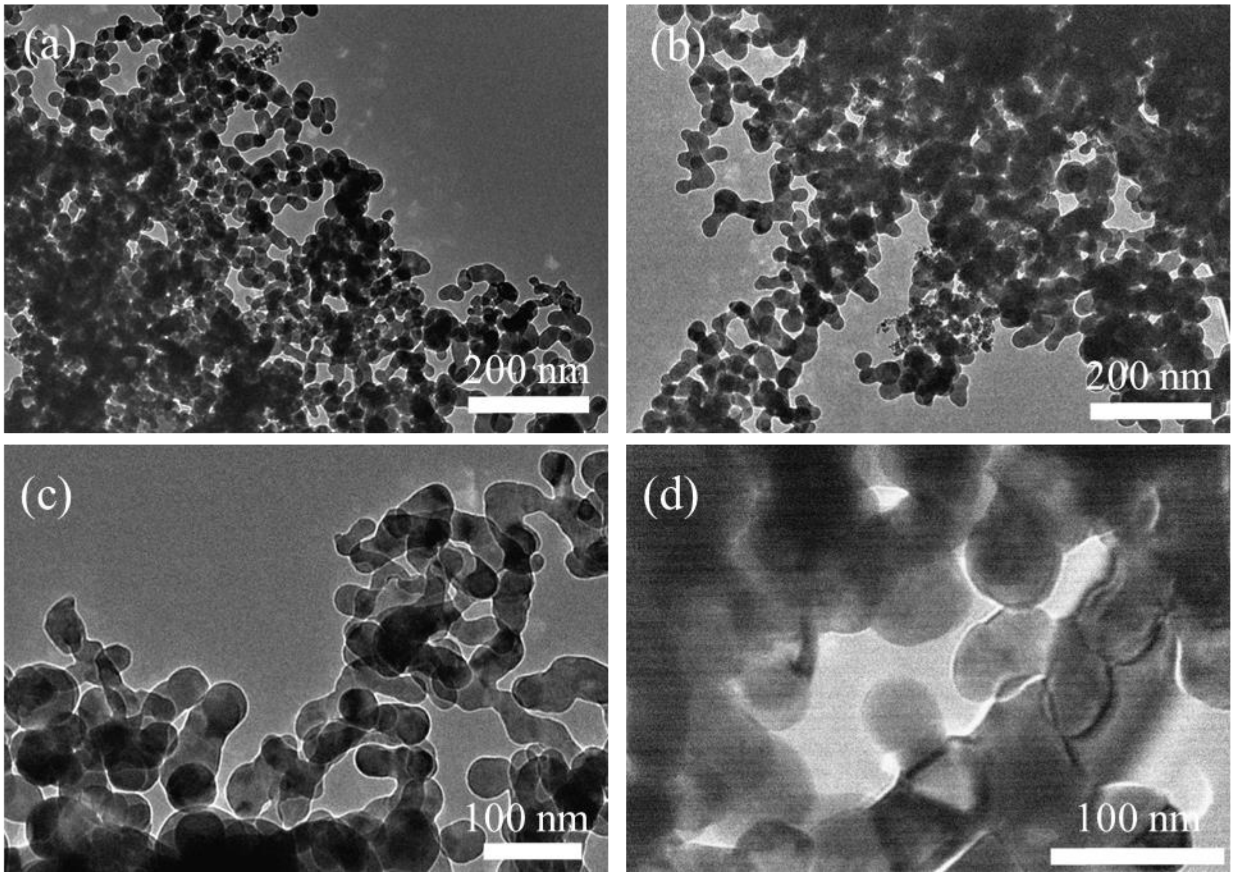

Figure 2.3 – TEM micrographs of a SiNPs alone, as-received from commercial supplier at various magnifications.

Figure 2.4 shows TEM micrographs of the RF-SiNPs sample at various magnifications. In all four micrographs, the SiNPs can be identified by their higher opacity and their smooth, round shape. The lowest magnification micrograph in Figure 2.4a shows SiNPs distributed within a single CX particle. The SiNPs seem to be fairly well-dispersed throughout it; however, agglomerations of SiNPs still persist. In Figure 2.4b and c, the SiNPs still seem to be located within the meso/macro-porosity of the CX particle rather than within its internal structure, although some agglomeration seems to have occurred on the exterior the CX particle. The highest magnification micrograph in Figure 2.4d more clearly shows how the SiNPs are integrated into the carbon structure. Although qualitative, the amount of the SiNPs surface in contact with the CX seems to be fairly good; that is, the SiNPs seem to be fairly well surrounded by the CX with various points of contact.

A particle size distribution of the SiNPs within the CX particles has been roughly calculated by manually measuring the diameter of ~100 SiNPs in a series of TEM micrographs. The results of this analysis can be found in the Supplemental Information in Figure S2.2a, which show a distribution of particle diameters between 20 and 120 nm with an average around 48 nm.

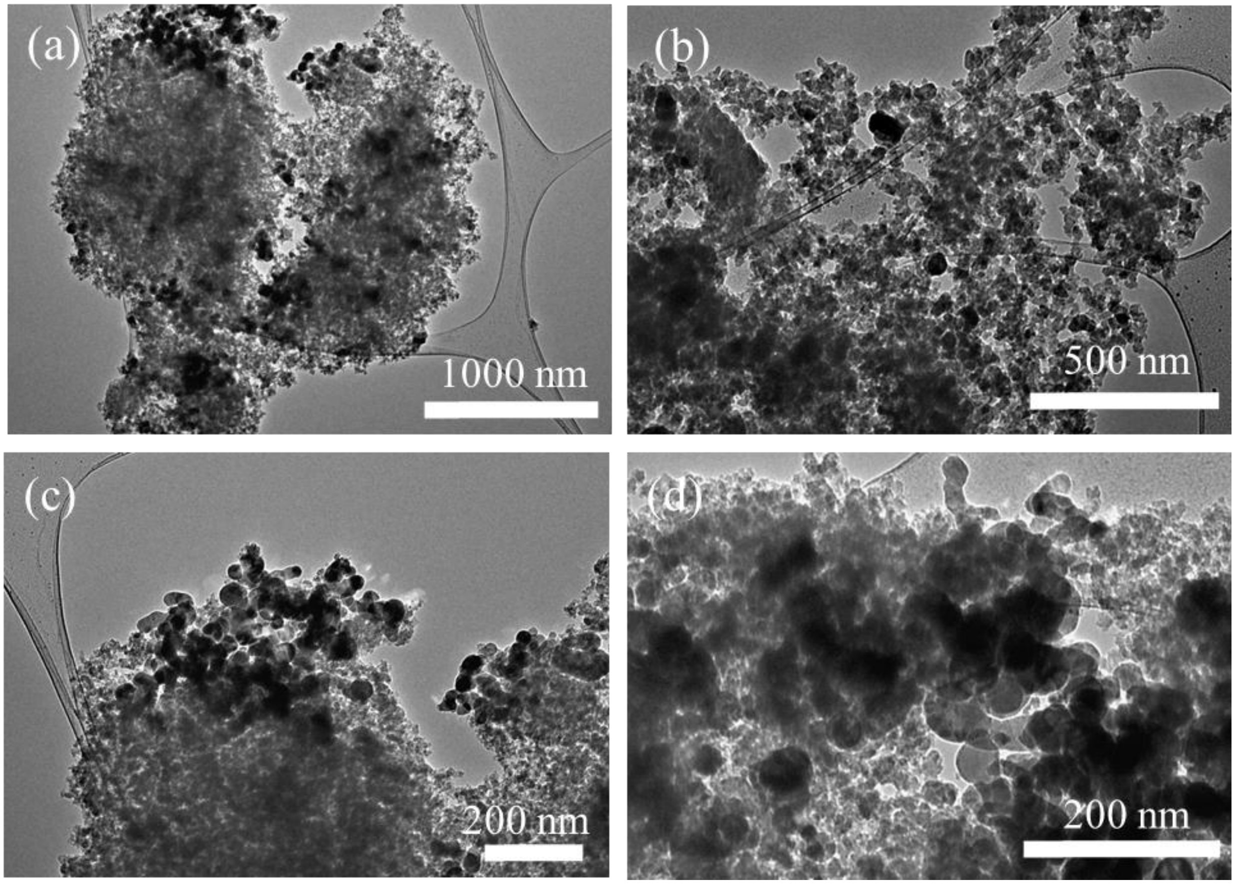

Figure 2.4 – TEM micrographs of RF-SiNPs sample at various magnifications.

Figure 2.5 shows TEM micrographs of the OX-SiNPs sample at various magnifications. The distribution of the SiNPs throughout the CX particles appears to be slightly different in this sample than the distribution of SiNPs in the RF-SiNPs sample. Figure 2.5a seems to show that the larger aggregates of SiNPs are deposited around the outside of the CX particle. This difference is likely due to the fact that the CX was already gelled before the SiNPs were introduced. In this synthesis, the distribution of SiNPs throughout the CX particles would depend on the diffusional characteristics of the SiNPs to enter into the pores of the CX. Therefore, it would be reasonable to assume that SiNPs or their aggregates with diameters greater than the meso/macropore diameter of the CX would not be able to enter into the CX particle and would be deposited on the surface of each particle, as shown in Figure 2.5a.

The higher magnification micrographs in Figure 2.5b and c seem to show that the smaller SiNPs may still have the ability to infiltrate into smaller parts of the CX. The highest magnification micrograph in Figure 2.5d mostly shows that these smaller SiNPs can in fact access more confined regions of the CX particle. Furthermore, Figure 2.5d shows roughly how the surface of the SiNPs interact with the surface of the CX. Clearly, the SiNPs are in contact with the CX at far fewer points as compared to the RF-SiNPs sample, especially given that many of the SiNPs are aggregated into large clusters. The lower contact area between the SiNPs and the CX in the RF-SiNPs sample will probably affect its electrochemical properties; this will be discussed further in the electrochemical characterization section. A particle size distribution of the SiNPs within the CX particles has been roughly calculated by manually measuring the diameter of the SiNPs in a series of TEM micrographs. The results of this analysis can be found in the supplemental information in Figure S2.2b, which shows a distribution of particle diameters between 40 and 120 nm with an average around 51 nm.

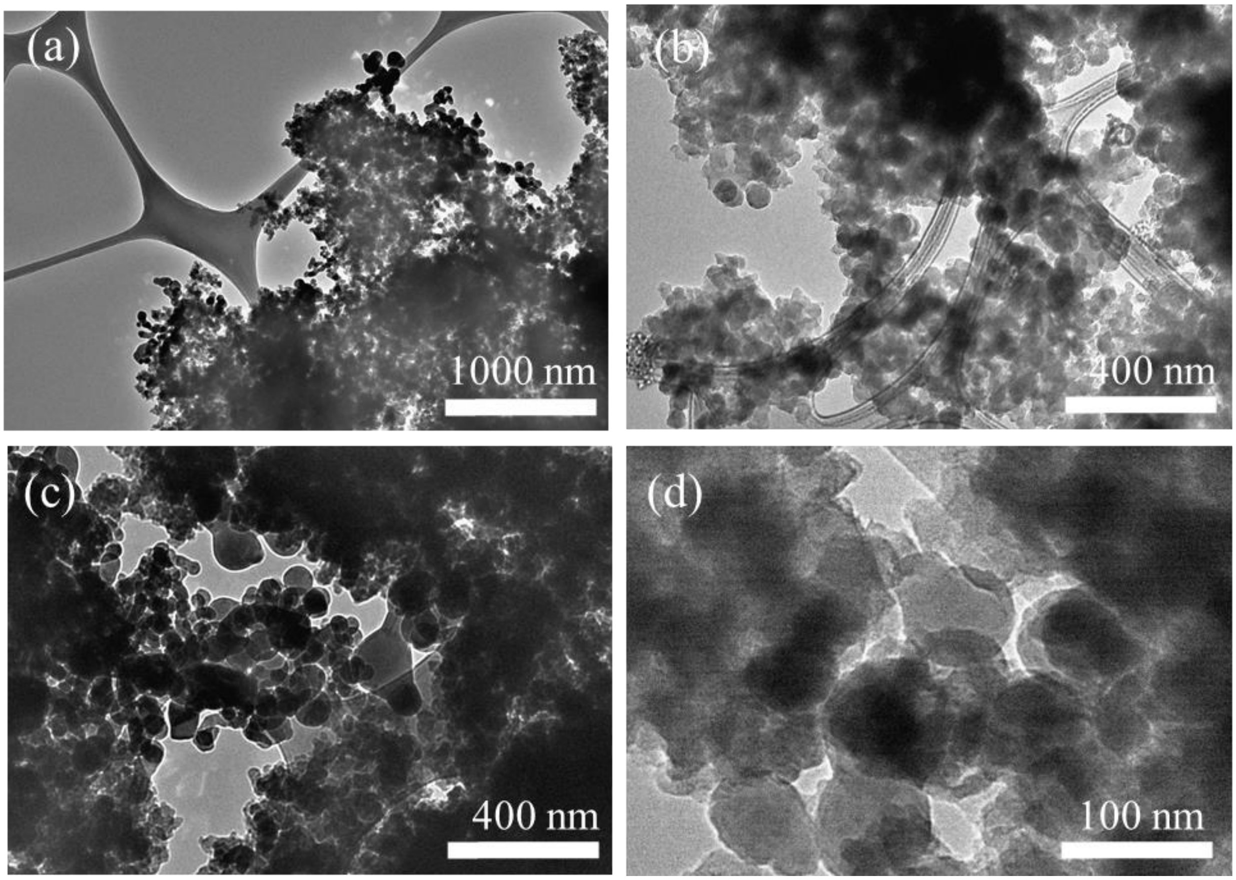

Figure 2.5 – TEM micrographs of OX-SiNPs sample at various magnifications.

Nitrogen adsorption-desorption

Nitrogen adsorption-desorption isotherms and the corresponding microporous (S_{micro}) and meso/maroporous (S_{ext}) surface areas of the SiNPs, CX, RF-SiNPs, and OX-SiNPs samples are shown in Figure 2.6. All surface area measurements are calculated per unit mass of active material (*i.e.* CX + SiNPs). N_2 adsorption measurements on the as-received SiNPs shows that the total specific surface area, S_{BET}, was found to be 50 m^2 g^{-1} with micropore and meso/macropore surface areas of 0 m^2 g^{-1} and 51 m^2 g^{-1}, respectively. Thus, for SiNPs, $S_{\text{BET}} = S_{\text{ext}}$. These measurements differ slightly with the specific surface area quoted by the manufacturer for the SiNPs, which was between 70-100 m^2 g^{-1} (non-microporous). The N_2 isotherm of the CX sample exhibits a type I/II isotherm, which corresponds to a material composed of both micropores as well as meso/macropores. The total specific surface area (S_{BET}) of the CX was measured to be 652 m^2 g^{-1} with a micropore and meso/macropore surface area of S_{micro} = 498 m^2 g^{-1} and S_{ext} = 153 m^2 g^{-1}, respectively.

The N_2 isotherms of the RF-SiNPs and OX-SiNPs samples also resemble a type II/IV isotherm, similar to the CX sample. For the RF-SiNPs sample, the total specific surface area (S_{BET}) was found to be 464 m^2 g^{-1} with micropore (S_{micro}) and meso/macropore (S_{ext}) surface areas of 388 m^2 g^{-1} and 76 m^2 g^{-1}, respectively. This yields a material that has 83% microporous surface. The total specific surface area (S_{BET}) of the OX-SiNPs sample was found to be 521 m^2 g^{-1} with a micropore (S_{micro}) and meso/macropore (S_{ext}) surface area of 399 m^2 g^{-1} and 122 m^2 g^{-1}, respectively. This yields a material that has 78% microporous surface. A summary of these values is given in Table 2.3.

The RF-SiNPs and OX-SiNPs samples have approximately the same specific microporous and meso/macroporous surface areas but with a slightly different percent of microporous surface area. This difference in the percent of microporous surface area between these two samples may be due to either (i) the distribution of the SiNPs in the CX or (ii) a change in the morphology of the CX or SiNPs as a result of the different synthesis procedures. Furthermore, both RF-SiNPs and OX-SiNPs samples have less total specific surface area than the CX. The loss of microporous and meso/macroporous surface area in these samples are likely due to the fact that since the SiNPs have no microporosity and significantly lower meso/macroporosity than the CX, all surfaces being reported by mass of Si-doped sample. Thus, the total amount of each specific surface area might decrease according to the mass percent of each component, *i.e.* CX or SiNPs, in each sample. In this case, the theoretical microporous and meso/macroporous surface area of both samples would be approximately 424 m^2 g^{-1} and 136 m^2 g^{-1}, given that the samples are composed of 15 wt% SiNPs. The difference between these theoretical values and the values measured could be due to either (i) the distribution of the SiNPs in the CX or (ii) a change in the morphology of the CX or SiNPs as a result of how the SiNPs were incorporated into the CX.

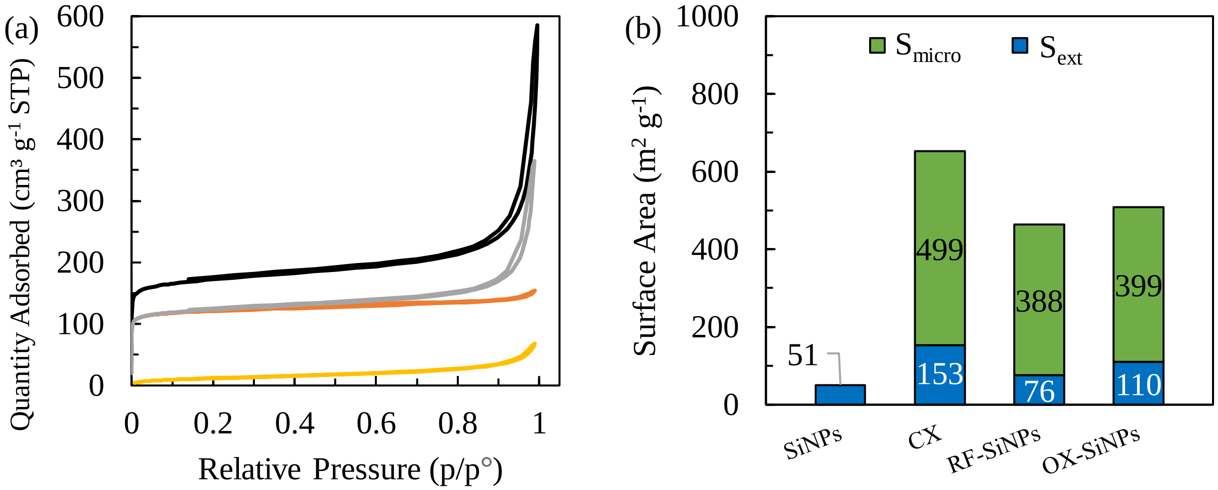

Figure 2.6 – (a) N_2 adsorption/desorption isotherms for the (—) SiNPs, (—) CX, (—) RF-SiNPs, and (—) OX-SiNPs powders. (b) Corresponding specific surface areas separated into microporous surface area (S_{micro}) and meso/macropore (S_{ext}) surface area. All surface area measurements are calculated per unit mass of active material (*i.e.* CX + SiNPs).

Table 2.3 – Nitrogen adsorption-desorption data for the CX, SiNPs, RF-SiNPs, and OX-SiNPs powders.

Sample	S_{micro} m² g⁻¹	S_{ext} m² g⁻¹	S_{BET} m² g⁻¹	**% microporous surfaces**
CX	498	153	652	76%
SiNPs	0	50	50	0%
RF-SiNPs	388	76	464	83%
OX-SiNPs	399	110	509	78%

X-ray diffraction

Figure 2.7 shows the XRD patterns of the CX, the RF-SiNPs, and the OX-SiNPs powders after ball-milling and pyrolysis. As shown previously in Chapter 1, the XRD pattern of the CX exhibits no clear crystallographic characteristics, given the lack of any strong diffraction peaks related to graphite or any other allotrope of carbon, but only exhibits three very wide peaks at around 2θ angles of 15°, 30°, and 42°, where the first two peaks are related to the oxygenated C(002) plane, and the former to the C(100) plane [23, 24]. Generally, these peaks indicate that the CX sample is, as expected, amorphous in nature. In fact, it is well known that carbon gels are non-graphitizable materials even at higher temperature, *i.e.* hard carbons [25].

The RF-SiNPs and OX-SiNPs powders, however, clearly show the characteristic silicon diffraction peaks of the Si(111), Si(220), Si(311), Si(400), Si(331), and Si(442) crystallographic planes at 2θ angles of 28°, 47°, 56°, 69°, 76°, and 88°, respectively [25, 26]. The underlying broad diffraction response between 5° and 50°, corresponding to the CX support, seems to be altered as compared to the CX without SiNPs.

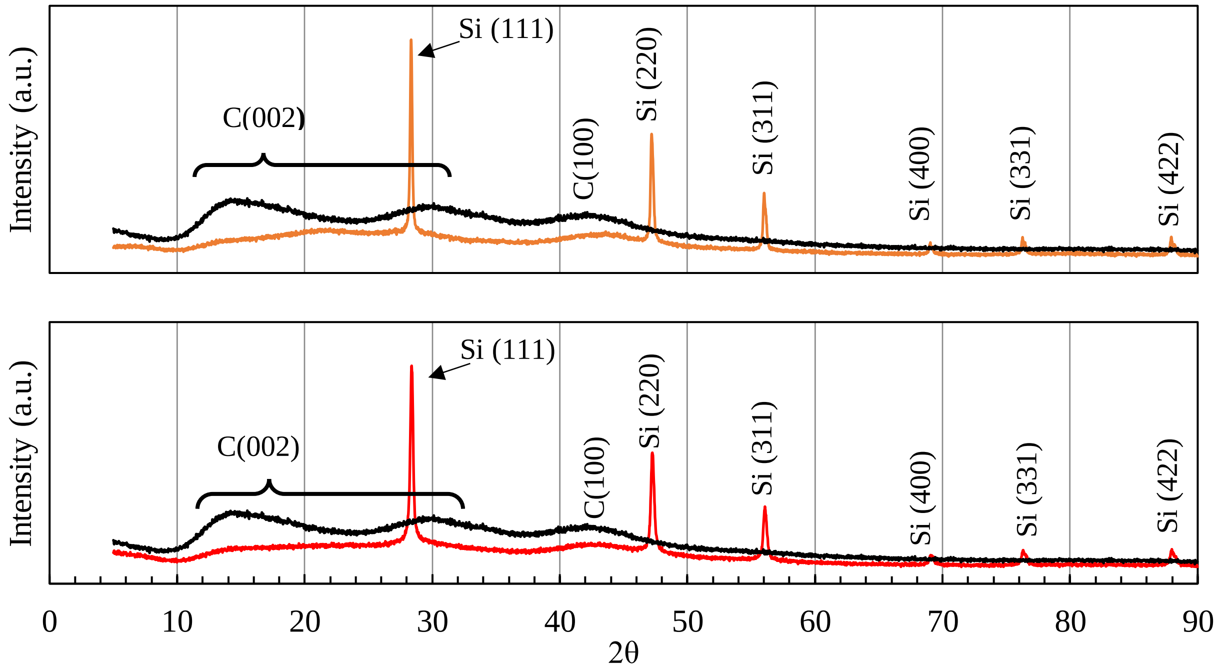

Figure 2.7 – XRD patterns of the (▬) CX, (▬) RF-SiNPs, and (▬) OX-SiNPs samples.

The Williamson-Hall method was used to determine the size broadening and microstrain broadening of the SiNPs in the OX-SiNPs and RF-SiNPs samples under a uniform deformation model (UDM). The crystallite size of the SiNPs in the RF-SiNPs sample, as measured by the size broadening of the crystallographic domains, was estimated to be 57 nm. This agrees well with the quoted average particle size of the SiNPs by the manufacturer ($d_{\text{particle}} < 50$ nm). The crystallite size of the SiNPs in the OX-SiNPs sample was measured to be 42 nm. The smaller average SiNPs size in the OX-SiNPs sample as compared to the RF-SiNPs sample suggests that the larger SiNPs and agglomerates have been filtered out of the OX-SiNPs sample, likely during the filtering step, as shown in Figure 2.2. These measurements would suggest that the SiNPs in both composites are likely monocrystalline since the size broadening measurements correspond with the particle size distributions shown in Figure S2.2. The monocrystalline nature of the SiNPs as well as the average particle size difference between the two samples will likely have an effect on their electrochemical performance, especially considering the high internal stresses that result from the lithiation and delithiation process for larger or agglomerated nanoparticles.

The crystallographic microstrain, which is a measure of a difference of volume of the crystallographic structure from its unstressed state due to some stress present in the crystal structure, was calculated to be 0.1% for the SiNPs in both the RF-SiNPs and OX-SiNPs samples. This amount of microstrain is considered very small and, therefore, it may be safe to conclude that there is no significant microstrain in the crystal structure of the SiNPs. Furthermore, the difference in synthesis procedure between the two samples does not have an effect on the microstrain of the SiNPs. A summary of the information obtained from the Williamson-Hall plot is given in Table 2.4.

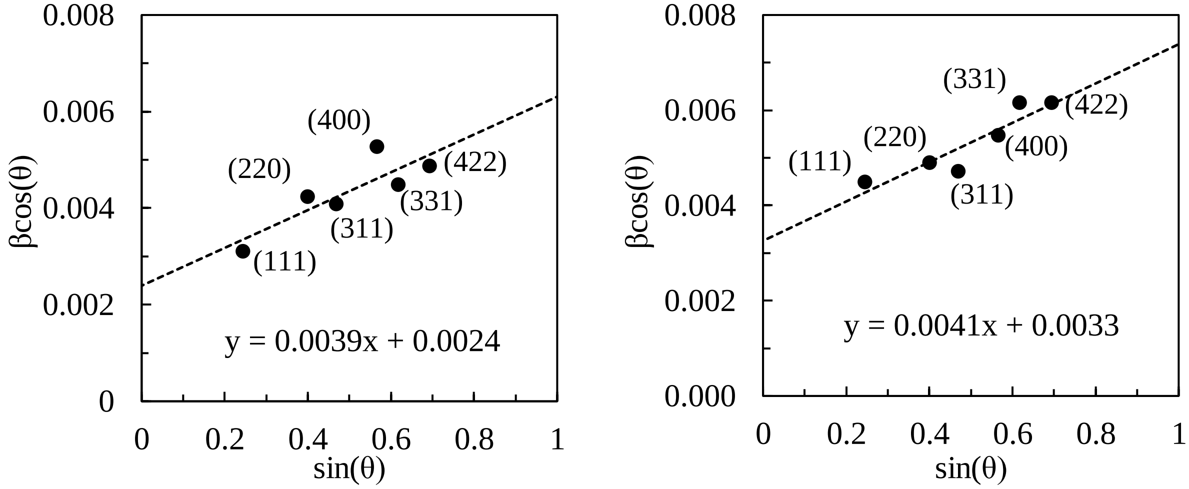

Figure 2.8 – Williamson-Hall plot of the silicon diffraction peaks in the (a) RF-SiNPs sample and (b) OX-SiNPs sample. Each point represents a diffraction peak of the SiNPs in each sample. The least-squares regression fit of these points gives information about the crystallite size (y-axis intercept) and microstrain (slope) of the diffracted material.

Table 2.4 – Crystallite size and microstrain of SiNPs.

Sample	**Crystallite size** nm	**Microstrain** %
RF-SiNPs	57	0.1
OX-SiNPs	42	0.1
SiNPs	< 50[a]	-[b]

[a] Value quoted from manufacturer. [b] Not measured.

2.3.2 Electrochemical characterization

Cyclic voltammetry

Cyclic voltammetry (CV) measurements conducted on the CX, RF-SiNPs, and OX-SiNPs composite electrodes are shown in Figure 2.9. CV measurements on an electrode synthesized with only SiNPs is shown in Figure S2.3 as a reference. All current measurements are reported per mass unit of active material (*i.e.* mass of CX + SiNPs). Figure 2.9a shows the CV measurements obtained for the electrode containing the CX sample. The pristine cycle of the CX shows three peaks at 1.3 V, 0.6 V, and ~ 0 V *vs.* Li^+/Li (Figure 2.9a). The reduction peaks during the pristine cycle at 1.3 V (peak 1) and 0.6 V (peak 2) *vs.* Li^+/Li may be attributed to either SEI formation or possibly to the trapping of Li^+ ions within the carbon xerogel. Indeed, SEI layers on carbon materials have been shown to form due to the instability of the electrolyte below approximately 1.3 V *vs.* Li^+/Li [27-29]. The underlying response that spans along the entire voltage window during lithiation, reaching a minimum at ~ 0 V *vs.* Li^+/Li, likely corresponds to the insertion of Li^+ ions into the CX (peak 3) [15]. The wide insertion window may be attributed to both the mesoporous structure of CX as well as the amorphous hard-carbon nature of the CX, as supported by the XRD measurements in this work and previous studies [15-17]. This wide insertion response, and similar de-insertion response, is different to that of conventional graphitic electrodes: the latter display a narrow insertion and de-insertion peak as a result of the regular spacing between graphitic layers.

Figure 2.9b shows the CV measurements obtained for the electrode containing RF-SiNPs. In the 1st cycle, the same SEI formation and Li^+ ion insertion peaks related to the CX are found; however, no lithiation or delithiation peaks corresponding to silicon are observed. In the 5th and 10th cycles the characteristic lithiation and delithiation peaks begin to appear. An alloying (lithiation) peak appears at 0.2 V *vs.* Li^+/Li (peak 4), which has been attributed to the lithiation of amorphous silicon [30-33]. Two de-alloying (delithiation) peaks appear between 0.3 V and 0.6 V *vs.* Li^+/Li (peaks 5), related to the removal of lithium from silicon [30-33]. The SEI formation peak of the silicon is not observed in the 1st cycle; however, it is likely present but probably too small to be seen given the reduced ability of the silicon to interact with the Li^+ ions in the electrolyte. This result may be the first sign of some change that could have occurred to the surface of the SiNPs during the synthesis procedure.

Figure 2.9c shows the CV measurements obtained for the electrode containing OX-SiNPs sample. The 1st cycle discharge exhibits similar peaks at 0.6 V *vs.* Li^+/Li related to SEI formation on the CX (peak 6). However, an additional strong lithiation peak appears below 0.1 V *vs.* Li^+/Li (peak 7); this peak is likely related to the initial alloying of crystalline silicon with lithium and SEI formation between the silicon and the electrolyte [30-33]. It is difficult to differentiate between these two phenomena. However, previous studies have come to similar conclusions regarding the initial electrochemical silicon-lithium alloying peaks. During the 1st delithiation, reduction peaks at 0.3 V to 0.6 V *vs.* Li^+/Li relate to the de-alloying of lithium from silicon (peak 8) [30-33]. During the 5th and 10th cycles, similar de-alloying peaks are observed; however, two alloying peaks appear at and below 0.2 V *vs.* Li^+/Li (peak 9 and 10), which has been attributed to the lithiation of amorphous silicon [30-33].

From these CV measurements, it seems that the RF-SiNPs composite electrode rendered the dopant SiNPs inactive to lithiation, at least during the first few cycles. This was exhibited by the lack of lithiation/delithiation peaks at the characteristic potentials, as was observed for the OX-SiNPs composite electrode. The RF-SiNPs composite electrode more closely resembled the CX electrode, with the characteristic SEI formation peaks and wide lithiation/delithiation potential of the CX only. In the 5th and 10th cycles, however, it seems that the SiNPs in the RF-SiNPs are “activated” to some degree given the slow appearance of the characteristic silicon lithiation/delithiation peaks. Since the diffraction pattern of the SiNPs persists in the RF-SiNPs XRD measurements, the surface of the SiNPs must have been altered in some way during the sample synthesis. The SiNPs surface may have changed due to the acidic precursor environment (such as forming an oxide layer) which rendered the SiNPs inaccessible or unable to be lithiated. Nevertheless, the exact cause for the lack of silicon redox peaks remains unknown.

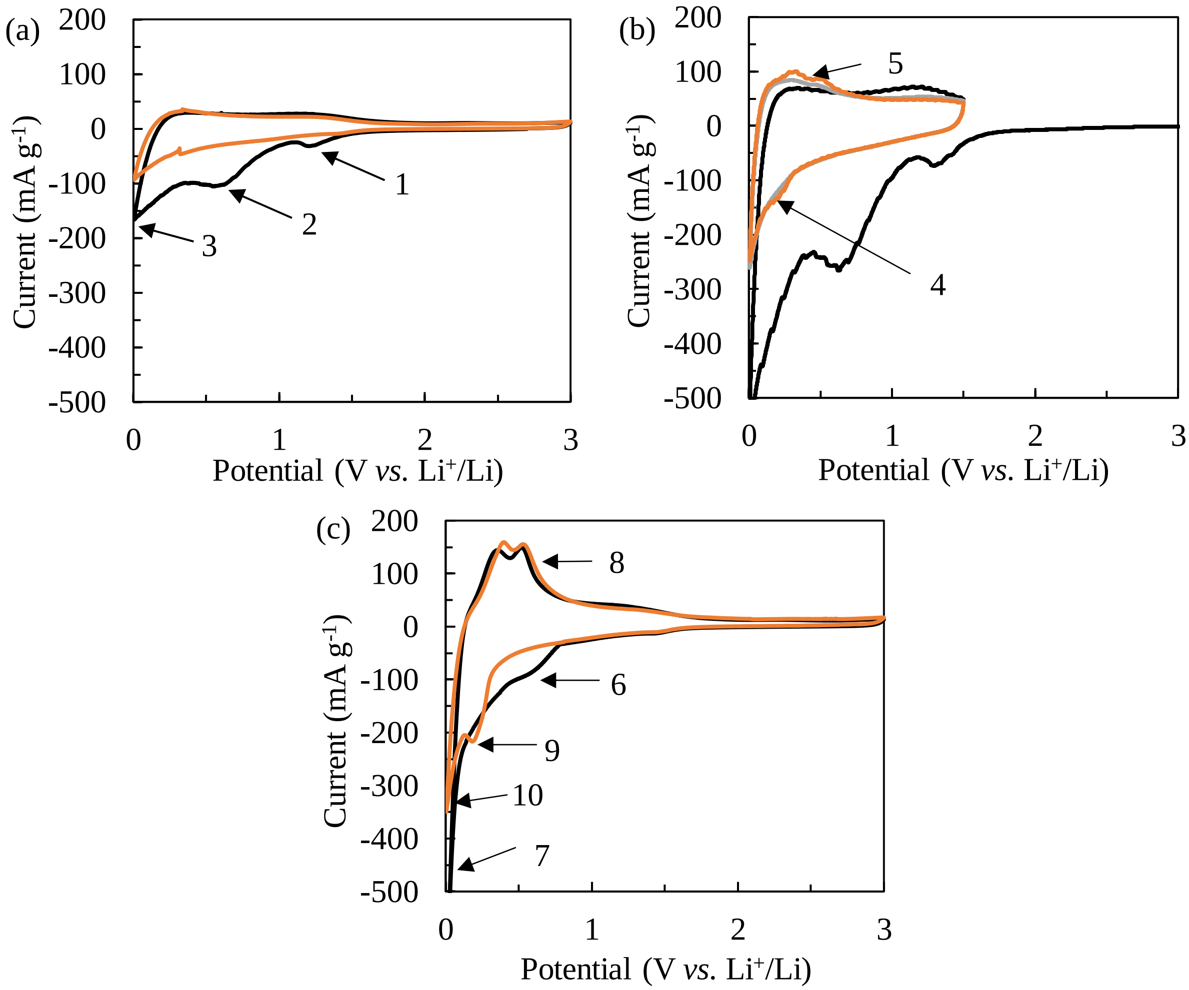

Figure 2.9 – Cyclic voltammetry measurements of electrodes containing samples (a) CX, (b) RF-SiNPs, and (c) OX-SiNPs. The scan rate was 50 μV s^{-1} between 0.005 V and 3 V or 1.5 V *vs.* Li$^+$/Li. (▬) 1st cycle, (▬) 5th cycle, and (▬) 10th cycle. Current normalized per unit mass of active material.

Galvanostatic cycling

Galvanostatic cycling was conducted on the CX, RF-SiNPs, and OX-SiNPs composite electrodes using PVDF as a binder. Measurements were performed at a rate of C/10 given the theoretical capacity of each respective composite electrode on a mass of active material basis. All capacities are reported per mass unit of active material (*i.e.* mass of CX + SiNPs) hereafter. Figure 2.10 shows the capacity of the RF-SiNPs composite electrode as compared to the CX electrode. The CX electrode shows a steady capacity of approximately 200 mAh g^{-1}.

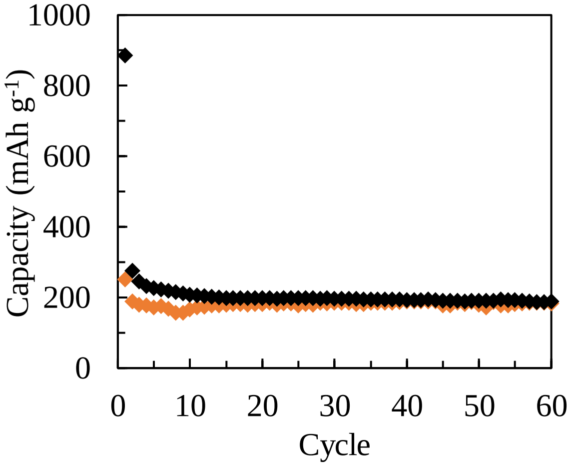

Figure 2.10 – Galvanostatic cycling conducted on the (◆) CX and (◆) RF-SiNPs composite electrodes with PVDF as a binder at a rate of C/10 between 0.005 V and 1.5 V *vs.* Li$^+$/Li.

The potential profile of the CX composite electrode, shown in Figure 2.11, exhibits a fairly linear lithiation and delithiation curve. This corresponds well with the CV measurements of the CX electrodes, which showed wide lithiation and delithiation potentials rather than sharp peaks at specific potentials. The RF-SiNPs composite electrode exhibits a poor initial capacity (Figure 2.10) with a value of around 250 mAh g^{-1} that slowly increased during cycling. This value is significantly less than the theoretical specific capacity of 800 mAh g^{-1} that would be expected for this sample given that the sample contains 15 wt% of silicon with a 4200 mAh g^{-1} specific capacity and the 85 wt% CX with approximately 200 mAh g^{-1} specific capacity. The corresponding potential profiles for the RF-SiNPs composite electrode are shown for the 5th, 20th, and 50th cycles in Figure 2.11b: one observes a slow appearance of the silicon lithiation and delithiation peaks between 0.2 V and 0.5 V *vs.* Li$^+$/Li. This is similar to what was observed in the CV measurements for this composite electrode and is a sign of the “deactivated” nature of the SiNPs dopant, *i.e.* the formation of an oxide layer on the silicon surface, in the RF-SiNPs sample.

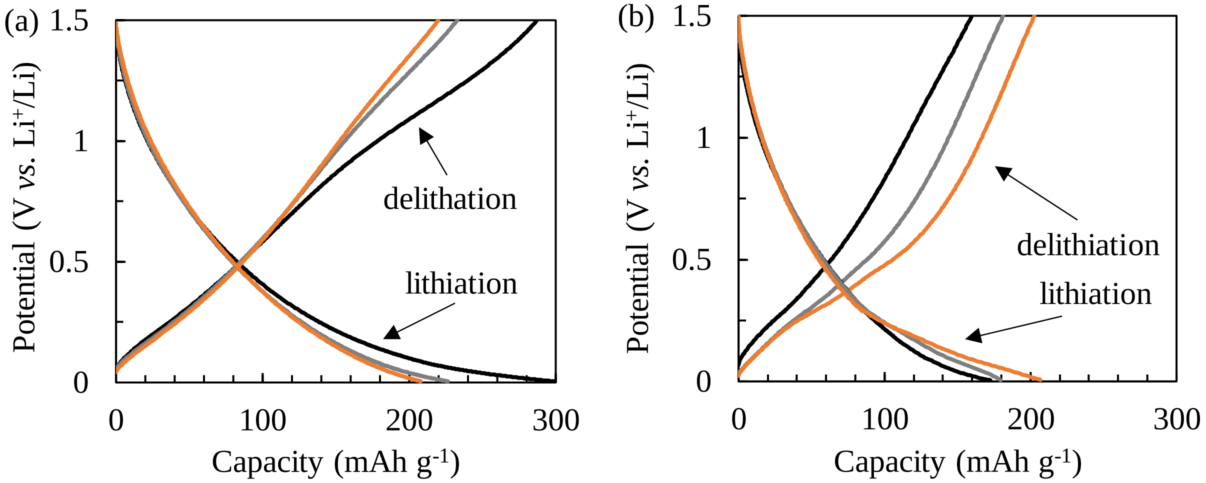

Figure 2.11 – Potential profile as a function of capacity of the composite electrodes with PVDF as a binder containing either (a) the CX sample or (b) the RF-SiNPs sample. Shown for the (▬) 5th, (▬) 20th, and (▬) 50th cycles.

Contrarily, galvanostatic cycling conducted on the OX-SiNPs composite electrode with PVDF as a binder exhibited capacity of approximately 700 mAh g^{-1}, *i.e.* close to the expected theoretical value of 800 mAh g^{-1} given the quantity of silicon and CX in the sample; it however showed poor capacity retention. The cycling performance (Figure 2.12a) shows that the OX-SiNPs composite electrode retained 50% of the initial capacity (350 mAh g^{-1}) after only the 12th cycle. The corresponding potential profiles of the OX-SiNPs sample with PVDF as a binder are shown for the 1st, 5th, and 50th cycles in Figure 2.12b; one observes a rapid disappearance of the silicon delithiation between 0.2 V and 0.5 V *vs.* Li^+/Li.

Galvanostatic cycling of an electrode formulated with only SiNPs and PVDF as a binder is also shown in Figure S2.4 in the supplemental information, for comparison. These results indicate that the SiNPs are more unstable as compared to the RF-SiNPs and OX-SiNPs composite electrodes given that the SiNPs composite electrode lost half of the initial capacity after the 4th cycle. Therefore, it seems that the use of the CX as a support structure and conductive additive modestly increases the cycling stability of SiNPs. The stability of the samples is, however, far from that requested for practical applications, where usually a cycling stability of 80% the initial capacity is retained for >200 cycles.

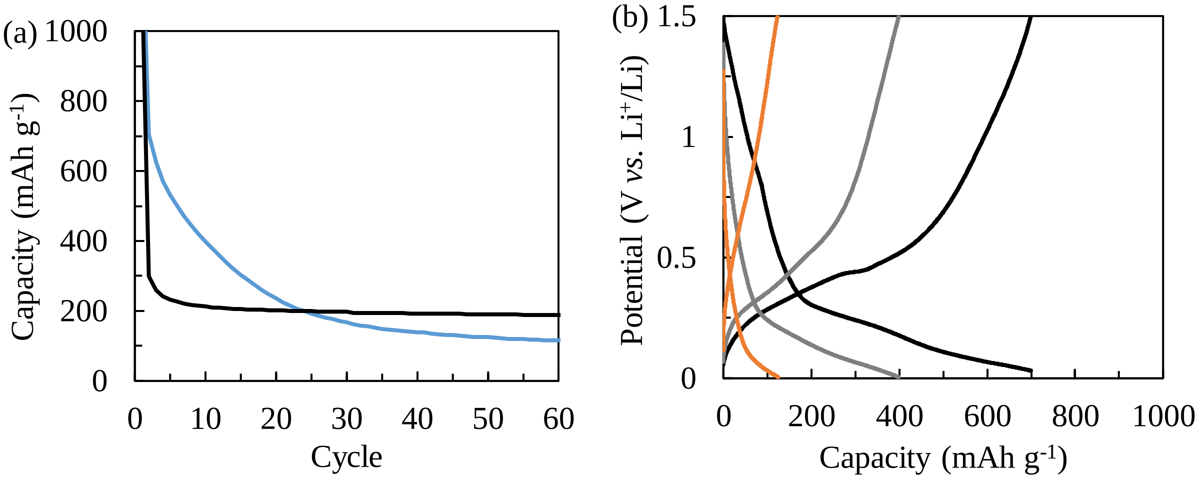

Figure 2.12 – (a) Galvanostatic cycling conducted on the (▬) CX and (▬) OX-SiNPs composite electrodes with PVDF as a binder and at a rate of C/10 given the theoretical capacity of the composite electrode. (b) Potential profile as a function of capacity of the OX-SiNPs composite electrode for the (▬) 1st, (▬) 5th, and (▬) 50th cycle.

Electrochemical impedance spectroscopy

EIS measurements were conducted on the RF-SiNPs and OX-SiNPs composite electrodes. The Nyquist plot and Bode diagram for the RF-SiNPs composite electrode are shown in Figure 2.13a and b. The Nyquist plot and Bode diagram for the OX-SiNPs composite electrode are shown in Figure 2.14a and b. The Randles cell along with its corresponding electrochemical quantities of equivalent series resistance (ESR), charge transfer resistance (R_{ct}) and capacitance (C_d), and diffuse properties, as shown in Annex 2.

The low frequency response, which relates to the diffusive behavior of charged species in the electrodes, shows a change between the 1st cycle and subsequent cycles for both composite electrodes. In the Bode diagrams, both composite electrodes change from approaching -90° phase shift to -45° phase shift between the 1st cycle and subsequent cycles. The 1st cycle behavior is more similar to what is expected with a supercapacitor since the phase shift in the Bode plot approaches -90°. This response is likely due to the fact that no SEI has been formed yet on the surface of the active material in the 1st cycle. Since the SEI facilitates Li^+ ion conduction, given that the R_{ct} usually decreases after the 1st cycle, the active layer acts more like a capacitor since diffusion is limited into the active material without the SEI [34]. The capacitive nature of the composite electrode is exacerbated by the fact that the CX has a rather large specific surface area.

The high-frequency (10^2 Hz to 10^6 Hz) response between the 1st cycle and subsequent cycles is notably different between these two composite electrodes. The OX-SiNPs composite electrode shows the appearance of two half-circles in the Nyquist diagram directly after the 1st cycle while the RF-SiNPs composite electrode only begins to exhibit this behavior after the 30th cycle. This change can also be seen in the Bode diagrams as the appearance of two dips in the phase shift instead of a single deep valley in this high frequency regime. As has been explained in Annex 2, the response of a half circle can generally be modelled as a resistance and a capacitance in parallel. This response is generally related to the formation or presence of an interphase that causes some type of charge separation. Therefore, this additional half-circle (or valley) is likely related to the interphase between the SiNPs and the electrolyte, which has a different kinetic time constant than the SEI between the CX and the electrolyte. The slower appearance of this response in the RF-SiNPs composite electrode may be due to the altered silicon surface that has likely been oxidized as a result of the RF-SiNPs sample synthesis conditions.

The evolution of the equivalent series resistance (ESR) is shown in Figure 2.13c and Figure 2.14c for the RF-SiNPs and the OX-SiNPs composite electrodes, respectively. The ESR remains relatively constant, except for an initial increase after the 1st cycle, for both the RF-SiNPs and OX-SiNPs composite electrodes. The relatively stable ESR is a sign that the conductivity of the electrolyte does not change drastically during cycling and that the contact between the active material and the current collector remained strong despite a loss of capacity for the OX-SiNPs composite electrode.

The evolution of C_d and R_{ct} are shown in Figure 2.13d and Figure 2.14d for the RF-SiNPs and the OX-SiNPs composite electrodes, respectively. R_{ct} decreases and C_d increases with cycling for both composite electrodes. These two phenomena support the idea that the active material is being pulverized by the volumetric change in the SiNPs during cycling. The decrease in the charge transfer resistance (R_{ct}) suggests that Li^+ ions are more easily transferred from the electrolyte to the active material while the increase in the charge transfer capacitance can primarily occur due to an increase in surface area between the electrolyte and the active material. These two phenomena would occur if active material was pulverized due to the volumetric change of the SiNPs during cycling. If the SiNPs break apart and cause the CX support to fragment as well, the specific surface area of the active material would increase and more surface area would be formed. This would allow Li^+ ions to transfer between the electrolyte and the CX with less resistance (*i.e.* lower R_{ct} due to more parallel conductive paths and the capacitive ability to increase *(i.e.* higher C_d) due to the larger surface area.

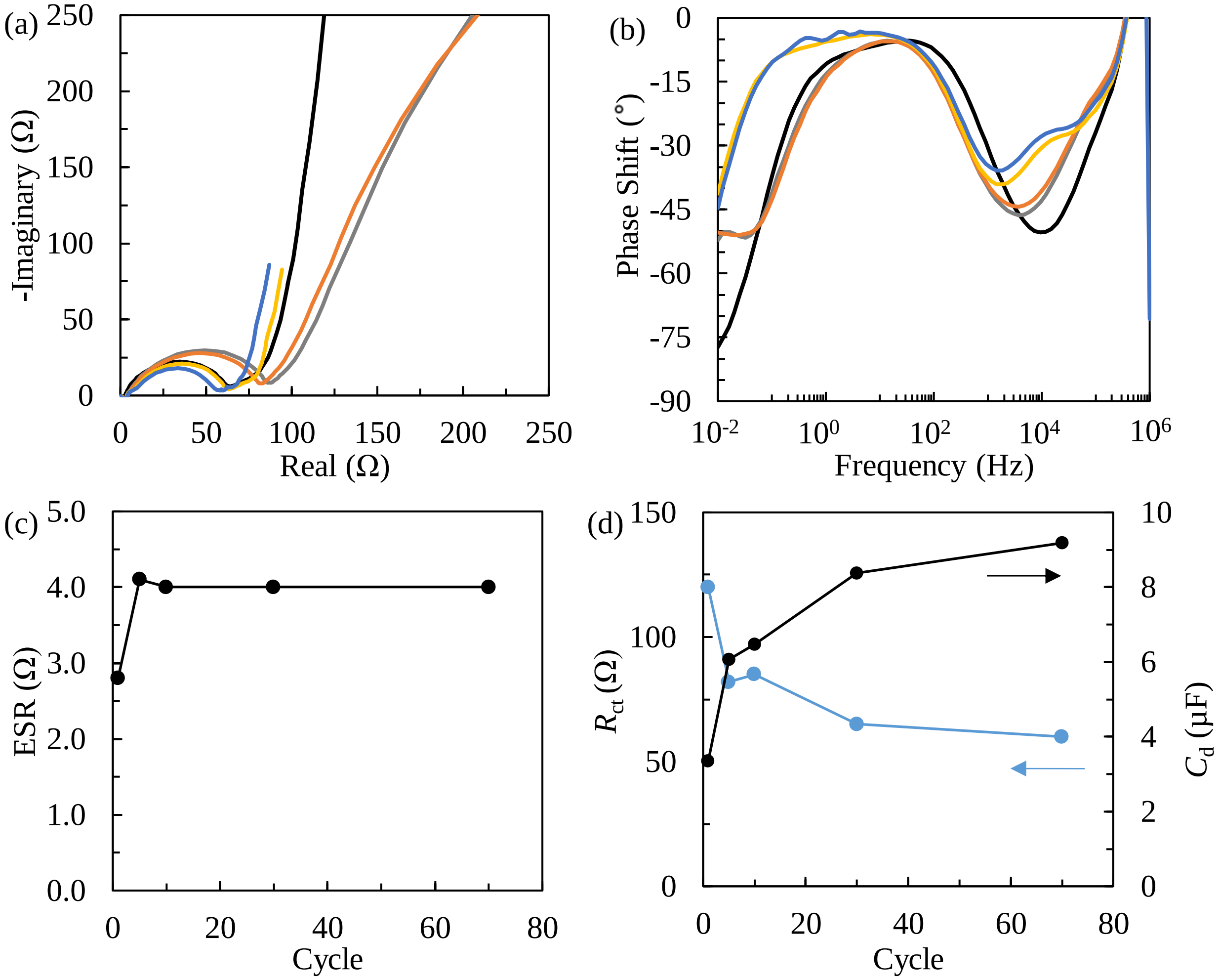

Figure 2.13 – EIS measurements for the RF-SiNPs composite electrode with PVDF as a binder. (a) Nyquist diagram and (b) Bode diagram: (—) Pristine, (—) 5th, (—) 10th, (—) 30th cycle, and (—) 70th cycle (Note: 30th and 50th cycles were completed after 1 month of not being cycled). (c) ESR as a function of galvanostatic cycles and (d) charge transfer resistance (R_{ct}) and charge transfer capacitance (C_d) as a function of galvanostatic cycles. Scan between 1 MHz and 100 mHz with 10 points per decade. Voltage amplitude of 10 mV.

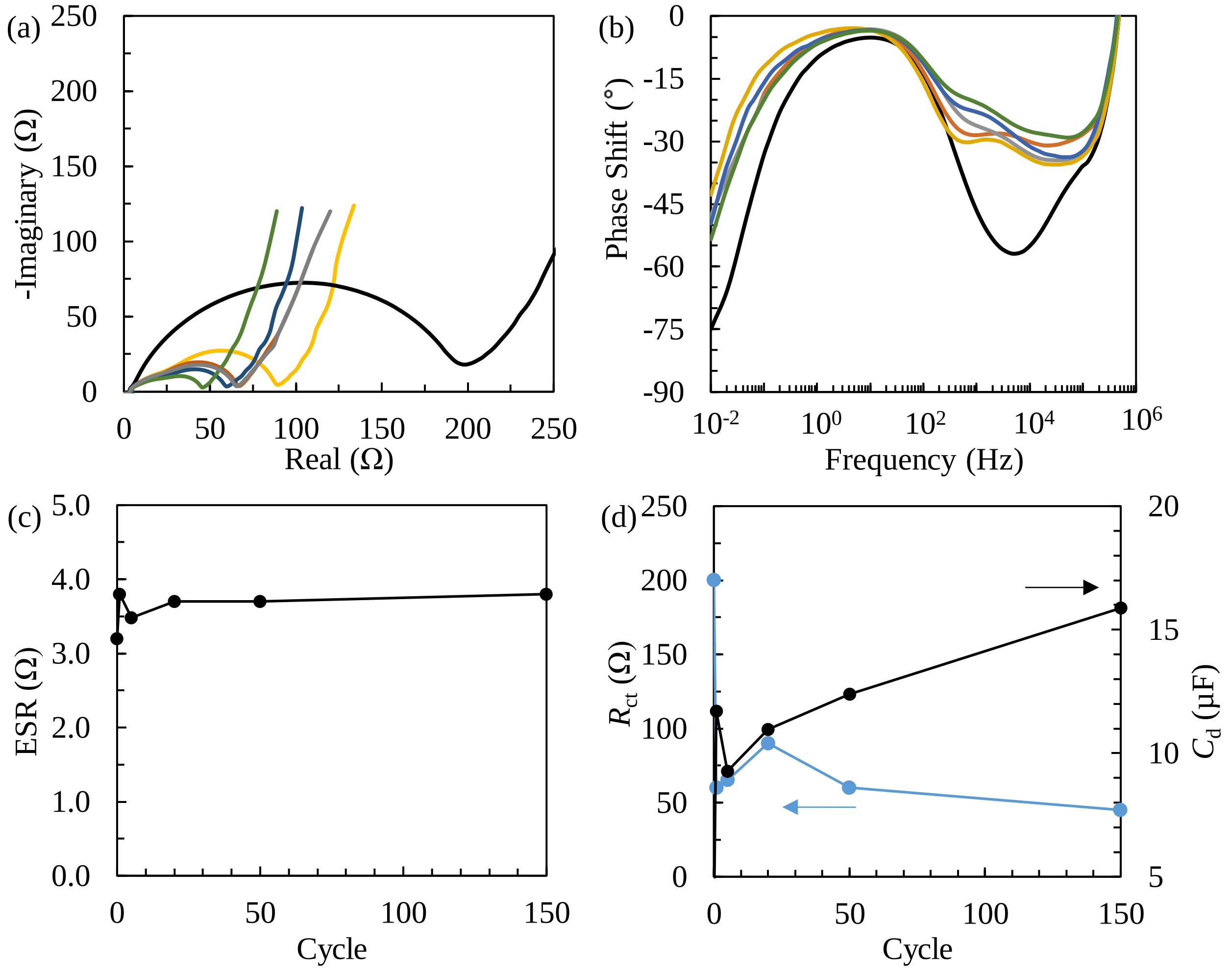

Figure 2.14 – EIS measurements for OX-SiNPs composite electrode with PVDF as a binder. (a) Nyquist diagram and (b) Bode diagram: (━) Pristine, (━) 1st, (━) 5th, (━) 20th, (━) 50th, and (━) 150th cycle. (c) ESR as a function of galvanostatic cycles and (d) charge transfer resistance (R_{ct}) and charge transfer capacitance (C_d) as a function of galvanostatic cycles. Scan between 1 MHz and 100 mHz with 10 points per decade. Voltage amplitude of 10 mV.

2.4 Conclusion

Silicon nanoparticles (SiNPs) were included in a carbon xerogel (CX) matrix in order to prepare Li^+ ion battery negative electrode material with high capacity and good cycling stability. The inclusion of SiNPs into a CX was carried out at two different stages during the carbon synthesis procedure to form CX-silicon composites. The SiNPs were incorporated either (i) in the resorcinol-formaldehyde precursor solution before gelation (RF-SiNPs) or (ii) in the xerogel after gelation and drying processes but before pyrolysis (OX-SiNPs) by soaking the dried gel into a suspension of SiNPs stabilized using a surfactant (PVP: poly(vinyl pyrrolidone)).

Transmission electron microscopy (TEM) and X-ray diffraction (XRD) analysis both confirmed the presence, size, nature, and distribution of the SiNPs in the RF-SiNPs and OX-SiNPs samples. The average particle size and lattice microstrain was calculated for the SiNPs in each sample from XRD patterns, *via* the Williamson-Hall method, using the uniform deformation model (UDM). A decrease in the average particle size was observed for the OX-SiNPs sample as compared to the RF-SiNPs sample, likely as a result of the filtering step in the synthesis procedure for the OX-SiNPs sample. The average particle size obtained *via* the Williamson-Hall method for the RF-SiNPs sample and OX-SiNPs sample was 57 nm and 42 nm, respectively. These values agreed with the particle size distribution determined *via* TEM. The reduction in average particle size for the RF-SiNPs sample may have been due to filtering step which lamented larger particles that did not adhere to the CX support. Microstrain of 0.1% in the SiNPs phase was observed for both samples, suggesting that the crystal structure of the SiNPs are under little or no stress.

N_2 adsorption analysis conducted on the CX, RF-SiNPs, OX-SiNPs, and SiNPs samples showed that the RF-SiNPs and OX-SiNPs samples have approximately the same meso/macroporous surface areas but with a slightly different percent of microporous surface area. Furthermore, both RF-SiNPs and OX-SiNPs samples have less specific surface area than the CX. The loss of microporous and meso/macroporous surface area in these samples are likely due to the fact that, since the SiNPs have no microporosity and significantly lower meso/macroporosity than the CX, the total amount of each specific surface area decreases according to the mass percent of SiNPs in the sample.

On the one hand, the RF-SiNPs composite electrode (~15 wt% SiNPs) with poly(vinylidene difluoride) (PVDF) as a binder exhibited a lower than expected capacity during cycling: 250 mAh g^{-1} as compared to the theoretical capacity of 800 mAh g^{-1}. However, the capacity remained relatively stable over 60 cycles. On the other hand, the OX-SiNPs composite electrode (~15 wt% SiNPs) exhibited a high initial capacity of 700 mAh g^{-1} but retained only 50% the initial capacity after only 12 cycles. The difference in the cycling performance of these two electrodes suggests that the point in the synthesis at which the SiNPs are introduced into the CX has a significant impact on the electrochemical properties of the electrode materials. Cyclic voltammetry (CV) and electrochemical impedance spectroscopy (EIS) analysis further confirm the inability of the silicon in the RF-SiNPs composite to be lithiated as well as the instability of both composites during cycling caused by pulverization of the active material due to the volumetric change of the SiNPs.

The inclusion of high specific energy SiNPs either before (RF-SiNPs sample) or after (OX-SiNPs sample) the gelation of a CX was accomplished; however, only the OX-SiNPs sample showed any increase in specific capacity. The SiNPs in the RF-SiNPs may have been “deactivated” due to the pyrolysis step (*i.e.* formation of an oxide layer), and further preparation of the RF-SiNPs sample, such as HF etching or other process, should be conducted in order to “activate” the SiNPs that have been deposited within the CX. Although the OX-SiNPs sample showed an increase in the initial specific capacity, the specific capacity quickly decreased during cycling, albeit slower than an electrode composed of only SiNPs without the CX support. Therefore, in the next chapter, in order to further improve the cycling stability of the OX-SiNPs sample, poly(sodium-4 styrene sulfonate) (PSS) will be used as a novel protective coating or binder.

2.5 References

[1] D. Ma, Z. Cao, and A. Hu, Si-based electrode materials for li-ion batteries: A mini review, Nano-Micro Lett. 6 (2014) 347–358.

[2] B. Liang, Y. Liu, and Y. Xu, Silicon-based materials as high capacity electrodes for next generation lithium ion batteries, J. Power Sources 267 (2014) 469–490.

[3] S.N. Houseman, T.J. Bartik, and T. J. Sturgeon, Measuring manufacturing: How the computer and semiconductor industries affect the numbers and perceptions, in: Measuring Globalization: Better Trade Statistics for Better Policy, Upjohn Institute for Employment Research (2015).

[4] M.T. McDowell, S.W. Lee, J.T. Harris, B.A. Korgel, C. Wang, W.D. Nix, and Y. Cui, In situ TEM of two-phase lithiation of amorphous silicon nanospheres, Nano Lett. 13 (2013) 758–764.

[5] X. H. Liu, L. Zhong, S. Huang, S.X. Mao, T. Zhu, and J.Y. Huang, Size-dependent fracture of silicon nanoparticles during lithiation, ACS Nano 6 (2012) 1522–1531.

[6] N. Dimov, S. Kugino, and M. Yoshio, Carbon-coated silicon as electrode material for lithium ion batteries: advantages and limitations. Electrochim. Acta 48, 11, (2003) 1579-1587.

[7] S.H. Ng, J. Wang, D. Wexler, K. Konstantinov, Z.P. Guo, and H.K. Liu, Highly Reversible Lithium Storage in Spheroidal Carbon-Coated Silicon Nanocomposites as Electrodes for Lithium-Ion Batteries, Angew. Chem. Int., 45, 6896-6899.

[8] W. Sun, R. Hu, H. Zhang, Y. Wang, L. Yang, J. Liu, and M. Zhu, A long-life nano-silicon electrode for lithium ion batteries: supporting of graphene nanosheets exfoliated from expanded graphite by plasma-assisted milling, Electrochim. Acta 187 (2016) 1-10.

[9] Y. Cui, N. Liu, H. Wu, M.T. McDowell, Y. Yao, and C. Wang, A Yolk-Shell Design for Stabilized and Scalable Li-Ion Battery Alloy Electrodes. Nano Lett. 12 (2012) 3315-3321.

[10] Zhi Wei Seh, W. Li, J. J. Cha, G. Zheng, Y. Yang, M.T. McDowell , P.C. Hsu, and Y. Cui, Sulphur–TiO_2 yolk–shell nanoarchitecture with internal void space for long-cycle lithium–sulphur batteries, Nature Comm. 4 (2013) 1331-1336.

[11] J. Lahaye and M.J. Wetterwald, Influence of carbon black properties on the behaviour of the cathode of a Leclanche-type battery, J. Appl. Electrochem. 14 (1984) 545-553.

[12] J. Xu, Q. Zhang, and Y.T. Cheng, High capacity silicon electrodes with nafion as binders for lithium-ion batteries, J. Electrochem. Soc. 163 (2016) A401-A405.

[13] N. Job, R. Pirard, J. Marien, and J.P. Pirard, Porous carbon xerogels with texture tailored by pH control during sol–gel process, Carbon 42 (2004) 619-628.

[14] N. Rey-Raap, M.L.C. Piedboeuf, A. Arenillas, J.A. Menéndez, A.F. Léonard, and N. Job, Aqueous and organic inks of carbon xerogels as models for studying the role of porosity in lithium-ion battery electrodes, Mater. Design 109 (2016) 282–288.

[15] X. Yuan, Y.J. Chao, Z.F. Ma, and M. Deng, Preparation and characterization of carbon xerogel (cx) and CX-SiO composite as anode material for lithium-ion battery, Electrochem. Commun. 9 (2007) 2591-2595.

[16] J.P. Lewicki, C.A. Fox, and M.A. Worsley, On the synthesis and structure of resorcinol-formaldehyde polymeric networks-precursors to 3D carbon macroassemblies, Technical report, Lawrence Livermore National Laboratory (2015).

[17] M.-L. Piedboeuf, A.F. Léonard, K. Traina, and N. Job, Influence of the textural parameters of resorcinol–formaldehyde dry polymers and carbon xerogels on particle sizes upon mechanical milling, Colloid Surface A 471 (2015) 124-132.

[18] M. Kim, S Osone, T. Kim, H. Higashi, and T. Seto, Synthesis of nanoparticles by laser ablation: a review, KONA Powder and Particle Journal 34 (2017) 80-90.

[19] W.O. Filtvedt, A. Holt, P.A. Ramachandran, and M.C. Melaaen, Chemical vapor deposition of silicon from silane: Review of growth mechanisms and modeling/scaleup of fluidized bed reactors. Sol. Energ. Mat. Sol. C 107 (2012) 188-200.

[20] A.F.B. Braga, S.P. Moreira, P.R. Zampieri, J.M.G. Bacchin, and P.R. Mei, New processes for the production of solar-grade polycrystalline silicon: A review. Sol. Energ. Mat. Sol. C Cells 92, 4 (2008) 418-424.

[21] J. Doyle, R. Robertson, G. H. Lin, M. Z. He, and A. Gallagher, Production of high-quality amorphous silicon films by evaporative silane surface decomposition. J. Appl. Phys. 64, (1988) 3215-3223.

[22] G. Wang, J. Yang, J. Park, X. Gou, B. Wang, H. Liu, and J. Yao, Facile Synthesis and Characterization of Graphene Nanosheets. J. Phys. Chem. C112 (2008) 8192-8195.

[23] R. Siburian, H. Sihotang, S. Lumban Raja, M. Supeno, and C. Simanjuntak, New Route to Synthesize of Graphene Nano Sheets. Orient. J. Chem. 34, 1 (2018) 182-187.

[24] M. Winter, J. O. Besenhard,* M. E. Spahr, and P. Novµk, Insertion Electrode Materials for Rechargeable Lithium Batteries. Adv. Mater. 10 (1998) 725-763.

[25] J. Westra, V. Vavruňková, P. Sutta, R.A.C.M.M. Van Swaaij, and M. Zeman, Formation of thin-film crystalline silicon on glass observed by in-situ XRD. Energy Proced. 2 (2010) 235-241.

[26] Y. Chen, X. Zhang, Y. Tian, and X. Zhao, Synthesis and Characterization of Silicon Nanoparticles Inserted into Graphene Sheets as High Performance Anode Material for Lithium Ion Batteries. J. Nanomater. (2014) 1-6.

[27] F. Joho, B. Rykart, A. Blome, P. Novák, H. Wilhelm, and M.E. Spahr, Relation between surface properties, pore structure and first-cycle charge loss of graphite as negative electrode in lithium-ion batteries, J. Power Sources 97-98 (2001) 78–82.

[28] S. An, J. Li, C. Daniel, D. Mohanty, S. Nagpure, D.L. Wood III, The state of understanding of the lithium-ion-battery graphite solid electrolyte interphase (SEI) and its relationship to formation cycling, Carbon 105 (2016) 52-76.

[29] E. Peled, D. Golodnitsky, C. Menachem, and D. Bar-Tow, An advanced tool for the selection of electrolyte components for rechargeable lithium batteries, J. Electrochem. Soc. 145 (1998) 3482-3486.

[30] X. Zuo, J. Zhu, P. Müller-Buschbaum, and Y.J. Cheng, Silicon based lithium-ion battery anodes: A chronicle perspective review, Nano Energy 31 (2017) 113-143.

[31] E. N. Attia, Tailoring the chemistry of blend copolymers boosting the electrochemical performance of si-based electrodes for lithium ion batteries, J. Mater. Chem. A5 (2017) 24159-24167.

[32] T. Reddy and D. Linden, Handbook of Batteries. McGraw-Hill Education, McGraw-Hill Education, 4th Ed., (2011).

[33] F.M. Hassan, R. Batmaz, J. Li, X. Wang, X. Xiao, A. Yu, and Z. Chen, Evidence of covalent synergy in silicon–sulfur–graphene yielding highly efficient and long-life lithium-ion batteries, Nat. Commun. 6 (2015) 8597-8608.

[34] S.J. An, J. Li, C. Daniel, D. Mohanty, S. Nagpure, and D.L. Wood, The state of understanding of the lithium-ion-battery graphite solid electrolyte interphase (SEI) and its relationship to formation cycling. Carbon 105 (2016) 52-76.

2.6 Supplemental information

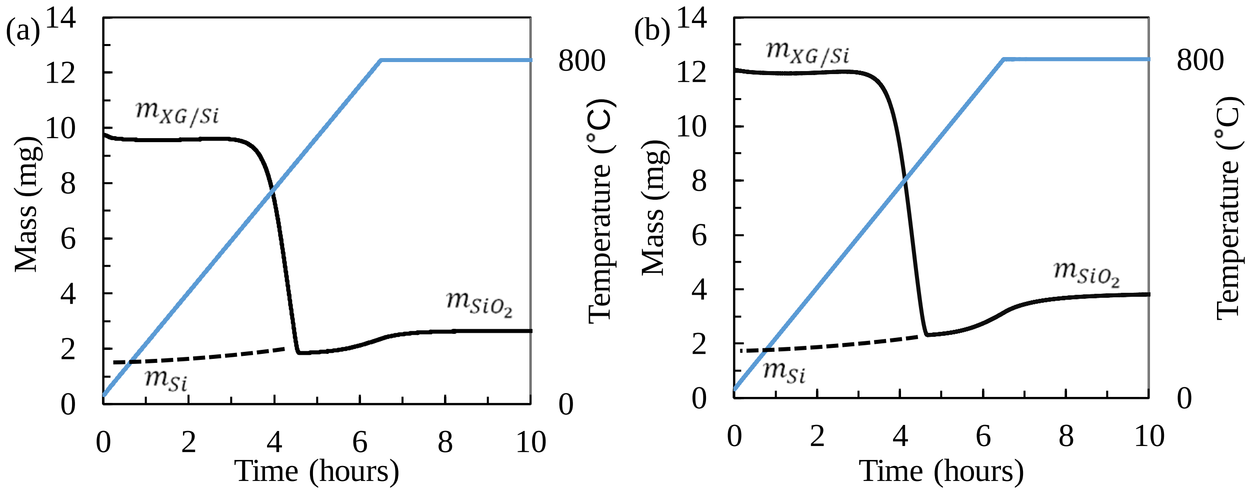

Figure S2.1 – (a) Thermogravimetric response of (a) RF-SiNPs sample and (b) OX-SiNPs sample. Heating procedure was 5°C min^{-1} up to 800°C and held at 800°C for 4 h in air. (▬) Temperature and (▬) mass of the sample.

The two following equations were used to determine the amount of silicon in the CX/SiNPs composite material:

$$\%Si = \frac{m_{\mathrm{Si}}}{m_{\frac{\mathrm{CX}}{\mathrm{SiNPs}}}} \tag{S2.1}$$

$$\mathrm{m}_{Si} = \mathrm{m}_{SiO_2}\left(\frac{\mathrm{M}_{Si}}{\mathrm{M}_{SiO_2}}\right) \tag{S2.2}$$

where the initial weight of silicon, m_{Si}, in the sample can be calculated by considering the molecular weights of silica, M_{SiO2}, and silicon, M_{Si}, along with the initial mass of the composite, $m_{\mathrm{CX/SiNPs}}$, given that the final weight measured of the sample after heating under air was considered to be the mass of silica only, m_{SiO2}. The mass percent of SiNPs in the RF-SiNPs sample and the OX-SiNPs sample was found to be 11.2 wt% and 14.8 wt%, respectively.

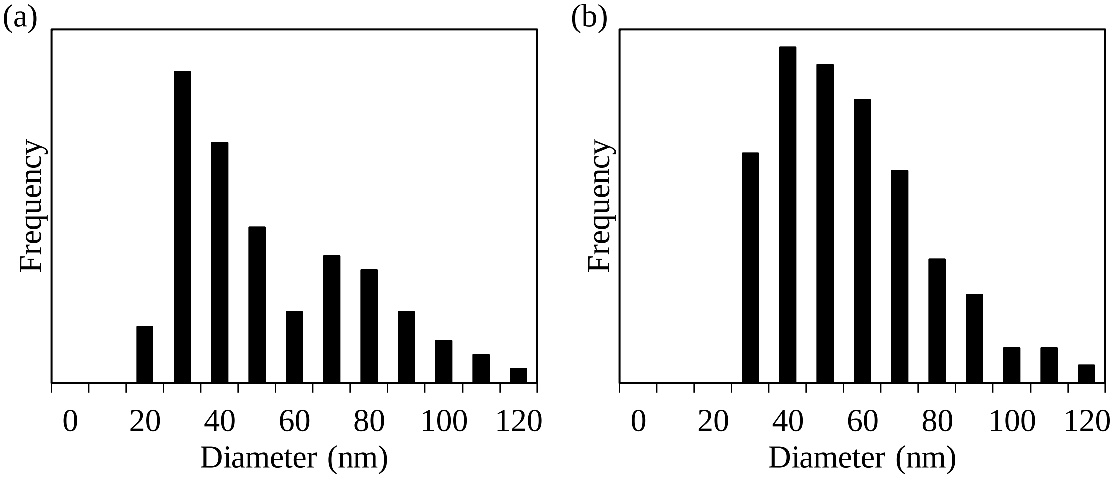

Figure S2.2 – Size distribution of SiNPs (over 100 particles) within the CX for (a) the RF-SiNPs sample and (b) the OX-SiNPs sample.

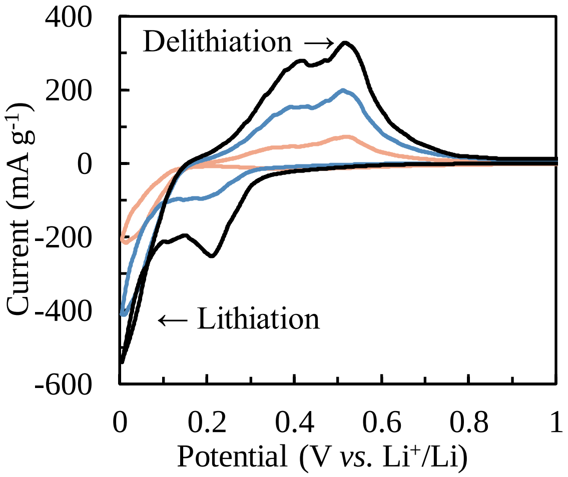

Figure S2.3 – CV Measurement of a SiNPs electrode with PVDF as a binder. The scan rate was 50 $\mu V\ s^{-1}$ between 0.005 V and 1.5 V *vs.* Li^+/Li. Shown for the (▬) 1st, (▬) 2nd and (▬) 3rd cycles.

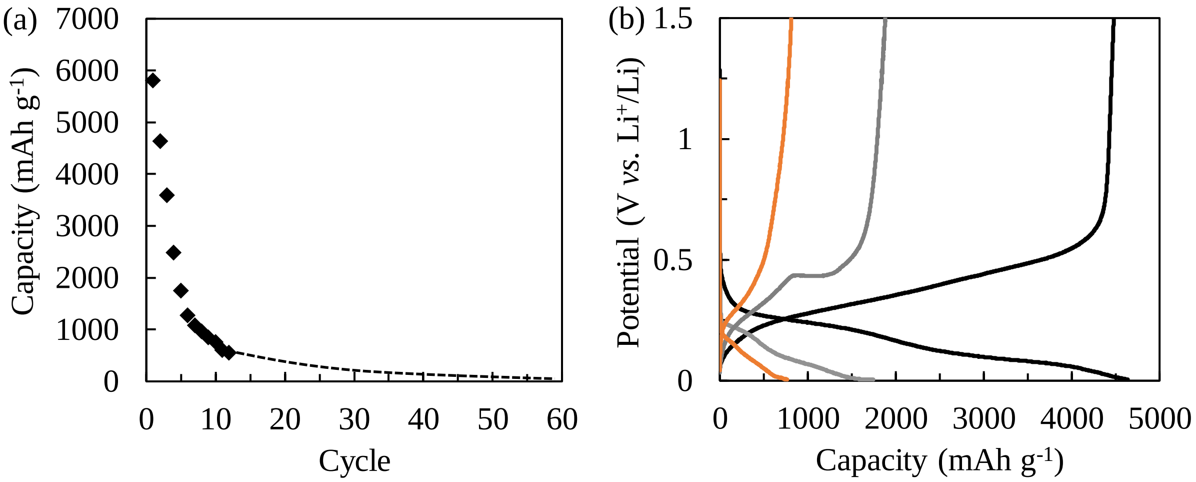

Figure S2.4 – (a) Galvanostatic cycling conducted on SiNPs only electrodes with PVDF as a binder at a rate of C/10. (b) Potential profile as a function of capacity for the (▬) 1st, (▬) 5th, and (▬) 10th cycles.

Chapter 3

Silicon-doped carbon xerogel with poly(sodium 4-styrenesulfonate) as a novel protective coating and binder

Abstract

A composite electrode comprised of silicon impregnated in a conductive carbon matrix as an anode material is an interesting path to improve the specific energy density of Li-ion batteries. However, the volume variation and SEI instability of silicon during cycling should be avoided to obtain stable electrodes. In the present study, silicon nanoparticles (SiNPs) impregnated in a 3D carbon xerogel matrix are synthesized with an ionically-conductive polymer, poly(sodium-4 styrene sulfonate) (PSS), as either a binder or a protective coating. The physico-chemical and electrochemical properties of this novel composite electrode with PSS as a coating or binder improves the retention of reversible capacity by a factor of five as compared to the same electrode using only a conventional poly(vinylidene difluoride) (PVDF) binder. Indeed, the composites with 10 wt% SiNPs utilizing PSS as a coating or binder retains a specific gravimetric energy density of 450 mAh g^{-1} composite after 40 cycles. Structural, textural, and electrochemical characteristics as well as prospects for further improvements of this composite electrode are discussed.

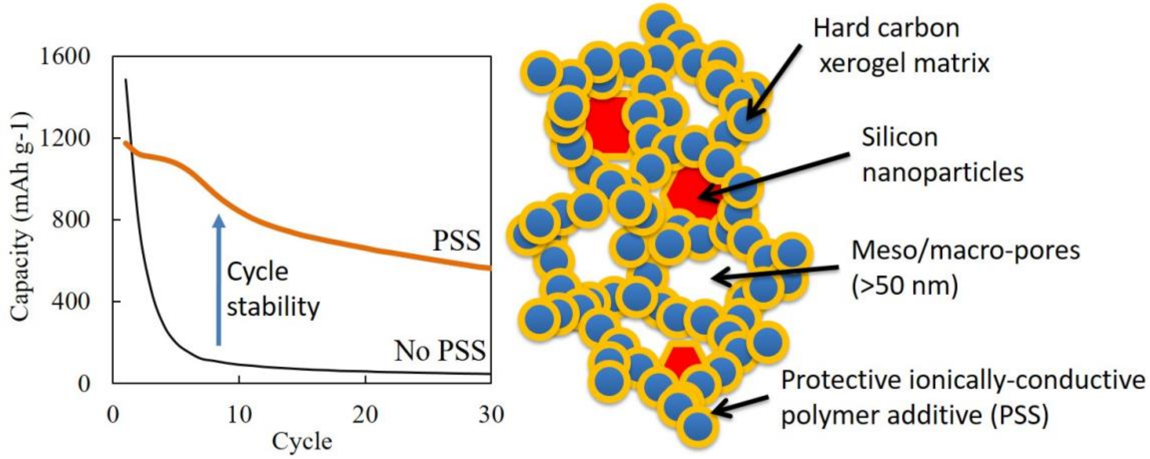

Keywords: batteries, lithium-ion, anode, silicon, xerogel, poly(sodium 4-styrenesulfonate)

3.1 Introduction

As discussed previously, the goal of this thesis is to include high specific energy density dopants, such as tin oxide and silicon, into a carbon xerogel (CX) in order to improve the cycling stability of these high energy density active materials for lithium-ion (Li^+ ion) battery negative electrodes. Silicon has been shown to be an interesting alloying-type material for a Li^+ ion battery negative electrode given (i) its low electrochemical lithiation/delithiation potential (< 0.5 V *vs.* Li^+/Li) and (i) its high theoretical energy density of up to 4200 mAh g^{-1} as compared to ~350 mAh g^{-1} for a conventional graphite electrode [1-8]. Unfortunately, the use of silicon as a Li^+ ion battery negative electrode has been limited due to instability arising from the large difference in volume (up to 300%) between the lithiated and delithiated silicon [3-8].

Reducing the size of silicon domains below 150 nm, i.e. using silicon nanoparticles (SiNPs), has been shown to reduce the pulverization of the silicon during lithiation and delithiation [9]. Therefore in the previous chapter, SiNPs were included into a CX in order to help mitigate the formation of an unstable solid electrolyte interphase (SEI) and pulverization of the SiNPs and the other electrode layer active materials that are surrounding the silicon, such as the CX or conductive additives. Although the inclusion of the SiNPs into the CX in the previous chapter did somewhat improve the cycling stability of composite electrodes, further improvements can still be made.

Since the sole use of a CX seemed to be insufficient to mitigate the problem related to SEI instability and active material pulverization, another route should be considered in order to further improve the performance of these composite electrodes. For example, a protective layer on the surface of the SiNPs would likely help prevent the SiNPs from breaking apart and probably help form a more stable SEI. There have been many studies on the addition of a carbon-based protective coating on the surface of the SiNPs, however, the synthesis of the nanostructures are often complex and impractical [3, 4, 6-8]. A simpler and more feasible route, however, would be to use an additional protective polymer, like Nafion or some other ionically-conductive polymer, as either a coating of the surface of the electrodes or as a binder to improve the cycling stability of these Si-doped CX composite electrodes [10]. The use of such a material would hopefully produce a material were direct contact between the SiNPs surface and the electrolyte could be avoided while maintaining ionic and electronic conductivity between the SiNPs, CX, electrolyte, and current collector.

Therefore in this work, a composite electrode comprised of silicon nanoparticles (SiNPs) supported by a carbon xerogel (CX) is proposed with an ionically conductive polymer, poly(sodium 4-styrenesulfonate) (PSS), as a protective coating or binder to further help mitigate the SEI instability. Electrodes were prepared with (i) PVDF as a binder (conventional), (ii) PSS as a binder, and (iii) PVDF as a binder with PSS as a coating deposited atop the electrode. These electrodes were electrochemically characterized and compared *via* galvanostatic cycling, electrochemical impedance spectroscopy (EIS), and cyclic voltammetry (CV). The synthesized CX and OX-SiNPs samples were also physico-chemically characterized with and without a binder to determine pertinent properties of the active material in order to better understand any degradation mechanisms at work during cycling and prevent degradation, if possible.

3.2 Experimental

Materials: Resorcinol (R, 99%), formaldehyde (F, 37 wt% in H_2O), sodium carbonate (C, 99.5%), polyvinylpyrrolidone (PVP, M_w= 40,000 g mol^{-1}), and poly(sodium 4-styrenesulfonate) (PSS, M_w= 70,000 g mol^{-1}) were purchased from Sigma-Aldrich. Silicon nanoparticles (SiNPs, diameter = 50 nm), poly(vinylidene difluoride) (PVDF), and N-methyl-2-pyrrolidone (NMP, ≥ 99%) were purchased from Alfa Aesar.

3.2.1 CX sample: Carbon xerogel synthesis

A carbon xerogel (CX) with an *R/C* ratio of 2000 was synthesized *via* the sol-gel polycondensation of resorcinol and formaldehyde in high purity water (*via* MilliQ process until R > 18 MΩ) [6-8]: see section 1.2.1 in Chapter 1 for the solution preparation, gelation, drying, ball-milling, and pyrolysis procedures). The specific capacity of the CX was found to be approximately 200 mAh g^{-1} when cycled between 0.005 V and 1.5 V *vs.* Li$^+$/Li (see Figure 2.11 and Figure 2.12a in Chapter 2 for the galvanostatic cycling and corresponding potential profiles, respectively).

3.2.2 OX-SiNPs sample: Organic xerogel doped with SiNPs by impregnation

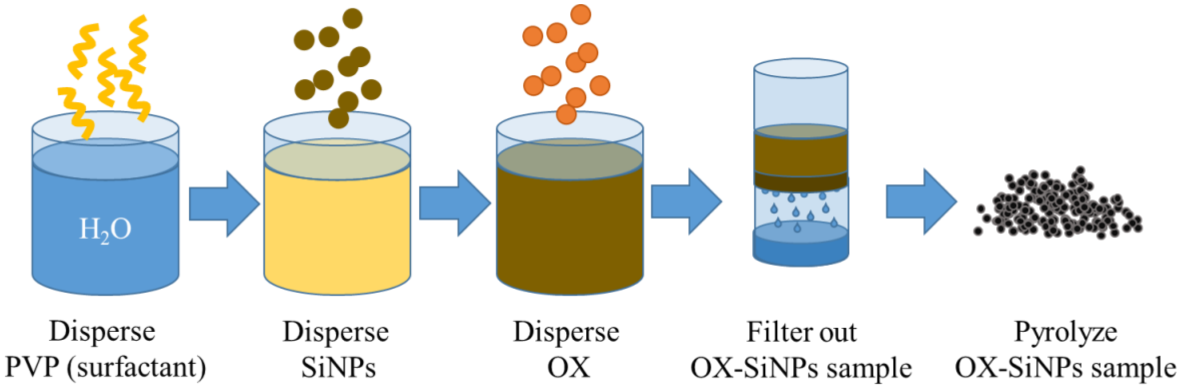

Figure 3.1 – Schematic diagram of the preparation of the OX-SiNPs sample: the SiNPs were impregnated into the xerogel after the gelation and drying steps.

Similar to the OX-SiNPs sample synthesis shown in section 2.2.3 in Chapter 2, three OX-SiNPs samples were synthesized with 10 wt%, 15 wt%, and 30 wt% of SiNPs. A surfactant, PVP, was dispersed in high purity water (MilliQ, R > 18MΩ) to a concentration of 20 mg of PVP/mL of H_2O to aid in the suspension of the SiNPs. The SiNPs were then added to the solution with a ratio of surfactant to SiNPs of 10 mg of PVP/mg of SiNPs. This suspension was ultrasonicated for 1 h in a Branson 2510 ultrasonic bath to obtain a well-dispersed suspension of the SiNPs. Then the previously prepared OX powder was added to the SiNPs/PVP suspension with a mass fraction of silicon to OX of approximately 5 wt%, 10 wt%, and 15 wt% of SiNPs, respectively. These suspensions were also ultrasonicated for an additional 1 h and mixed for 4 h with a magnetic stirrer at 500 rpm at 25°C. The solvent was removed by vacuum filtration through a 0.024 μm PVDF microporous filter. The collected OX-SiNPs samples were subsequently dried for 24 h at 80°C and 2.5 kPa in a vacuum oven.

The three OX-SiNPs samples were then pyrolyzed in a similar manor as the CX sample. The recovered pyrolyzed materials, referred to as OX-10SiNPs, OX-15SiNPs, OX-30SiNPs hereafter, was black in color and the mass had reduced by approximately half, likely due to the carbonization process. Given the loss of mass of the xerogel during pyrolysis, the final silicon mass percent was expected to be approximately 10 wt% SiNPs, 15 wt% SiNPs, and 30 wt% SiNPs, respectively (confirmed *via* thermogravimetric analysis, see Figure S3.1 in the supplemental information).

3.2.3 Preparation of CX and OX-SiNPs inks and electrodes

Three types of electrodes were then prepared with the CX sample and the three OX-SiNPs samples as active material. Composite electrodes with either (i) PVDF as a binder (conventional), (ii) PSS as a binder, or (iii) PVDF as a binder with PSS as a coating deposited atop the electrode were synthesized. The inks with PVDF as a binder were prepared by mixing 90 wt% of active material and 10 wt% of PVDF in N-methyl-2-pyrrolidone (NMP, ≥99%, Alfa Aesar) under magnetic stirring at 1000 rpm for 5 h. The inks with PSS as a binder were prepared by mixing 90 wt% of active material and 10 wt% of PSS in high purity water (MilliQ, R > 18 MΩ) under magnetic stirring at 1000 rpm for 5 h. A solvent-to-solids mass ratio of 20:1 was used in both cases.

Both types of inks were spray-coated onto pre-weighed 15.5 mm diameter stainless steel disks. Stainless steel disks were used instead of a conventional copper foil in order to accurately measure the mass of the deposited material on each electrode. Stainless steel was confirmed to be stable as a current collector for Li-ion anodes *via* CV measurements on the stainless steel disks with a lithium counter electrode. These disks were fixed on a 70°C heated surface. The coating was performed using a Harder & Steenbeck Evolution Silverline 2 airbrush. A high solvent-to-solids ratio was used to ensure that the prepared inks flowed easily through the airbrush and lead to a homogeneous coating on the stainless steel disks. After spray-coating, the electrodes were dried at 70°C for 2 h at ambient pressure and then at 120°C at 2.5 kPa overnight. The electrodes were then weighed to determine the mass of the deposited material prior to their electrochemical characterization. Excess dried material surrounding the electrodes, which was deposited around the disks during the spray-coating process, was collected for further characterization.

For the third type of electrode, a PSS layer was applied to the electrodes synthesized with PVDF as a binder by drop coating a 10 wt% solution of PSS in high purity water (MilliQ, R > 18 MΩ) onto the surface of the spray-coated active layer. Three drops of PSS (1 drop ≈ 50 µL) were deposited onto the electrode surface. The drop-coated electrodes were subsequently dried once more at 120°C at 2.5 kPa overnight. Approximately 15 wt% of PSS with respect to the amount of spray-coated active material was deposited, measured *via* a mass balance before and after the PSS coating procedure.

Figure 3.2 – Schematic of the procedure for PSS coating of the synthesized composite electrodes.

Half-cells of the CX and the three OX-SiNPs composite electrodes were assembled in CR2032 coin-cells with a lithium metal foil as the counter-electrode (Li-metal, MTI Corporation). In this half-cell configuration, the insertion of Li^+ ions into the active material corresponds to a decrease in potential, whereas the de-insertion corresponds to an increase in potential. This setup is opposite to that of a full-cell, where the OX-SiNPs composite electrode would be the negative electrode and a metal oxide, such as $LiCoO_2$ for instance, would be the positive electrode. Two porous polyethylene separators (Celgard, 25µm thickness, MTI Corporation) soaked with 80 µL of electrolyte (1 M $LiPF_6$ in a 1:1:1 ratio of ethylene carbonate: diethylene carbonate: dimethyl carbonate, Selectilyte LP71, Merck) were placed between the Li-metal disk and the OX-SiNPs electrode. The half-cells were assembled in an Argon-filled glovebox (MBraun MB200B).

The theoretical specific capacity of the OX-10SiNPs, OX-15SiNPs, and OX-30SiNPs composite electrodes should be 600 mAh g^{-1}, 800 mAh g^{-1}, and 1400 mAh g^{-1}, respectively, when considering only the active materials (*i.e.* not counting the mass of the binder).

3.2.4 Physico-chemical and electrochemical characterization

Physico-chemical and electrochemical characterizations carried out in this chapter are outlined in Annex 1. The physico-chemical characterizations included nitrogen adsorption-desorption, transmission electron spectroscopy, scanning electron spectroscopy with EDX analysis, and X-ray diffraction. N_2 adsorption was used to determine the BET surface area (S_{BET}) and the corresponding microporous (S_{micro}) and meso/macroporous (S_{ext}) surface areas. XRD and TEM with EDS analysis was used to determine the SiNPs crystallite size, particle size and distribution, elemental characterization, and crystallographic microstrain of the dopant silicon nanoparticles.

Electrochemical characterization consisted of cyclic voltammetry (CV), galvanostatic cycling, and electrochemical impedance spectroscopy (EIS). CV characterizations show the redox potentials of the electrochemically active components as well as how these reactions evolve during cycling, cycling gives the specific capacity and stability of the prepared composite electrodes. EIS analysis was used to determine how the equivalent series resistance (ESR), charge transfer resistance (R_{ct}), charge transfer capacitance (C_d) and the diffusive properties of the composite electrodes evolves during cycling. An overview of these parameters and the electrochemical model for these electrodes can be found in Annex 2.

3.3 Results

3.3.1 Physico-chemical characterization

Transmission electron microscopy

TEM micrographs were taken of a CX without a binder, SiNPs, and the OX-10SiNPs sample without a binder. The OX-10SiNPs sample shown is given as an example since all the other OX-SiNPs samples had similar morphologies. Figure 3.3a shows the xerogel support without SiNPs with the typical "string-of-pearl"-like structure. The structure is composed of a cluster of spherical nodules linked together that forms a meso/macro-porous material [11-15]. Although the CX has microporosity, as confirmed by the N_2 analysis, these micropores located in the nodules are not identifiable in these images given their small size. Figure 3.3b shows SiNPs as-received from the supplier. The SiNPs surprisingly have the same "string-of-pearl"-like morphology, similar to that of the CX. The aggregation of the particles into long chains forms a much larger macrostructure on the order of hundreds of nanometers, even though the average diameter quoted by the supplier was less than 50 nm.

However Figure 3.3c and d, after suspension and impregnation into the xerogel support, the aggregation of the SiNPs seemed to decrease, possibly due to the loss of the larger SiNPs aggregates during filtration that did not adhere to the CX. The silicon phase was identified by the difference in shape and texture compared to the CX as well as EDS analysis performed in the TEM (see Figure S3.2 and Figure S3.3 for the dark field images and EDS spectra, respectively). The larger SiNPs seem to also aggregate around the outside of the CX particles while the smaller SiNPs have the ability to infiltrate further into the CX possibly as a result of the size of the CX meso/macropores. The particle size distribution of the SiNPs in the OX-10SiNPs sample is given in Figure S3.4 in the supplemental information.

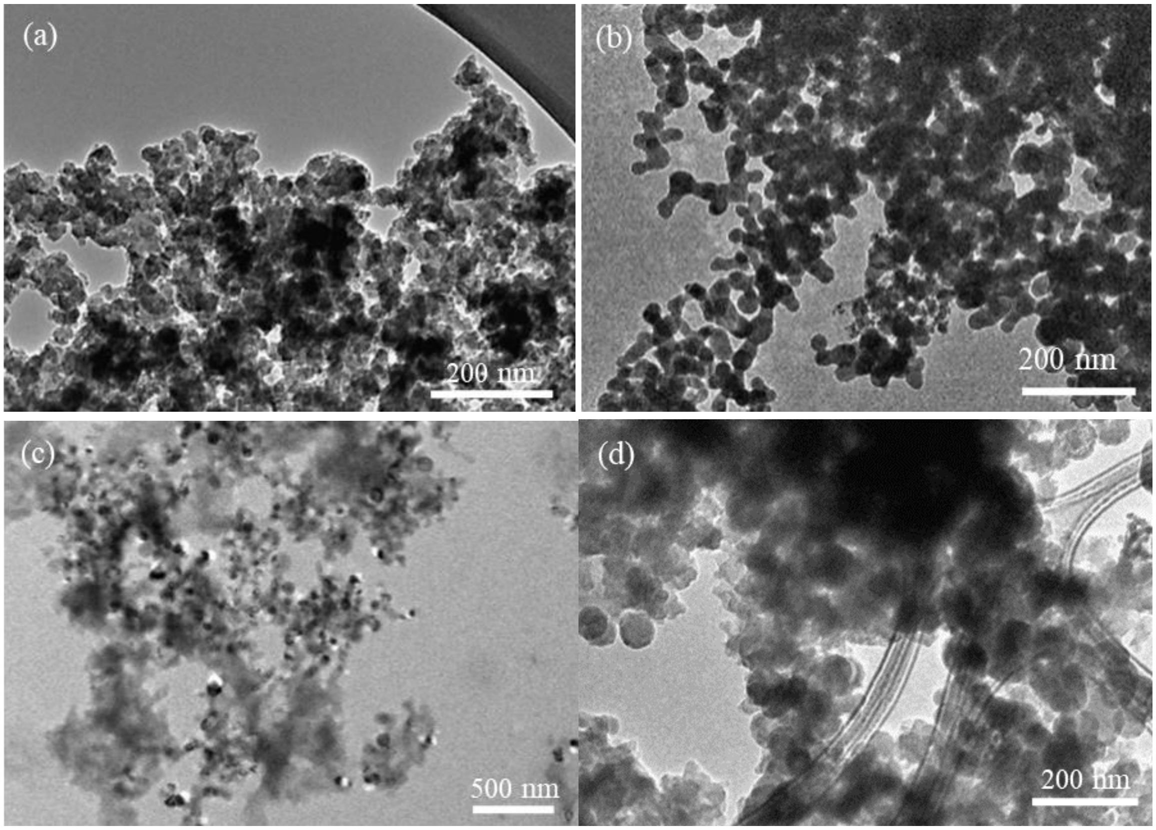

Figure 3.3 – TEM micrographs of the (a) CX sample, (b) as-received commercial silicon nanoparticles, (c) OX-10SiNPs sample and (d) OX-10SiNPs sample at higher magnification.

Scanning electron microscopy

Figure 3.4 shows SEM micrographs of the active material layer of OX-15SiNPs composite electrode with PVDF as a binder (Figure 3.4a) or PSS as a binder (Figure 3.4b). The OX-15SiNPs composite electrodes are given as an example since all the other OX-SiNPs samples had similar morphologies. The OX-15SiNPs sample particles seem to be less densely packed with PVDF as a binder compared to with PSS as a binder. Following the same method as in the Chapter 1, the density of the active layer with PVDF as a binder and PSS as a binder was calculated to be approximately 43 mg cm^{-3} and 61 mg cm^{-3}, respectively (see Figure 1.5 in Chapter 1).

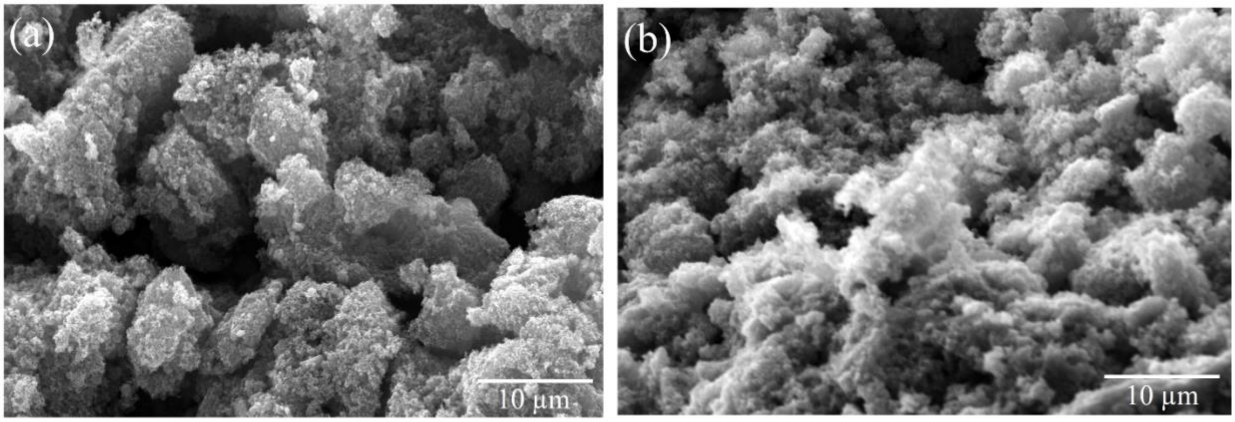

Figure 3.4 – SEM images of OX-15SiNPs composite active with (a) PVDF as a binder and (b) PSS as a binder.

Nitrogen adsorption-desorption

In order to further understand the interaction of the binder with the CX sample, nitrogen adsorption-desorption analysis was performed on the CX sample (i) without a binder, (i) with PSS as a binder, and (iii) with PVDF as a binder. The latter two were recovered from the electrode processing by scratching the material from the surface surrounding the electrodes. Corresponding N_2 isotherms are shown of these three materials in Figure 3.5a. The CX without a binder resembles a type I/II isotherm, corresponding to a material that includes micropores as well as a distribution of largeness-macropores, which agrees with the results obtained from Hg porosimetry. Interestingly, the CX with either PSS or PVDF as a binder shows a decrease in the adsorbed quantity of nitrogen at low relative pressure (*i.e.* before the plateau in Figure 3.5), which corresponds to a decrease in the micropore surface area. The reduction of micropore surface area is greater for the CX with PVDF as a binder as compared to the CX with PSS as a binder (see Figure 3.5b). The inaccessibility of the micropore surface area during this analysis is an indication that these surfaces would also be inaccessible to the electrolyte in the half-cell configuration [11, 15].

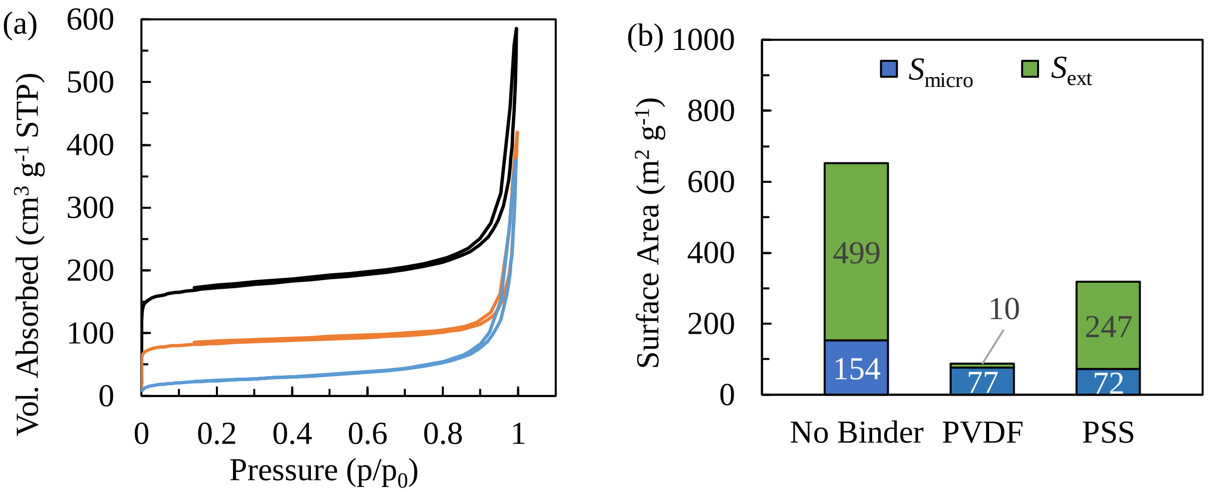

Figure 3.5 – (a) Nitrogen adsorption isotherms of the CX sample. (▬) pristine CX, (▬) CX composite with PSS as a binder, and (▬) CX composite with PVDF as a binder. (b) Microporous surface area (S_{micro}) and meso/macro-porous surface area (S_{ext}) of the CX sample with no binder, PVDF as a binder, or PSS as a binder.

The actual morphology of the CX with either binder remains an open question. For the CX with PVDF as a binder, given that the micropores surface area is completely lost, the possible morphologies must be that either (i) the PVDF completely fills the micropores or (ii) the PVDF homogeneously covers all the micropores. As for the CX with PSS as a binder, since the micropore surface area is not completely lost, possible morphologies must include either that (i) the PSS partially fills the volume of micropores, (ii) the PSS heterogeneously covers some micropores that leaves an interior micropore surface that is not measurable by N_2 adsorption, or (iii) the PSS adheres to the micropore surfaces to some extent but does not fill the volume of the micropores (see Figure 3.6). These configurations depend on several parameters, such as the wettability of the CX, the nature of the binder, and the size of the solvent molecules and binder oligomers. As an example, the surface hydroxyl groups usually present on the CX surface should give the CX a more hydrophilic nature, which would help aid the wetting of the micropore surfaces given the solvent is water [12, 16]. It was indeed previously suggested that water could enter the small pores of the CX structure more easily than NMP, which would help the binder to enter the micropores as well [12]. However, no exact mapping of the binder location could be achieved to date. A high resolution image of the OX-15SiNPs composite with PSS is given in Figure S3.6 in the supplemental information, however, it is not possible to observe the PSS in the TEM images due to the low electron density of the polymer.

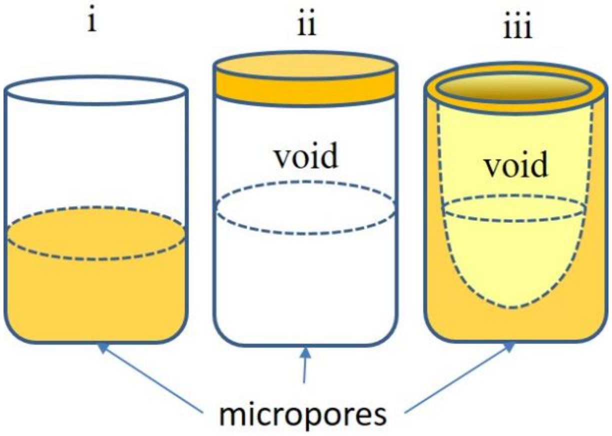

Figure 3.6 – Representation of possible morphologies of the PSS binder within a cylindrical micropore. (i) The PSS partially fills the volume of micropores, (ii) the PSS covers some micropores, leaving an internal void volume, or (iii) the PSS adheres to the micropore surfaces to some extent but does not fill the volume of the micropores. The internal surfaces are indicated by the dotted lines.

Nevertheless, it is possible to partially discriminate between the aforementioned configurations. In order to rule out the possibility that either binder is just filling in the micropores rather than covering the micropores, a calculation was performed of the respective amounts of micropore volume in the CX and volume of binder applied. The available micropore volume of the CX powder was found to be approximately 2 and 5 times larger than the volume of PSS or PVDF available during the synthesis, respectively (Table 1). Additionally, the topographical polar surface area (TPSA), which is a measure of the physical size of any given molecule, shows that the NMP solvent molecule, with a TPSA = 20 Å^2, is much larger than the water molecule (TPSA = 1 Å^2) [17, 18]. Therefore, PVDF dispersed in NMP should not infiltrate the micropores as easily compared to the PSS in water, especially given that these pores have a maximum pore diameter of 2 nm (surface area = 300 Å^2). As a result, the PVDF should be located mainly on the external surface area of the microporous carbon nodules, *i.e.* at the meso/macro-pore surface of the CX, rather than depositing inside the micropores. On the contrary, the likely hydrophilic nature of the CX and physical size of the water molecule would facilitate the ability of the PSS to infiltrate into the confined volume of the micropores. If one assumes that PSS does not completely fill some micropores while others are left empty, the most probable morphology for the PSS on the CX should be that the PSS is able to partially enter all the micropores homogeneously and retain some of the internal surface. Nevertheless, it cannot be said with certainty that these proposed morphologies are correct. Table 3.1 gives an overview of the N2 adsorption data for CX powder without a binder, with PSS, or with PVDF as binder.

Table 3.1 – N_2 adsorption data for CX powder without a binder, with PSS, or with PVDF as binder.

Sample	S_{BET} $m^2\ g^{-1}$	S_{ext} $m^2\ g^{-1}$	S_{micro} $m^2\ g^{-1}$	V_{DUB}[a] cm^3	V_{binder}[b] cm^3
CX powder	653	154	499	0.052	-[c]
CX + PVDF	87	77	10	-[d]	0.011
CX + PSS	399	87	312	-[d]	0.025

[a] Calculated *via* the Dubinin-Radushkevich method and given the mass of CX powder used during synthesis. [b] Calculated given v_{PVDF} = 0.56 $cm^3\ g^{-1}$, v_{PSS} = 1.25 $cm^3\ g^{-1}$, and the mass of binder used during synthesis. [c] Not relevant. [d] Not calculated. V_{binder} should be compared to V_{DUB} of the CX powder.

X-ray diffraction

Figure 2.7 shows the XRD patterns of the CX and the OX-10SiNPs powders after ball-milling and pyrolysis. Similar to what was shown in Chapter 1 and 2, the XRD pattern of the CX exhibits no clear crystallographic characteristics, given the lack of any strong diffraction peaks related to graphite or any other allotrope of carbon, but only exhibits three very wide peaks at around 2θ angles of 15°, 30°, and 42°, where the first two peaks are related to the oxygenated C(002) plane, and the former to the C(100) plane [19, 20]. Generally, these peaks indicate that the CX sample is, as expected, amorphous in nature. In fact, it is well known that carbon gels are non-graphitizable materials even at higher temperature, *i.e.* hard carbons [21].

Similar to the OX-SiNPs sample in Chapter 2, the OX-10SiNPs powders in this chapter also clearly show the characteristic silicon diffraction peaks of the Si(111), Si(220), Si(311), Si(400), Si(331), and Si(442) crystallographic planes at 2θ angles of 28°, 47°, 56°, 69°, 76°, and 88°, respectively [22, 23]. The underlying broad diffraction response between 5° and 50°, which corresponds to the CX support, seems to be slightly changed as compared to the CX without SiNPs.

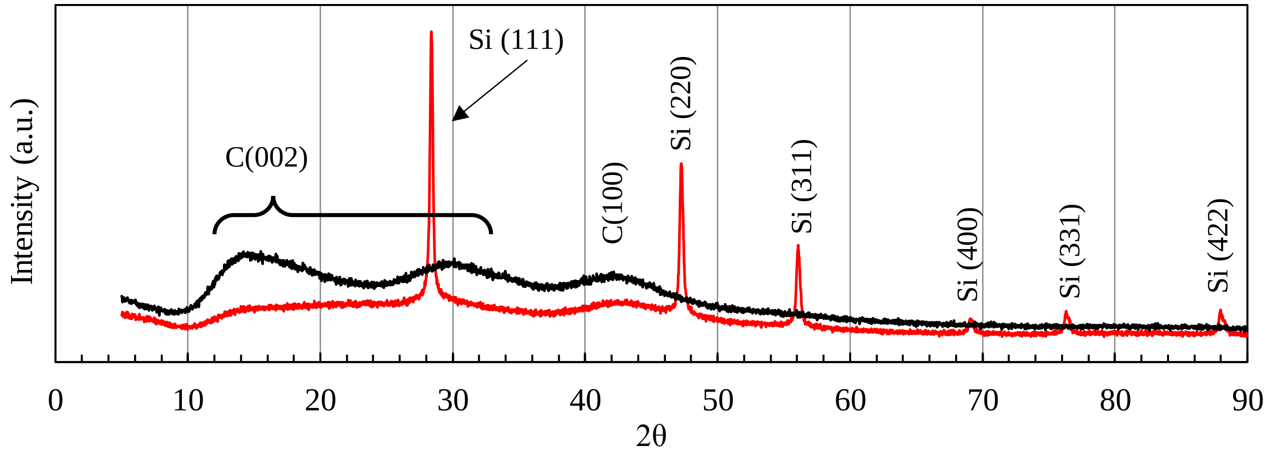

Figure 3.7 – XRD patterns of the (—) CX and (—) OX-10SiNPs samples.

The Williamson-hall method was used to determine the size broadening and microstrain broadening of the SiNPs in the OX-10SiNPs samples under a uniform deformation model (UDM), as shown previously in Chapter 2 (section 2.3.1). The crystallite size of the SiNPs in the OX-10SiNPs sample was measured to be 42 nm while the microstrain of the SiNPs in the OX-10SiNPs samples was calculated to be 0.1%. This amount of microstrain is considered very small and, therefore, it may be safe to conclude that there is no significant microstrain in the crystal structure of the SiNPs.

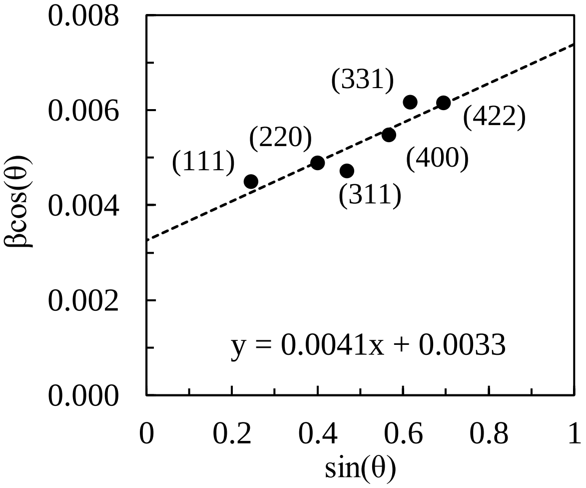

Figure 3.8 – Williamson-Hall plot of the silicon diffraction peaks of the OX-SiNPs sample. Each point represents a diffraction peak of the SiNPs in each sample and how the FWHM of each peak varies with increasing 2θ angle. The least-squares regression fit of these points gives information about the crystallite size (y-axis intercept) and microstrain (slope) of the diffracted material.

3.3.2 Electrochemical characterization

Cyclic voltammetry

Cyclic voltammetry (CV) measurements were conducted on the CX, OX-10SiNPs, and SiNPs composite electrodes (Similar results for the OX-10SiNPs composite electrodes were found for the OX-15SiNPs and OX-30SiNPs samples). The CV measurement of the SiNPs composite electrode with PVDF as a binder is given in Figure S3.5 in the supplemental information in order to compare with the CV measurements of the OX-10SiNPs composite electrodes.

Figure 3.9 shows results for the CX composite electrode with either (a) PVDF or (b) PSS as a binder. Both CX composite electrodes shows three peaks at 1.3 V, 0.6 V, and ≈0 V *vs.* Li^+/Li. The reduction peaks during the pristine cycle at 1.3 V and 0.6 V *vs.* Li^+/Li may be attributed to either SEI formation or possibly the trapping of Li^+ ions within the carbon xerogel. SEI layers on carbon materials have been shown to form due to the instability of the electrolyte below approximately 1.3 V *vs.* Li^+/Li [24–27]. The underlying peak that spans along the entire voltage window during lithiation, reaching a minimum around 0 V *vs.* Li^+/Li, likely corresponds to the insertion of lithium into the CX [12]. The wide insertion window may be attributed to both the mesoporous structure of CX as well as the amorphous hard-carbon nature of the graphitic layers in the CX, as supported by previous studies [11-15]. This is contrary to conventional graphitic anodes that have a narrow insertion and de-insertion potential as a result of the regular spacing between graphitic layers. Figure 3.9a, the disappearance of the two lithiation peaks after the pristine cycle indicates the formation of a stable SEI. An additional peak at 0.75 V *vs.* Li^+/Li during the pristine discharge in the composite electrode with PSS as a binder (Figure 3.9b) suggests that PSS undergoes some type of reaction with lithium, however, the nature of this reaction is not presently known and it is unclear if this reaction is reversible.

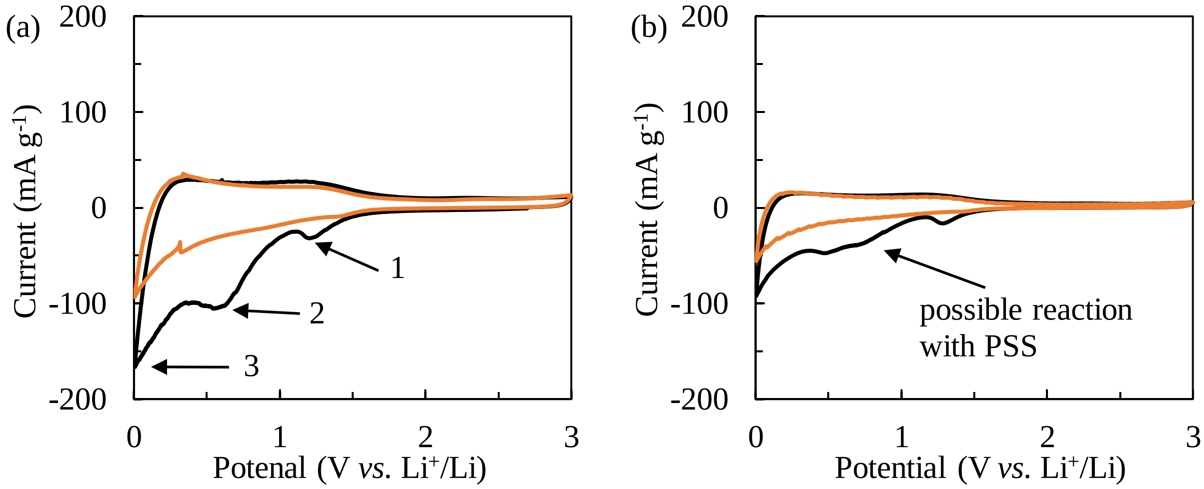

Figure 3.9 – CV Measurements of a CX electrode with (a) PVDF as a binder or (b) PSS as a binder. The scan rate was 50 μV s^{-1} between 0.005 V and 3 V *vs.* Li^+/Li. (▬)1st cycle and (▬) 5th cycle are shown.

Figure 3.10 shows the CV measurements obtained using the OX-10SiNPs composite electrodes with PVDF as a binder. The 1st cycle discharge exhibits similar peaks at 0.6 V *vs.* Li^+/Li related to SEI formation on the CX (peak 1). However, an additional strong lithiation peak below 0.1 V *vs.* Li^+/Li (peak 2) is likely related to the initial alloying of crystalline silicon with lithium and SEI formation between the silicon and electrolyte. It is difficult to differentiate between these two phenomena. However, previous studies have come to similar conclusions regarding the initial electrochemical silicon-lithium alloying peaks. [28–32]. During the 1st delithiation, reduction peaks at 0.3 V to 0.6 V *vs.* Li^+/Li relate to the de-alloying of lithium from silicon (peak 3) [32]. During the 5th cycle, similar de-alloying peaks are observed; however, an alloying peak appears at 0.2 V *vs.* Li^+/Li, which has been attributed to the lithiation of amorphous silicon (peak 4) [28–32].

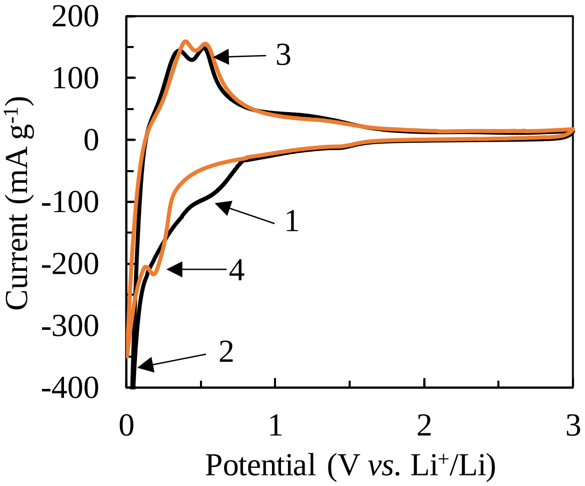

Figure 3.10 – CV Measurements of the OX-10SiNPs composite electrode doped with PVDF as binder. The scan rate was 50 μV s^{-1} between 0.005 V and 3 V *vs.* Li$^+$/Li. Shown for (▬) 1st cycle and (▬) 5th cycle.

Galvanostatic cycling

Galvanostatic cycling was conducted on the CX composite electrode and all three OX-SiNPs composite electrodes (10 wt%, 15 wt%, 30 wt% SiNPs) with either PVDF as a binder, PSS as a binder, or PVDF as a binder with PSS as a coating.

The CX composite electrode with PSS as a coating exhibited a 24% increase in the specific capacity compared to the composite electrode with PVDF as a binder with the same cycling stability (Figure 3.11a). This suggests that the PSS undergoes some type of reversible reaction with lithium. Cyclic voltammetry measurements shown in Figure 3.9b suggest that this reaction occurs at 0.7 V *vs.* Li$^+$/Li. The CX composite electrodes with PSS or PVDF as a binder both show <1% loss of capacity after 80 cycles. This also suggests that PSS as a binder is stable in the electrolyte and is not soluble to any significant degree.

The OX-SiNPs composite electrode with 10 wt% SiNPs and PVDF as a binder is shown in Figure 3.11b as the solid line, retained 50% of the 1st cycle specific capacity (700 mAh g^{-1}) after only 15 cycles. However, the reversible capacity retention of the same OX-SiNPs composite electrode with either PSS as a binder or PSS as a coating reached 70 cycles and 60 cycles, respectively, before the reversible capacity dropped below 50% of the 1st cycle capacity. Similar cycle stability results were obtained for the OX-SiNPs composite electrodes with 15 wt% and 30 wt% SiNPs, shown in Figure 3.12c and d. The OX-SiNPs composite with 15 wt.% SiNPs and 30 wt% SiNPs exhibited 1st cycle specific capacity of 1100 mAh g^{-1} and 1400 mAh g^{-1}, respectively, which is slightly higher than the expected theoretical values one would expect from the amount of SiNPs and CX in each sample. This extra capacity may be due to the PSS, which was shown to have some reversible capacity, as previously discussed.

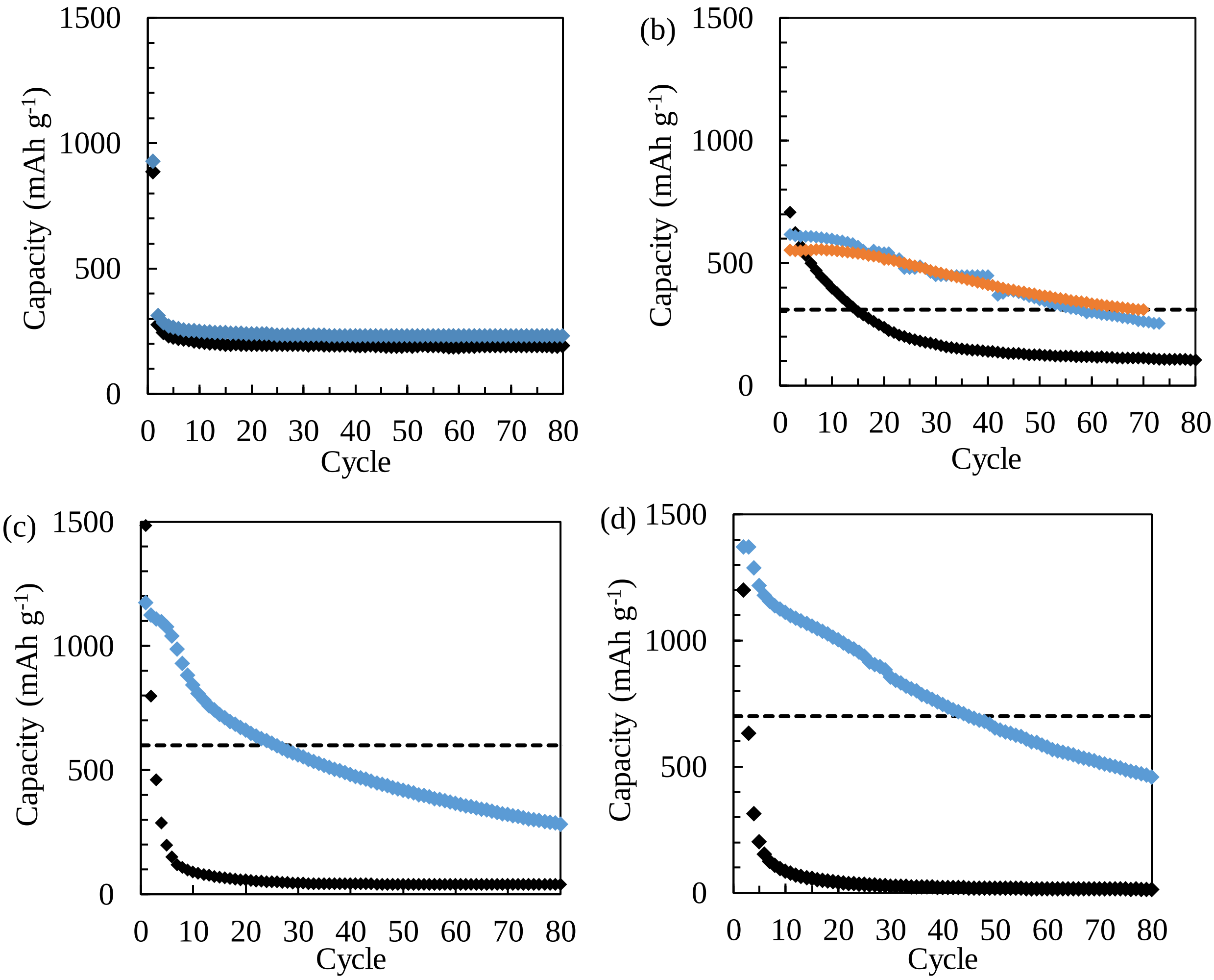

Figure 3.11 – Galvanostatic cycling of the (a) CX composite electrode and OX-SiNPs composite electrode with (b) 10 wt% SiNPs, (c) 15 wt% SiNPs, and (d) 30 wt.% SiNPs. (◆) PVDF as a binder, (◆) PSS as a binder only, or (◆) PVDF as a binder with PSS as a coating. The dotted line (---) signifies 50% of the initial capacity of each respective composite electrode.

A comparison of the composite electrodes with various amounts of SiNPs is shown in Figure 3.12. This data is the same as was shown in Figure 3.11 and is given here just for comparison purposes. This figure more clearly shows that the loss of capacity during cycling seems to be fairly independent of the amount of SiNPs in the composite electrode. The major difference between the cycling stability seems to be the initial loss of capacity that occurs during the first 10 cycles. Although speculative, this initial loss of capacity may be due to the loss of SiNPs that have not deposited sufficiently into the CX and are quickly lost during cycling. For example, SiNPs that have aggregated on the exterior of the CX particles may be lost to the electrolyte during these first few cycles as the internal stresses and volume change of the SiNPs cause them to quickly detach from the CX.

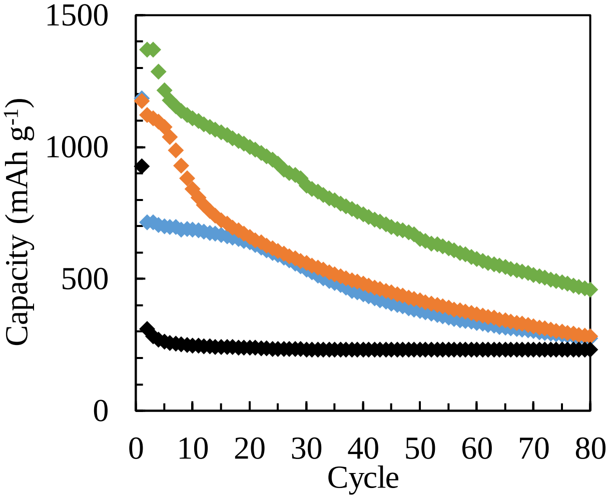

Figure 3.12 – Galvanostatic cycling of the (⬛) CX, (🟦) OX-10SiNPs, (🟧) OX-15SiNPs, and (🟩) OX-30SiNPs with PSS as a binder.

Electrochemical impedance spectroscopy

EIS responses for OX-15SiNPs composite electrodes with either PVDF as a binder (Figure 3.13), PSS as a binder (Figure 3.14), or PVDF as a binder with PSS as a coating (Figure 3.15) have been collected. The Nyquist diagrams are given in Figure 3.13a, Figure 3.14a, Figure 3.15a, respectively. The Bode plots are given in Figure 3.13b, Figure 3.14b, Figure 3.15b, respectively. Similar results were obtained with OX-10SiNPs and OX-30SiNPs composite electrodes.

As shown in the Nyquist plots, the R_{ct} of the pristine half-cells (before cycling) are higher for the OX-15SiNPs composite electrode that have PSS as a binder or coating as compared to composite electrode with PVDF as a binder, given that the diameter of these half-circles are smaller for the PSS-based composite electrodes as compared to the PVDF-based composite electrodes. The diameter of the half-circle decreases for all the OX-15SiNPs composite electrodes between the pristine half-cells and the 1st cycle. This can be related to a lower R_{ct} likely due to the mechanical stability and ionically-conductive nature of the SEI. A progressive increase in the diameter of the charge transfer half-circle is observed between the 1st and 50th cycle for the composite electrode with PVDF as a binder. Contrarily, a decrease in the diameter of the charge transfer half-circle is observed for the first 20 cycles of the composite electrode with PSS as a binder and PSS as a coating with a PVDF binder. However, a dramatic increase of the diameter of the charge transfer half circle at 50 cycles is observed for the composite electrode with PSS as a binder. Likewise, the 50th cycle for the composite electrode with PSS as a coating shows an irregular response at lower frequencies. A second half circle at or after the 50th cycle is observed at high frequency for all three types of the OX-15SiNPs composite electrodes, most likely due to the excessive buildup of SEI, which possibly forms a secondary kinetically-limited layer.

The major difference shown in the Bode diagrams (Figure 3.13b, Figure 3.14b, and Figure 3.15b) occurs in the low frequency regime, which relates to the diffusive behavior of changed species in the electrodes. All three composite electrodes change from approaching -90° phase shift to -45° phase shift for between the 1st cycle and subsequent cycles. The 1st cycle behavior is more similar to what is expected with a supercapacitor since the phase shift in the Bode plot approaches -90°. This response is likely due to that no SEI has been formed yet on the surface of the active material in the 1st cycle. Since the SEI facilitates lithium conduction, the active layer acts more like a capacitor since diffusion is limited into the active material without the SEI. The capacitive nature of the composite electrode is exacerbated by the fact that the CX has a rather large specific surface area.

In Figure 3.13, Figure 3.14, and Figure 3.15, show (c) the evolution of the ESR and (d) charge transfer resistance and capacitance, respectively. Generally, the ESR of these composite electrodes increases during cycling. The composite electrode with PVDF as a binder showed the most stable ESR while the composite electrode with PSS as a binder showed the least stable ESR. The R_{ct} and C_{d} of these composite electrodes decreases and increases, respectively with cycling. The R_{ct} and C_{d} for the composite electrode with PSS as a binder, however, seems to have reached a minimum and maximum, respectively, between the 20th and 50th cycle.

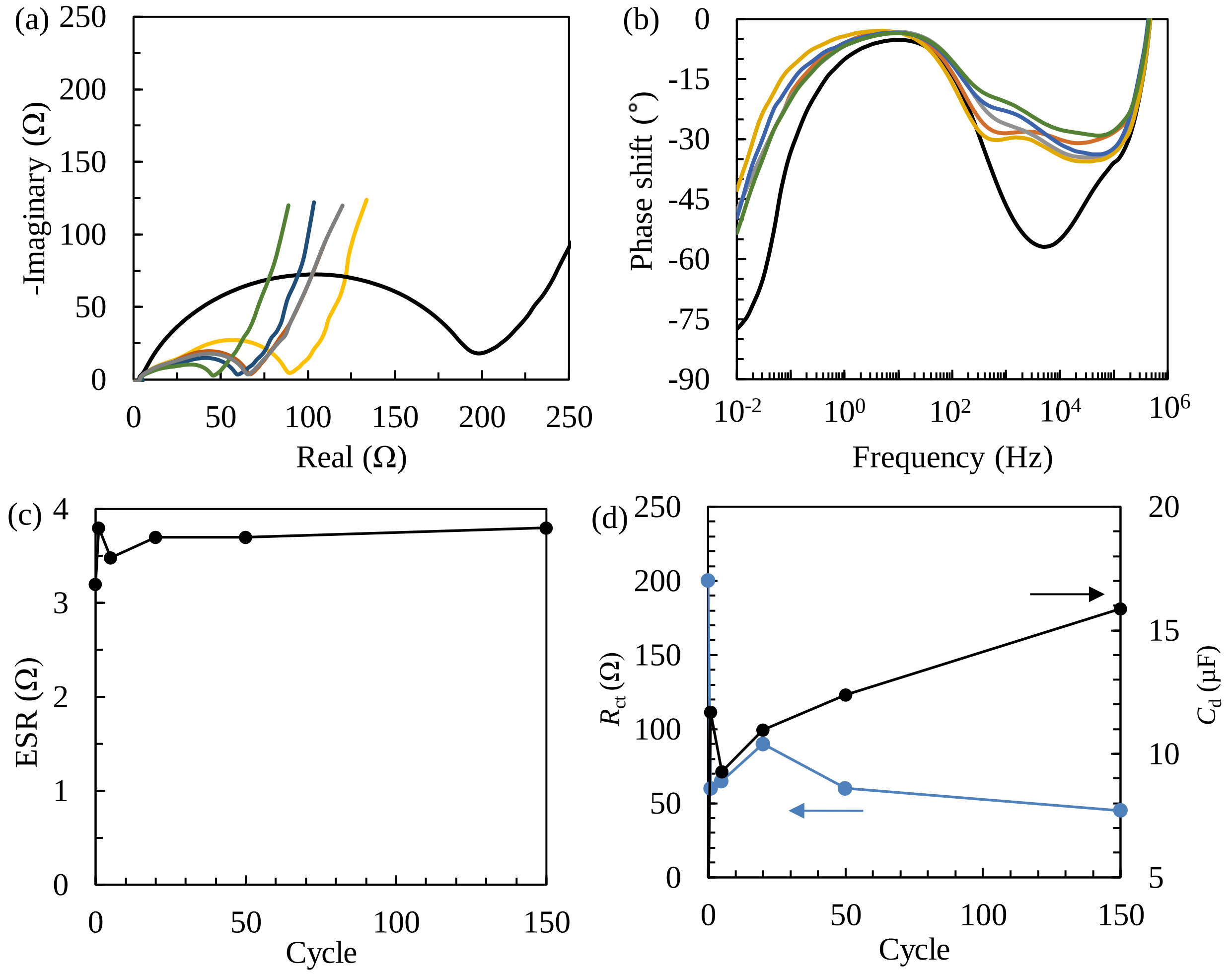

Figure 3.13 – Electrochemical impedance spectroscopy of the OX-15SiNPs composite electrode with PVDF as a binder. (a) Nyquist diagram and (b) Bode plot. (▬) Pristine, (▬) 1st, (▬) 5th, (▬) 20th, (▬) 50th, and (▬) 150th cycle. (c) The trend of ESR as a function of galvanostatic cycles. (d) Charge transfer resistance (R_{ct}) and charge transfer capacitance (C_d) trends as a function of galvanostatic cycles. Scan between 1 MHz and 100 mHz with 10 points per decade. Voltage amplitude of 10 mV.

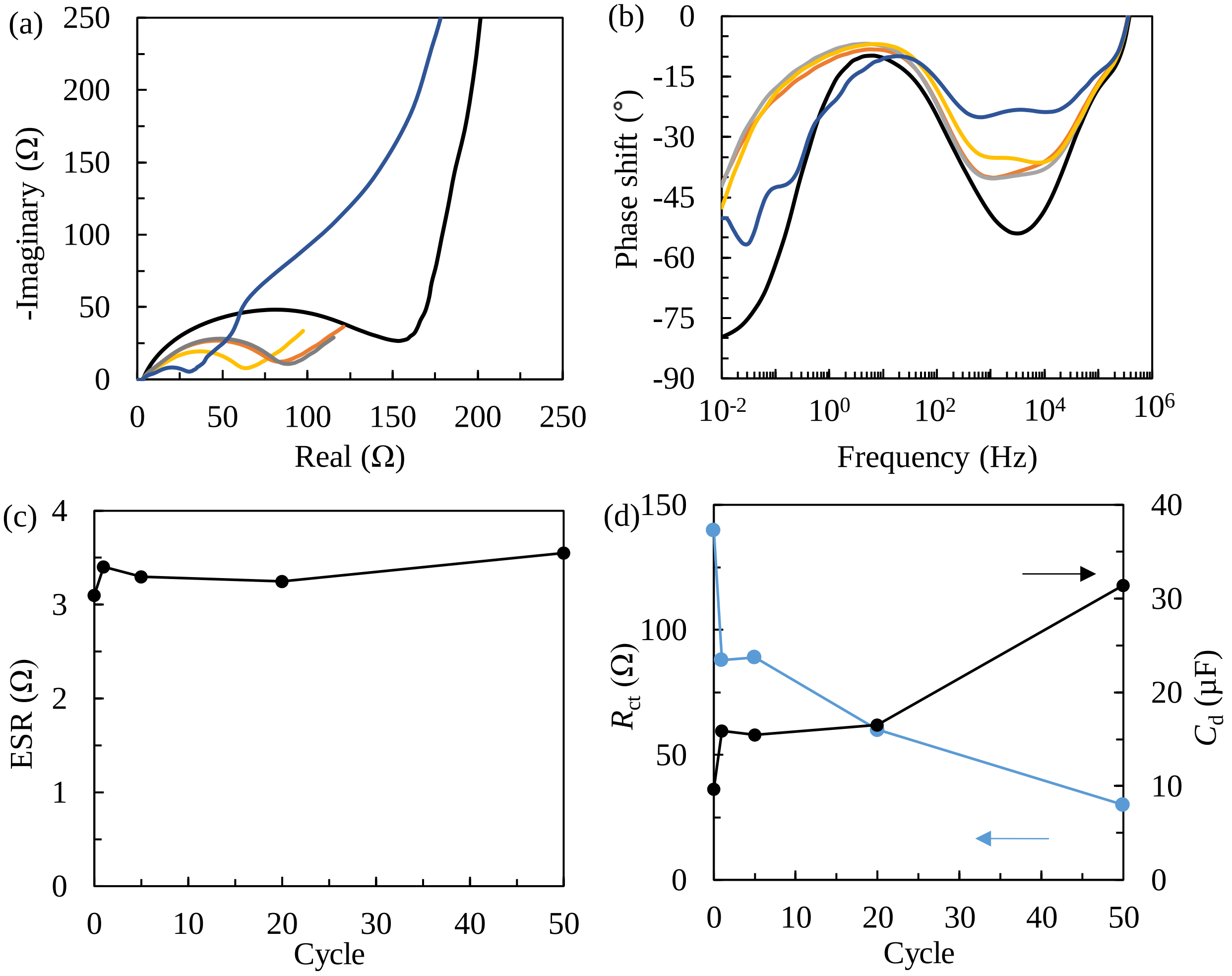

Figure 3.14 – Electrochemical impedance spectroscopy of the OX-15SiNPs composite electrode with a PSS coating and PVDF as a binder. (a) Nyquist diagram and (b) Bode plot. (▬) Pristine, (▬) 1st, (▬) 5th, (▬) 20th, and (▬) 50th. (c) The trend of ESR as a function of galvanostatic cycles. (d) Charge transfer resistance (R_{ct}) and charge transfer capacitance (C_d) trends as a function of galvanostatic cycles. Scan between 1 MHz and 100 mHz with 10 points per decade. Voltage amplitude of 10 mV.

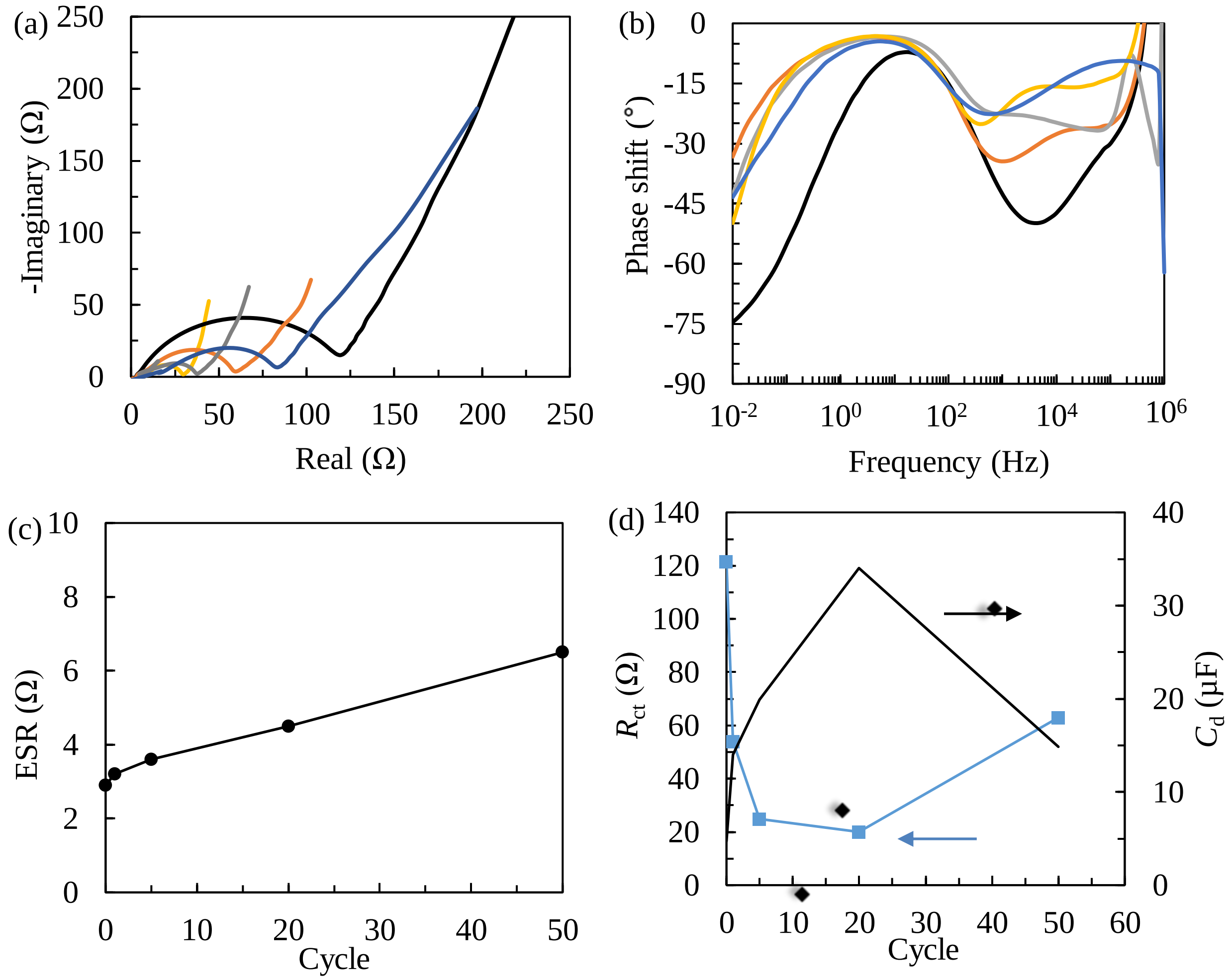

Figure 3.15 – Electrochemical impedance spectroscopy of the OX-15SiNPs composite electrode with PSS as a binder. (a) Nyquist diagram and (b) Bode plot. (▬) Pristine, (▬) 1st, (▬) 5th, (▬) 20th, (▬) 50th. (c) The trend of ESR as a function of galvanostatic cycles. (d) Charge transfer resistance (R_{ct}) and charge transfer capacitance (C_d) trends as a function of galvanostatic cycles. Scan between 1 MHz and 100 mHz with 10 points per decade. Voltage amplitude of 10 mV.

3.4 Discussion

Improved stability of the reversible capacity of OX-10SiNPs composite electrodes with PSS as binder or PSS as a coating as compared to an electrode with PVDF as a binder has been observed. The improved cycle stability may be due to the ionic conductivity of the PSS and improved interface properties between the PSS and the OX-10SiNPs samples. However, composite electrodes that included PSS as a binder or coating still only exhibited a rather short period of stable reversible capacity followed by a gradual loss of capacity. This phenomenon may be due to the loss of PSS into the electrolyte, which would have two effects on the impedance of the half-cell: (i) a constant increase in the electrolyte resistance caused by the poisoning of the electrolyte with PSS and (ii) a decrease in charge transfer resistance (R_{ct}) that reaches a minimum as the layer of PSS becomes thinner followed by an increase of the R_{ct} as the SiNPs pulverize and form an unstable SEI. Interestingly, there is evidence for this model if one considers the EIS measurements presented in Figure 3.15, where PSS is used as a binder. The R_{ct} half circles are shown to be decreasing in diameter, corresponding to faster charge transfer of Li^+ ions into the active material up until 20 cycles. Then an increase in the R_{ct} diameter is observed between 20 and 50 cycles; this could correspond to an unstable SEI layer which leads to an excessive buildup of SEI, which consumes electrolyte. Likewise, a gradual increase in electrolyte resistance is observed during the entire duration of the cycling, which may correspond to the poisoning of the electrolyte by PSS and the loss of electrolyte to SEI formation. Figure 3.16 displays the R_{ct} and electrolyte resistance together and a possible corresponding morphology of the SiNPs and the SEI layer for each regime.

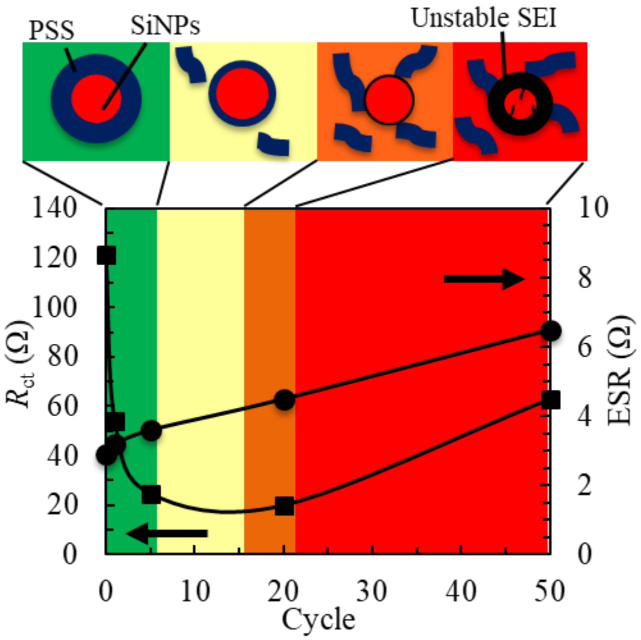

Figure 3.16 – Charge transfer resistance (■) and electrolyte resistance (●) *vs.* cycle number for an OX-15SiNPs composite electrode with PSS as a binder. Values for the charge transfer resistance, R_{ct}, and equivalent series resistance, ESR, were calculated by considering the half circle diameter and abscissa intercept at high frequency, respectively, for the EIS measurement shown in Figure 6c. A proposed schematic representation of PSS dispersion and SEI instability on the SiNPs are shown below the figure. The yellow outline and fragments rep-resent the PSS dispersing into the electrolyte. The thickening black outline represents the excessive SEI formation on the silicon nanoparticle surface after PSS has broken away.

A possible cause for the better cycling stability for OX-10SiNPs composite electrodes with PSS as a binder or PSS as a coating may also be due to a difference in the morphology of the active layer as compared to the composite electrodes with PVDF as a binder. The change in the active layer morphology could be explained by considering how each respective binder covers the available surfaces of the CX. Previous studies as well as this work have shown that it is likely that PVDF preferentially deposits on the meso/macro-pore surface of the active material [33, 34]. This observation is supported in this work by the N_2 adsorption/desorption analysis showing how the PVDF covers the micropores and only deposits on the surface outside of the carbon nodules, *i.e.* S_{ext} of the CX. The morphology between the CX and PSS proposed in this work was that the PSS likely enters the micropores of the CX to some extent, due to the properties of the solvent and binder and the surface chemistry of the CX. As a consequence of these different morphologies, the active layers with PVDF as a binder was observed to be less dense than the active layers with PSS as a binder. A proposed reason for this effect is that the PVDF forms thick, bridge-like connections between particles while the PSS forms a thinner, point-like connection between particles. If true, PVDF would therefore act as a better binder since there is more PVDF available to mechanically bind particles to each other, *via* bridges on their external surface, and less so for PSS since more of the PSS is used to coat the micropore surfaces. However, PSS would arguably be a better protective material due to its better contact between surfaces on the active material, better structural integrity of the active layer due to the higher density, and its ionically conductive nature.

3.5 Conclusion

Carbon xerogel and SiNPs composite electrodes were synthesized with an ionically conductive polymer as either a protective coating or binder. OX-SiNPs composite electrodes with 0 wt%, 10 wt%, 15 wt%, and 30 wt% SiNPs were synthesized with PSS as a binder or coating and compared to the same OX-SiNPs composite electrode synthesized with PVDF as a binder. The reversible capacity retention of OX-SiNPs composite electrodes were improved when either PSS as a coating or PSS as a binder was used rather than only PVDF as a binder. The OX-SiNPs composite electrodes with either PSS as a coating or PSS as a binder reached 80% the initial capacity after ≈40 cycles while the composite electrodes with PVDF as a binder reached 80% the initial capacity after only 6 cycles. However, sharp decreases in the capacity were observed for the first few cycles for composites with higher weight fractions of silicon (15 wt% and 30 wt%). These OX-SiNPs composites with high weight fractions of silicon tended to follow a similar loss of capacity as the low weight fraction of silicon composites after this initial sharp decrease after the first 5 cycles. The morphology of the PSS on the surface of the OX-SiNPs composites as well as a denser and more adhered active layer may have helped protect the active material from breaking apart and ensure ionic and electronic conductivity throughout the active later. Impedance measurements indicated that a loss of PSS into the electrolyte may be the cause of the cycle instability of these composites. Further study into PSS as a protective layer may be focused on reducing the brittleness of PSS by cross-linking or by using elastic co-polymers, which would help maintain adhesion of the protective layer to the silicon and carbon support.

3.6 References

[1] R. Yazami, Surface chemistry and lithium storage capability of the graphite-lithium electrode, Electrochimica Acta 45 (1999) 87–97.

[2] R. Yazami, A reversible graphite-lithium negative electrode for electrochemical generators, J. Power Sources 45 (1983) 87–97.

[3] J. Sakabe, N. Ohta, T. Ohnishi, K. Mitsuishi, and K. Takada, Porous amorphous silicon film anodes for high capacity and stable all-solid-state lithium batteries, Comm. Chem. 1 (2018) 1 – 24.

[4] R. A. Huggins, Lithium alloy negative electrodes, J. Power Sources 81 (1999)13–19.

[5] S.N. Houseman, T.J. Bartik, and T. J. Sturgeon, Measuring manufacturing: How the computer and semiconductor industries affect the numbers and perceptions, in: Measuring Globalization: Better Trade Statistics for Better Policy, Upjohn Institute for Employment Research (2015).

[6] D. Ma, Z. Cao, and A. Hu, Si-based anode materials for li-ion batteries: A mini review, Nano-Micro Lett. 6 (2014) 347–358.

[7] Y. Cui, N. Liu, H. Wu, M.T. McDowell, Y. Yao, and C. Wang, A Yolk-Shell Design for Stabilized and Scalable Li-Ion Battery Alloy Electrodes. Nano Lett. 12 (2012) 3315-3321.

[8] M. T. McDowell, S.W. Lee, J.T. Harris, B.A. Korgel, C. Wang, W.D. Nix, and Y. Cui, In situ tem of two-phase lithiation of amorphous silicon nanospheres, Nano Lett. 13 (2013) 758–764.

[9] X. H. Liu, L. Zhong, S. Huang, S.X. Mao, T. Zhu, and J.Y. Huang, Size-dependent fracture of silicon nanoparticles during lithiation, ACS Nano 6 (2012) 1522–1531.

[10] J. Xu, Q. Zhang, and Y.T. Cheng, High capacity silicon electrodes with nafion as binders for lithium-ion batteries, J. Electrochem. Soc. 163 (2016) A401-A405.

[11] N. Job, R. Pirard, J. Marien, and J.P. Pirard, Porous carbon xerogels with texture tailored by pH control during sol–gel process, Carbon 42 (2004) 619-628.

[12] N. Rey-Raap, M.L.C. Piedboeuf, A. Arenillas, J.A. Menéndez, A.F. Léonard, and N. Job, Aqueous and organic inks of carbon xerogels as models for studying the role of porosity in lithium-ion battery electrodes, Mater. Design 109 (2016) 282–288.

[13] X. Yuan, Y.J. Chao, Z.F. Ma, and M. Deng, Preparation and characterization of carbon xerogel (cx) and CX-SiO composite as anode material for lithium-ion battery, Electrochem. Commun. 9 (2007) 2591-2595.

[14] J.P. Lewicki, C.A. Fox, and M.A. Worsley, On the synthesis and structure of resorcinol-formaldehyde polymeric networks-precursors to 3D carbon macroassemblies, Technical report, Lawrence Livermore National Laboratory (2015).

[15] M.-L. Piedboeuf, A.F. Léonard, K. Traina, and N. Job, Influence of the textural parameters of resorcinol–formaldehyde dry polymers and carbon xerogels on particle sizes upon mechanical milling, Colloid Surface A 471 (2015) 124-132.

[16] C. Alegre, D. Sebastián, E. Baquedano, M.E. Gálvez, R Moliner, and M.J. Lázaro, Tailoring synthesis conditions of carbon xerogels towards their utilization as pt-catalyst supports for oxygen reduction reaction (orr), Catalysts 2 (2012) 466–489.

[17] PubChem Compound Database, National center for biotechnology information, Water [CID=962]. Available: https://pubchem.ncbi.nlm.nih.gov/compound/962. Accessed on: April 4, 2021.

[18] PubChem Compound Database, National center for biotechnology information, NMP [CID=13387]. Available: https://pubchem.ncbi.nlm.nih.gov/compound/13387. Accessed on: April 4, 2021.

[19] B. Kartick, S. K. Srivastava, and I. Srivastava, Green Synthesis of Graphene. J. of Nanoscience and Nanotechnology 13 (2013) 4320–4324.

[20] G. Wang, J. Yang, J. Park, X. Gou, B. Wang, H. Liu, and J. Yao, . J. Phys. Chem. C112 (2008) 8192.

[21] R. Siburian, H. Sihotang, S. Lumban Raja, M. Supeno, and C. Simanjuntak, New Route to Synthesize of Graphene Nano Sheets. Orient. J. Chem., Vol. 34(1), 182-187(2018)

[22] M. Winter, J. O. Besenhard,* M. E. Spahr, and P. Novµk, Insertion Electrode Materials for Rechargeable Lithium Batteries. Adv. Mater. 10 (1998) 725-763.

[23] J. Westra, V. Vavruňková, P. Sutta, R.A.C.M.M. Van Swaaij, and M. Zeman, Formation of thin-film crystalline silicon on glass observed by in-situ XRD. Enrgy Proced. 2 (2010) 235-241.

[24] F. Joho, B. Rykart, A. Blome, P. Novák, H. Wilhelm, and M.E. Spahr, Relation between surface properties, pore structure and first-cycle charge loss of graphite as negative electrode in lithium-ion batteries, J. Power Sources 97-98 (2001) 78–82.

[25] S. An, J. Li, C. Daniel, D. Mohanty, S. Nagpure, D.L. Wood III, The state of understanding of the lithium-ion-battery graphite solid electrolyte interphase (SEI) and its relationship to formation cycling, Carbon 105 (2016) 52-76.

[26] E. Peled, D. Golodnitsky, C. Menachem, and D. Bar-Tow, An advanced tool for the selection of electrolyte components for rechargeable lithium batteries, J. Electrochem. Soc. 145 (1998) 3482-3486.

[27] N. Sun, H. Liu, and B. Xu, Facile synthesis of high performance hard carbon anode materials for sodium ion batteries, J. Mater. Chem. A 3 (2015) 20560–20566.

[28] C.K. Chana, R. Ruffo, S.S. Hong, and Y. Cui, Surface chemistry and morphology of the solid electrolyte interphase on silicon nanowire lithium-ion battery anodes, J. Power Sources 189 (2009) 1132–1140.

[29] X. Zuoa, J. Zhua, P. Müller-Buschbaum, and Y.J. Chenga, Silicon based lithium-ion battery anodes: A chronicle perspective review, Nano Energy 31 (2017) 113–143.

[30] E. N. Attia, Tailoring the chemistry of blend copolymers boosting the electrochemical performance of si-based anodes for lithium ion batteries, J. Mater. Chem. A5 (2017) 24159–24167.

[31] T. Reddy, D. Linden, Handbook of Batteries. McGraw-Hill Education, McGraw-Hill Education, 4th edition edition, 2011.

[32] F.M. Hassan, R. Batmaz, J. Li, X. Wang, X. Xiao, A. Yu, and Z. Chen, Evidence of covalent synergy in silicon–sulfur–graphene yielding highly efficient and long-life lithium-ion batteries, Nat. Commun. 6 (2015) 8597–8608.

[33] M. Yoo and C. Frank, Surface Chemistry and morphology of binders in graphite anodes of lithium ion batteries, Technical Report, Stanford University, 2019.

[34] M. Yoo, C.W. Frank, S. Mori, and S. Yamaguchi, Interaction of poly(vinylidene fluoride) with graphite particles. 2. Effect of solvent evaporation kinetics and chemical properties of pvdf on the surface morphology of a composite film and its relation to electrochemical performance, Chem. Mater. 16 (2004) 1945–1953.

3.7 Supplemental information

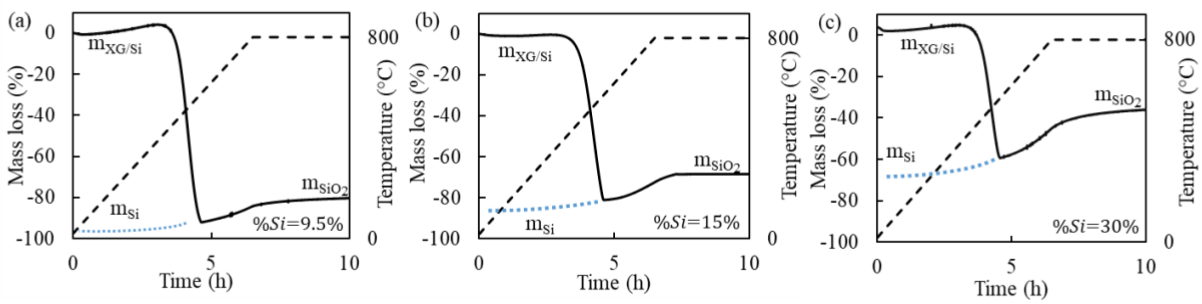

Figure S3.1 – Thermogravimetric response of OX-SiNPs electrode active material with varying amounts of silicon. Heating procedure was 5°C min^{-1} up to 800°C and held at 800°C for 4 h. (a) approximately 10 wt% silicon, (b) 15 wt% silicon, and (c) 30 wt% silicon.

The two following equations were used to determine the amount of silicon in the OX-SiNPs composite material.

$$\%Si = \frac{m_{\mathrm{Si}}}{m_{\frac{\mathrm{CX}}{\mathrm{SiNPs}}}} \qquad\qquad m_{Si} = m_{\mathrm{SiO_2}}\left(\frac{M_{\mathrm{Si}}}{M_{\mathrm{SiO_2}}}\right)$$

Given that the final weight measured of the sample after heating under air was considered to be the mass of silica only, m_{SiO2}, the initial weight of silicon, m_{Si}, in the sample can be calculated by considering the molecular weights of silica, M_{SiO2}, and silicon, M_{Si} along with the initial mass of the composite, $m_{\mathrm{OX\text{-}SiNPs}}$.

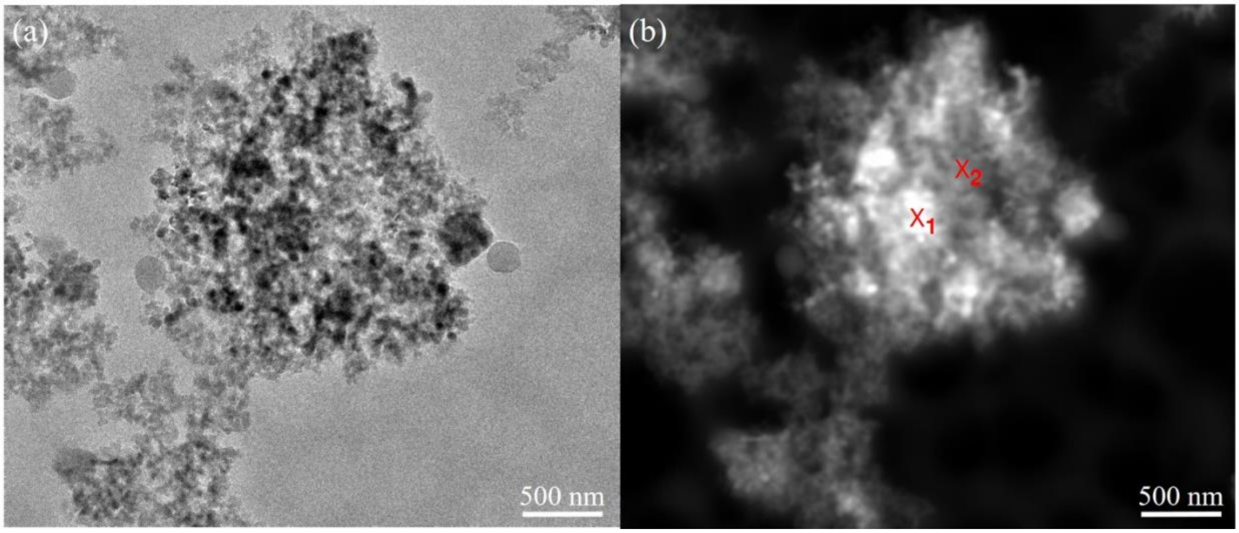

Figure S3.2 – (a) Bright field and (b) dark field TEM micrographs of the OX-SiNPs composite. The points marked as X_1 and X_2 were used to collect EDX spectra in order to discriminate between the carbon and silicon phases

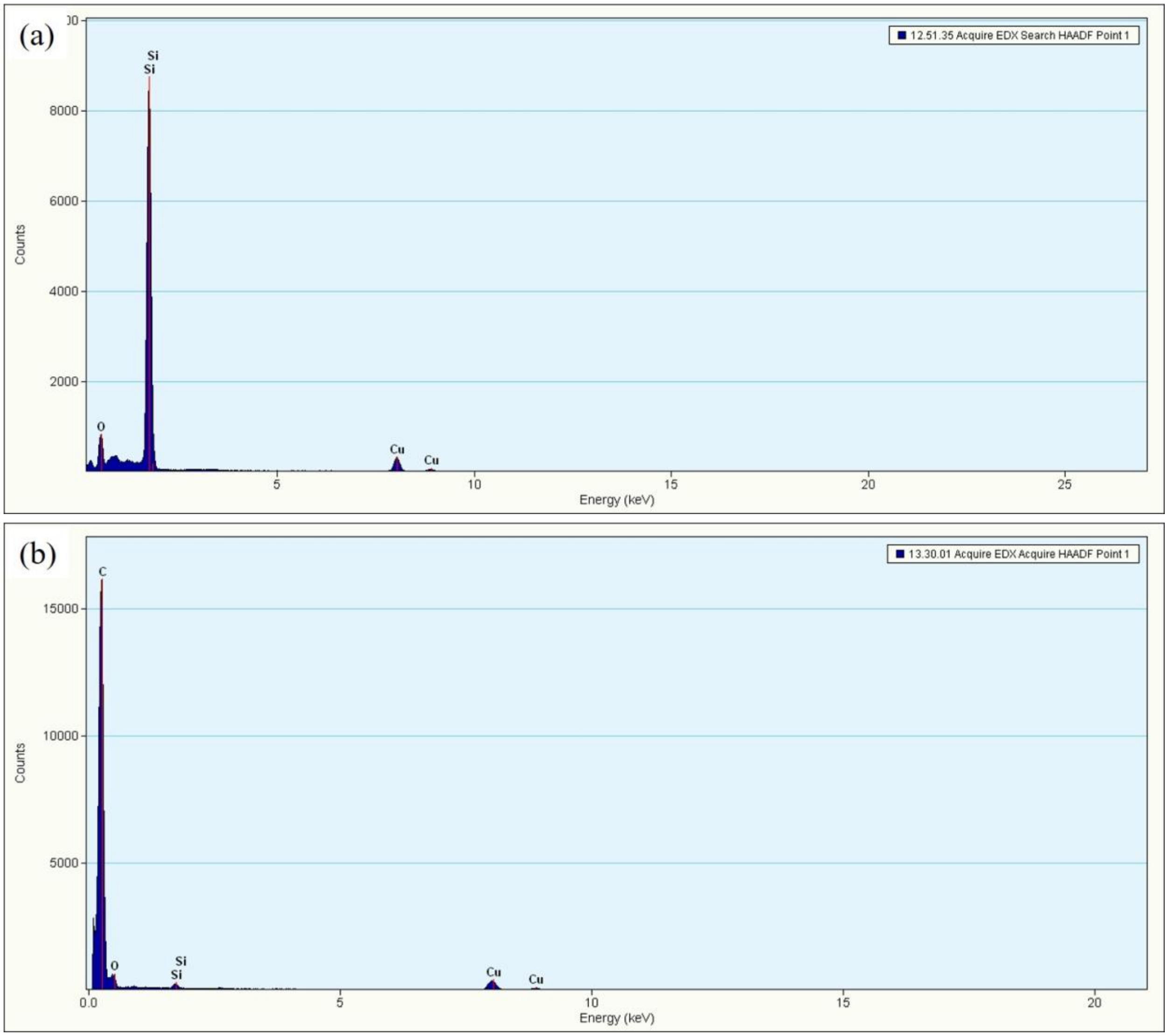

Figure S3.3 – (a) EDS spectra for the point, X2, in Figure S3, which identifies the silicon phase (b) EDS spectra for the point, X1, in Figure S3, which identifies the carbon phase.

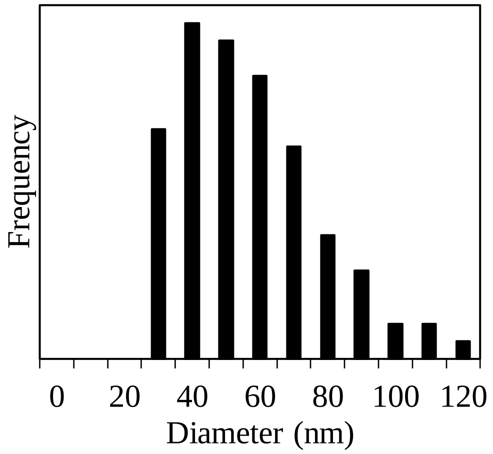

Figure S3.4 – The particle size number distribution of the SiNPs in the OX-10SiNPs sample. An average diameter of 51 nm was calculated for the silicon nanoparticles from this analysis.

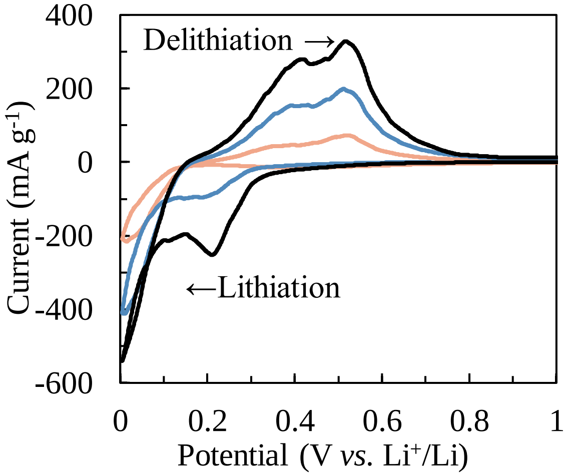

Figure S3.5 – CV Measurement of a SiNPs electrode with (a) PVDF as a binder. The scan rate was 50 µV s^{-1} between 0.005 V and 1.5 V *vs.* Li$^+$/Li. Shown for the (▬) 1st, (▬) 2nd and (▬) 3rd cycle.

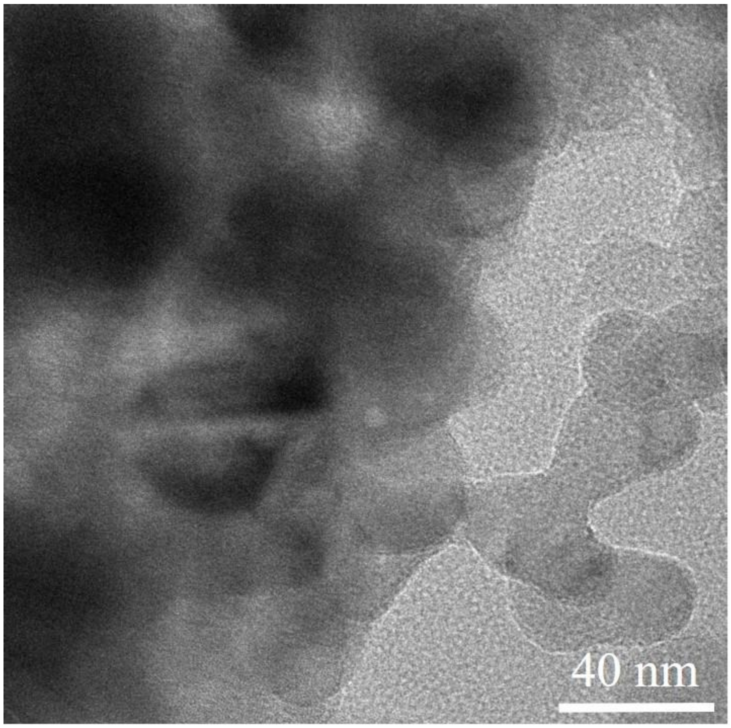

Figure S3.6– The image above is a high magnification micrograph of the OX-15SiNPs composite with PSS as a binder. It is not possible to see the binder given the low electron density in the polymer)

Chapter 4

Silicon-doped carbon xerogel *via* magnesiothermal reduction of silica

Abstract

In the present work, two active materials composed of a mixture of a CX and silicon were synthesized for the negative electrode for lithium-ion batteries. Silicon was included in the CX structure *via* a precursor silica that was *in situ* reduced into silicon *via* magnesiothermal reduction. Silica was introduced either (i) as commercial silica nanoparticles or (ii) as TEOS-derived silica. The TEOS-derived silica was in situ hydrolyzed and reduction within the CX particles. Physico-chemical characterization was performed to determine the morphology and composition of the samples at various stages throughout the synthesis procedure. Electrochemical characterization was carried out by assembling a composite electrode consisting of the active material (the CX and silicon mixture) with poly(vinylidene difluoride) (PVDF) or poly(sodium 4-styrenesulfonate) (PSS) as a binder. The composite electrodes with the silica nanoparticles-derived silicon exhibited the expected silicon lithiation and delithiation potentials during cyclic voltammetry measurements and a 1st cycle capacity of up to 600 mAh g^{-1} for 80 wt.% CX and 20 wt.% silicon. These composite electrodes reached 20 cycles before reducing to 50% of the initial capacity. The loss of capacity during cycling is likely due to the unreacted silica causing stresses within the active material, which leads to both an unstable solid-electrolyte interphase and pulverization of the active layer. Furthermore, the heterogeneous distribution of the silica nanoparticles throughout the CX likely contributed to the quick loss of capacity. The composite electrodes with the TEOS-derived silicon did not show any silicon redox peaks in CV measurements and only exhibited a capacity of 100 mAh g^{-1}, despite the expected silicon loading of 20 wt% silicon. This suggests that the silica was not reduced properly during the magnesiothermal reduction. Electrochemical impedance spectroscopy was performed to determine how the electrodes changed during cycling, which gave evidence for the formation of SEI during the 1st cycle and morphology change in subsequent cycles. Although the composite electrodes with TEOS-derived silica did not show any evidence of significant conversion of silica into silicon, the use of TEOS as a silicon precursor could still be a promising synthesis route if magnesiothermal reduction of this material can be improved.

4.1 Introduction

As discussed in the previous chapters, silicon is an interesting material for a lithium-ion (Li^+ ion) battery negative electrode due to its low electrochemical lithiation and delithiation potential (< 0.35 V *vs.* Li^+/Li) and its high theoretical energy density (up to 4200 mAh g^{-1}) [1-4]. Silicon is also a relatively abundant element in the earth's crust that has a large pre-existing mining and manufacturing economy, mostly due to the semiconductor industry [5]. Unfortunately, silicon undergoes a large volume change of up to 300% between its lithiated and delithiated states [1-4]. This volume change leads to (i) an unstable solid electrolyte interface (SEI) and (ii) pulverization of the silicon and the other surrounding active material [1-4]. In Chapters 2 and 3, it was shown that silicon nanoparticles (SiNPs) could be successfully included within a carbon xerogel (CX). A CX, as discussed previously, is a unique carbonaceous material consisting of a 3D interconnected meso-macroporous matrix [6-8]. The tunable nature of the CX meso/macropores makes them a great candidate as a host matrix for alloying-type materials for Li^+ ion batteries, such as silicon [6-8]. In Chapter 2, the inclusion of SiNPs into the CX was accomplished by either mixing commercially available SiNPs within the precursor xerogel solution prior to gelation or in an aqueous suspension of dried organic xerogel (OX) particles prior to filtration and pyrolysis. These samples were then used as negative electrode materials for Li^+ ion batteries with promising results, although SEI instability and silicon pulverization still persisted. In Chapter 3, the use of poly(sodium 4-styrenesulfonate) (PSS) was used as a protective coating or binder to help improve the cycling stability of these silicon-doped CXs. Although the results using PSS as a protective coating or binder were positive, further improvements can still be made to the stability of these composite electrodes.

Therefore, the goal of the work in this chapter is to further reduce the negative effects caused by the volumetric change of the silicon during cycling by more intimately including silicon into the CX, using a new synthesis technique. Rather than impregnating previously-synthesized silicon nanoparticles into the CX (see Chapters 2 and 3), a silicon precursor could be introduced into the CX and subsequently transformed into silicon. The most well-known silicon precursor, silane, can be used to synthesize high purity silicon metal *via* a CVD process, which is widely used in the production of solar cells and other precision electronic devices [9-11]. However, a CVD process would likely be too expensive and difficult to use in the production of batteries. Therefore, an alternative approach was considered that would be cheaper and more practical for large scale production. This approach consists of using silica as the silicon precursor.

Silica is a good choice for a silicon precursor because it is widely abundant on earth, easy to produce, available commercially with a wide range of nanostructures, and can be transformed into silicon in a few different ways. Previously-synthesized silica nanoparticles could be easily included within the CX in a similar way as the silicon nanoparticles, like in Chapters 2 and 3, and then subsequently reduced into silicon. However, since the goal of this work is to more closely integrate the silicon phase with the CX phase, a nanostructured silica that could intimately integrate with host CX would be preferable.

One possible solution would be to use a silica precursor, like tetraethyl orthosilicate (TEOS), to deposit silica within the CX. TEOS is a liquid silica precursor that forms silica nanostructures *via* a simple, safe, and cheap sol-gel process [12, 13]. Similar to the CX sol-gel process, the microstructure of the TEOS-derived silica can be easily tuned by controlling the hydrolysis and condensation conditions of the TEOS, such as the pH, type of solvent, and dilution ratio [12,13].

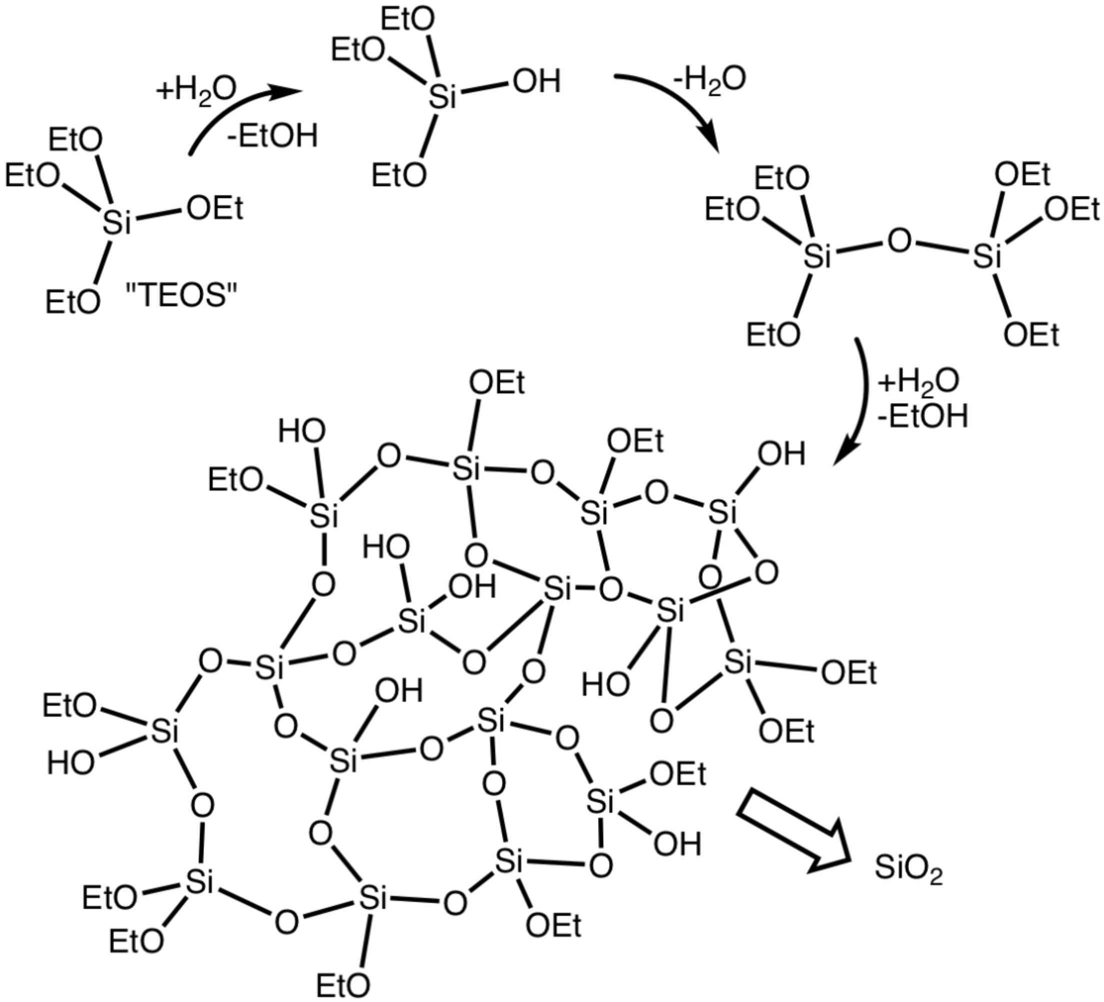

Figure 4.1 – Tetraethyl orthosilicate (TEOS) hydrolysis and condensation. Reprinted from [14].

Once the silica nanoparticles or TEOS-derived silica have been deposited within the CX, it must be transformed into silicon. The most well-known way to produce silicon from silica is by carbothermal reduction [15]. This process, however, only proceeds at exceedingly high temperatures (> 2000°C) that would melt the resulting silicon upon transformation, which would cause the nanostructure from the parent silica to be lost [15]. Therefore, it is necessary to convert the silica into silicon at a reaction temperature below the melting point of silicon (1414°C) in order to maintain the nanostructure of the parent silica. One such reaction that exists is the reaction of silica with magnesium. During magnesiothermal reduction, magnesium reacts with silica in either a liquid or gas phase at moderately elevated temperatures (> 650°C) to produce silicon metal and other by-products [16-22]. The three most likely reactions between silica and magnesium are shown below. Two of the reactions can produce silicon metal; however, a third reaction produces Mg_2Si instead of silicon [22].

$$2\mathrm{Mg(g)} + \mathrm{SiO_2(s)} \rightarrow 2\mathrm{MgO(s)} + \mathrm{Si(s)} \qquad \Delta G_T^0(700°\mathrm{C}) = -19.68\,\frac{\mathrm{kJ}}{\mathrm{mol}} \tag{4.1}$$

$$2\mathrm{Mg(l)} + \mathrm{SiO_2(s)} \rightarrow 2\mathrm{MgO(s)} + \mathrm{Si(s)} \qquad \Delta G_T^0(700°\mathrm{C}) = -17.84\,\frac{\mathrm{kJ}}{\mathrm{mol}} \tag{4.2}$$

$$4\mathrm{Mg(l)} + \mathrm{SiO_2(s)} \rightarrow 2\mathrm{MgO(s)} + \mathrm{Mg_2Si(s)} \qquad \Delta G_T^0(700°\mathrm{C}) = -18.70\,\frac{\mathrm{kJ}}{\mathrm{mol}} \tag{4.3}$$

Fortunately, it is possible to suppress the reactions in Equations 4.2 and 4.3 by maintaining magnesium in the gas phase so that only the reaction in Equation 4.1 can proceed. Through this reaction, one would be able to safely transform silica into silicon while maintaining the nanostructure of the parent silica.

Unfortunately, the magnesiothermal reduction reaction shown in Equation 4.1 releases a large amount of heat ($\Delta H_f^0 = -587\ \mathrm{kJ/mol_{silica}}$), which is likely sufficient to induce local reaction temperatures far exceeding the melting point of silicon [16-22]. Previous studies have shown that NaCl can be used as a heat scavenger to keep the reaction temperature below the melting point of silicon [18, 21]. This is accomplished by allowing the heat released during the magnesiothermal reduction to be redirected into the fusion of the NaCl ($\Delta H_{\mathrm{fusion}} = 28.8\ \mathrm{kJ/mol}$) rather than into the CX-silica-silicon material [18, 21]. If a sufficient amount of NaCl is added, the reaction temperature should be halted around the melting point of NaCl (~800°C) and the nanostructure of the parent silica can be maintained.

So, in the present work, two CX-silicon samples were synthesized *via* the magnesiothermal reduction of (i) previously synthesized silica nanoparticles or (ii) TEOS-derived silica using NaCl as a heat scavenger. The inclusion of previously synthesized silica nanoparticles was used in order to determine if the magnesiothermal reduction process is sensitive to how silica is deposited into the CX. The first sample consisted of mixing the silica nanoparticles and a gelled carbon xerogel particles in a solvent. The CX with TEOS-derived silica sample was synthesized by first impregnating TEOS into the gelled carbon xerogel particles then the TEOS was hydrolyzed and condensed into silica. Both samples were then reduced into silicon *via* magnesiothermal reduction.

The samples were physico-chemically characterized *via* Hg porosimetry, N_2 adsorption/desorption, XRD, and TEM imaging. Composite electrodes of the samples were then prepared with either poly(vinylidene difluoride) (PVDF) or poly(sodium 4-styrenesulfonate) (PSS) as a binder. PVDF or PSS were used as a binder to determine if PSS still offers the same protective properties to the instabilities of the silicon dopant as observed in Chapter 3. These composite electrodes were electrochemically characterized and compared *via* galvanostatic cycling, cyclic voltammetry (CV), and electrochemical impedance spectroscopy (EIS).

4.2 Experimental

Materials: Resorcinol (R, 99%), formaldehyde (F, 37 wt.% in H_2O), sodium carbonate (C, 99.5%), poly(sodium 4-styrenesulfonate) (PSS, M_w = 70,000 g mol^{-1}), magnesium (Mg, chip 4+30 mesh, 99.98%), tetraethyl orthosilicate (TEOS, >99.0%) , and silicon dioxide (S1, nanopowder, 5-20 nm particle size (BET), 99.5% trace metals basis) were purchased from Sigma-Aldrich. N-methyl-2-pyrrolidone (NMP, ~99%) was purchased from Alfa Aesar.

4.2.1 CX sample: Carbon xerogel synthesis

A carbon xerogel (CX) with an *R/C* ratio of 2000 was synthesized *via* the sol-gel polycondensation of resorcinol and formaldehyde in high purity water (*via* MilliQ process until R > 18 MΩ) [6-8]: see section 1.2.1 in Chapter 1 for the solution preparation, gelation, drying, ball-milling, and pyrolysis procedures). The specific capacity of the CX was found to be approximately 200 mAh g^{-1} when cycled between 0.005 V and 1.5 V *vs.* Li^+/Li (see Figure 2.11 and Figure 2.12a in Chapter 2 for the galvanostatic cycling and corresponding potential profiles, respectively).

4.2.2 CXS-S1 sample: Mixing of silica nanoparticles and carbon xerogel in suspension

The silica nanoparticles (S1) were included into the bare CX *via* mixing in a solvent. 100 mg of S1 and 100 mg of CX were added to 10 mL of high purity water. The suspension was ultrasonicated for 2 h then magnetically stirred at 1000 rpm for 4 h. The solid was subsequently recovered *via* centrifugation. The recovered material was dried in a vacuum oven at 90°C and 1500 Pa for 24 h. The recovered material was then redispersed into a solution of 1 g of NaCl, which was used as a heat scavenger, in 10 mL of high purity water. The solution was ultrasonicated for 2 h then magnetically stirred at 1000 rpm for 4 h. The water was then removed *via* evaporation in a vacuum oven at 90°C and 1500 Pa for 24 h and the material, referred to as CXS-S1, was recovered as a powder. Another sample was prepared without NaCl as a heat scavenger for comparative purposes and will be referred to as CXS-S1n.

4.2.3 CXS-TEOS sample: *In situ* hydrolysis and condensation of tetraethyl orthosilicate in carbon xerogel

Tetraethyl orthosilicate (TEOS), which is as a precursor to silica, was impregnated into a carbon xerogel host matrix. A two-step procedure consisting of an acid-catalyzed hydrolysis and a base-catalyzed condensation reaction was carried out to form the silica within the carbon xerogel. 1.5 g of CX powder was added to a solution of 4.8 mL of TEOS in 10 mL of ethanol. Hydrolysis was initiated by adding 2.16 mL of 0.001 M oxalic acid dropwise under stirring at 500 rpm. The solution was stirred for 24 h to ensure complete hydrolysis of the TEOS. Condensation of the hydrolyzed TEOS was initiated by adding 0.76 mL of 1 M NH_4OH. The solution was again stirred for 24 h to ensure the condensation reaction was complete. The recovered sample, CXS-TEOS was washed multiple times before being dried in a vacuum oven at 90°C and 1500 Pa for 24 h. The recovered material was then redispersed into a solution of 1 g of NaCl in 10 mL of high purity water. The solution was ultrasonicated for 2 h then magnetically stirred at 1000 rpm for 4 h. The water was then removed *via* evaporation in a vacuum oven at 90°C and 1500 Pa for 24 h and the material, referred to as CXS-TEOS, was recovered as a powder. No samples were prepared without NaCl as a heat scavenger.

4.2.4 Magnesiothermal reduction of CXS-S1 and CXS-TEOS samples

The CXS-S1 and CXS-TEOS samples were then subsequently reduced *via* magnesiothermal reduction. The samples were reduced within a stainless-steel reactor in an inert argon environment given that the magnesiothermal reduction reaction would also react with other materials, such as quartz. The reactor consisted of a 15 cm long stainless-steel pipe nipple with a diameter of 2 inches with two corresponding screw ends (RONI 20/150 ES). The CXS-S1 and CXS-TEOS samples were placed into sample holders hand-formed from stainless steel foil. Two other sample holders were formed to hold the magnesium chips separate from the CXS-S1 and CXS-TEOS samples (see Figure 4.2 for a reference of the reactor setup). The sample holders were inserted and sealed into the stainless-steel pipe reactor within an argon-filled glovebox. A pyrolysis oven, situated nearby the glovebox, was prepared by flowing argon through the oven. The sealed reactor was then quickly inserted into the oven and sealed, while argon flowed. The oven was then heated up to 700°C at a rate of 10°C min^{-1}. The oven was held at this temperature for 10 h, then let to cool down to room temperature. After the reactor had cooled below 50°C, the reactor was quickly transferred into the argon-filled glovebox again to be opened. The samples were left in the argon environment for 24 h prior to any analysis.

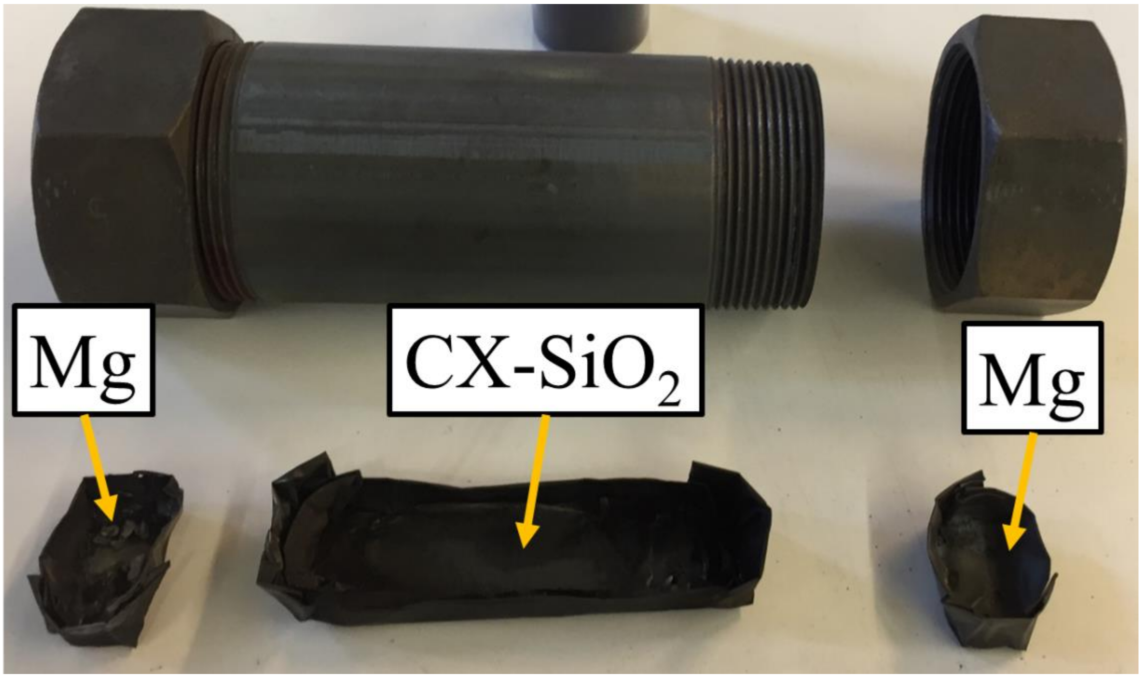

Figure 4.2 – Magnesiothermal reactor made of 304 stainless-steel. The sample holders for the magnesium chips and CX-silica samples were constructed out of 304 stainless steel foil.

The recovered materials (referred to as rCXS-S1 and rCXS-TEOS, where “r” is for “reduced”) were then washed several times with high purity water (MilliQ, R > 18 MΩ) to remove the NaCl. Then, the samples were washed several times with a 1 M HCl solution to remove the unreacted magnesium, magnesia, and other by-products. The samples were once again washed multiple times with high purity water to remove any remaining HCl. The samples were then gently dried in an oven at 60°C and 1500 Pa for 24 h. The expected mass percent of silicon in the rCXS-S1 and rCXS-TEOS samples was approximately 30 wt% silicon with an expected theoretical capacity of approximately 1000 mAh g^{-1} if all the silica had been converted into silicon.

4.2.5 Preparation of inks and composite electrodes

Electrodes were prepared using the CX, rCXS-S1 and rCXS-TEOS powder as the active material. First, ink slurries were prepared for subsequent electrode preparation and electrochemical characterization. Inks were formulated with either PSS or PVDF as a binder in order to determine whether PSS has a protective effect, like in Chapter 3. 90 wt% of active material and 10 wt% of either PSS or PVDF were dispersed in high purity water (MilliQ, R > 18 MΩ) or NMP, respectively, under magnetic stirring at 1000 rpm for 5 h. The coatings were deposited using a Harder & Steenbeck Evolution Silverline 2 airbrush. A solvent-to-solids mass ratio of 20:1 was used to ensure that the prepared inks flowed easily through the airbrush. After spray-coating, the electrodes were dried at 70°C for 2 h and then at 120°C under vacuum for 24 h. The electrodes were then weighed to determine the mass of the deposited material prior to their electrochemical characterization. Excess dried material surrounding the electrodes, which was deposited around the disks during the spray-coating process, was collected for further characterization.

4.2.6 Physico-chemical characterization and electrochemical characterization

Physico-chemical and electrochemical characterizations carried out in this chapter are outlined in Annex 1. The physico-chemical characterizations included nitrogen adsorption-desorption, transmission electron spectroscopy, and X-ray diffraction (XRD). N_2 adsorption was used to determine the specific surface area (S_{BET}) and the corresponding microporous (S_{micro}) and meso/macroporous (S_{ext}) surface areas of the CX, rCXS-1, and rCXS-TEOS powders as well as the composites with PVDF or PSS as a binder. XRD and TEM with EDS analysis was used to determine the SiNPs crystallite size, particle size and distribution, elemental characterization, and crystallographic microstrain of the dopant silicon in the rCXS-1 and rCXS-TEOS samples. XRD was also performed on the unreduced CXS-1 and CXS-TEOS samples as well as the CX sample.

Electrochemical characterization consisted of cyclic voltammetry (CV), galvanostatic cycling, and electrochemical impedance spectroscopy (EIS) on the CX, rCXS-1, and rCXS-TEOS composite electrodes. CV characterizations show the redox potentials of the electrochemically active components as well as how these reactions evolve during cycling. Cycling gives the specific capacity and stability of the prepared composite electrodes. EIS analysis was used to determine how the equivalent series resistance (ESR), charge transfer resistance (R_{ct}), charge transfer capacitance (C_{d}) and the diffusive properties of the composite electrodes evolves during cycling. An overview of these parameters and the electrochemical model for these electrodes can be found in Annex 2.

4.3 Results and discussion

4.3.1 Physico-chemical characterization

Transmission electron microscopy

TEM micrographs were collected on the S1, CXS-S1, CXS-TEOS, rCXS-S1, and rCXS-TEOS samples. TEM micrographs of the CX sample (*R/C* = 2000) are given in Chapters 1, 2, and 3. Figure 4.3 shows TEM micrographs of the silica nanoparticles (S1) received from the supplier. These micrographs show aggregates of particles that seem to be overlapping each other or even connected into longer chains.

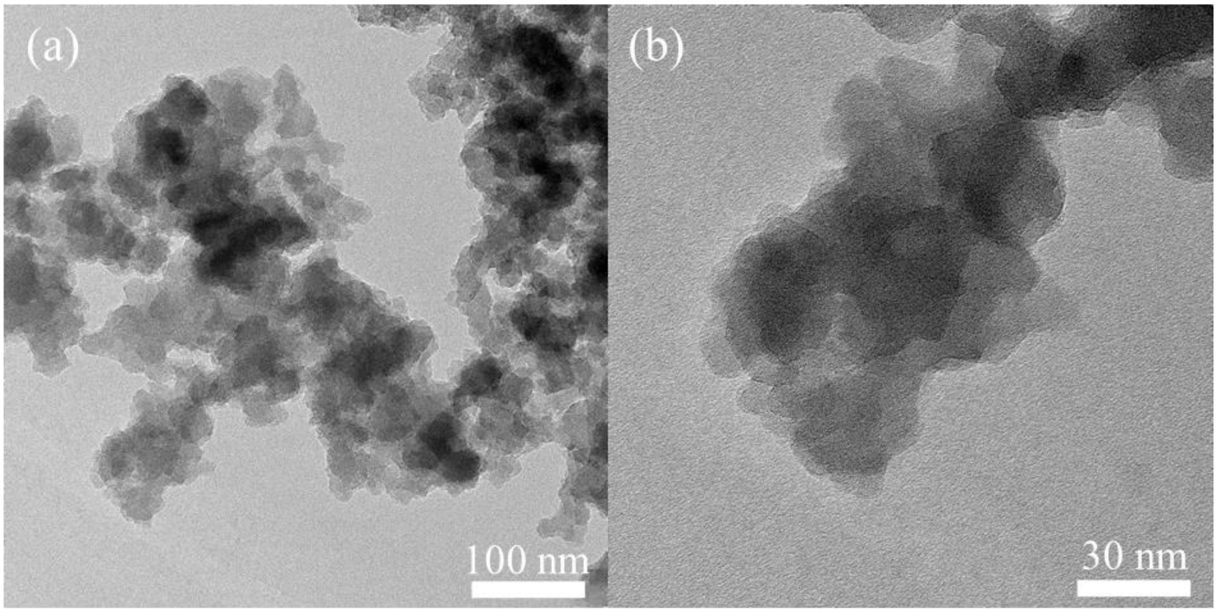

Figure 4.3 – TEM micrographs of a silica nanoparticles S1 at various magnifications.

TEM micrographs of the CXS-1 and CXS-1n samples are shown in Figure 4.4. Figure 4.4a shows the CXS-1 sample. The CXS-1n sample is not shown given that the morphology was similar. It is difficult to differentiate between the CX and S1 phases given that the morphology of the S1 and the CX are similar. The rCXS-1n sample seemed to have formed large agglomerations of silicon particles, as shown by the red arrow in Figure 4.4b. Given that the magnesiothermal reduction of silica into silicon is highly exothermic, the local reaction temperature surrounding the silica particles likely came close to or exceeded the melting point of silicon (> 1400°C). Then, due to the high temperature reached during the reduction process, the silicon would have become a liquid and agglomerated into larger particles.

Therefore, as outlined in the synthesis procedure for the CXS-S1 sample, NaCl was used as a heat scavenger in order to maintain the temperature of the sample during magnesiothermal reduction below the melting point of silicon. Figure 4.4c shows how the morphology of the silica nanoparticles in the sample seems to be preserved when NaCl is used as a heat scavenger. The reduced silica phase can be differentiated from the CX phase by their difference in appearance, as indicated by the two red arrows. These TEM micrographs confirm that NaCl can be successfully used as a heat scavenger during the magnesiothermal reduction of the silica nanoparticles, given that the morphology of the parent silica is at least partially retained after the magnesiothermal reduction into silicon.

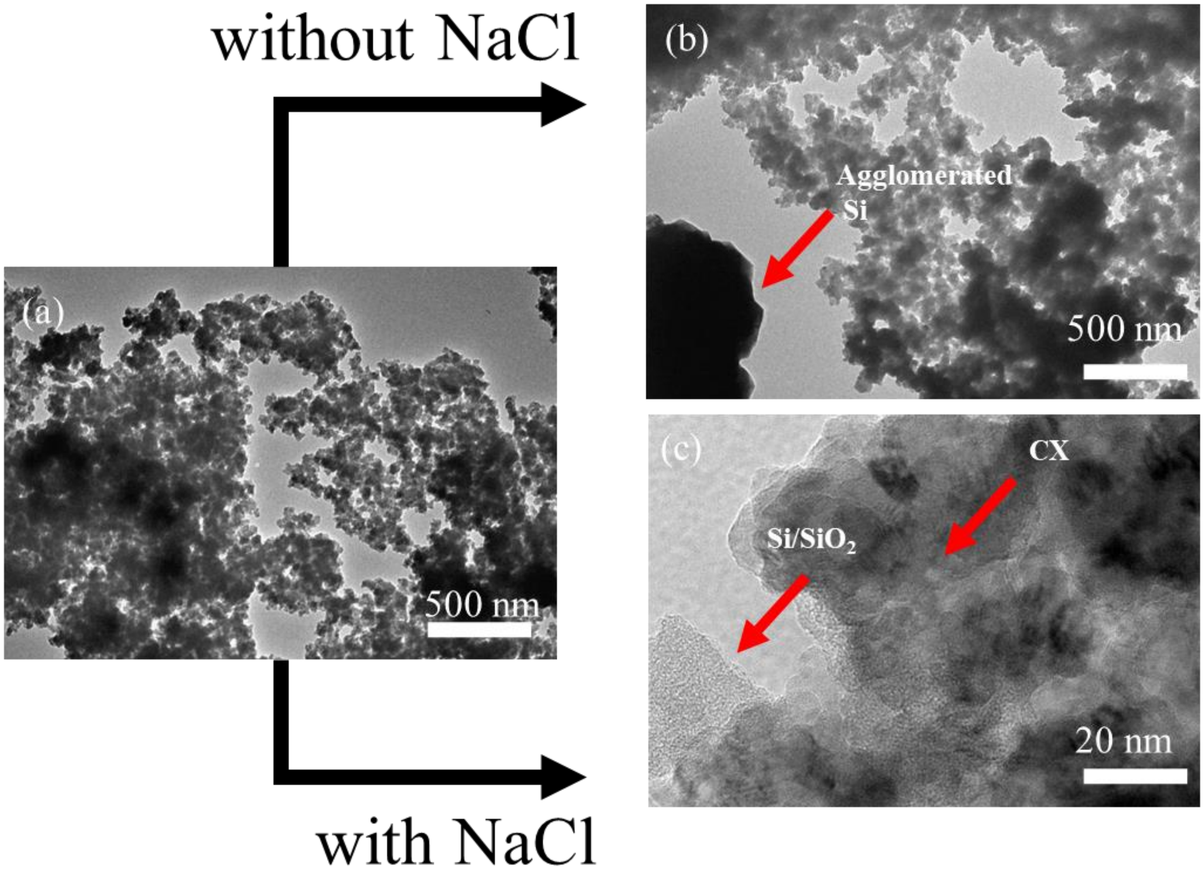

Figure 4.4 – (a) TEM micrograph of the (a) CXS-S1 before magnesiothermal reduction. TEM micrographs of (b)the rCXS-S1n sample (without NaCl as a heat scavenger) and (c) rCXS-S1 (with NaCl as a heat scavenger) after magnesiothermal reduction with the silicon, silicon dioxide, and CX phases indicated by the red arrows.

TEM micrographs of the CXS-TEOS sample (*i.e.* before magnesiothermal reduction) are shown in Figure 4.5. The deposited material from the TEOS condensation is identifiable by the notably different texture from the CX. Therefore, it is likely that the TEOS was able to successfully deposit silica, or at least some material, into the CX.

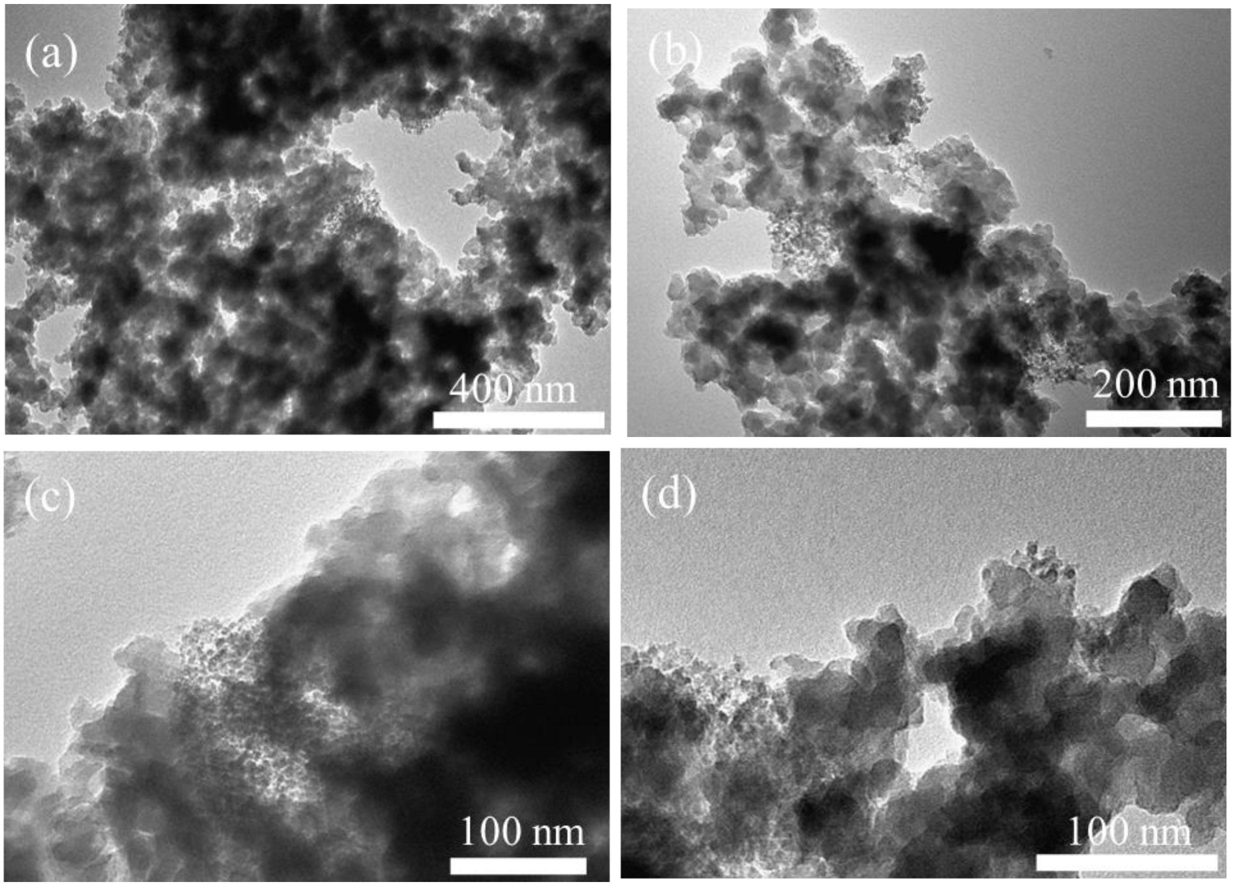

Figure 4.5 – TEM micrographs of CXS-TEOS sample synthesized *via* the magnesiothermal reduction of silica formed by *in situ* hydrolysis and condensation of TEOS with NaCl as a heat scavenger. at various magnifications.

TEM micrographs at various magnifications of the rCXS-TEOS sample after magnesiothermal reduction using NaCl as a heat scavenger are shown in Figure 4.6. The micrographs seem to only show a single material given that there is no difference in textures, unlike what is shown in the micrographs of the unreduced CXS-TEOS sample. It is unclear if the material was lost during magnesiothermal reduction, converted to something else, or is simply indistinguishable from the CX phase once it was converted into silicon.

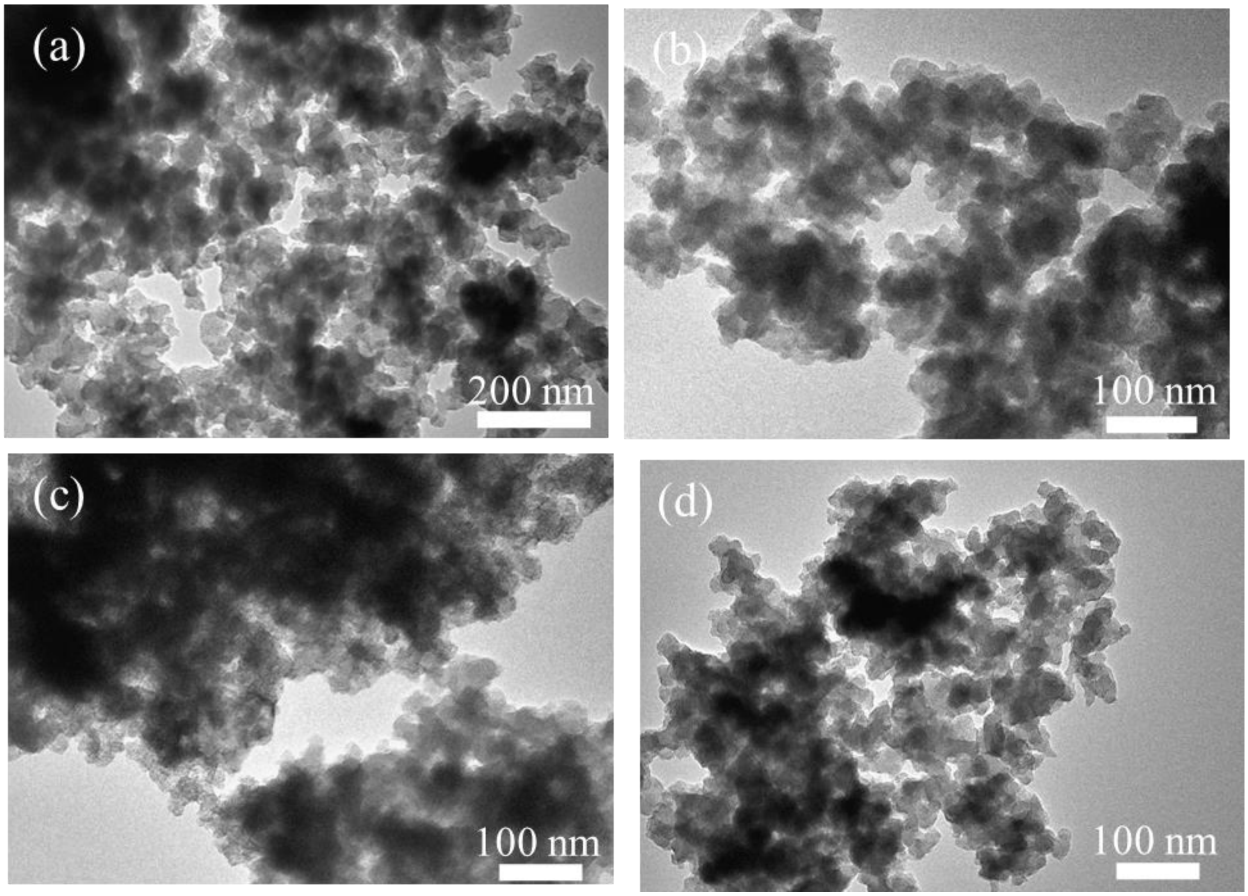

Figure 4.6 – TEM micrographs of rCXS-TEOS sample synthesized *via* the magnesiothermal reduction of silica formed by *in situ* hydrolysis and condensation of TEOS with NaCl as a heat scavenger.

Nitrogen adsorption-desorption

Nitrogen adsorption-desorption analysis was conducted on the CX, rCXS-S1, and rCXS-TEOS samples. The N_2 isotherms on the CX, rCXS-S1, and rCXS-TEOS samples are shown in Figure 4.7a. The corresponding micropore (S_{micro}) and meso/macropore (S_{ext}) surface areas of all samples are shown in Figure 4.7b per gram of the total sample (CX + Si/SiO_2). The isotherm of the CX without any dopant resembles a type I/II isotherm, which corresponds to a macroporous material that also includes micropores. The total specific surface area (S_{BET}) of the bare CX was measured to be 652 m^2 g^{-1} with a S_{micro} and S_{ext} of 498 m^2 g^{-1} and 153 m^2 g^{-1}, respectively. This gives a material where 76% of the surfaces are microporous surfaces. The S_{BET} of the rCXS-S1 sample was measured to be 178 m^2 g^{-1} with a S_{micro} and S_{ext} of 102 m^2 g^{-1} and 76 m^2 g^{-1}, respectively. This gives a material that contains 57% as microporous surfaces. The S_{BET} was found to be 366 m^2 g^{-1} with a S_{micro} and S_{ext} of 191 m^2 g^{-1} and 175 m^2 g^{-1}, respectively.

Since it is not possible to measure the reduced silicon nanoparticles independently, the specific surface area of the silica nanoparticles received from the supplier will be used. The specific BET surface area, S_{BET}, of the silica nanoparticles before magnesiothermal reduction are quoted to be approximately 640 m^2 g^{-1}. By considering that the specific surface area of a spherical silica nanoparticle with a diameter of 15 nm would have a surface area of 140 m^2 g^{-1}, the amount of microporous surface area, S_{micro}, can then be estimated to be approximately 500 m^2 g^{-1} in sample by subtracting 140 m^2 g^{-1} from 640 m^2 g^{-1}. This yields a material that has 52% microporous surfaces. A summary of these values is given in Table 4.1.

For the rCXS-S1, a change in the morphology of the CX and silica nanoparticles must have occurred as a result of the reaction of the magnesium and silica given that both the meso/macro-pore surface area and the micropore surface area decreased significantly as compared to the bare CX. However, it is unclear by which mechanism the surface area of the CX has been altered given that the silica that was used in the rCXS-S1 sample was in form of previously-synthesized nanoparticles. It is possible that if the reaction temperature increased locally above 700°C, the silica phase may have locally melted or deformed, which may have caused the microporosity to be lost.

For the rCXS-TEOS sample, however, a large reduction of microporous surface area was observed while the meso/macro-pore surface area slightly increased. This suggests that the silica precursor was able to either block or fill in the micropores of the CX. This model is supported by the measured microporous and meso/macro-porous surface area of the rCXS-TEOS sample. It is likely that the deposited material from the silica precursor is, in fact, occupying the micropores of the CX in the rCXS-TEOS sample, given that the amount of microporous surface area was reduced as compared to the bare CX.

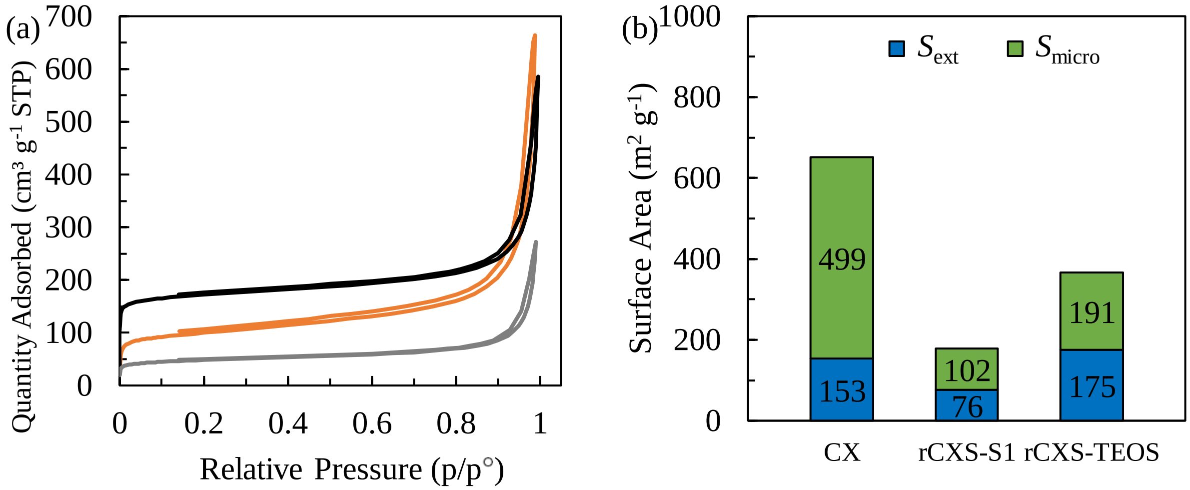

Figure 4.7 – (a) N_2 adsorption/desorption isotherms for (▬) CX, (▬) rCXS-S1, and (▬) rCXS-TEOS. (b) Corresponding specific surface separated into microporous surface area (S_{micro}) and meso/macroporous surface area (S_{ext}) per gram of the total sample (CX + Si/SiO_2).

Table 4.1 – Nitrogen adsorption-desorption data for the CX, rCXS-S1, rCXS-TEOS, and SiO_2 NPs powders

Sample	**S_{micro}** m² g⁻¹	**S_{ext}** m² g⁻¹	**S_{BET}** m² g⁻¹	**% microporous surfaces**
CX	499	153	653	76%
rCXS-S1	102	76	176	57%
rCXS-TEOS	191	175	366	52%
SiO_2 NPs	500[a]	140[a]	640[b]	78%

[a]Values calculated considering the BET surface area given by the supplier and the theoretical external surface area calculated for a silica nanoparticle with a diameter of 15 nm. [b]Value given by the supplier.

X-ray diffraction

XRD patterns were collected for the CX, CXS-S1, CXS-TEOS, rCXS-S1, and rCXS-TEOS samples. Figure 4.8 shows the difference in the XRD responses between the bare CX, CXS-S1, and CXS-TEOS (*i.e.* the CX-silica samples before magnesiothermal reduction). The XRD pattern of the bare CX exhibits three very wide peaks at 2θ angles of approximately 15°, 30°, and 42° corresponding to interplanar spacing, *via* Bragg's Law, of 0.261 nm, 0.517 nm, and 0.765 nm, respectively. The first two peaks are likely related to the interplanar spacing of the graphitic sheets of the carbon xerogel, *i.e.* the C(002) planar direction [23-25]. Normally in a graphitic material, the (002) diffraction peak would be located at a 2θ angle of 26° for the X-ray source used in these experiments. Interestingly, however, the CX exhibits two (002) diffraction peaks. This suggests that there is roughly two populations of C(002) interplanar spacing in the material. The peak at 15° may be related to oxygenate graphitic sheets, similar to graphene oxide or graphite oxide, while the peak at 30° may be just related to the amorphous nature of the CX [24, 25]. The peak at a 2θ angle of 42° likely corresponds to the C(001). These three peaks are not well-defined, which suggests that the CX is, in fact, an amorphous carbon with no well-defined crystallographic plane spacing between graphitic layers. The CXS-S1 sample exhibits a slightly modified XRD response between the 2θ angles of 10° and 30°. This modification is likely related to the S1 silica dopant, which is likely amorphous cristobalite, which would exhibit a broad diffraction response around a 2θ angle of 20° [26-28].

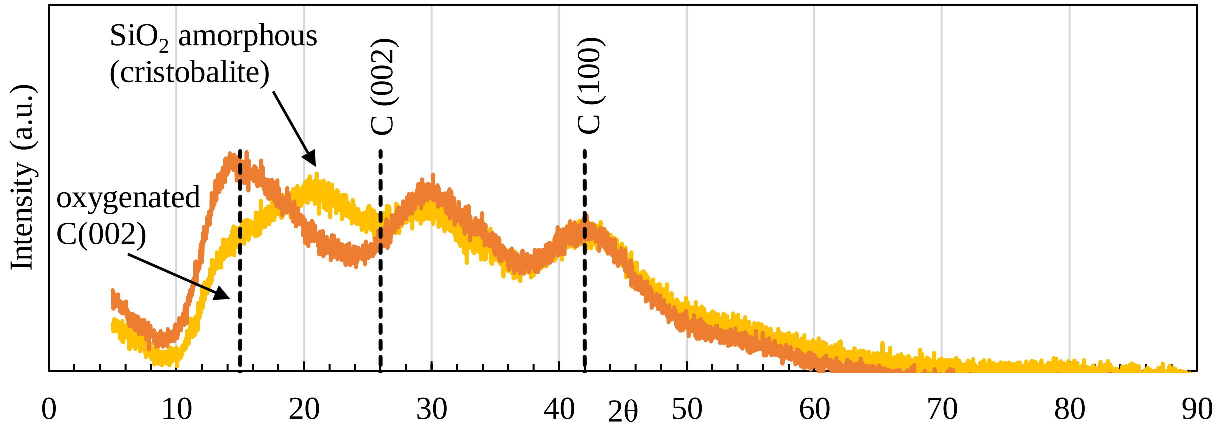

Figure 4.8 – XRD patterns of (▬) CX, (▬) CXS-S1. The oxygenated C(002), C(002), and C(100) diffraction peaks are labelled with a dotted line. The peak of amorphous silica, likely cristobalite, are also labeled with an arrow.

XRD pattern of the rCXS-S1 sample before and after the HCl treatment is shown in Figure 4.9. The XRD pattern of the rCXS-S1 sample before the HCl treatment clearly shows the presence of both crystalline silicon and MgO, which are the products of the magnesiothermal reduction reactions shown in Equations 1.1 and 1.2. Silicon diffraction peaks at 2θ angles of 28.4°, 47°, 56°, and 89° correspond to the Si(111), Si(220), Si(311), Si(422) crystallographic planes, respectively [29, 30]. The silicon diffraction peaks at 2θ angles of 69.1° and 76.3° corresponding to the Si(400) and Si(331) crystallographic planes, respectively, were also observed, but were very weak [29, 30]. The MgO diffraction peaks at 2θ angles of 40°, 43°, 62°, and 78° likely correspond to the MgO(111), MgO(200), MgO(220), MgO(222) crystallographic planes, respectively [31]. After the HCl treatment, however, the MgO diffraction peaks vanished, which is evidence that the selective etching of MgO by the HCl was successful. There is also evidence that some amount of silica persists in the rCXS-S1 sample given that the XRD pattern of the rCXS-S1 sample after HCl treatment seems to retain the same XRD response between 2θ angles of 10° and 30°, corresponding to the response of the amorphous silica. However, it is inconclusive whether or not some amorphous silica persists in the rCXS-1 sample.

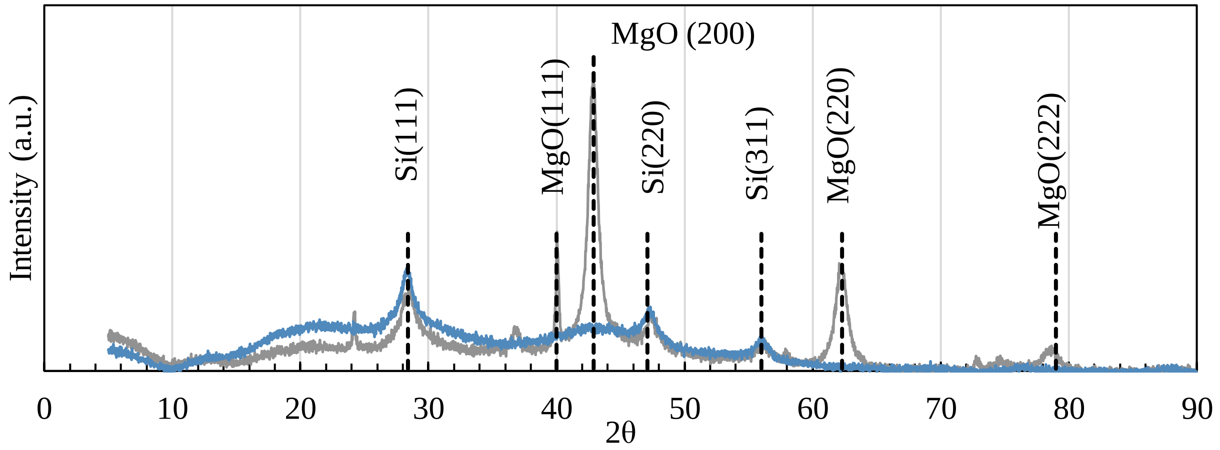

Figure 4.9 – XRD patterns of rCXS-S1 (▬) before and (▬) after HCl treatment. These spectra both confirm the presence of silicon and the selective etching of MgO by HCl.

The crystallite size broadening and microstrain broadening of the rCXS-S1 sample after HCl treatment was determined *via* the Williamson-Hall plot and is shown in Figure 4.10. The silicon diffraction peaks at 2θ angles of 69.1° and 76.3° corresponding to the Si(400) and Si(331) crystallographic planes, respectively, were not considered given their very weak response and the difficulty to accurately fit the peaks to determine the peak broadening. The silicon crystallite size, determined considering the y-axis intercept of the least squares regression fit, was 6.1 nm. This value corresponds well with the size of the precursor silica nanoparticles (5-20 nm) that were used in the synthesis. The micro-strain in the crystal lattice, determined *via* the slope of the least squares regression fit, was found to be < -0.5%. Negative values for microstrain seem to be related to either systemic error in the peak fitting or possibly anisotropy in the strain for different crystallographic directions. However, it is likely that there is no microstrain within the silicon phase given that the microstrain is relatively small, similar to that of the silicon nanoparticles in Chapters 2 and 3 which showed approximately the same amount of microstrain, albeit with a positive value. The absence of microstrain in the rCXS-S1 sample may be a result of the high temperature during the magnesiothermal reduction step, which allows for a relaxation of stresses within the silicon phase.

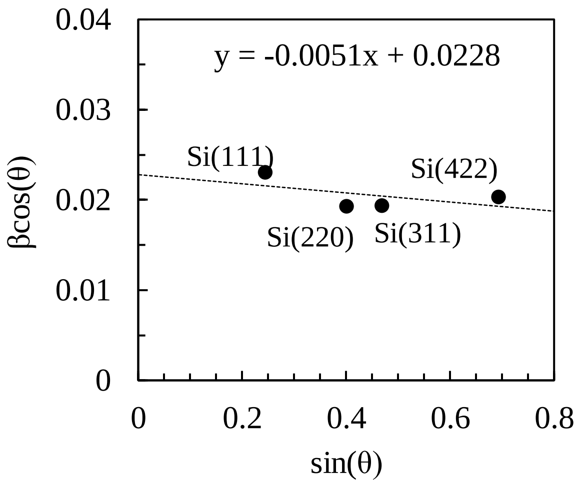

Figure 4.10 – Williamson-Hall plot of the silicon diffraction peaks in the rCXS-S1 sample after HCl treatment.

Figure 4.11 shows the XRD response of the CXS-TEOS and rCXS-TEOS samples. The rCXS-TEOS spectrum shows only weak diffraction peaks at 2θ angles of 29°, 36°, and 56° related to the Si(111), Si(220), and Si(311) crystallographic planes, respectively. The silicon diffraction peaks at 2θ angles of 69.1° and 76.3° corresponding to the Si(400) and Si(331) crystallographic planes, respectively, were similarly weak or not observed. This suggests that only a very small quantity of silicon may have been produced during the synthesis process. The appearance of various small diffraction peaks at 2θ angles of 31.6°, 35.7°, 45.4°, 60°, and 72° suggests that at least some of the amorphous silica was transformed into other types of crystalline silica (*i.e.* quartz, cristobalite, tridymite, *etc.*) or other carbon-silicon compounds rather than into silicon [26-28].

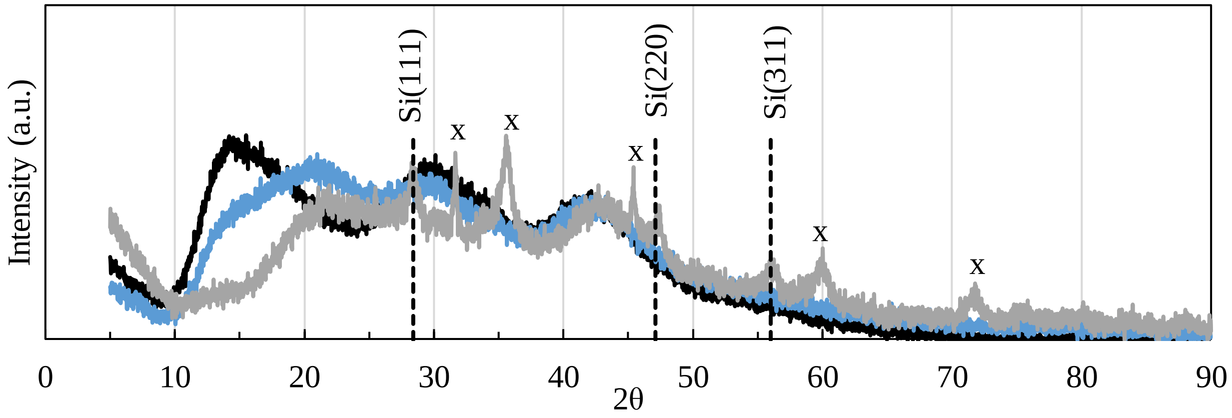

Figure 4.11 – XRD patterns of samples (▬) CXS-TEOS, and (▬) rCXS-TEOS after HCl treatment. The diffraction peaks labelled with an "x" are likely related to various types of crystalline silica or carbon-silicon compounds.

4.3.2 Electrochemical characterization

Cyclic voltammetry

CV measurements were conducted on composite electrodes with CX, rCXS-S1, and rCXS-TEOS as the active material with PSS as a binder; Figure 4.12 shows the curves corresponding to the 1st, 5th, and 10th cycles. Quite similar results (not shown) were obtained for the composite electrodes with PVDF as a binder. The current measurements were normalized with respect to the mass of active material in order to compare the responses between the composite electrodes.

The CV response for the CX composite electrode is reproduced in Figure 4.12a for comparative purposes. The 1st cycle of the CX composite electrode shows three peaks at 1.3 V (peak 1), 0.6 V (peak 2), and ~0 V (peak 3) *vs.* Li^+/Li [32-37]. The Li^+ ion insertion (lithiation) peaks during the 1st cycle at 1.3 V and 0.6 V *vs.* Li^+/Li may be attributed to either SEI formation or possibly to the trapping of Li^+ ions within the carbon xerogel. Indeed, SEI layers on carbon materials have been shown to form due to the instability of the electrolyte below approximately 1.3 V *vs.* Li^+/Li [32-37]. The underlying response that spans along the entire voltage window during lithiation, reaching a minimum at ~0 V *vs.* Li^+/Li, likely corresponds to the insertion of Li^+ ions into the CX [8]. The wide Li^+ ion insertion window may be attributed to both the mesoporous structure of CX as well as the amorphous nature of the CX, as supported by the XRD measurements in this work and previous studies [6-9]. This wide Li^+ ion insertion response, and similar Li^+ ion de-insertion response, is contrary to conventional graphitic electrodes that have a narrow Li^+ ion insertion and de-insertion potential as a result of the regular spacing between graphitic layers.

Figure 4.12b shows the CV response for the rCXS-S1 composite electrode. Li^+ ion insertion (lithiation) during the 1st cycle exhibits a peak at 0.7 V *vs.* Li^+/Li, (peak 4), which is likely related to SEI formation on the silicon phase. This SEI formation peak is slightly different than the SEI formation peaks of the CX composite electrode, which were located at approximately 1.3 V and 0.6 V *vs.* Li^+/Li. The strong Li^+ ion de-insertion (delithiation) peak observed below 0.1 V *vs.* Li^+/Li (peak 5) is likely related to the initial alloying of crystalline silicon with lithium [32-37]. Previous studies have come to similar conclusions regarding the initial electrochemical silicon-lithium alloying peaks [37]. During the 1st delithiation, peaks between 0.3 V and 0.6 V *vs.* Li^+/Li (peak 6) are related to the de-alloying (Li^+ ion de-insertion) of lithium from silicon [37]. During the 5th and 10th cycles, similar de-alloying (Li^+ ion de-insertion) peaks are observed; however, an alloying (Li^+ ion insertion) peak appears at approximately 0.2 V *vs.* Li^+/Li (peak 7), which has been attributed to the lithiation of amorphous silicon [37]. The silicon lithiation/delithiation peaks are noticeably weaker than for active material synthesized directly with silicon nanoparticles (see Figure 2.9/c in Chapter 2). This may be a sign that the silicon phase formed in this synthesis are less stable or less available to lithiation than for CX-silicon active materials composed of commercial silicon nanoparticles.

Figure 4.12c shows the CV response for the rCXS-TEOS composite electrode. The silicon SEI formation peak that is present in the rCXS-S1 composite electrode at 0.6 V *vs.* Li$^+$/Li is not observed for the rCXS-TEOS composite electrode. The silicon lithiation/delithiation formation peaks that are present in the rCXS-S1 composite electrode are not observed for the rCXS-TEOS composite electrode for any cycle as well. This suggests that either no silicon was formed during the synthesis procedure or that the silicon is inaccessible to lithiation. The lithiation (Li$^+$ ion insertion) peak below 0.1 V *vs.* Li$^+$/Li is the only peak observed as well as the wide, albeit weak underlying lithiation/delithiation response of the CX.

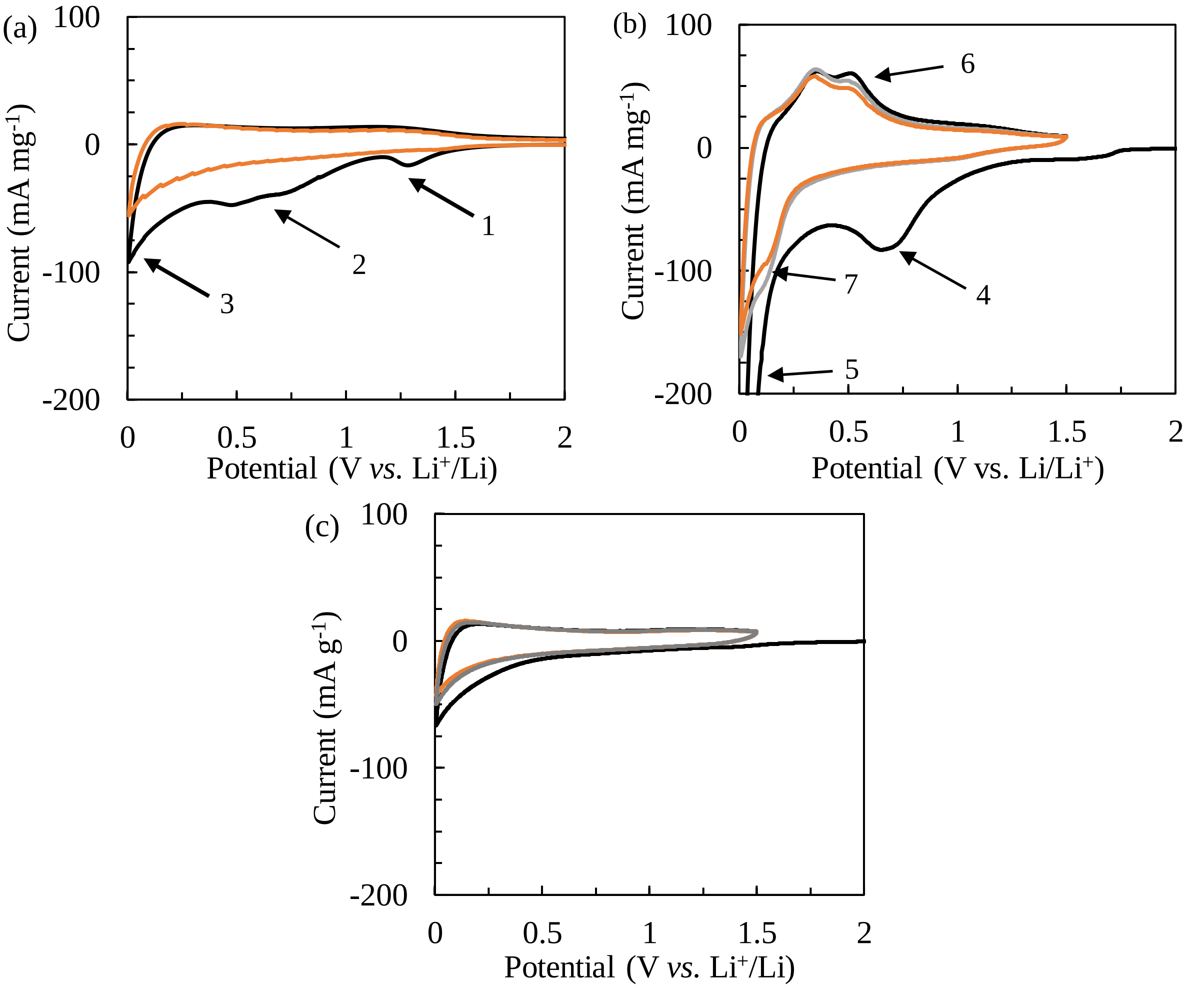

Figure 4.12 – Cyclic voltammetry of (a) the bare CX, (b) rCXS-S1 and (c) rCXS-TEOS composite electrodes with PSS as a binder. (▬) 1st cycle, (▬) 5th cycle, and (▬) 10th cycle. The scan rate was 50 µV s^{-1} between 0.005 V and 3 V or 1.5 V *vs.* Li$^+$/Li. Current is normalized per unit mass of active material.

Galvanostatic cycling

The galvanostatic cycling of the rCXS-S1 and rCXS-TEOS composite electrodes are given in Figure 4.13a and b, respectively. The specific capacity of the rCXS-1 composite electrode with PSS as a binder quickly decreased during cycling: it retained only 50% of the 1st cycle capacity after 20 cycles. Furthermore, the capacity of the rCXS-S1 composite for the 1st cycle was only 600 mAh g^{-1}, which is less than the expected capacity of ~1000 mAh g^{-1} given that 100% of the silica in the CXS-S1 sample was converted into silicon in the rCXS-S1 sample. The lower than expected specific capacity suggests that either the silica was (i) not fully reduced, (ii) transformed into other by-products, or (iii) lost during some other step in the synthesis procedure. In the case that the silica was not fully reduced or transformed into other inactive by-products, such as Mg_2Si, stresses between the active silicon and inactive silica and Mg_2Si likely cause the active material to pulverize and form an unstable SEI during cycling. Since the silicon volume changes during lithiation and delithiation, stresses between the inactive silica and other inactive by-products likely cause the similar pulverization of the dopant material. The presence of the amorphous silica diffraction response in the rCXS-S1 sample XRD pattern suggests that this option is the most likely; however, further verification would be needed, such as with TGA analysis, to confirm this hypothesis.

Galvanostatic cycling conducted on the rCXS-TEOS composite electrode is shown in Figure 4.13b. The cycling of this composite electrode with either PSS or PVDF as a binder exhibited a significant decrease in specific capacity during cycling as compared to the bare CX. The specific capacity of the rCXS-TEOS composite electrode with PSS or PVDF as a binder was measured to be about 100 mAh g^{-1} and 40 mAh g^{-1}, respectively, as compared to 200 mAh g^{-1} for the bare CX composite electrode. This result suggests that although silica may have been deposited into the CX, as confirmed by the XRD analysis and TEM micrographs, the silica was not able to be transformed into silicon, and therefore remained as inactive material. This would effectively reduce the specific capacity of the composite electrode since the silica, or whichever material resides in the active material after the magnesiothermal reductions step, would act as an inactive mass. Therefore, the capacity would be expected to decrease by half if half of the mass in the active material is actually inactive.

The lower capacity for the rCXS-TEOS composite electrode with PVDF as a binder as compared to the composite electrode with PSS as a binder also suggests that PSS is able to act as an active material, as was shown in Figure 3.11a in Chapter 3. Another possible explanation for the higher capacity exhibited by the rCXS-TEOS composite electrode with PSS as a binder is that the PSS allows for better charge transfer characteristics between the active material and the electrolyte. This phenomenon will be explored in the following section on EIS analysis.

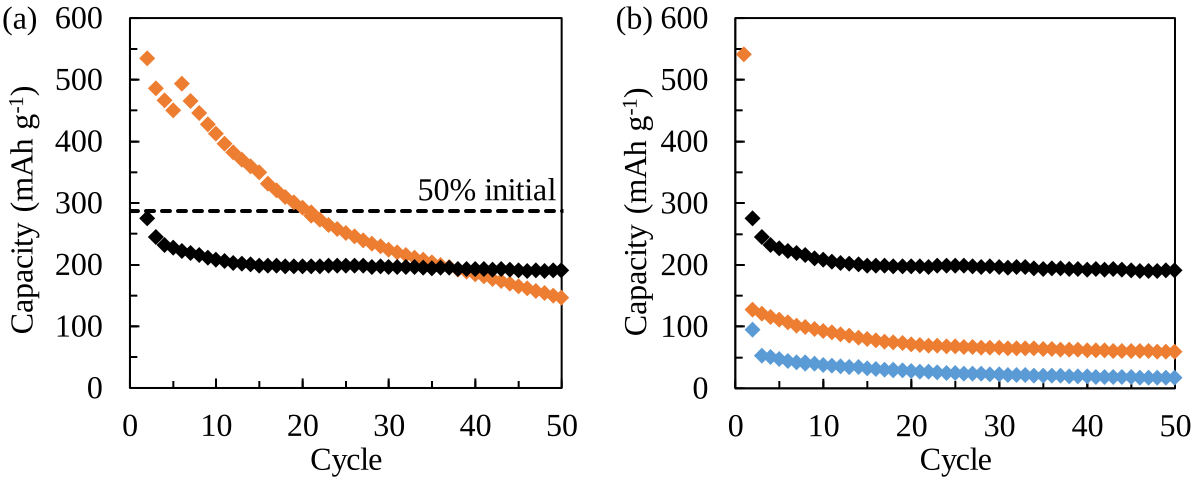

Figure 4.13 – (a) Galvanostatic cycling of the (◆) CX and (◆) rCXS-S1 composite electrodes with PSS as a binder. (---) 50% of initial capacity. (b) Galvanostatic cycling of the (◆) CX with PSS as a binder and the rCXS-TEOS composite electrode with either (◆) PSS as a binder or (◆) PVDF as a binder. Note: Capacity of composite electrodes are calculated on a mass of active material basis (*i.e.* CX + Si/SiO_2).

Electrochemical impedance spectroscopy

EIS spectra for the rCXS-S1 and rCXS-TEOS composite electrodes with PSS as a binder are shown in Figure 4.14a and b and Figure 4.15a and b, respectively, for the pristine, 1st, 5th, 20th, and 50th cycles in order to observe how the electrode changes during cycling. EIS spectra. Similar results were obtained for the samples with PVDF as a binder. The Randles cell electrochemical model is shown in Annex 2, which outlines the pertinent electrochemical elements, such as ESR, charge transfer resistance (R_{ct}) and capacitance (C_d), and diffusion characteristics, that should apply to these CX-based half cells.

For both rCXS-S1 and rCXS-TEOS composite electrodes, the impedance response of the 1st cycle exhibits a high R_{ct} and capacitor-like response at the low frequency; indeed, the phase shift approaches -90°, as shown in the respective Bode diagrams (Figure 4.14b and Figure 4.15b). This behavior suggests that, in this state, the electrodes behave more like a capacitor, and therefore resemble a model more close to the one presented in Figure 1.7 in Chapter 1. This may be due to the fact that an SEI has not yet been formed between the active materials and the electrolyte and, therefore, diffusion into the active material is inhibited [38].

In the subsequent cycles, however, the phase shift in the low frequency region for the rCXS-S1 and rCXS-TEOS composite electrodes, shown in the Bode plot in Figure 4.14b and Figure 4.15b, respectively, exhibited two different responses. The rCXS-S1 composite electrode showed a phase shift of -45°, which is characteristic of a Warburg impedance, and therefore, the model shown in

Annex 2 could be an appropriate model for these electrodes. It is therefore possible that the formation of the SEI after the 1st cycle enhances the diffusion of Li^+ ion into the active material. Contrarily, the low frequency response of the rCXS-TEOS composite electrode showed a phase shift that approaches -90°, similar to the 1st cycle response. This is a sign that the diffusion of Li^+ ions may have stayed inhibited, even after the 1st cycle discharge. This result, in addition to the absence of the SEI formation peak in the CV measurements (see Figure 4.12c) and low cycling performance, shown in Figure 4.13b suggests that a stable SEI was not formed on these electrodes or that Li+ ions do not diffuse into a significant portion of the active material.

The ESR progressively decreases as a function of cycles for both composite electrodes (Figure 4.14c and Figure 4.15c). The slight decrease in the ESR that is observed is likely related to the improved wetting of the active layer by the electrolyte; however, this conclusion is not definitive.

For the rCXS-S1 composite electrode, the R_{ct} and C_d per total specific surface area progressively decreased and increased, respectively, between the 1st and 50th cycles (Figure 4.14d.). The decrease in the R_{ct} between the pristine and 1st cycle is further evidence that an SEI layer had been formed, which facilitates the charge transfer between the electrolyte and active material. Subsequent cycles also show a decrease in the R_{ct} and increase in the C_d which is a sign of better charge transfer properties between the active layer and electrolyte. This response is likely related to the pulverization of the active layer, which is caused by the silicon instability during cycling. The pulverization forms smaller particles that allows more facile transport of charge with the electrolyte.

For the CXS-TEOS composite electrode, a relatively stable R_{ct} and C_d per total specific surface area is evidence that no lithiation or delithiation of silicon occurs. This is evidence that unreduced silica or some other inactive material persists in the active material that causes the composite electrode to remain stable in the EIS measurements and show a reduced capacity, as shown in Figure 4.13b.

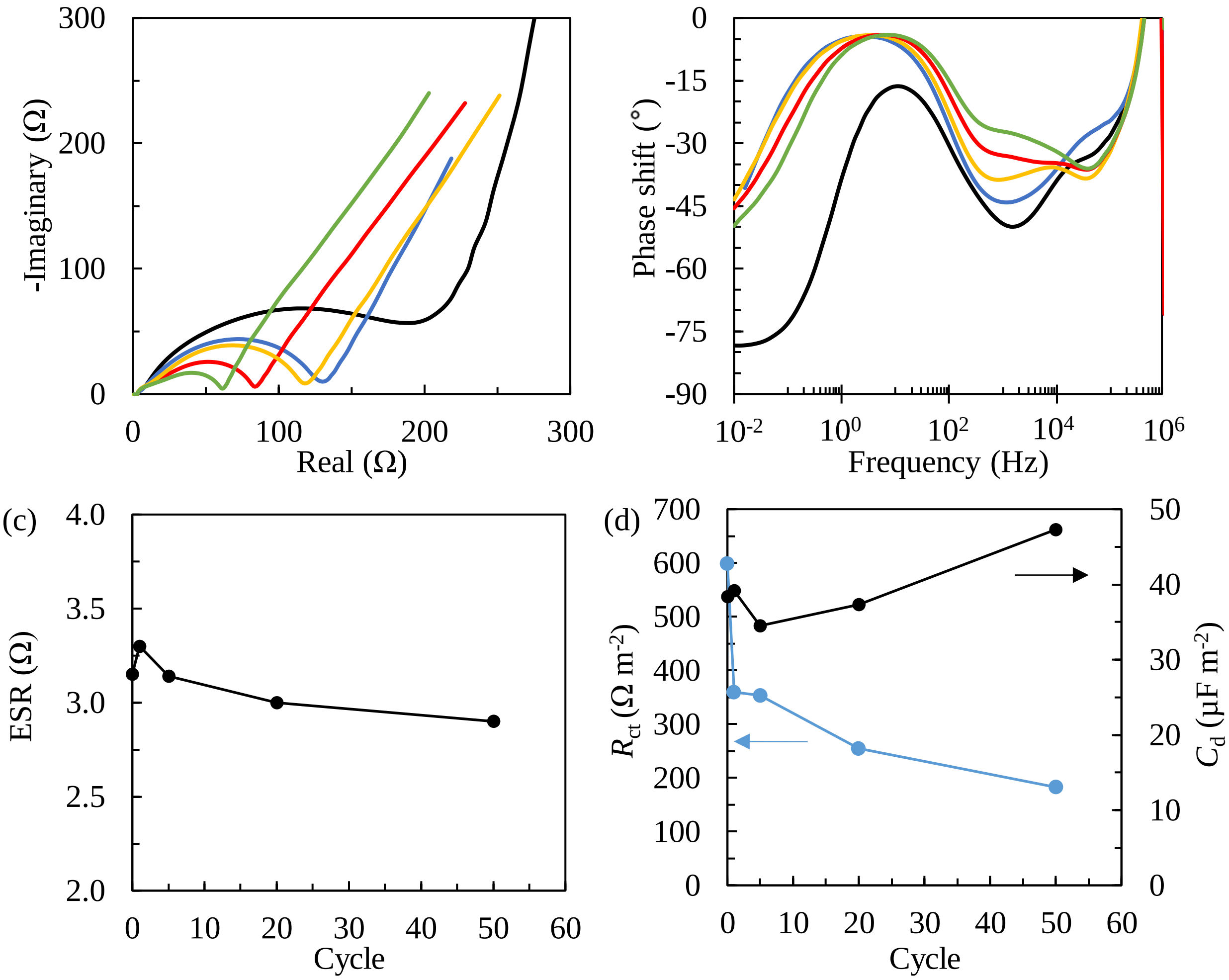

Figure 4.14 – Electrochemical impedance spectroscopy of an rCXS-S1 composite electrode with PSS as a binder. (a) Nyquist plot and (b) phase shift diagram: (▬) Pristine, (▬) 1st cycle, (▬) 5th cycle, (▬) 20th cycle, and (▬) 50th cycle. (c) ESR as a function of galvanostatic cycles. (d) Charge transfer resistance (R_{ct}) and charge transfer capacitance (C_d) per total specific surface area as a function of galvanostatic cycles. Scan between 1 MHz and 100 mHz with 10 points per decade. Voltage amplitude of 10 mV.

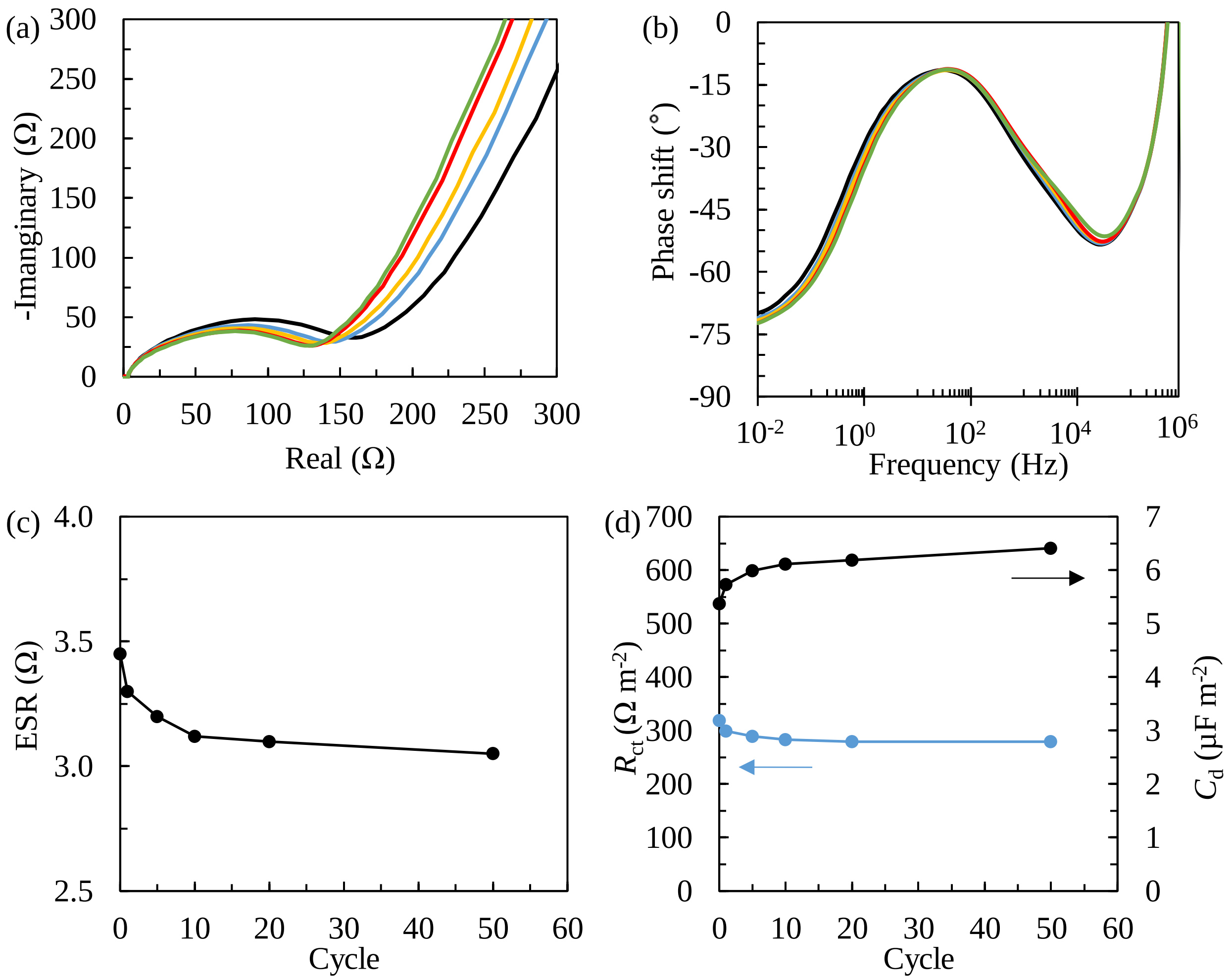

Figure 4.15 – Electrochemical impedance spectroscopy of rCXS-TEOS composite electrode with PSS as a binder. (a) Nyquist plot and (b) phase shift diagram: (▬) Pristine, (▬) 1st cycle, (▬) 5th cycle, (▬) 20th cycle, and (▬) 50th cycle. (c) ESR as a function of galvanostatic cycles. (d) Charge transfer resistance (R_{ct}) and charge transfer capacitance (C_d) per total specific surface area as a function of galvanostatic cycles. Scan between 1 MHz and 100 mHz with 10 points per decade. Voltage amplitude of 10 mV.

4.4 Conclusion

Two CX-silicon active materials were synthesized *via* the magnesiothermal reduction of two different silica precursors. The first material, rCXS-S1, was synthesized by impregnating previously-synthesized silica nanoparticles with a diameter between 5 and 15 nm into a CX. The second material, rCXS-TEOS, used a liquid silica precursor, TEOS, which was infiltrated into the porosity of the CX. The TEOS then underwent hydrolysis and condensation into silica within the CX. These active materials subsequently underwent magnesiothermal reduction of the impregnated silica into silicon. The magnesiothermal reduction was conducted in the presence of NaCl that was deposited within the sample, which acted as a heat scavenger to maintain the reaction temperature below the melting point of silicon, in order to preserve the nanostructure of the parent silica.

For the rCXS-S1 sample, the presence of silicon and unreacted silica after magnesiothermal reduction was confirmed *via* TEM imaging and XRD analysis. Broadening of the silicon diffraction peaks in the XRD patterns also suggests that the silica nanoparticles retained their nanostructured morphology after their conversion into silicon. This indicates that the NaCl successfully acted as a heat scavenger during the magnesiothermal reduction step. TEM micrographs of the rCXS-S1 sample confirmed the presence of silicon by comparing the micrographs of the bare CX, silica nanoparticles, and the rCXS-S1 sample. The selective removal of MgO from the rCXS-S1 sample *via* washing with HCl was also confirmed *via* XRD analysis. Electrochemical characterization of the rCXS-S1 sample showed that, although silicon was present, the precursor silica may not have been fully reduced into silicon during the magnesiothermal reduction. Galvanostatic cycling of the rCXS-S1 sample show only a capacity of 600 mAh g^{-1} when the expected capacity should have been closer to 1000 mAh g^{-1}. This suggests that the silica was either not fully reduced during the magnesiothermal reduction or transformed into other by-products. Likewise, the silica could have been lost during some other step in the synthesis procedure, such as during the washing or HCl treatment steps. In any case, cyclic voltammetry measurements clearly show redox peaks associated with silicon lithiation and delithiation.

For the rCXS-TEOS sample, TEM imaging of the unreduced sample, CXS-TEOS, gave evidence of the presence of silica in the CX. These images showed the presence of some other material dispersed throughout the CX support structure, as identified by the difference in texture, shape, and size as compared to the bare CX micrographs. However, this material was not definitely confirmed to be silica. XRD analysis of the rCXS-TEOS sample did give further evidence for the presence of crystalline silica, however, these silica XRD peaks were relatively weak. XRD analysis of the rCXS-TEOS sample also showed that little, if any, silicon was formed, given the lack of any prominent silicon or MgO diffraction peaks. Galvanostatic cycling of electrodes with the rCXS-TEOS sample showed a reduced a capacity of only 100 mAh g^{-1} for the composite electrode with

PSS as a binder when the expected capacity should have been closer to 1000 mAh g^{-1}. This suggests that there may have been silica in the sample that was not reduced during the magnesiothermal reduction, which would effectively reduce the capacity of the composite electrode to less than the CX by itself. Cyclic voltammetry measurements showed no redox peaks associated with silicon lithiation and delithiation. Furthermore, EIS analysis suggest that Li^+ ion diffusion into the rCXS-TEOS composite electrode with PSS as a binder may have been limited by some process given the absence of evidence that an SEI was formed.

Overall, it has been shown that the magnesiothermal reduction of silica into silicon can in fact be carried out within a carbon xerogel. Further study into the best synthesis procedure for TEOS-derived silica is needed to take advantage of this unique synthesis technique.

4.5 References

[1] J. Sakabe, N. Ohta, T. Ohnishi, K. Mitsuishi, and K. Takada, Porous amorphous silicon film anodes for high capacity and stable all-solid-state lithium batteries, Comm. Chem. 1 (2018) 1 – 24.

[2] D. Ma, Z. Cao, and A. Hu, Si-based anode materials for li-ion batteries: A mini review, Nano-Micro Lett. 6 (2014) 347–358.

[3] B. Liang, Y. Liu, and Y. Xu, Silicon-based materials as high capacity anodes for next generation lithium ion batteries, J. Power Sources 267 (2014) 469-490.

[4] R. A. Huggins, Lithium alloy negative electrodes. J. Power Sources 81 (1999) 13-19.

[5] S.N. Houseman, T.J. Bartik, and T. J. Sturgeon, (2015) Measuring manufacturing: How the computer and semiconductor industries affect the numbers and perceptions, in: Measuring Globalization: Better Trade Statistics for Better Policy, Upjohn Institute for Employment Research.

[6] M.-L. Piedboeuf, A.F. Léonard, K. Traina, and N. Job, Influence of the textural parameters of resorcinol–formaldehyde dry polymers and carbon xerogels on particle sizes upon mechanical milling, Colloid Surface A 471 (2015) 124-132.

[7] N. Job, R. Pirard, J. Marien, and J.P. Pirard, Porous carbon xerogels with texture tailored by pH control during sol–gel process, Carbon 42 (2004) 619-628.

[8] N. Rey-Raap, M.L.C. Piedboeuf, A. Arenillas, J.A. Menéndez, A.F. Léonard, and N. Job, Aqueous and organic inks of carbon xerogels as models for studying the role of porosity in lithium-ion battery electrodes, Mater. Design 109 (2016) 282-288.

[9] W.O. Filtvedt, A. Holt, P.A. Ramachandran, and M.C. Melaaen, Chemical vapor deposition of silicon from silane: Review of growth mechanisms and modeling/scaleup of fluidized bed reactors. Sol. Energ. Mat. Sol. C 107 (2012) 188-200.

[10] A.F.B. Braga, S.P. Moreira, P.R. Zampieri, J.M.G. Bacchin, and P.R. Mei, New processes for the production of solar-grade polycrystalline silicon: A review. Solar Energy Materials and Solar Cells 92, 4 (2008) 418-424.

[11] J. Doyle, R. Robertson, G. H. Lin, M. Z. He, and A. Gallagher. Production of high-quality amorphous silicon films by evaporative silane surface decomposition. Journal of Applied Physics 64 (1988) 3215-3223.

[12] J. Lim, S.W. Ha, and J.K. Lee, Precise size-control of silica nanoparticles *via* alkoxy exchange equilibrium of tetraethyl orthosilicate (TEOS) in the mixed alcohol solution. Bull. Korean Chem. Soc. 33, 3 (2012) 1067-1070.

[13] H. Xu, H. Zhang, Y. Huang, and Y. Wang. Porous carbon/silica composite monoliths derived from resorcinol–formaldehyde/TEOS. Journal of Non-Crystalline Solids 356 (2010) 971-976.

[14] User: Smokefoot, Wikipedia. Simplified representation of the condensation induced by hydrolysis of TEOS. Available:

https://en.wikipedia.org/wiki/Sol%E2%80%93gel_process#/media/File:StoberSyn.svg. Accessed on: April 4, 2021.

[15] D.H. Filsinger and D.B. Bourrie, Silica to Silicon: Key Carbothermic Reactions and Kinetics 73, 6 (1990) 1726-1732

[16] J. Entwistle, A. Rennie and S. Patwardhan. A review of magnesiothermic reduction of silica to porous silicon for lithium-ion battery applications and beyond. J. Mater. Chem. A. 6 (2018) 18344-18356.

[17] Z. Bao , M.R. Weatherspoon , S. Shian , Y. Cai, P.D. Graham, S.M. Allan, G. Ahmad, M.B. Dickerson, B.C. Church, Z.Kang, H.W. Abernathy III, C.J. Summers, M. Liu, and K.H. Sandhage. Chemical reduction of three-dimensional silica micro-assemblies into microporous silicon replicas. Nature Letters 446 (2007) 172-175.

[18] D.T. Ngo, H.T.T. Le, X.M. Pham, C.N. Park, and C.J. Park, Facile Synthesis of Si@SiC Composite as an Anode Material for Lithium-Ion Batteries. ACS Appl. Mater. Interfaces 9 (2017) 32790-32800.

[19] Z. Favors, W. Wang, H. Hosseini Bay, Z. Mutlu, K. Ahmed, C. Liu, M. Ozkan, and C.S. Ozkan. Scalable Synthesis of Nano-Silicon from Beach Sand for Long Cycle Life Li-ion Batteries. Sci. Rep. 4, (2014) 5623-5629.

[20] M. Choi, J.C. Kim, and D.W. Kim. Waste Windshield-Derived Silicon/ Carbon Nanocomposites as High Performance Lithium-Ion Battery Anodes. Scientific Reports 8 (2018) 960-971.

[21] I. Hong, B. Scrosati, and F. Croce, Mesoporous, Si/C composite anode for Li battery obtained by 'magnesium-thermal' reduction process. Solid State Ionics 232, (2013) 24-28.

[22] A. Nadiradze, I. Baratashvili, I. Pulariani, and K. Ukleba, Thermodynamic Probability of Realization of the Process of Silicon Dioxide Reduction by Magnesium at High Temperatures. Bull. Georg. Natl. Acad. Sci 3, 2 (2009) 95-99.

[23] B. Kartick, S. K. Srivastava, and I. Srivastava, Green Synthesis of Graphene. J. of Nanoscience and Nanotechnology 13 (2013) 4320-4324.

[24] G. Wang, J. Yang, J. Park, X. Gou, B. Wang, H. Liu, and J. Yao, Facile Synthesis and Characterization of Graphene Nanosheets. J. Phys. Chem. C112 (2008) 8192-8195.

[25] R. Siburian, H. Sihotang, S. Lumban Raja, M. Supeno, and C. Simanjuntak, New Route to Synthesize of Graphene Nano Sheets. Orient. J. Chem. 34, 1 (2018) 182-187.

[26] P. Velmurugan, J. Shim, K.J. Lee, M. Cho, S.S. Lim, S.K. Seo, K.M. Cho, K.S. Bang, and B.T. Oh, Extraction, characterization, and catalytic potential of amorphous silica from corn cobs by sol-gel method. J. of Industrial and Engineering Chem. 29 (2015) 298-303.

[27] U. Kalapathy, A. Proctor, and J. Shultz, A simple method for production of pure silica from rice hull ash. Bioresource Technology 73, 3 (2000) 257-262,

[28] A.L. Rivas, G. Vera, V. Palacios, M. Cornejo, A. Rigail, G. Solórzano, (2018) Phase Transformation of Amorphous Rice Husk Silica. In: Frontiers in Materials Processing,

Applications, Research and Technology. Muruganant M., Chirazi A., Raj B. (eds). Springer, Singapore.

[29] C. R. Hubbard, H.E. Swanson, and F.A. Mauer, A Silicon powder diffraction standard reference material, J. Appl. Crystl. 8 (1975) 45-48.

[30] J. Westra, V. Vavruňková, P. Sutta, R.A.C.M.M. Van Swaaij, and M. Zeman. Formation of thin-film crystalline silicon on glass observed by in-situ XRD. Energy Procedia 2 (2010) 235-241.

[31] X.H. Shi, J.J Ban, L. Zhang, Z.P. Sun, D.Z Jia, and G.C. Xu. Preparation and exceptional adsorption performance of porous MgO derived from a metal–organic framework. RSC Adv., 7 (2017) 16189-16195.

[32] F. Joho, B. Rykart, A. Blome, P. Novák, H. Wilhelm, and M.E. Spahr, Relation between surface properties, pore structure and first-cycle charge loss of graphite as negative electrode in lithium-ion batteries, J. Power Sources 97-98 (2001) 78-82.

[33] S. An, J. Li, C. Daniel, D. Mohanty, S. Nagpure, D.L. Wood III, The state of understanding of the lithium-ion-battery graphite solid electrolyte interphase (SEI) and its relationship to formation cycling, Carbon 105 (2016) 52-76.

[34] E. Peled, and S. Menkin, Review—SEI: Past, Present and Future. J. of the Electrochem. Soc. 164, 7 (2017) A1703-A1719.

[35] Y.X. Lin, Z.L., K.L. Leung, L.Q. Chen, P. Lu, and Y. Qi, Connecting the irreversible capacity loss in Li-ion batteries with the electronic insulating properties of solid electrolyte interphase (SEI) components. J. Power Sources 309 (2016) 221-230.

[36] N. Sun, H. Liu, and B. Xu, Facile synthesis of high performance hard carbon anode materials for sodium ion batteries, J. Mater. Chem. A 3 (2015) 20560-20566.

[37] X. Zuo, J. Zhu, P. Müller-Buschbaum, and Y.J. Cheng, Silicon based lithium-ion battery anodes: A chronicle perspective review, Nano Energy 31 (2017) 113-143.

[38] S.J. An, J. Li, C. Daniel, D. Mohanty, S. Nagpure, and D.L. Wood, The state of understanding of the lithium-ion-battery graphite solid electrolyte interphase (SEI) and its relationship to formation cycling. Carbon 105 (2016) 52-76.

Chapter 5

Carbon xerogel doped with tin oxide nanoparticles

Abstract

Previous chapters of this thesis have shown that high specific energy dopants can be included within a carbon xerogel (CX) in order to improve both the cycling stability and energy density of a lithium-ion (Li^+ ion) battery negative electrode. Therefore in this chapter, another high specific energy density material, tin oxide, will be included into a CX, similar to how the silicon nanoparticles were included into a CX in Chapter 2. Tin oxide is considered a promising candidate for the active material in Li^+ ion batteries given its high theoretical energy density thanks to the conversion and alloying reactions that occur at low potential (< 2 V *vs.* Li^+/Li). These two reactions give tin oxide a theoretical specific capacity of up to 1500 mAh g^{-1}. However, the tin oxide conversion reaction has been shown to be only partially reversible while the alloying reaction undergoes large volumetric change (>300%) during cycling, which causes unstable SEI formation and pulverization of the tin oxide. In order to address these issues, an active material was synthesized consisting of a CX doped with tin oxide *via* the solution mixing of tin oxide nanoparticles with a pyrolyzed CX. The resulting synthesis yielded a CX with tin oxide that had been deposited within the meso/macropores of the carbon xerogel. Physico-chemical characterization *via* TEM, XRD, and N_2 adsorption were conducted. Composite electrodes of the CX-SnO_2 active material were synthesized using either a conventional binder, poly(vinylidene difluoride), or an ionically-conductive polymer, poly(sodium-4 styrene sulfonate) (PSS), as a binder. PSS has been shown in previous chapters to improve cycling stability and charge transfer characteristics of composite electrodes. The composite electrodes were cycled up to either 1 V or 2 V *vs.* Li^+/Li to compare the characteristics between utilizing only the alloying reaction or both the conversion and alloying reaction, respectively. The composite electrode was more stable when cycled up to 1 V *vs.* Li^+/Li using PSS as a binder. The composite electrode with PSS as a binder cycled up to 1 V *vs.* Li^+/Li maintained 88% of the initial capacity after 60 cycles while the composite electrode with PVDF as a binder maintained only 54% of the initial capacity. Cyclic voltammetry and electrochemical impendence spectroscopy measurements were also made in order to further electrochemically characterize these CX-SnONPs composite electrodes.

5.1 Introduction

Previous chapters of this thesis have shown that silicon, a high specific energy dopant, can be included within a carbon xerogel (CX) to improve both the cycling stability and energy density of a lithium-ion (Li^+ ion) battery negative electrode. Therefore, in this chapter, another high specific energy density material, tin oxide, will be included into a CX in a similar fashion as silicon was in Chapter 2. Tin oxide is an interesting active material that can act as both an alloying-type and conversion-type material. Tin oxide has a theoretical energy density of up to ~1500 mAh g^{-1} due to the conversion-type and alloying-type reactions with lithium that tin oxide can undergo [1-9]. These reactions include (i) the conversion reaction from SnO_2 → SnO → Sn, which has a specific energy of 711 mAh g^{-1} and (ii) an alloying reaction between the tin metal that is produced from the conversion reaction with lithium to form Sn-Li alloy, which has a specific energy density of 783 mAh g^{-1} [10]. These reactions are given in the following equations:

$$SnO_2 + 4Li^+ + 4e^- \rightarrow Sn + 2Li_2O \qquad \text{capacity} \approx 711 \text{ mAh g}^{-1} \qquad (5.1)$$

$$Sn + xLi^+ + xe^- \rightarrow Li_xSn\ (0 < x < 4.4) \qquad \text{capacity} \approx 783 \text{ mAh g}^{-1} \qquad (5.2)$$

Unfortunately, the conversion reaction of tin oxide into tin has been shown to be only partially reversible. However, this mechanism is still not well understood [10]. *Ex situ* TEM analysis has shown that tin oxide does not reappear during cycling and that only SnO is formed during delithiation accompanied by a corresponding increase and decrease of the quantity of Li_2O, which is inactive and nonconductive [10]. The cause of the irreversible nature of the conversion reactions may be due to either the formation of the Li_2O species or due to electrolyte decomposition, given the observation of LiOH species; however, this has not been shown to be conclusive [10].

The alloying reaction of tin with lithium is fully reversible. However, similar to other alloying-type materials, tin undergoes a large volumetric change between the lithiated and delithiated states (around 300%) [1-10]. The volumetric expansion of tin can lead to unstable SEI formation as well as internal stresses, which can cause fracturing, pulverization, and loss of electrical conductivity to the current collector, similar to what occurs with silicon as shown in previous chapters [11]. Tin oxide nanoparticles (SnONPs) could be used to reduce the size of the tin or tin oxide domains and increase the cycling stability of the tin oxide phase. However, protecting the surface of these particles to form a stable solid-electrolyte interphase (SEI) is also key to long-term cycling stability [12-14]. Techniques to mitigate these negative characteristics usually include coating the surface of the material with some protective element, such as carbon. However, many of the synthesis techniques to accomplish these coatings require harsh chemicals or complicated synthesis procedures to produce the necessary nanostructures [12-14]. Instead, as has been done with the silicon nanoparticles in previous chapters, a CX can be used as a host matrix for supporting the

SnONPs as well as the use of poly(sodium-4-styrene sulfonate) (PSS) as a protective binder and interphase between the SnONPs and the electrolyte.

The inclusion of SnONPs into the CX matrix can be done in a wide variety of ways. For example, one could incorporate previously synthesized SnONPs particles into the xerogel at various points through the CX synthesis procedure, similar to what was done with the silicon nanoparticles (*i.e.* in the xerogel precursor solution, before xerogel pyrolysis, or after xerogel pyrolysis). Since previous experiments with doping the CX with silicon in the precursor solution yielded poor capacity during galvanostatic cycling, it was decided to perform tin oxide doping by impregnation of the already formed solid xerogel, either before or after pyrolysis.

Therefore, the inclusion of these SnONPs *via* impregnation into the xerogel could be carried out by mixing the SnONPs (i) with the unpyrolyzed xerogel after gelation (OX), or (ii) with the pyrolyzed carbon xerogel (CX). However, carbothermal reduction of tin oxide may occur at the elevated temperatures (~800°C) *via* the following reduction reactions [15]:

$$SnO_2(s) + C(s) \rightarrow Sn(s,l) + CO_2(g) \quad (5.3)$$

$$SnO_2(s) + 2CO(g) \rightarrow Sn(s,l) + 2CO_2(g) \quad (5.4)$$

Furthermore, since the melting point of tin metal is only 231°C, the nanostructure of the parent SnONPs would not be retained. Therefore, the following work consists of solution mixing SnONPs with the pyrolyzed carbon xerogel followed be a subsequent recovery and characterization. The sample was physico-chemically characterized *via* Hg porosimetry, N_2 absorption/desorption, XRD, and TEM imaging. Composite electrodes of the sample were then prepared with either poly(vinylidene difluoride) (PVDF) or poly(sodium 4-styrene sulfonate) (PSS) as a binder. As has been shown in previous chapters, PSS can improve the cycling stability of silicon-doped CX given its unique electrochemical and physico-chemical properties, namely its ionic conductivity and water solubility. Therefore, PSS was used as a binder for the SnONPs-doped CX to determine if these same protective characteristics apply similarly for SnONPs-doped CXs. Electrochemical characterization of these CX-SnONPs composite electrodes with PVDF or PSS as a binder consisted of galvanostatic cycling, electrochemical impedance spectroscopy (EIS), and cyclic voltammetry (CV). During cycling, some electrodes were cycled up to 1 V and 2 V *vs.* Li^+/Li in order to compare the cycling performance when either (i) both the conversion and tin alloying reaction occur or (ii) only the tin alloying reaction occurs.

5.2 Experimental

Materials: Resorcinol (R, 99%), formaldehyde (F, 37 wt% in H_2O), sodium carbonate (C, 99.5%), polyvinylpyrrolidone (PVP, M_w = 40,000 g mol^{-1}), poly(sodium 4-styrene sulfonate) (PSS, M_w = 70,000 g mol^{-1}), and tin oxide nanoparticles (SnONPs, d = 5-15 nm) were purchased from Sigma-Aldrich. N-methyl-2-pyrrolidone (NMP, ~99%) was purchased from Alfa Aesar.

5.2.1 CX sample: Carbon xerogel synthesis

A carbon xerogel (CX) with an R/C ratio of 2000 was synthesized *via* the sol-gel polycondensation of resorcinol and formaldehyde in water. [16-19]. See section 2.2.1 in Chapter 2 for the solution preparation, gelation, drying, ball-milling, and pyrolysis procedures. The CX sample has a specific capacity of either 165 mAh g^{-1} or 275 mAh g^{-1} when cycled up to 1 V or 2 V *vs.* Li^+/Li, respectively (see Figure S5.1 in the supplemental information).

5.2.2 CX-SnONPs sample: Carbon xerogel doped with SnONPs by impregnation

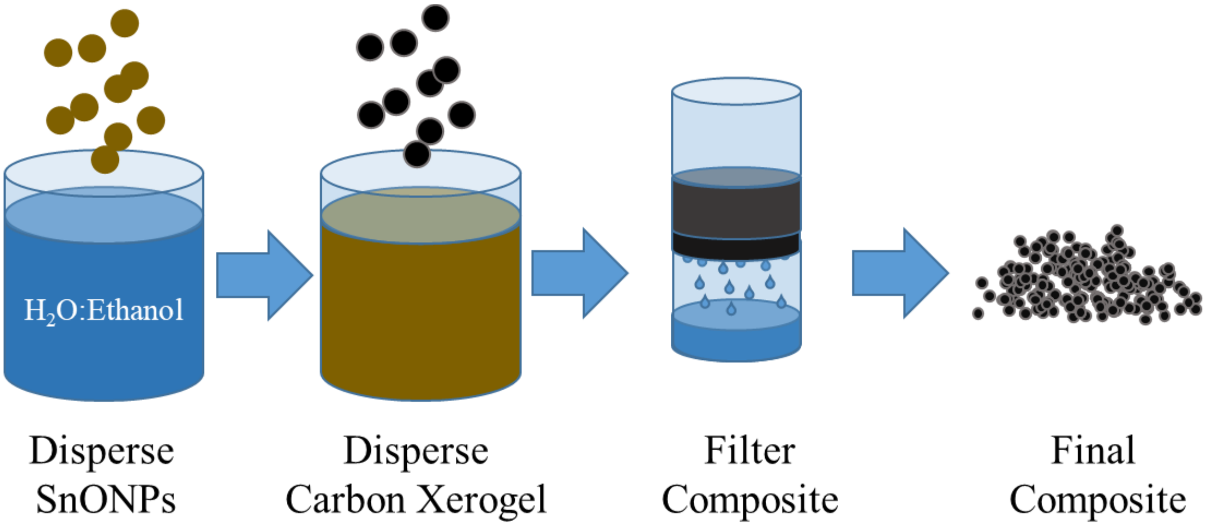

Figure 5.1 – Synthesis diagram of tin oxide-doping of a carbon xerogel to produce a CX-SnONPs active material.

The doping of the CX consisted of mixing the CX powder (d = 10 µm) and SnONPs in a 1:1 solution of ethanol and high purity water (*via* MilliQ process until R > 18 MΩ). 400 mg of SnONPs were dispersed into 25 mL of a 1:1 mixture of ethanol:H_2O and ultrasonicated for 2 h. Then, 400 mg of bare CX powder was dispersed into the SnONPs suspension. The suspension was placed in an ultrasonic bath for 2 h and subsequently mixed *via* a magnetic stirrer for 24 h to allow for the SnONPs to diffuse into the CX particles. The CX-SnONPs sample was then filtered through 100 nm microporous filter paper and dried at 90°C at a pressure of 1500 Pa for 24 h in a vacuum oven. The final mass percent of tin oxide in the CX-SnONPs sample should be 50 wt%. The theoretical specific capacity of the CX-SnONPs active material if both the conversion and alloying reactions take place would be approximately 900 mAh g^{-1}. If only the alloying reaction takes place, the theoretical specific capacity of the CX-SnONPs active material would be approximately 500 mAh g^{-1}.

5.2.3 Preparation of CX and CX-SnONPs inks and electrodes

Electrodes were processed using the CX and CX-SnONPs samples as the active material with PVDF or PSS as a binder. First, ink slurries were prepared for subsequent electrode preparation and electrochemical characterization. The ink with PVDF as a binder were prepared by mixing 90 wt% of the active material and 10 wt% of PVDF in NMP. The ink with PSS as a binder were prepared by mixing 90 wt% of the active material and 10 wt% of PSS in high purity water (*via* MilliQ process until R > 18 MΩ). The inks were stirred under magnetic stirring at 1000 rpm for 4 h. The inks were spray-coated onto pre-weighed 15.5 mm diameter stainless steel disks. These disks were fixed on a 70°C heated surface. The coatings were deposited using a Harder & Steenbeck Evolution Silverline 2 airbrush. A solvent-to-solids ratio of 20:1 was used to ensure that the prepared inks flowed easily through the airbrush. After spray-coating, the electrodes were dried at 70°C for 2 h and then at 120°C under vacuum overnight. The electrodes were then weighed to determine the mass of the deposited material prior to their electrochemical characterization. Excess dried material surrounding the electrodes, which was deposited around the disks during the spray-coating process, was collected for further characterization.

5.2.4 Physico-chemical characterization and electrochemical characterization

Physico-chemical and electrochemical characterizations carried out in this chapter are outlined in Annex 1. The physico-chemical characterizations included, nitrogen adsorption-desorption, transmission electron spectroscopy, and X-ray diffraction. N_2 adsorption was used to determine the BET surface area (S_{BET}) and the corresponding microporous (S_{micro}) and meso/macroporous (S_{ext}) surface areas of the CX and CX-SnONPs samples as well as the composites with PVDF or PSS as a binder. XRD and TEM with EDX analysis was used to determine the SiNPs crystallite size, particle size and distribution, elemental characterization, and crystallographic microstrain of the dopant tin oxide nanoparticles in the CX-SnONPs sample.

An additional *in situ* XRD measurement was conducted on the CX-SnONPs sample using a specialized sample holder, as shown below in Figure 5.2. 15 mg of the CX-SnONPs sample was deposited within the sample holder. Excess a 1M $LiPF_6$ solution in 1:1 mixture of EC:DMC solvent was used as the electrolyte with a Fiberglass separator. XRD measurements between 2θ angles of 20° and 40° were recorded every hour during galvanostatic cycling between 2 V and 0.005 V vs. Li^+/Li with an applied current of 0.85 mA during charging and discharging.

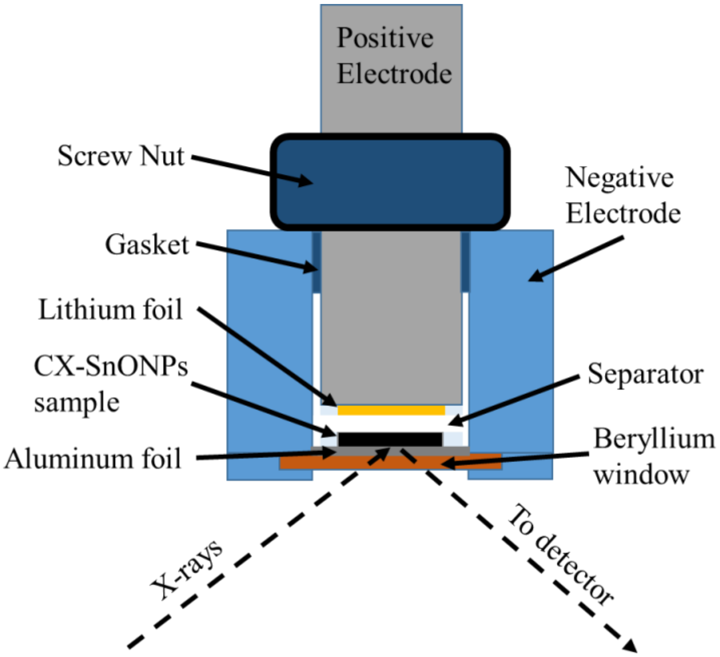

Figure 5.2 – Schematic of *in situ* XRD sample holder.

Electrochemical characterization consisted of cyclic voltammetry (CV), galvanostatic cycling, and electrochemical impedance spectroscopy (EIS) on the CX-SnONPs composite electrodes. CV characterizations show the redox potentials of the electrochemically active components as well as how these reactions evolve during cycling, cycling gives the specific capacity and stability of the prepared composite electrodes. EIS analysis was used to determine how the equivalent series resistance (ESR), charge transfer resistance (R_{ct}), charge transfer capacitance (C_d) and the diffusive properties of the composite electrodes evolves during cycling. An overview of these parameters and the electrochemical model for these electrodes can be found in Annex 2.

5.3 Results and discussion

5.3.1 Preliminary characterization of CX doped before pyrolysis with SnONPs

Preliminary characterization of the CX doped with SnONPs before pyrolysis showed that some of the tin oxide had been transformed into tin metal during the pyrolysis step. Furthermore, since the melting point of tin metal is only 231°C, the nanostructure of the SnONPs had been lost and the tin had formed large agglomerates that could be seen visually in the sample powder after pyrolysis. TEM analysis of this sample would further confirm the presence of large agglomerates of tin/tin oxide (Figure 5.3) as well as the formation of tin metal *via* XRD analysis (Figure 5.4). Therefore, it was decided that the only synthesis route that would be considered would be to dope the CX with SnONPs after pyrolysis.

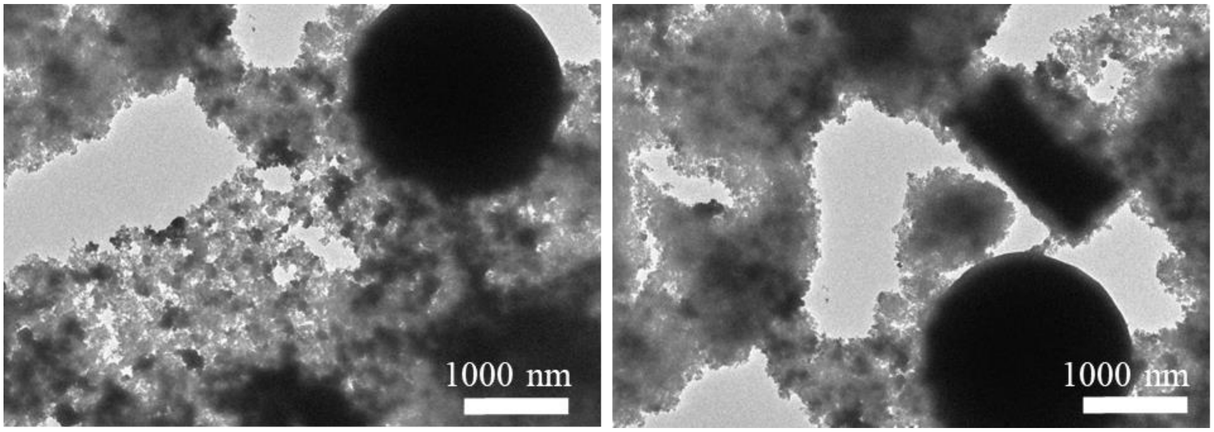

Figure 5.3 – TEM micrographs of a CX-SnONPs sample doped with SnONPs before pyrolysis. The high temperature of the pyrolysis oven in this synthesis procedure caused the SnONPs to be reduced into tin *via* carbothermal reduction.

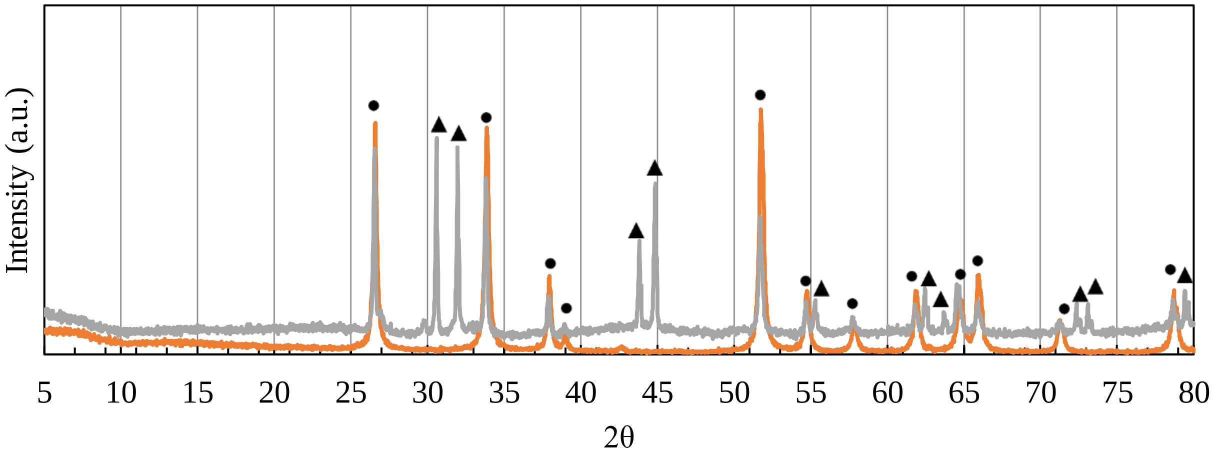

Figure 5.4 – XRD patterns of a CX-SnONPs doped with SnONPs before pyrolysis. (━) before and (━) after pyrolysis. Diffraction peaks are labelled for (●) tin oxide and (▲) tin.

5.3.2 Physico-chemical characterization

Transmission electron microscopy

TEM micrographs of the bare CX, SnONPs, and CX-SnONPs samples have been collected. Figure 1.1 in Chapter 1 shows the bare CX at various magnifications. An explanation of these micrographs is also given in Chapter 1. Micrographs of the SnONPs are shown in Figure 5.5 at various magnifications. The SnONPs exhibit a faceted particle shape with an average particle size of approximately 91 nm (measured manually, see Annex 1, Transmission Electron Microscopy for characterization procedure). The high magnification images in Figure 5.5c and d show the diffraction pattern of the tin oxide crystal structure. The SnONPs seem to be monocrystalline in nature since the imaged nanoparticle in Figure 5.5d does not show any apparent grain boundaries.

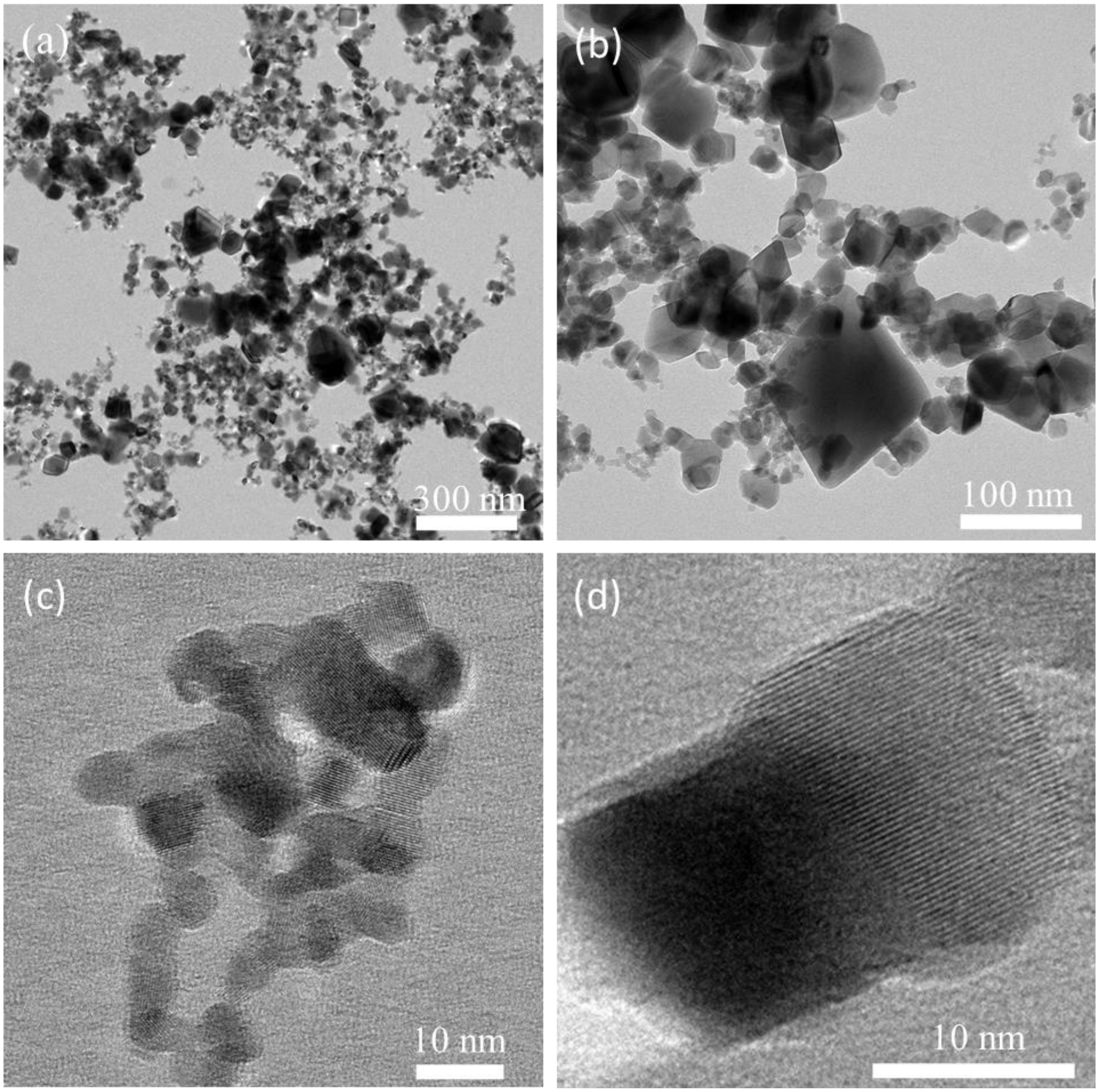

Figure 5.5 – TEM micrographs of the SnONPs at various magnifications.

Figure 5.6 shows micrographs of the CX-SnONPs sample at various magnifications. The SnONPs can be distinguished from the CX by the difference in shape and contrast. The SnONPs can be identified by their faceted shape, similar to the bare SnONPs and higher contrast in the TEM micrograph as a result of their higher atomic mass of tin as compared to carbon. The average particle size of the SnONPs within the CX-SnONPs sample was measured manually to be 30 nm.

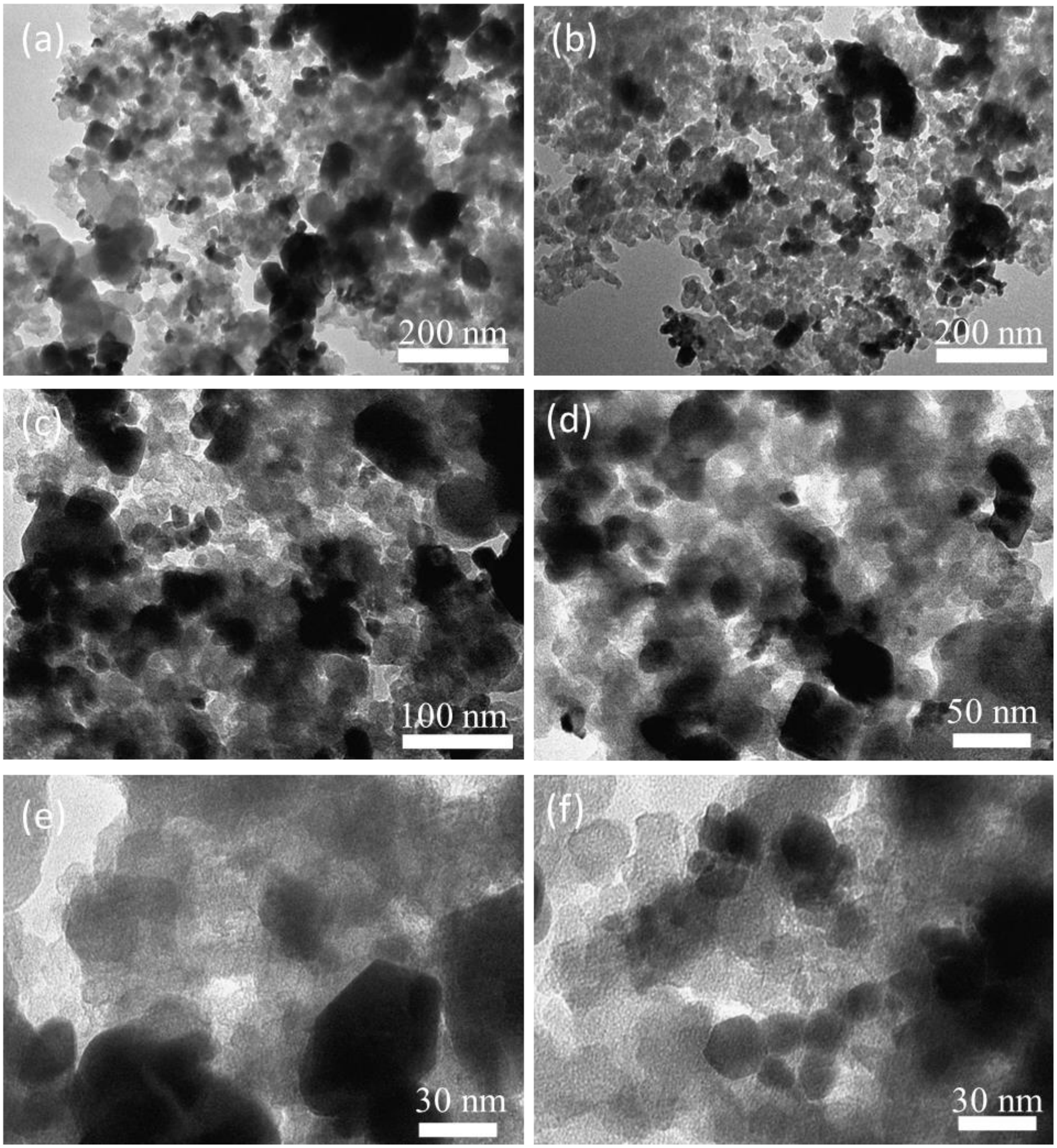

Figure 5.6 – TEM micrographs of the CX-SnONPs sample at various magnifications.

The particle size distribution of the bare SnONPs and the SnONPs in the CX-SnONPs sample is given in Figure 5.7a and b, respectively. Interestingly, it seems that the larger SnONPs were selectively removed during the synthesis of the CX-SnONPs sample, which is why the average particle size of the SnONPs decreased from 91 nm to 30 nm when the SnONPs were included in the CX-SnONPs sample.

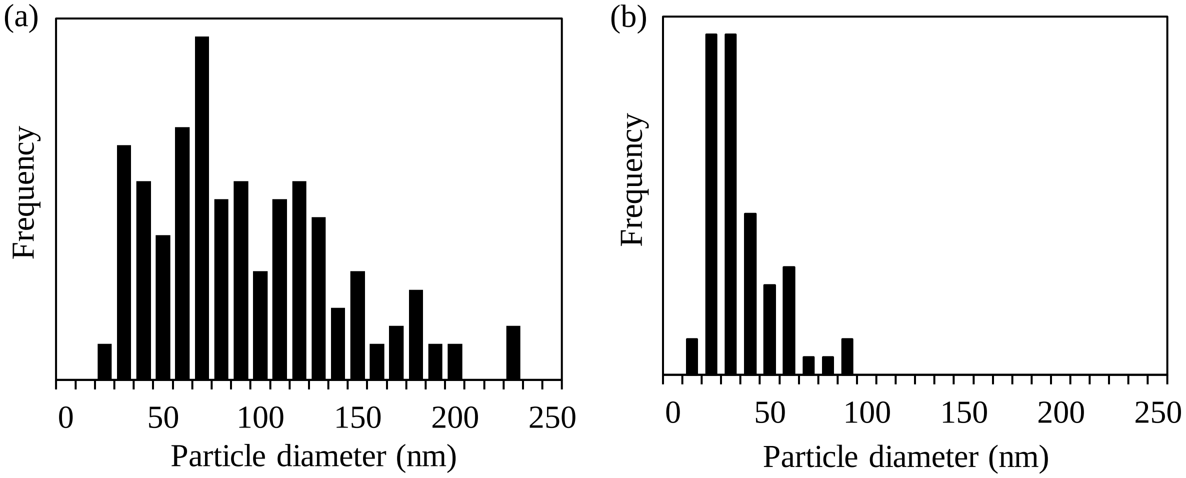

Figure 5.7 – (a) Particle size distribution of SnONPs as received from supplier. (b) Particle size distribution of SnONPs within the CX-SnONPs sample.

Nitrogen adsorption-desorption analysis

Figure 5.8a shows the N_2 adsorption isotherms of the CX, SnONPs, and CX-SnONPs powders. The isotherms of the CX and CX-SnONPs resemble a type II isotherm, which corresponds to a micro-macroporous material. The bare SnONPs powder resembles a type III isotherm, which corresponds to a meso-macroporous material without any microporosity.

The corresponding total specific surface area, S_{BET}, with the constituent microporous surface area, S_{micro}, and meso/macroporous surface area, S_{ext}, for the CX, SnONPs, and CX-SnONPs powders are shown in Figure 5.8b. The total specific surface area was reduced from 680 $m^2 g^{-1}$ to 346 $m^2 g^{-1}$ when the tin oxide nanoparticles area were included in the CX host matrix. However, the decrease in the total surface area was mainly at the cost of the S_{micro}, reducing from 482 $m^2 g^{-1}$ to 229 $m^2 g^{-1}$. The loss of S_{micro} is likely due to the fact that tin oxide nanoparticles have no microporosity (< 1 $m^2 g^{-1}$); therefore, the total amount of S_{micro} decreases per unit mass of the sample. Furthermore, since the SnONPs are not small enough to occupy the micropores of the CX, the SnONPs should be simply occupying the meso/macroporosity of the CX. Considering that this is the case, the theoretical S_{micro} and S_{ext} of the CX-SnONPs sample *via* the weighted mass average of the constituent CX and SnONPs would be approximately 112 $m^2 g^{-1}$ and 240 $m^2 g^{-1}$, respectively. The measured values of the S_{micro} and S_{ext} in the CX-SnONPs sample was found to be 117 $m^2 g^{-1}$ and 229 $m^2 g^{-1}$, which corresponds well with these theoretical values. Therefore the CX-SnONPs sample is likely composed of SnONPs included within the meso/macroporosity of the CX and not within the microporosity of the CX. A summary of the N_2 adsorption-desorption analysis is given in Table 5.1.

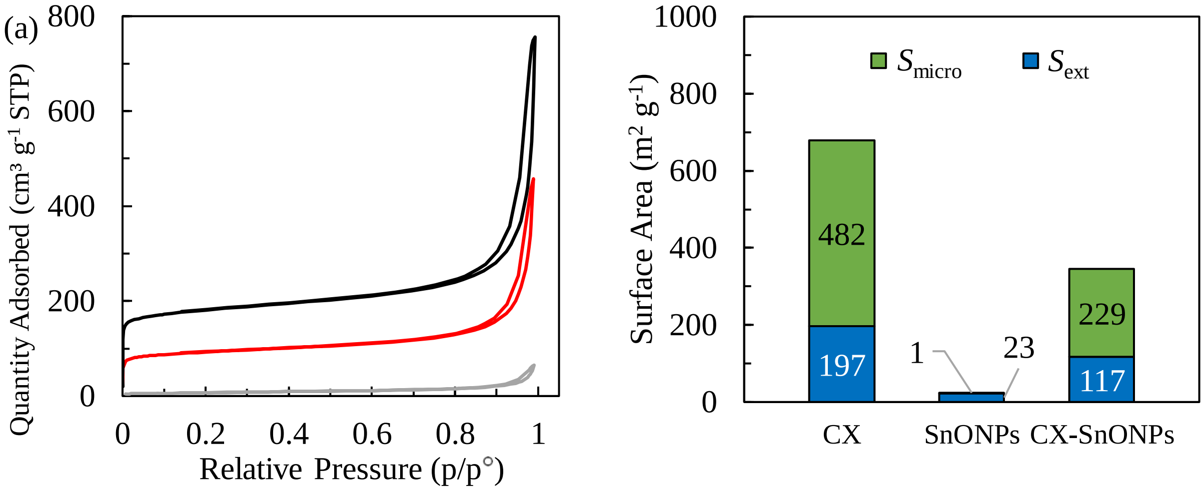

Figure 5.8 – (a) N_2 isotherms for (▬) CX, (▬) SnONPs, and (▬) CX-SnONPs powders. (b) Corresponding specific surface areas divided into the constituent microporous surface area (S_{micro}) and meso/macroporous surface area (S_{ext}).

Table 5.1 – Nitrogen adsorption-desorption data for the CX, SnONPs, CX-SnONPs powder

Sample	**S_{micro}** m² g⁻¹	**S_{ext}** m² g⁻¹	**S_{BET}** m² g⁻¹	**% microporous surfaces**
CX	482	197	680	76%
SnONPs	1	23	24	4%
CX-SnONPs	229	117	346	66%

X-ray diffraction

XRD patterns of the CX and CX-SnONPs samples are shown in Figure 5.9. The diffraction pattern of the CX sample shows the same wide peaks at around 2θ angles of 15°, 30°, and 42°. These peaks indicate that the CX sample is, as expected, amorphous in nature. In fact, it is well known that carbon gels are non-graphitizable materials even at higher temperature, *i.e.* hard carbons. The peak at 15° may be related to oxygenate graphitic sheets, similar to graphene oxide or graphite oxide, while the peak at 30° may be just related to the amorphous nature of the CX [20, 21]. The peak at a 2θ angle of 42° likely corresponds to the C(001).

The XRD pattern of the CX-SnONPs sample confirms the presence of tin oxide in the CX-SnONPs sample given the presence of the characteristic SnO_2 diffraction peaks of the SnO_2(110), SnO_2(101), SnO_2(200), SnO_2(111), SnO_2(211), SnO_2(220), SnO_2(002), SnO_2(310), SnO_2(112), SnO_2(301), SnO_2(202), and SnO_2(321) crystallographic planes [22-24]. However, it seems that the CX diffraction peaks in the CX-SnONPs sample have changed as compared to the bare CX sample. The diffraction peak at 30° may seems to have been eliminated while the diffraction peak at 42° seems to be reduced to a small, albeit sharper peak.

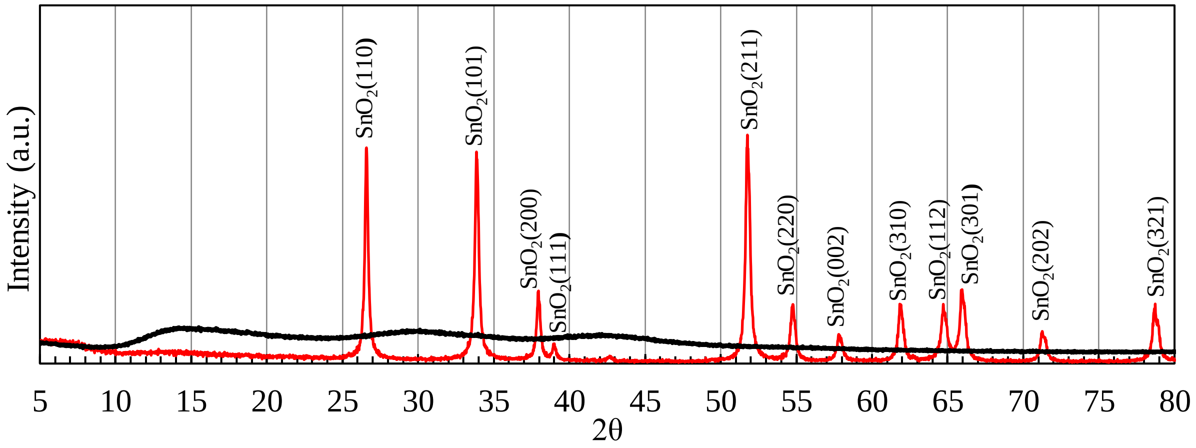

Figure 5.9 – XRD pattern of (▬) an undoped CX and (▬) a CX-SnONPs sample with the diffraction peaks of tin oxide labelled.

The Williamson-Hall plot of the CX-SnONPs sample shows that some of the line broadening of the tin oxide diffraction peaks are due to internal microstrain of the tin oxide crystal lattice. The SnONPs crystallite size, determined considering the y-axis intercept in Figure 5.10, was 25 nm. This value corresponds well with the average particle size calculated manually with the TEM micrographs taken of the CX-SnONPs sample of 30 nm. Therefore, it is likely that each individual particle is monocrystalline, which corresponds well with the TEM micrographs. The microstrain in the crystal lattice was found to be 0.15%; this value was determined considering Eq. A1.4 and the slope of the least squares regression fit in Figure 5.10. The microstrain of the SnONPs in the CX-SnONPs sample was approximately the same as the microstrain observed in the silicon nanoparticles used in Chapters 2 and 3. The microstrain in the SnONPs in the CX-SnONPs sample may be a result of the synthesis procedure of the SnONPs themselves or possibly due to the lack of a pyrolysis step to relax the stresses inherent in the SnONPs.

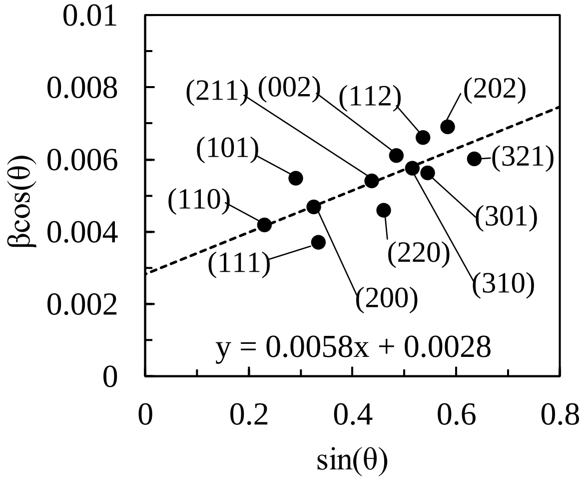

Figure 5.10 – Williamson-Hall plot of the tin oxide diffractions peaks in the CX-SnONPs sample.

5.3.3 Electrochemical characterization

Cyclic voltammetry

Cyclic voltammetry (CV) of the CX-SnONPs composite electrodes with either PVDF or PSS as a binder are shown in Figure 5.11a and b, respectively. CV measurements of the CX sample can be found in section 2.3.2 in Chapter 2. For both composite electrodes with PVDF or PSS as a binder, the first lithiation exhibits a strong peak at around 0.8 V *vs.* Li^+/Li that is likely related to the degradation of the electrolyte and formation of the SEI [1-3, 10]. The conversion reaction from tin oxide into tin occurs between 1.2 V *vs.* Li^+/Li and 0.8 V *vs.* Li^+/Li with the additional formation of Li_2O [1-3,10]. The tin-lithium alloying reaction occurs below 0.8 V *vs.* Li^+/Li [10]. Subsequent discharges after the 1st discharge show two peaks corresponding to the conversion reaction at 1.3 V and 1 V *vs.* Li^+/Li and two peaks corresponding to Li-Sn alloying reaction at 0.6 V and 0.3 V *vs.* Li^+/Li.

During the 1st delithiation, the two de-alloying peaks can be found at around 0.5 V and 0.65 V *vs.* Li^+/Li [1-3, 10]. The two de-conversion peaks, *i.e.* from tin to tin oxide, exhibit a much broader peak response located at around 1.25 V and 1.84 V *vs.* Li^+/Li [1-3, 10]. As discussed in the introduction, the conversion reaction between tin and its oxides may not be completely reversible, and this seems to be reflected in these CV measurements. The 5th and 10th cycle shows a decrease in the total area under the de-conversion peak at 1.25 V and 1.84 V *vs.* Li^+/Li as compared to the 1st cycle. This is an indication that this reaction is in fact only partially reversible given that the response persists over many cycles but slowly decreases with intensity over time. Contrarily, the total area under the dealloying peaks at 0.5 V and 0.65 V *vs.* Li^+/Li remains fairly constant for each successive cycle. The decrease in intensity of the de-alloying peak at 0.5 V *vs.* Li^+/Li and the subsequent increase in intensity of the de-alloying peak at 0.65 V *vs.* Li^+/Li may be an indication of the amount of the Sn-Li alloys with different lithium content that is being formed during each cycle [1-3, 10].

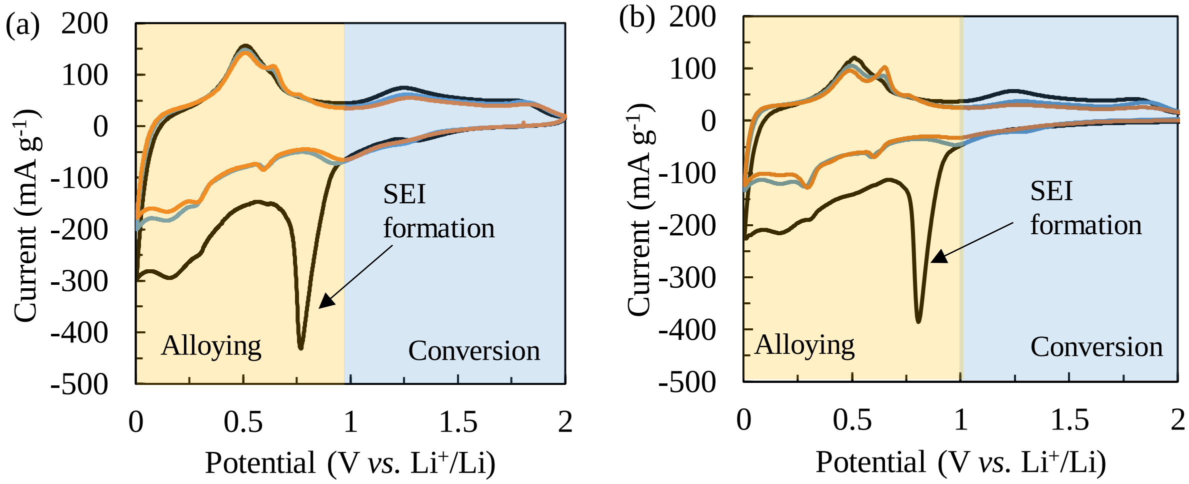

Figure 5.11 – Cyclic voltammetry of CX-SnONPs composite electrodes with either (a) PVDF as a binder or (b) PSS as a binder. The (▬) 1st, (▬) 5th, and (▬) 10th cycles are shown. The potential windows associated with the alloying and conversion reaction are labelled in yellow and blue, respectively. The scan rate was 50 μV s^{-1} between 0.005 V and 2 V *vs.* Li^+/Li.

Galvanostatic cycling

Galvanostatic cycling for the CX-SnONPs composite electrodes with either PVDF or PSS as a binder confirms both the partially irreversible nature of the conversion reaction as well as the reversible Sn-Li alloying reaction. The CX-SnONPs electrodes prepared with PVDF as a binder (Figure 5.12a) show less stability than the CX-SnONPs electrodes prepared with PSS as binder (Figure 5.12b) when cycled up to both 1 V and 2 V *vs.* Li^+/Li. The alloying reaction, which mainly occurs below 1 V *vs.* Li^+/Li, is relatively stable during cycling. The conversion reaction between tin and tin oxide, which generally occurs above 1 V *vs.* Li^+/Li, shows a more rapid loss in capacity during cycling. See Table 5.2 for an overview of the differences in cycling stability between the electrodes prepared with PVDF or PSS as a binder.

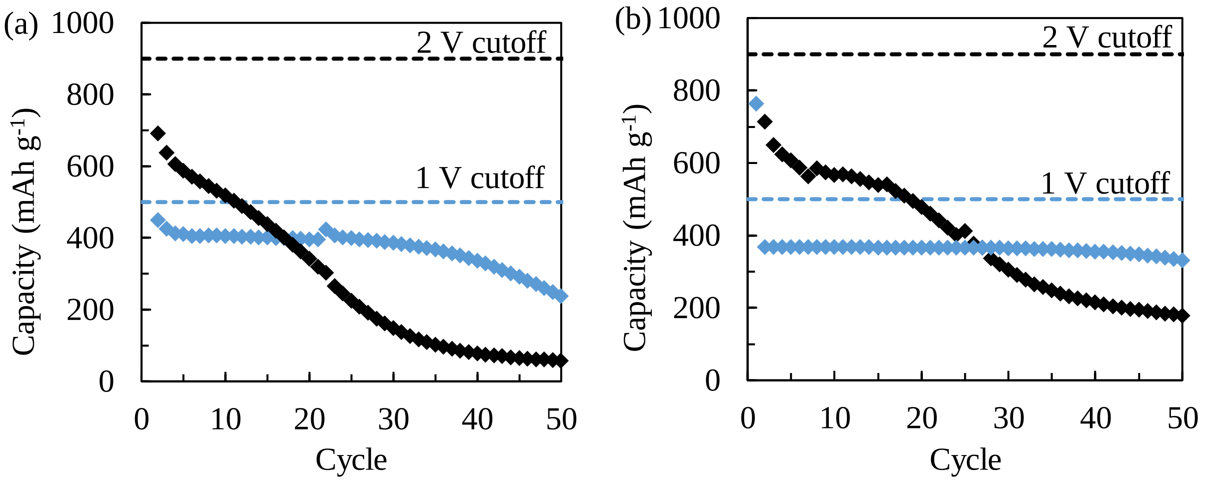

Figure 5.12 – Galvanostatic cycling was conducted on the CX-SnONPs composite electrodes with either (a) PVDF as a binder or (b) PSS as a binder. Discharge rate was C/10 up to either (◆) 1V or (◆) 2V *vs.* Li$^+$/Li. The dotted lines represent the theoretical capacity of the CX-SnONPs composite electrodes at either (---) 2V or (---) 1V *vs.* Li$^+$/Li cutoff potential.

Table 5.2 – Comparison of capacity and percent of the initial capacity after 50 cycles for the CX-SnONPs composite electrodes.

Sample	**Cap$_{1V}$** mAh g^{-1}	**% retained**	**Cap$_{2V}$** mAh g^{-1}	**% retained**
PVDF Binder	225	54%[a]	57	8%[b]
PSS Binder	335	88%[c]	181	26%[b]

[a]initial capacity = 450 mAh g^{-1}. [b]initial capacity = 700 mAh g^{-1}. [c]initial capacity = 375 mAh g^{-1}.

The effect of the cutoff potential and binder can be observed by considering the potential profiles during cycling of the composite electrodes. Figure 5.13a and c show the potential profile cycled up to 1 V *vs.* Li$^+$/Li for the CX-SnONPs composite electrodes with PVDF and PSS as a binder, respectively. The CX-SnONPs composite electrode with PSS as a binder clearly shows better stability after 50 cycles as compared to the composite electrode with PVDF as a binder. Likewise, the composite electrode with PSS as a binder (Figure 5.13b) is also more stable compared to the composite electrode with PVDF as a binder (Figure 5.13d) when cycled up to 2 V *vs.* Li$^+$/Li.

Cycling the CX-SnONPs composite electrodes with either PVDF or PSS as a binder up to 2 V *vs.* Li$^+$/Li seems to cause the alloying reaction to degrade faster than if the electrodes were only cycled up to 1 V *vs.* Li$^+$/Li. This would suggest that the partially reversible nature of the conversion reaction, which occurs above 1 V *vs.* Li$^+$/Li, has an adverse effect on the alloying reaction. It seems likely that the irreversible nature of the conversion reaction consumes the tin species in the electrode or that the tin becomes deactivated in some other way. It is unclear, however, in what way specifically the conversion reaction of the tin oxide effects the alloying reaction of the tin.

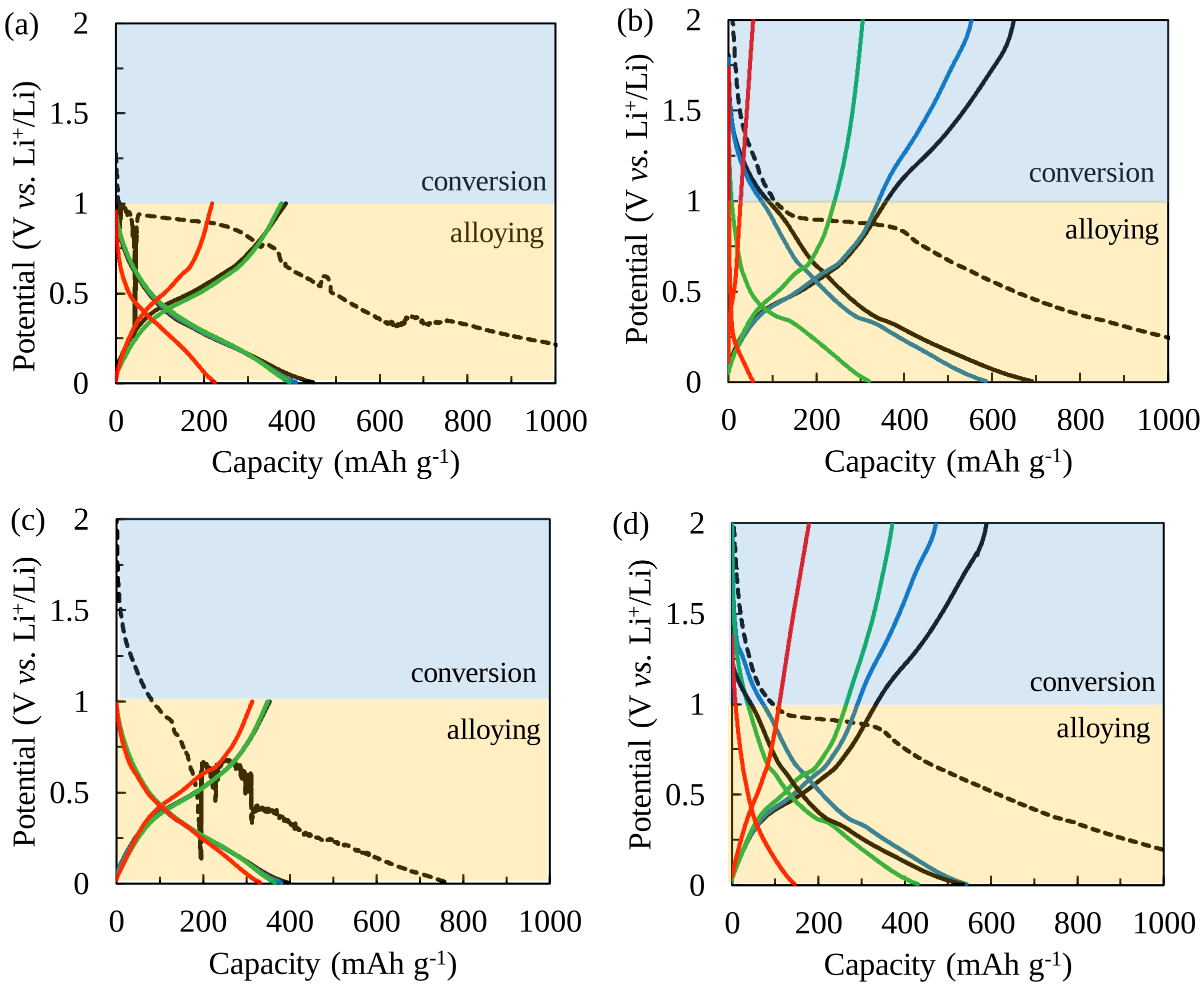

Figure 5.13 – Potential profile as a function of capacity for the CX-SnONPs composite electrode with PVDF as a binder cycled up to either (a) 1 V *vs.* Li^+/Li or (b) 2 V *vs.* Li^+/Li. Potential profile as a function of capacity for the CX-SnONPs composite electrode with PSS as a binder cycled up to either (c) 1 V *vs.* Li^+/Li or (d) 2 V *vs.* Li^+/Li. (---) pristine discharge, (▬) 1st cycle (▬) 5th cycle, (▬) 20th cycle, and (▬) 50th cycle.

Galvanostatic cycling with *in situ* X-ray diffraction

In situ XRD measurements of the CX-SnONPs sample during galvanostatic cycling are shown in Figure 5.14. The XRD measurement of the pristine CX-SnONPs sample clearly shows the diffraction peaks related to the SnO_2(110) and SnO_2(101) crystallographic planes. As the sample was lithiated during the pristine cycle, these two diffraction peaks decrease in intensity, likely related to the conversion of SnO_2 into SnO and Sn and amorphization of the SnONPs. At the same time, a very weak signal for the diffraction peaks of Sn(200) and Sn(101) briefly appears during this first lithiation. During the 1st delithiation (*i.e.* from 0.005 V to 2V vs. Li^+/Li) a stronger signal related to these two tin diffraction peaks appears. However, as the sample is once again lithiated, these peaks disappear. The tin diffraction peaks appear again during the 2nd cycle delithiation, however, they neither appear during the lithiation nor delithiation in the subsequent cycle. Nevertheless, these weak tin diffraction peaks are evidence that the tin oxide indeed converts back and forth with tin during cycling. Furthermore, as the sample is cycled, the amorphization of the tin oxide likely causes amorphization of the tin that is formed during lithiation. The absence of the tin diffraction peaks after the 2nd cycle is likely related to both the amorphization of the tin and tin oxide as well as the binder-less preparation of the active layer for this analysis.

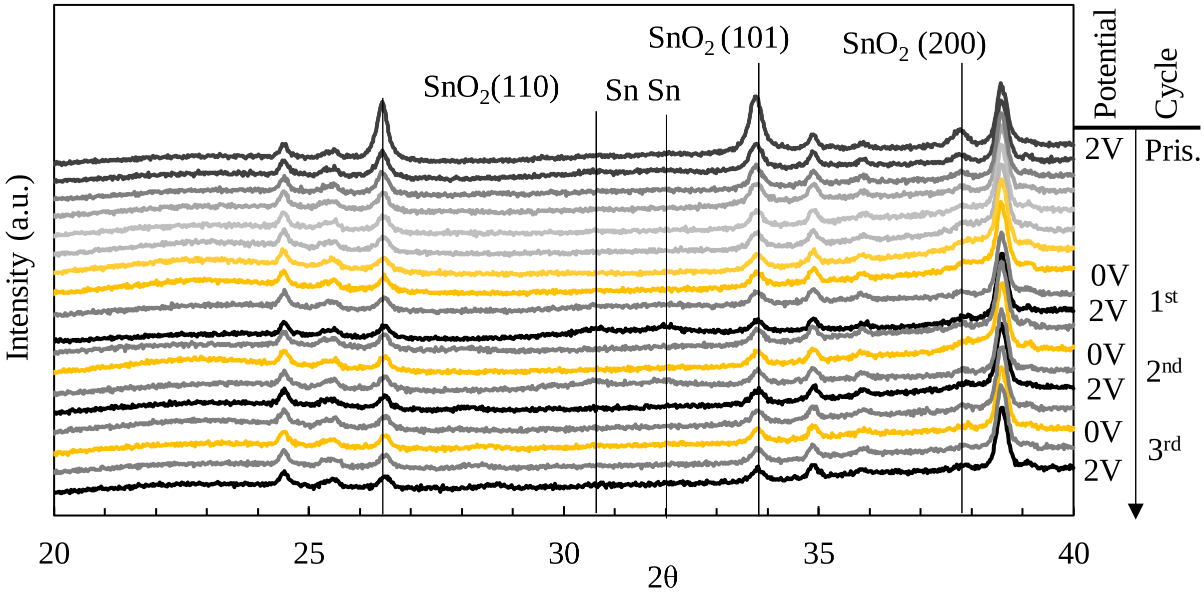

Figure 5.14 – *In situ* XRD measurement of the CX-SnONPs sample over 3 cycles. Tin oxide and tin diffraction peaks are labeled accordingly. The potential (vs. Li+/Li) and cycle number are shown to the right of each corresponding diffraction curve.

The corresponding potential profiles of the *in situ* XRD analysis are shown in Figure 5.15. It should be noted that the cycling performance was significantly affected by the lack of a binder and the significantly larger amount of sample used as compared to the composite electrodes synthesized in this chapter (15 mg as compared to approximately 3 mg per electrode). A large ohmic loss is observed as an initial increase in potential from 0 V to ~0.5 V vs. Li^+/Li during lithiation and a similar initial decrease in potential from 2 V to 1 V vs. Li^+/Li during delithiation. The specific capacity was significantly decreased compared to the composite electrodes presented in the previous section. Furthermore, the characteristic potential profile of a tin oxide-based electrode is only barely identifiable. Nevertheless, the XRD measurements in Figure 5.14 and corresponding potential profiles in Figure 5.15 confirm that (i) the tin oxide undergoes a pseudo-reversible conversion reaction into tin, (ii) tin can be transformed back into tin oxide, and (iii) the tin oxide/tin species are amorphized during cycling.

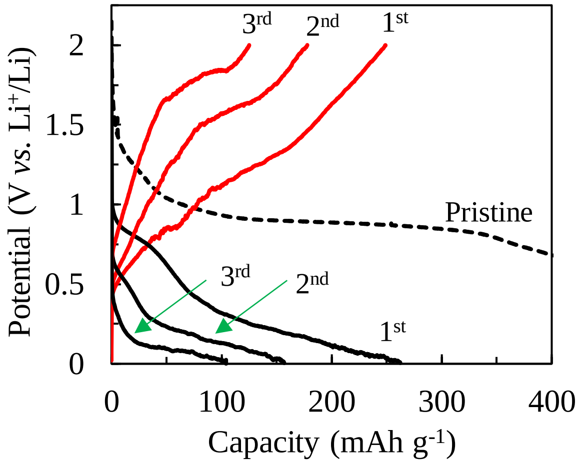

Figure 5.15 – Potential profile as a function of capacity of the CX-SnONPs sample during *in situ* XRD measurements. Cycled up to 2 V *vs.* Li^+/Li at a current density of 0.057 mA mg^{-1}. (▬) Lithiation and (▬) delithiation.

Electrochemical impedance spectroscopy

EIS spectra for the CX-SnONPs composite electrodes with PVDF or PSS as a binder are shown in Figure 5.16 and Figure 5.17, respectively. The Randles cell electrochemical model is shown in Annex 2 that outlines the pertinent electrochemical elements, such as the equivalent series resistance (ESR), charge transfer resistance (R_{ct}) and capacitance (C_d), and diffusion characteristics that should apply to these CX-based half cells.

The Nyquist plot and Bode diagram of the CX-SnONPs composite electrode with PVDF as a binder cycled up to 2 V *vs.* Li^+/Li are shown in Figure 5.16a and b, respectively. The Nyquist plot shows a continuously changing response during CV cycling. Notably, the diameter of the charge transfer half circle becomes smaller between the pristine and 1st cycle, followed by a continuously increasing diameter between the 1st and 50th cycle. In the Bode diagram, the diffusion region response, which takes place at low frequency, shows a change in the phase shift from approaching -90° to approaching -45° between the pristine and 50th cycle. As has been discussed in previous chapters, the formation of a SEI allows for the more facile diffusion of Li^+ ions into the active material, which causes this change from a capacitive (-90°) to diffusive response (-45°).

The evolution of the ESR and R_{ct}/C_d of the CX-SnONPs composite electrode with PVDF as a binder are shown in Figure 5.16c and d, respectively. The ESR progressively increases from 3 Ω to 5 Ω between the pristine and 50th cycle. Likewise, the R_{ct} progressive increases in a similar fashion between the pristine and 50th cycle. The increase in ESR and R_{ct} are a sign that the active layer is pulverizing as a result of the instability of the dopant SnONPs. Contrarily, the C_d increases during the first 5 cycles followed by a progressive decrease up until the 50th cycle. This suggests that specific surface area of the active layer begins to increase up to the 5th cycle, then decrease up until the 50th cycle. This suggests that the active layer is in fact pulverizing for the first 5 cycles, given the increase in surface area. Then, excessive pulverization likely causes the active material to become detached from the current collector, resulting in the progressive decrease in specific surface area and C_d, correspondingly.

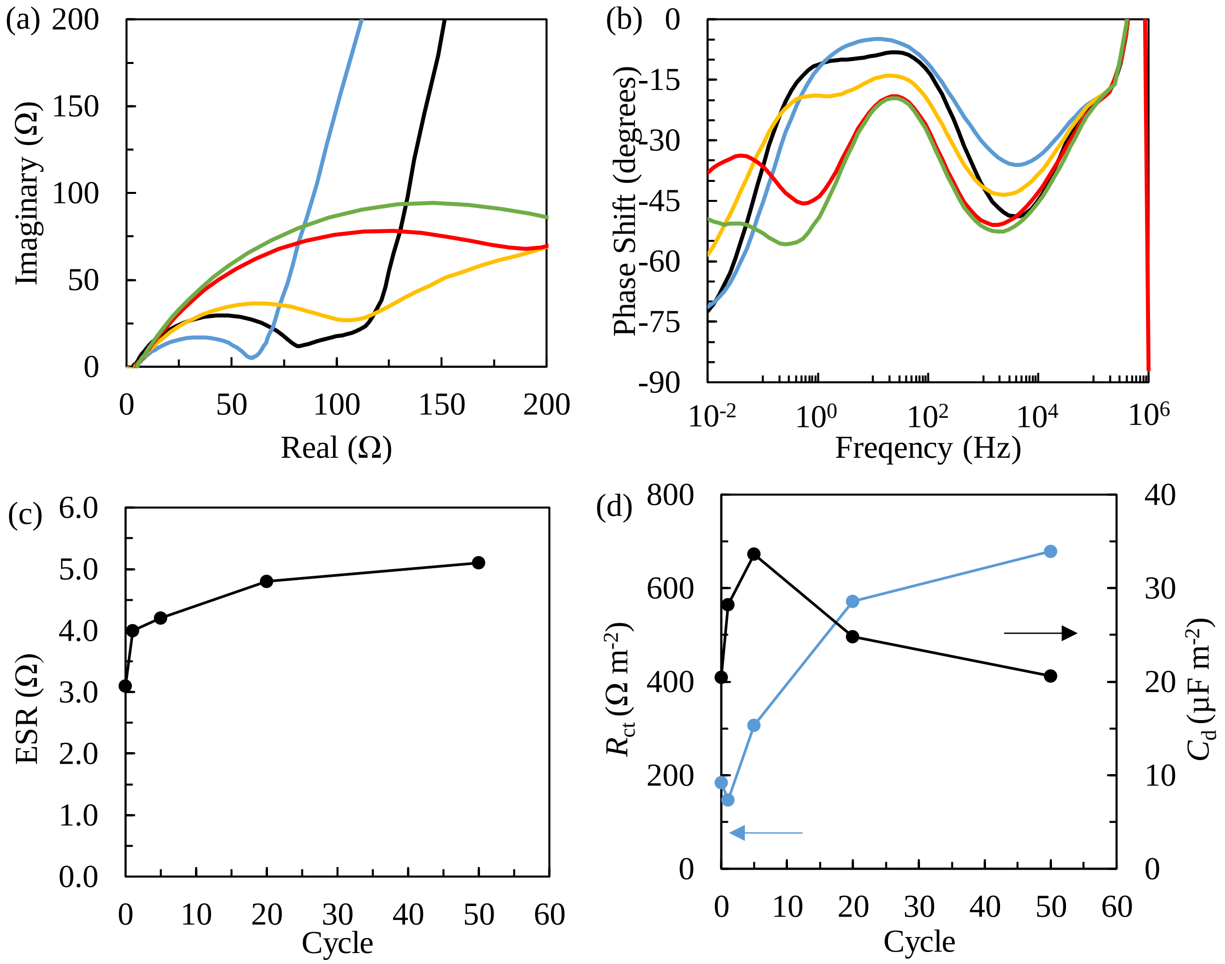

Figure 5.16 – (a) Nyquist plot and (b) Bode diagram of a CX-SnONPs composite electrode with PVDF as a binder cycled between 0.005 V and 2 V *vs.* Li$^+$/Li. Shown for the (▬) Pristine, (▬) 1st, (▬) 5th, (▬) 20th cycle, and (▬) 50th cycle. (c) ESR as a function of CV cycles and (d) charge transfer resistance (R_{ct}) and capacitance (C_d) as a function of cycles for the CX-SnONPs composite electrode with PVDF as a binder. The scan rate was 50 µV s^{-1} between 0.005 V and 3 V or 1.5 V *vs.* Li$^+$/Li.

The CX-SnONPs composite electrode with PSS as a binder seems to be more stable than the CX-SnONPs composite electrode with PVDF as a binder. The Nyquist plot and Bode diagram of the CX-SnONPs composite electrode with PSS as a binder are shown in Figure 5.17a and b, respectively. The Nyquist plot shows a relatively stable response during galvanostatic cycling. The major change during cycling appeared only between the pristine and 1st cycle, which exhibited a different shaped charge transfer half circle and diffuse region response. In the Bode diagram, the diffusion region response, which takes place at low frequency, shows a quick change in the phase shift from approaching -90° to approaching -45° between the pristine and 1st cycle. This was contrary to the response of the composite electrode with PVDF as a binder, which showed this transition occurring ate lest over the first 20 cycles. This suggest that the formation of the SEI was more stable for the composite electrode with PSS as a binder than with PVDF as a binder.

The evolution of the ESR and R_{ct} / C_d of the CX-SnONPs composite electrode with PSS as a binder are shown in Figure 5.17c and d, respectively. The ESR remains relatively constant at approximately 3.5 Ω between the pristine and 50th cycle. Likewise, the R_{ct} and C_d remained relatively constant between the pristine and 10th cycle. However, for the 50th cycle, the R_{ct} and C_d dramatically increased and decreased, respectively. The stability of the R_{ct} and C_d during the first 10 cycles and the ESR for the entire cycling are a sign that the active layer in the composite electrode with PSS as a binder is more stable electrochemical and mechanically than the composite electrode with PVDF as a binder. The sharp increase of the C_d between the pristine and 1st cycle is also a sign of the relatively fast and stable formation of an SEI on the surface of the CX-SnONPs active material with PSS as a binder. The decrease of C_d between the 10th and 50th cycle also suggests pulverization of the active material and a loss of contact with current collector, similar to what was observed for the composite electrode with PVDF as a binder.

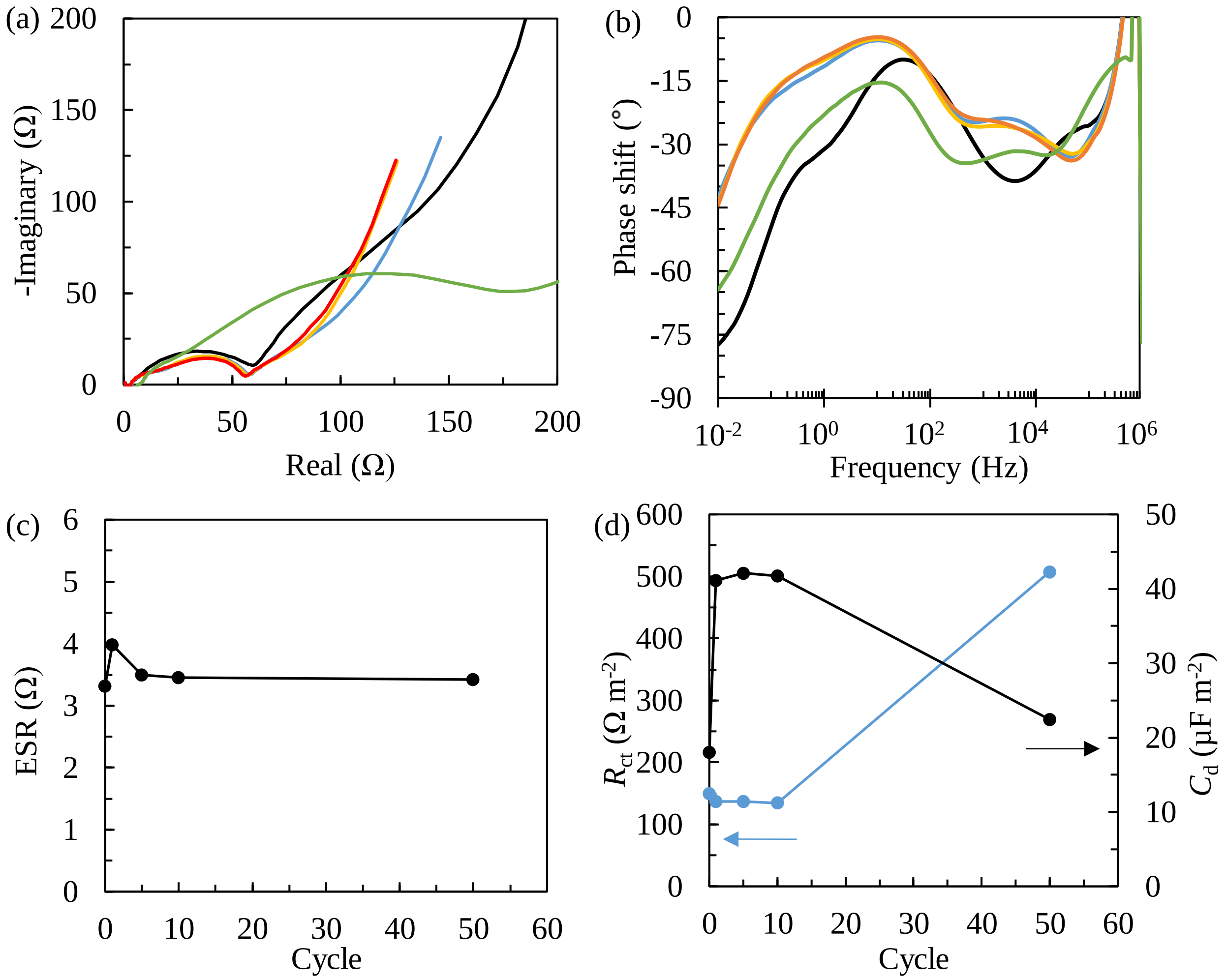

Figure 5.17 – (a) Nyquist plot and (b) Bode diagram of a CX-SnONPs composite electrode with PSS as a binder cycled between 0.005 V and 2 V *vs.* Li^+/Li. Shown for (▬) Pristine, (▬) 1st, (▬) 5th, (▬) 10th, and (▬) 50th cycles. (c) ESR as a function of galvanostatic cycles, and (d) charge transfer resistance (R_{ct}) and capacitance (C_d) as a function of cycles for the CX-SnONPs composite electrode with PSS as a binder. The scan rate was 50 µV s^{-1} between 0.005 V and 3 V or 1.5 V *vs.* Li^+/Li.

In general, it seems that the CX-SnONPs composite electrode with PSS as a binder showed a more stable electrochemical response during cycling as compared to the composite electrode with PVDF as a binder. Notably, the composite electrode with PSS as a binder exhibited a more stable and quick formation of the SEI between the pristine and 1st cycle and a relatively stable R_{ct} and C_d for the first 10 cycles. Additionally, the R_{ct} of the composite electrode with PSS as a binder was lower than the composite electrode with PVDF as a binder during the first 10 to 20 cycles. It should be noted, however, that the cycling in CV mode vs. galvanostatic mode may have affected the results of these measurements. Nevertheless, the comparison between these two composite electrodes seem to show that the composite electrode with PSS as a binder exhibited a more electrochemically stable response.

5.4 Conclusion

A carbon xerogel (CX) was doped with tin oxide *via* the solution mixing of a CX powder with previously synthesized tin oxide nanoparticles (SnONPs). The particle size distribution of the SnONPs in the CX-SnONPs sample showed that CX effectively filtered out particles larger than the average diameter of the meso/macropores of the CX. Nitrogen adsorption analysis of the CX-SnONPs sample showed that the inclusion of the non-microporous tin oxide nanoparticles into the CX resulted in a material with a microporous and meso/macroporous surface area that would be expected if the SnONPs simply occupied the meso/macroporosity of the CX. X-ray diffraction of the CX and CX-SnONPs sample showed that the average diameter of the SnONPs in the CX-SnONPs were 30 nm with a microstrain of approximately 0.6%.

Electrochemical characterization of CX-SnONPs was carried out by synthesizing a composite electrode with either PVDF or PSS as a binder. Cyclic voltammetry of both composite electrodes showed a strong SEI during the pristine discharge (lithiation). The Li-Sn alloying reaction is shown to takes place below 0.8 V *vs.* Li^+/Li while the conversion reaction of tin oxide and tin take place above 0.8 V *vs.* Li^+/Li. Galvanostatic cycling of the composite electrodes up to 1V or 2V *vs.* Li^+/Li was carried out in order to distinguish the performance between the alloying reaction and conversion reaction. The composite electrodes cycled up to 1V or 2V *vs.* Li^+/Li showed an initial capacity of 400 mAh g^{-1} or 600 mAh g^{-1}, respectively. The composite electrodes with PSS as a binder retained 88% and 26% the initial capacity when cycled up to 1 V or 2V *vs.* Li^+/Li, respectively. The composite electrodes with PVDF as a binder retained 54% and 8% the initial capacity when cycled up to 1 V or 2V *vs.* Li^+/Li, respectively. Furthermore, cycling up to 2 V *vs.* Li^+/Li for both composite electrodes caused the stability of the alloying reaction to decrease. Electrochemical impedance spectroscopy showed that the composite electrode with PSS as a binder formed a more stable SEI layer than the composite electrode with PVDF as a binder. The composite electrode with PSS as a binder exhibited a relatively stable charge transfer resistance, capacitance, and equivalent series resistance during cycling as compared to the composite electrode with PVDF as a binder.

5.5 References

[1] J.H. Shin and J.Y. Song, Electrochemical properties of Sn-decorated SnO nanobranches as an anode of Li-ion battery. Nano Convergence 3 (2016) 3-9.

[2] T. Brousse, R. Retoux, U. Herterich, and D.M .Schleich, Metal oxide anodes for Li-ion batteries. Ionics 3 (1997) 332–337.

[3] Y. Idota, T. Kubota, A. Matsufuji, Y. Maekawa, and T. Miyasaka, Tin-Based Amorphous Oxide: A High-Capacity Lithium-Ion-Storage Material. Science 276, 5317 (1997) 1395-1397.

[4] T. Brousse, R. Retoux, U. Herterich and D. M. Schleich, Thin-Film SnO_2-Lithium Electrodes. J. Electrochem. Soc. 145, 1 (1998) 1-4.

[5] H. Liu, D. Long, X. Liu, W. Qiao, L. Zhan, and L. Ling, Facile synthesis and superior anodic performance of ultrafine SnO_2-containing nanocomposites. Electrochim. Acta. 54, 24 (2009) 5782-5788.

[6] S. Nam S. Kim, S. Wi, H. Choi, S. Byun, S.M. Choi, S.I. Yoo, K.T. Lee, and B. Park, The role of carbon incorporation in SnO_2 nanoparticles for Li rechargeable batteries. J. Power Sources. 211, 1 (2012) 154-160.

[7] Y. Yu, L. Gu, A. Dhanabalan, C.H. Chen, and C. Wang, Three-dimensional porous amorphous SnO_2 thin films as anodes for Li-ion batteries. Electrochim. Acta. 54, 28 (2009) 7227-7230.

[8] S.Y. Lee, K.Y. Park, W.S. Kim, S. Yoon, S.H. Hong, K. Kang, and M. Kim, Unveiling origin of additional capacity of SnO_2 anode in lithium-ion batteries by realistic ex situ TEM analysis. Nano Energy 19 (2016) 234-245.

[9] M.G. Beier, C. Ziegler, K. Wegner, A. Benad, F. Simon, S. Kaskel, and A. Eychmüller, A fast route to obtain modified tin oxide aerogels using hydroxostannate precursors. Mater. Chem. Front., 2018, 2, 710-717.

[10] F. Zoller, D. Bohm, T. Bein, and D. Fattakhova-Rohlfing. Tin Oxide Based Nanomaterials and Their Application as Anodes in Lithium-Ion Batteries and Beyond. ChemSusChem 12 (2019) 4140-4159.

[11] X. H. Liu, L. Zhong, S. Huang, S.X. Mao, T. Zhu, and J.Y. Huang, Size-dependent fracture of silicon nanoparticles during lithiation, ACS Nano 6 (2012) 1522-1531.

[12] Y. Cui, N. Liu, H. Wu, M.T. McDowell, Y. Yao, and C. Wang, A Yolk-Shell Design for Stabilized and Scalable Li-Ion Battery Alloy Electrodes. Nano Lett. 12 (2012) 3315-3321.

[13] S. Chen, Z. Chen, Y. Luo, M. Xia and C. Cao, Silicon hollow sphere anode with enhanced cycling stability by a template-free method. Nanotechnology 28 (2017) 165404-16511.

[14] A.P. Nowak, Composites of tin oxide and different carbonaceous materials as negative electrodes in lithium-ion batteries. J. Solid State Electrochem. 22 (2018) 2297–2304.

[15] R. Padilla and H.Y. Sohn, The reduction of stannic oxide with carbon. Metal Mater. Trans. B 10 (1979) 109-115.

[16] N. Job, R. Pirard, J. Marien, and J.P. Pirard, Porous carbon xerogels with texture tailored by pH control during sol–gel process. Carbon 42 (2004) 619-628.

[17] N. Rey-Raap, M.L.C. Piedboeuf, A. Arenillas, J.A. Menéndez, A.F. Léonard, and N. Job, Aqueous and organic inks of carbon xerogels as models for studying the role of porosity in lithium-ion battery electrodes, Mater. Design 109 (2016) 282–288.

[18] X. Yuan, Y.J. Chao, Z.F. Ma, and M. Deng, Preparation and characterization of carbon xerogel (cx) and CX-SiO composite as anode material for lithium-ion battery, Electrochem. Commun. 9 (2007) 2591-2595.

[19] M.-L. Piedboeuf, A.F. Léonard, K. Traina, and N. Job, Influence of the textural parameters of resorcinol–formaldehyde dry polymers and carbon xerogels on particle sizes upon mechanical milling, Colloid Surface A 471 (2015) 124-132.

[20] G. Wang, J. Yang, J. Park, X. Gou, B. Wang, H. Liu, and J. Yao, Facile Synthesis and Characterization of Graphene Nanosheets. J. Phys. Chem. C112 (2008) 8192-8195.

[21] I.A. Courtney and J. R. Dahn, Electrochemical and *In Situ* X-Ray Diffraction Studies of the Reaction of Lithium with Tin Oxide Composites. J. Electrochem. Soc. 144 (1997) 2045-2052.

[22] K.M. Lee, D.J. Lee and H. Ahn, XRD and TEM studies on tin oxide (II) nanoparticles prepared by inert gas condensation. Materials Letters 58, 25 (2004) 3122-3125.

[23] S. Gnanam and V. Rajendran, Synthesis of tin oxide nanoparticles by sol–gel process: effect of solvents on the optical properties. J. Sol-Gel Sci. Techn. 53 (2010) 555–559.

[24] R. Siburian, H. Sihotang, S. Lumban Raja, M. Supeno, and C. Simanjuntak, New Route to Synthesize of Graphene Nano Sheets. Orient. J. Chem. 34, 1 (2018) 182-187.

5.6 Supplemental information

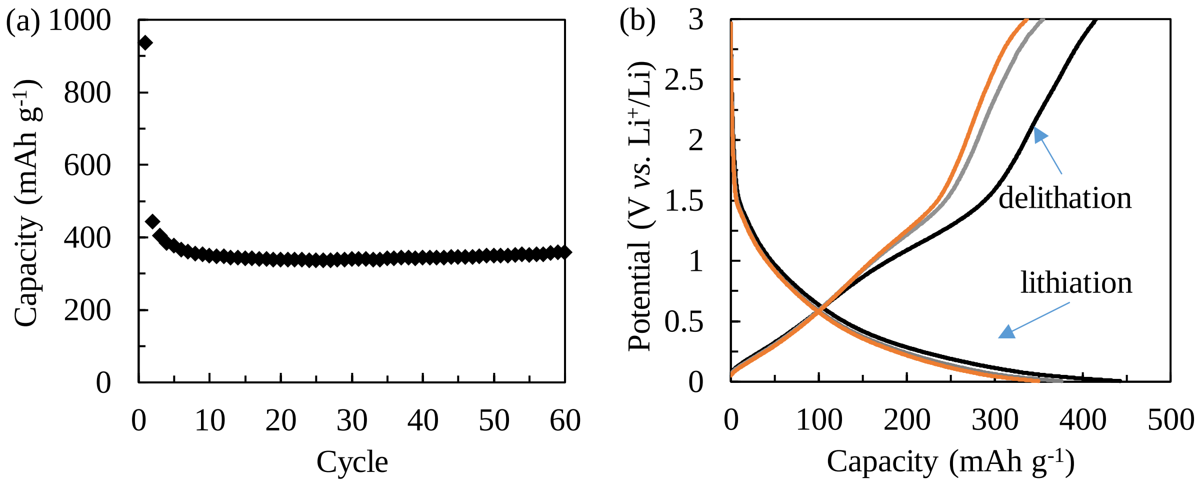

Figure S5.1 – (a) Capacity vs. cycling and corresponding (b) potential profiles of a CX composite electrode with PVDF as a binder cycled between 0.005 V and 3 V *vs.* Li^+/Li at a rate of C/10. (▬) 1st cycle, (▬) 5th cycle, and (▬) 10th cycle.

Chapter 6

Tin oxide-doped carbon xerogel *via* impregnation of sodium stannate trihydrate precursor

Abstract

Tin oxide is considered a promising candidate for the active material in negative electrodes of lithium-ion batteries given its high theoretical energy density thanks to the conversion and alloying reactions that occur at low potential (< 2 V *vs.* Li^+/Li). These two reactions give tin oxide a theoretical specific capacity of up to 1500 mAh g^{-1}. However, the tin oxide conversion reaction has been shown to be only partially reversible while the alloying reaction undergoes large volumetric change (> 300%) during cycling, which causes unstable SEI formation and pulverization of the tin oxide. In order to address these issues, a composite electrode was synthesized consisting of a carbon xerogel doped with tin oxide *via in situ* condensation of sodium stannate trihydrate (Na_2SnO_3-$3H_2O$). The resulting synthesis yielded a material in which tin oxide had been deposited within the micropores and mesopores of the CX. Physico-chemical characterization *via* TEM, XRD, and N_2 adsorption were conducted in order to determine the morphology of the CX-SnO_2 samples. CX-SnO_2 composite electrodes were synthesized with either 30 wt% or 60 wt% tin oxide using the ionically-conductive polymer, poly(sodium-4 styrene sulfonate) (PSS) as a binder, which has been shown to improve the cycling stability of these CX-based composite electrodes. These composites were cycled up to 1 V or 2 V *vs.* Li^+/Li to compare the difference between utilizing only the alloying reaction or both the conversion and alloying reaction, respectively. All composites were more stable when cycled up to only 1 V *vs.* Li^+/Li and when PSS was used as a binder, reaching up to 400 mAh g^{-1} after 50 cycles. Cyclic voltammetry and electrochemical impedance spectroscopy were also used to further electrochemically characterize these composite electrodes.

6.1 Introduction

In the previous chapter, tin oxide was discussed as a possible alloying-type and conversion-type material for a lithium-ion (Li^+ ion) battery anode. Tin oxide nanoparticles (SnONPs) were included into a carbon xerogel (CX) support in order to determine the stability, capacity, and other electrochemical and physico-chemical characteristics. The results from the synthesis in the previous chapter showed promising results and gave some interesting insights into the stability and mechanisms of the alloying and conversion reactions that take place with tin oxide. However, the SnO_2-doped CX discussed in the previous chapter still had problems with respect to (i) controlling the homogeneity of the tin oxide dopant distributed throughout the CX particles, (ii) controlling the size of the dopant particles, and (iii) sufficiently protecting the tin oxide dopant from degradation. These three problems likely led to the pulverization of the tin oxide dopant and excessive solid electrolyte interphase (SEI) formation as a result of the difference of volume between the lithiated and delithiated states of the tin oxide dopant [1-4].

In order to address these issues, the tin oxide dopant should somehow be more intimately and homogeneously incorporated within the CX particles. This would increase the ability of the CX to act as a mechanical support and be a good conductive path to the current collector. Therefore, a synthesis that does not depend on the diffusion of SnONPs into the CX but rather on the impregnation of a liquid precursor, similar to the technique expressed in Chapter 4 for silicon, was considered. This liquid precursor for tin oxide could then be subsequently transformed into solid tin oxide within the CX. This technique could potentially allow for a more homogenously distributed tin oxide phase throughout the porosity of the CX while also controlling the size of the dopant by controlling the average pore size of the CX.

The liquid precursor for tin oxide that was used to impregnate the CX after gelation and pyrolysis was an aqueous solution of sodium (IV) stannate trihydrate [5-8]. This precursor is ideal for impregnation into the CX particles given that it can easily undergo condensation in weak acidic environment into tin oxide *via* a simple sol-gel process [5, 8]. The aqueous nature of the precursor also makes it well-suited to impregnate the microporosity and meso/macroporosity of the CX given that the impregnation of the CX occurred more easily for aqueous solvents as compared to other solvents, like NMP, which was presented previously in Chapter 3 and 4. Equation 1.1 shows the sol-gel condensation reaction of an aqueous solution of sodium (IV) stannate trihydrate into tin oxide:

$$\mathrm{Na_2SnO_3 \cdot 3H_2O \xrightarrow{2H^+} SnO_2 + 2Na^+ + 4H_2O} \tag{6.1}$$

Similar to the CX sol-gel reaction, the morphology of the resultant tin oxide can be adjusted by tuning the precursor concentration, hydrolyzation and condensation parameters, as well as the solvent type [5, 8]. The two sol-gel techniques for CX and tin oxide synthesis could allow for a clean, easy, and cheap synthesis procedure while being able to precisely control of the morphology of the CX and tin oxide. The addition of the CX into the tin oxide sol-gel reaction will undoubtedly have an effect on the resultant tin oxide morphology. Therefore, the resultant CX-SnO_2 samples will be physico-chemically characterized *via* TEM imaging, X-ray diffraction (XRD), and N_2 adsorption.

As has been shown in previous chapters, PSS has the ability to improve the cycling stability of both silicon nanoparticles and tin oxide nanoparticles incorporated in a CX as a result of its unique electrochemical and physico-chemical properties, namely its ionic conductivity and water solubility. Therefore, in this chapter, CX-SnO_2 electrodes were prepared using either poly(vinylidene difluoride) (PVDF) or poly(sodium 4-styrene sulfonate) (PSS) as a binder for comparison. Electrochemical characterization of these CX-SnO_2 composite electrodes consisted of galvanostatic cycling, electrochemical impedance spectroscopy (EIS), and cyclic voltammetry (CV). These composites were cycled up to 1 V or 2 V *vs.* Li^+/Li to compare the difference between utilizing only the alloying reaction or both the conversion and alloying reaction, respectively.

6.2 Experimental

Materials: Resorcinol (R, 99%), formaldehyde (F, 37 wt% in H_2O), and poly(sodium 4-styrene sulfonate) (PSS, M_w = 70,000 g mol^{-1}) were purchased from Sigma-Aldrich. N-methyl-2-pyrrolidone (NMP, ~99%), sodium (IV) stannate trihydrate ($Na_2SnO_3 \cdot 3H_2O$), and poly(vinylidene difluoride) (PVDF) were purchased from Alfa Aesar. Nitric acid (65%, AnalaR NORMAPUR) was purchased from VWR.

6.2.1 CX sample: carbon xerogel synthesis

A carbon xerogel (CX) with an *R/C* ratio of 2000 was synthesized *via* the sol-gel polycondensation of resorcinol and formaldehyde in high purity water (*via* MilliQ process until R > 18 MΩ) [16-19]: see section 2.2.1 in Chapter 2 for the solution preparation, gelation, drying, ball-milling, and pyrolysis procedures. The specific capacity of the CX was either 165 mAh g^{-1} or 275 mAh g^{-1} when cycled up to either 1 V or 2 V *vs.* Li^+/Li, respectively (see Figure S5.1 in the supplemental information for the galvanostatic cycling and corresponding potential profiles).

6.2.2 CXSnO30/60 samples: SnO_2-doped carbon xerogel *via* impregnation of sodium stannate trihydrate precursor synthesis

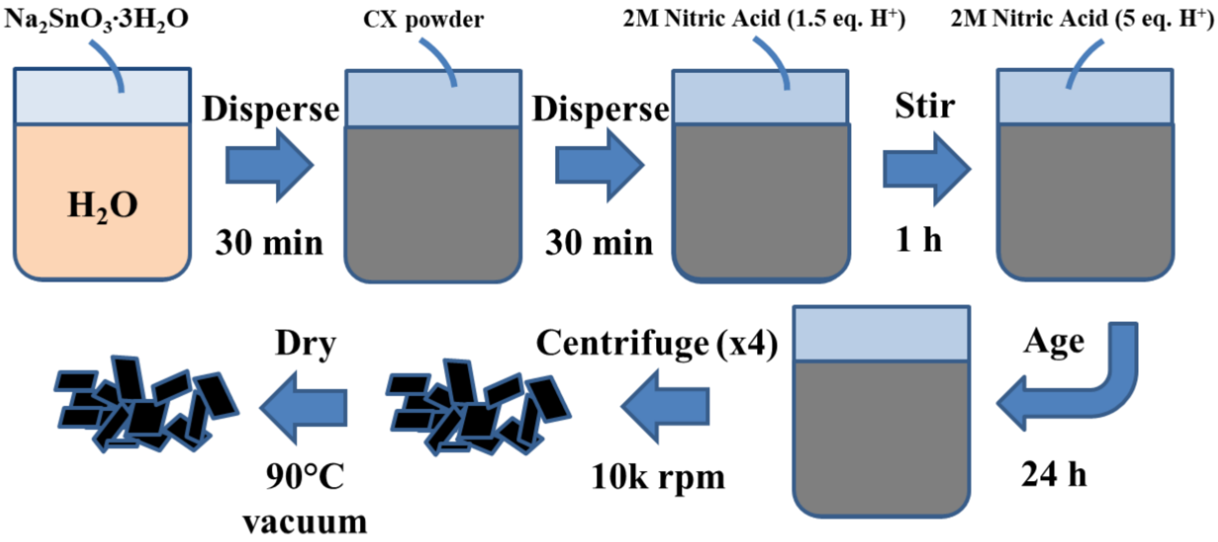

Figure 6.1 – Synthesis schematic of the CXSnO30/60 samples.

The synthesized CX sample was then doped with tin oxide *via* the impregnation of sodium stannate trihydrate (Na_2SnO_3-$3H_2O$) and subsequent condensation into tin oxide. A modification of an all-inorganic procedure, proposed by Beier *et al.* [5], was used to deposit tin oxide in the CX host matrix.

Two solutions with either 0.033 M or 0.066 M sodium stannate trihydrate in 50 mL of high purity water (*via* MilliQ process until R > 18 MΩ) were prepared under vigorous magnetic agitation set to 500 rpm. Then, 200 mg of the CX sample was dispersed into each solution and the mix was stirred for at least 30 min. Then, using 2 M nitric acid, 1.5 equivalents (eq.) H^+ ions per sodium stannate trihydrate molecule were quickly added to each solution while stirring. The solutions were stirred for at least 1 h after this first addition of nitric acid. The complete condensation of the sodium stannate trihydrate into tin oxide was induced by adding more 2 M nitric acid to the solutions, for a total amount of 5 eq. H^+ ions per sodium stannate trihydrate molecule. This final addition of nitric acid was also done under vigorous agitation. The stirring was stopped 5 min after this final addition of nitric acid and the two solutions were let to age for 24 h. The two samples were washed four times *via* centrifugation at 10,000 rpm for 10 min in high purity water (*via* MilliQ process until R > 18 MΩ) in order to remove the nitric acid and other non-reacted species. The two samples were then recovered after the last centrifugation and dried at 90°C at 1500 Pa for 24 h in a vacuum oven. The theoretical mass percent of tin oxide in the samples prepared with 0.033 M or 0.066 M sodium stannate trihydrate was 30 wt% or 60 wt% tin oxide, respectively. The samples will be referred to as CXSnO30 and CXSnO60, respectively, hereafter.

6.2.3 Preparation of inks and electrodes

Electrodes were processed using the CX, CXSnO30, and CXSnO60 samples as the active material with PVDF or PSS as a binder. First, ink slurries were prepared for subsequent electrode preparation and electrochemical characterization. The inks with PVDF as a binder were prepared by mixing 80 wt% of the active material and 20 wt% of PVDF in NMP. The inks with PSS as a binder were prepared by mixing 80 wt% of the active material and 20 wt% of PSS in high purity water (*via* MilliQ process until $R > 18\ M\Omega$). A solvent-to-solids ratio of 20:1 was used for both inks. The inks were magnetically stirred at 1000 rpm for 4 h before being spray-coated onto pre-weighed 15.5 mm diameter stainless steel disks. These disks were fixed on a 70°C heated surface. The coatings were deposited using a Harder & Steenbeck Evolution Silverline 2 airbrush. A high solvent-to-solids ratio was used to ensure that the prepared inks flowed easily through the airbrush. After spray-coating, the electrodes were dried at 70°C for 2 h and then at 120°C under vacuum overnight. The electrodes were then weighed to determine the mass of the deposited material prior to their electrochemical characterization. Excess dried material surrounding the electrodes, which was deposited around the disks during the spray-coating process, was collected for further characterization.

6.2.4 Physico-chemical and electrochemical characterization

Physico-chemical and electrochemical characterizations carried out in this chapter are outlined in Annex 1. The physico-chemical characterizations included nitrogen adsorption-desorption, transmission electron spectroscopy, and X-ray diffraction. N_2 adsorption was used to determine the BET surface area (S_{BET}) and the corresponding microporous (S_{micro}) and meso/macroporous (S_{ext}) surface areas of the CX and CXSnO30/60 samples as well as the CXSnO30/60 composites with PVDF or PSS as a binder. XRD and TEM with EDX analysis was used to determine the tin oxide crystallite size, particle size and distribution, elemental characterization, and crystallographic microstrain in the CXSnO30/60 samples with PSS as a binder.

Electrochemical characterization consisted of cyclic voltammetry (CV), galvanostatic cycling, and electrochemical impedance spectroscopy (EIS) on the CX and CXSnO30/60 composite electrodes. CV characterizations show the redox potentials of the electrochemically active components as well as how these reactions evolve during cycling; cycling gives the specific capacity and stability of the prepared composite electrodes. EIS analysis was used to determine how the equivalent series resistance (ESR), charge transfer resistance (R_{ct}), charge transfer capacitance (C_d) and the diffusive properties of the composite electrodes evolves during cycling. An overview of these parameters and the electrochemical model for these electrodes can be found in Annex 2.

The theoretical specific capacity of the CXSnO30 and CXSnO60 active material if both the conversion and alloying reactions take place (up to 2 V *vs.* Li^+/Li) would be approximately 563 mAh g^{-1} and 971 mAh g^{-1}, respectively, given that the specific capacity of the CX mentioned in section 7.3.1 is equal to 275 mAh g^{-1} [1-4]. If only the alloying reaction takes place (up to 1 V *vs.* Li^+/Li), the theoretical specific capacity of the CXSnO30 and CXSnO60 active material would be approximately 325 mAh g^{-1} and 476 mAh g^{-1}, respectively, given that the specific capacity of the CX mentioned in section 7.3.1 is equal to 165 mAh g^{-1} [1-4]. These theoretical values, summarized in Table 6.1, will be used as a comparison threshold for the real electrode performance. The C-rate used in the galvanostatic cycling is C/10 and is based on the theoretical specific capacities expressed in Table 6.1.

Table 6.1 – Summary of the theoretical specific capacities of the CXSnO30 and CXSnO60 samples when cycled up to either 1 V or 2 V vs. Li^+/Li.

Sample	**SnO_2** %	**CX** %	**Specific capacity 1 V** mAh g^{-1}	**Specific capacity 2 V** mAh g^{-1}
CX	0	100	165	275
CXSnO30	30	70	325[a]	563[b]
CXSnO60	60	40	476[a]	971[b]

[a]Assuming a specific capacity of 563 mAh g_{-1} for the tin oxide. [b]Assuming a specific capacity of 971 mAh g^{-1} for the tin oxide.

6.3 Results and discussion

6.3.1 Physico-chemical characterization

Transmission electron spectroscopy

TEM micrographs were obtained on the CX, CXSnO30, and CXSnO60 samples (Note: the CXSnO30 sample imaged in this section had already been process with PSS as a binder while the CXSnO60 sample is the powder before slurry preparation). Figure 1.1 in Chapter 1 shows the bare CX (*R/C* = 2000) at various magnifications and is followed by a description of the material. TEM micrographs of the CXSnO30 are shown in Figure 6.2. The tin oxide seems to have been deposited within the host CX matrix as nano-sized aggregates instead of defined nanoparticles, like what is observed for the tin oxide nanoparticles (SnONPs) used in Chapter 5. These aggregates are not of a specific size or shape and seem to be fairly heterogeneously distributed throughout the CX. The lack of facets on the deposited tin oxide aggregates observed in Figure 6.2 suggest that the deposited material does not have long range order, which is characteristic of an amorphous material. This is in contrast to the commercial SnONPs used in the previous chapter, which show faceted edges. TEM micrographs of CXSnO60 sample (Figure 6.3) also seem to show that tin oxide was deposited within the host CX matrix as larger nanoparticles than the CXSnO30 sample.

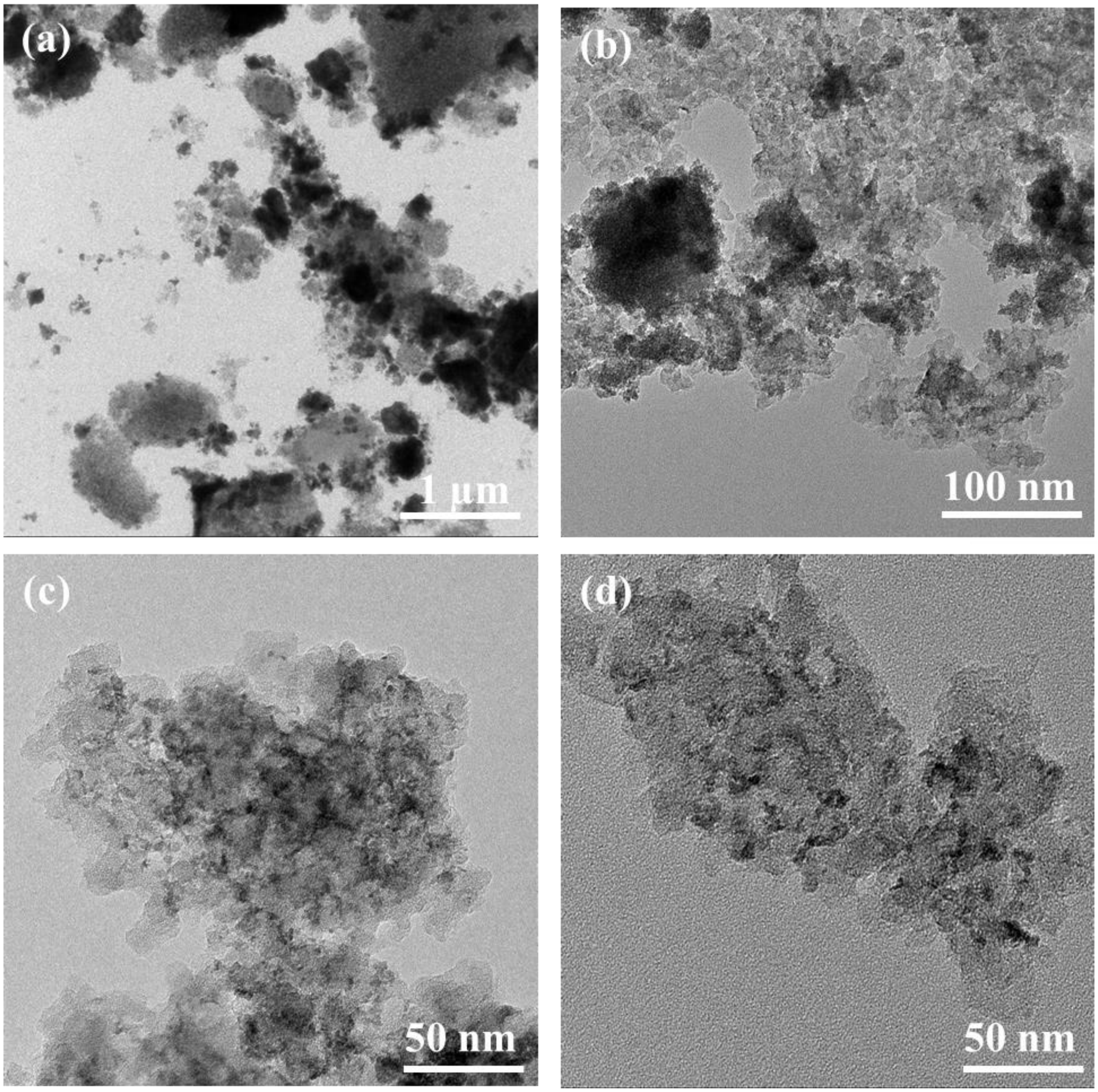

Figure 6.2 – TEM micrographs of the CXSnO30 sample with PSS as a binder at various magnifications.

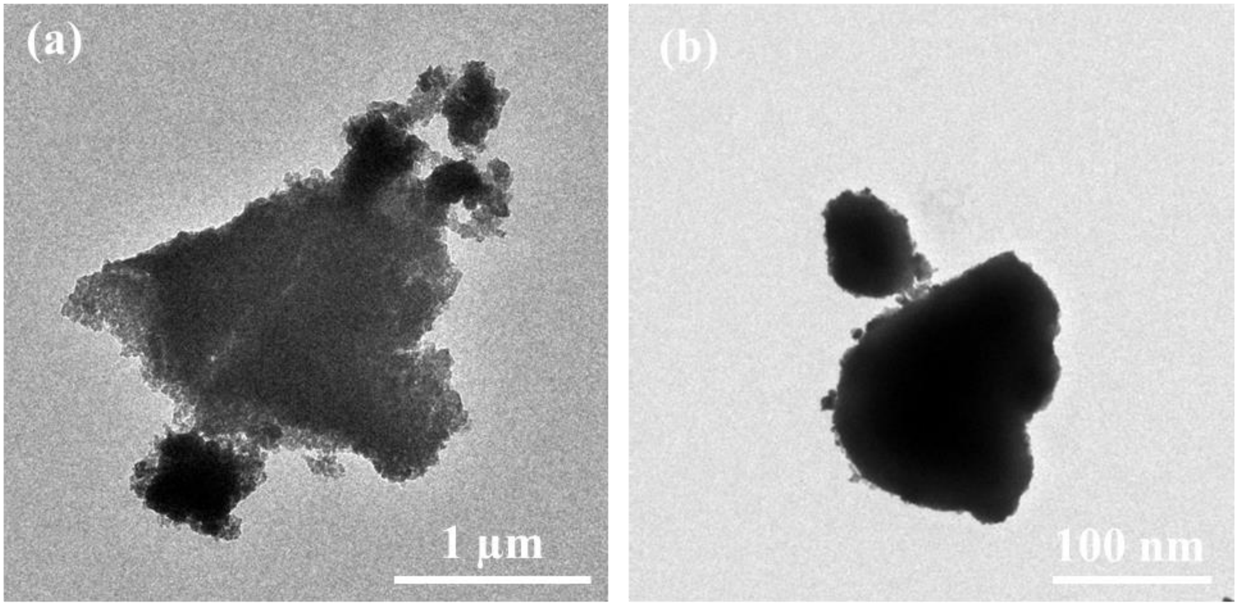

Figure 6.3 – TEM micrographs of CXSnO60 sample at various magnifications.

Figure 6.4 shows TEM bright field and dark field micrographs of individual grains of CXSnO30 and CXSnO60 samples. Figure 6.4a and c show the dark field micrographs of the CXSnO30 and CXSnO60 samples, respectively. In these micrographs, the lighter regions correspond to higher atomic mass elements. Therefore, since the micrograph consisted of primarily carbon and tin oxide, the brighter regions are likely rich in tin and oxygen while the darker region is likely primarily consisting of carbon. Similarly, Figure 6.4b and d show the bright field micrographs of the sample CXSnO30 and CXSnO60 particles, respectively. In these micrographs, the tin oxide phase can be identified by the darker regions dispersed throughout the CX particle.

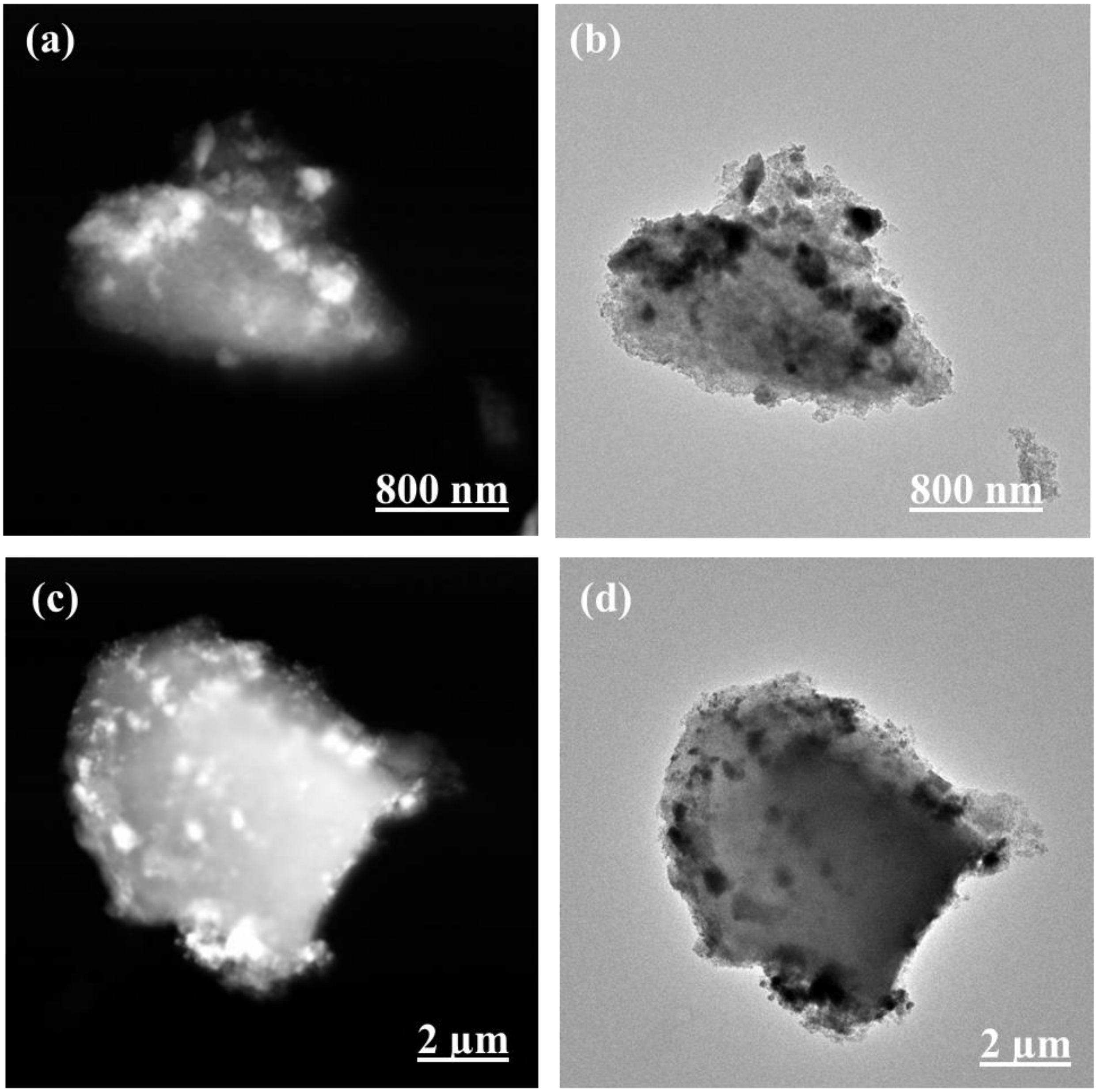

Figure 6.4 – (a) TEM dark field micrograph and (b) bright field micrograph and of the CXSnO30 sample with PSS as a binder. (c) TEM dark field micrograph and (d) bright field micrograph and of CXSnO60 sample.

Elemental analysis of the CXSnO30 and CXSnO60 samples pictured in Figure 6.4 were conducted via EDX analysis in the TEM and the spectra are shown in Figure 6.5 and Figure 6.6, respectively. These spectra clearly show the presence of tin oxide, as shown by the labeled X-ray energy peaks related to tin and oxygen. The additional peaks corresponding to sulfur and sodium in Figure 1.4 are likely a result of the fact that the CXSnO30 powder analyzed had already been processed with PSS. The copper peaks are likely due to the fact the TEM microgrid is made of copper.

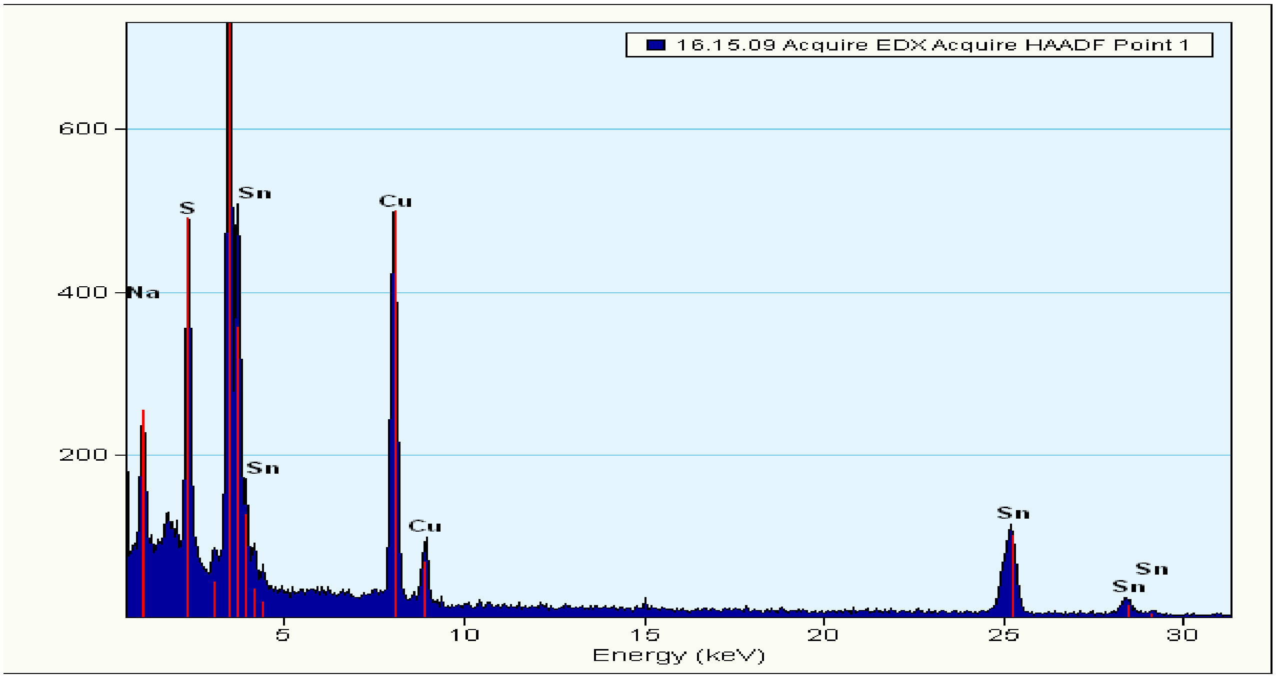

Figure 6.5 – EDX compositional analysis of the CXSnO30 (composite sample with PSS as a binder).

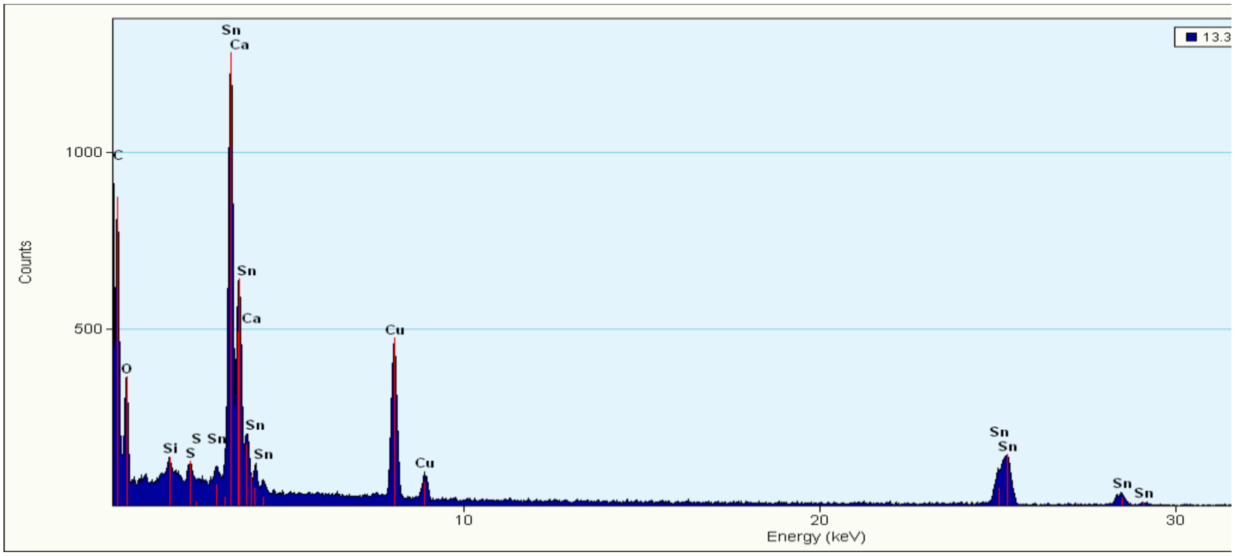

Figure 6.6 – EDX compositional analysis of the CXSnO60 sample (no binder present).

X-ray diffraction

XRD patterns of the CX and CXSnO30 samples are shown in Figure 6.7. The diffraction pattern of the CX sample, similar to previous chapters, shows the same wide peaks at around 2θ angles of 15°, 30°, and 42°. As discussed previously, the peak at 15° may be related to oxygenate graphitic sheets, similar to graphene oxide or graphite oxide, while the peak at 30° may be just related to the amorphous nature of the CX [9-11]. The peak at a 2θ angle of 42° likely corresponds to the C(001) [9-11]. The XRD pattern of the CXSnO30 sample shows the presence of some other material, which is likely tin oxide; however, the peaks exhibited a high degree of line broadening that makes the identification of the material more difficult.

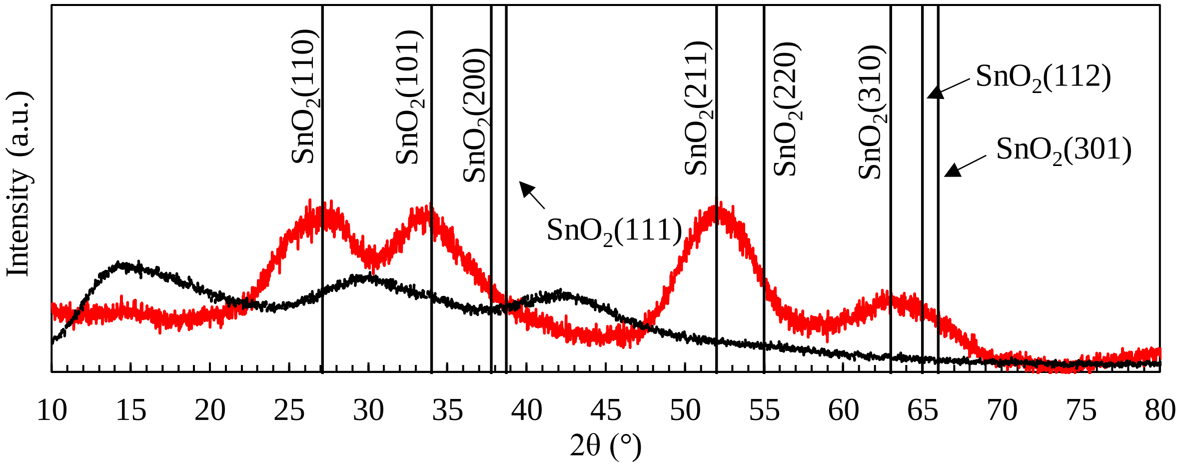

Figure 6.7 – XRD patterns of (▬) the bare CX without any dopant and (▬) sample CXSnO30.

The calculation of the Williamson-Hall plot of the CXSnO30 sample proved to be difficult as well given that the significant line broadening caused some of the diffraction peaks to overlap. Nevertheless, deconvolution of the tin oxide diffraction peaks at SnO_2(110), SnO_2(101), SnO_2 (200), SnO_2(111), SnO_2(211), SnO_2(220), SnO_2(311), SnO_2(112), and SnO_2(301) was conducted using the LIPRAS software and the procedure outlined in Annex 1 [12-14]. The fitting of the deconvolutions performed are shown in Figure S6.2. The Williamson-Hall plot in Figure 6.8 showed that the microstrain in the crystal lattice was found to be -1.8% when considering Equation A1.4 and the slope of the least squares regression fit in Figure 6.8. Similar to the results obtained for the magnesiothermally reduced silica in Chapter 4, it is unclear what the meaning of this negative microstrain signifies. The slope of the least squares regression fit is a measure of the variance of lattice parameters from their normal positions in the tin oxide phase; therefore, the microstrain of a material cannot be negative by definition [15-17]. It is thus likely that either (i) the significant line broadening caused systematic error in the deconvolution of the constituent diffraction peaks, or (ii) there is some type of anisotropic strain in the tin oxide phase. However, it is difficult to determine the actual cause of this negative microstrain value. The crystallite size of the tin oxide phase was determined to be 1.5 nm, considering equation A1.4 and the y-axis intercept of the least squares regression fit in Figure 6.8. This confirms that the tin oxide phase is almost amorphous in nature given that extremely small crystallographic domain sizes are observed.

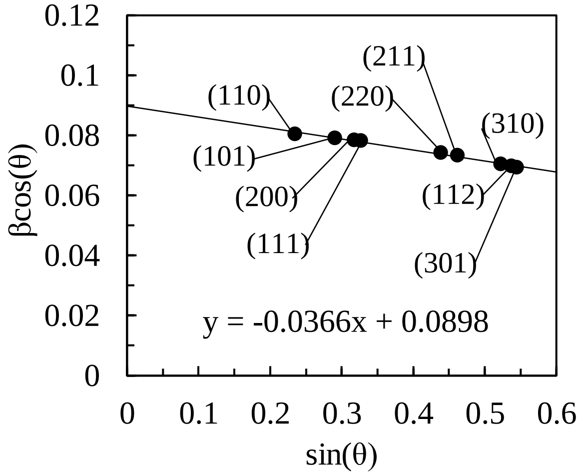

Figure 6.8 – Williamson-Hall plot for the tin oxide diffraction peaks in the CXSnO30 sample.

Nitrogen adsorption-desorption analysis

N_2 adsorption-desorption isotherms of the CX, CXSnO30, and CXSnO60 samples, measured on the powders, are shown in Figure 6.9a. The N_2 isotherms of these samples correspond mostly to a type I/IV isotherm, which corresponds to a material composed of both micropores as well as large meso/macropores. All three isotherms exhibit a small hysteresis during the desorption step, showing the presence of large mesopores.

Figure 6.9b shows the specific surface area, S_{BET}, divided into the constituent microporous surface area, S_{micro}, and meso/macroporous surface area, S_{ext}, of these samples. The S_{BET} of the CX was measured to be 707 m^2 g^{-1} with the constituent S_{micro} and S_{ext} equal to 444 m^2 g^{-1} and 263 m^2 g^{-1}, respectively. The S_{BET} of the CXSnO30 sample was measured to be 536 m^2 g^{-1} with the constituent S_{micro} and S_{ext} equal to 236 m^2 g^{-1} and 300 m^2 g^{-1}, respectively. The S_{BET} of the CXSnO60 sample was measured to be 326 m^2 g^{-1} with the constituent S_{micro} and S_{ext} equal to 115 m^2 g^{-1} and 211 m^2 g^{-1}, respectively.

The N_2 isotherms of the CXSnO30 and CXSnO60 samples evidence that the tin oxide phase occupies the micropores of the CX rather than being deposited only in the meso/macro-porosity of the CX given that the S_{micro} decreased as the quantity of tin oxide increased. Furthermore, the amount of S_{ext} remained relatively constant as the quantity of tin oxide increased. The fraction of the surface area that is microporous decreases from 63% for the bare CX to 44% and 42% for the CXSnO30 and CXSnO60 samples, respectively. A summary of the N_2 adsorption-desorption data is given in Table 6.2.

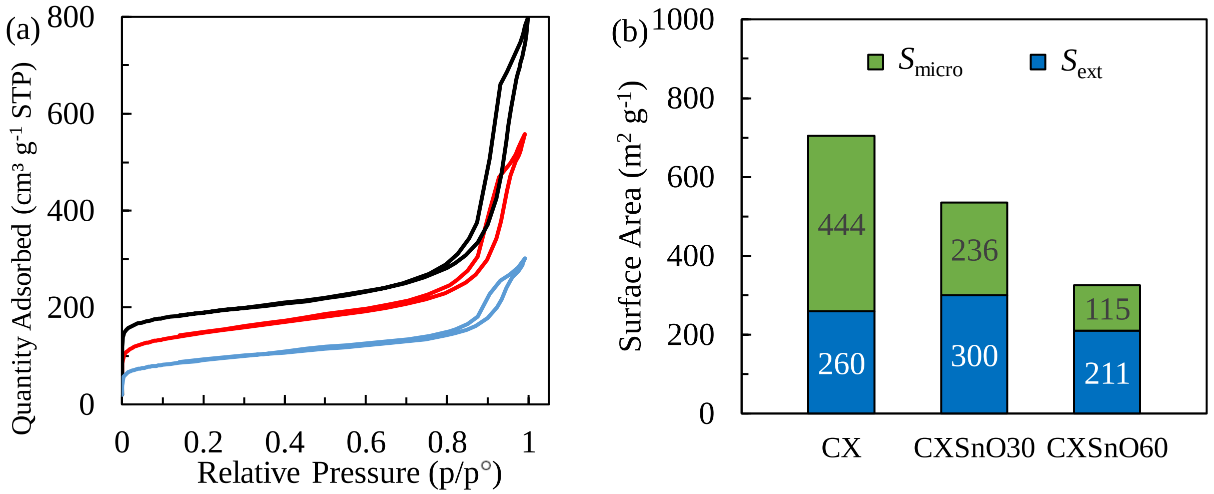

Figure 6.9 – (a) N$_2$ adsorption-desorption isotherms for (▬) the CX, (▬) CXSnO30, and (▬) CXSnO60 powder samples without binder. (b) Corresponding specific surface area (S_{BET}) divided into the constituent microporous surface area (S_{micro}) and meso/macroporous surface area (S_{ext}).

Table 6.2 – Nitrogen adsorption-desorption data for the CX, CXSnO30, and CXSnO60 powder samples without binder.

Sample	**S_{micro}** (m^2 g^{-1})	**S_{ext}** (m^2 g^{-1})	**S_{BET}** (m^2 g^{-1})	**% microporous surfaces**
CX	444	260	704	63%
CXSnO30	236	300	536	44%
CXSnO60	155	211	366	42%

N$_2$ adsorption-desorption isotherms for the CX, CXSnO30, and CXSnO60 composite samples (*i.e.* recovered after electrode preparation) with either PSS or PVDF as a binder were collected and are shown in Figure 6.10a, b, and c, respectively. Figure 6.10d shows the specific surface areas for these 6 samples divided into the constituent S_{micro} and S_{ext}. As expected, the samples with PSS as a binder retained more microporosity than the same samples with PVDF as a binder. For the samples with PVDF as a binder, as the quantity of tin oxide increased, the amount of microporosity that was retained also increased. Contrarily, for the samples with PSS as a binder, the amount of microporosity that was retained decreased as the quantity of tin oxide increased. This result suggests that the tin oxide phase likely changes the way the binder, whether it be PSS or PVDF, interacts with the porosity of the active material.

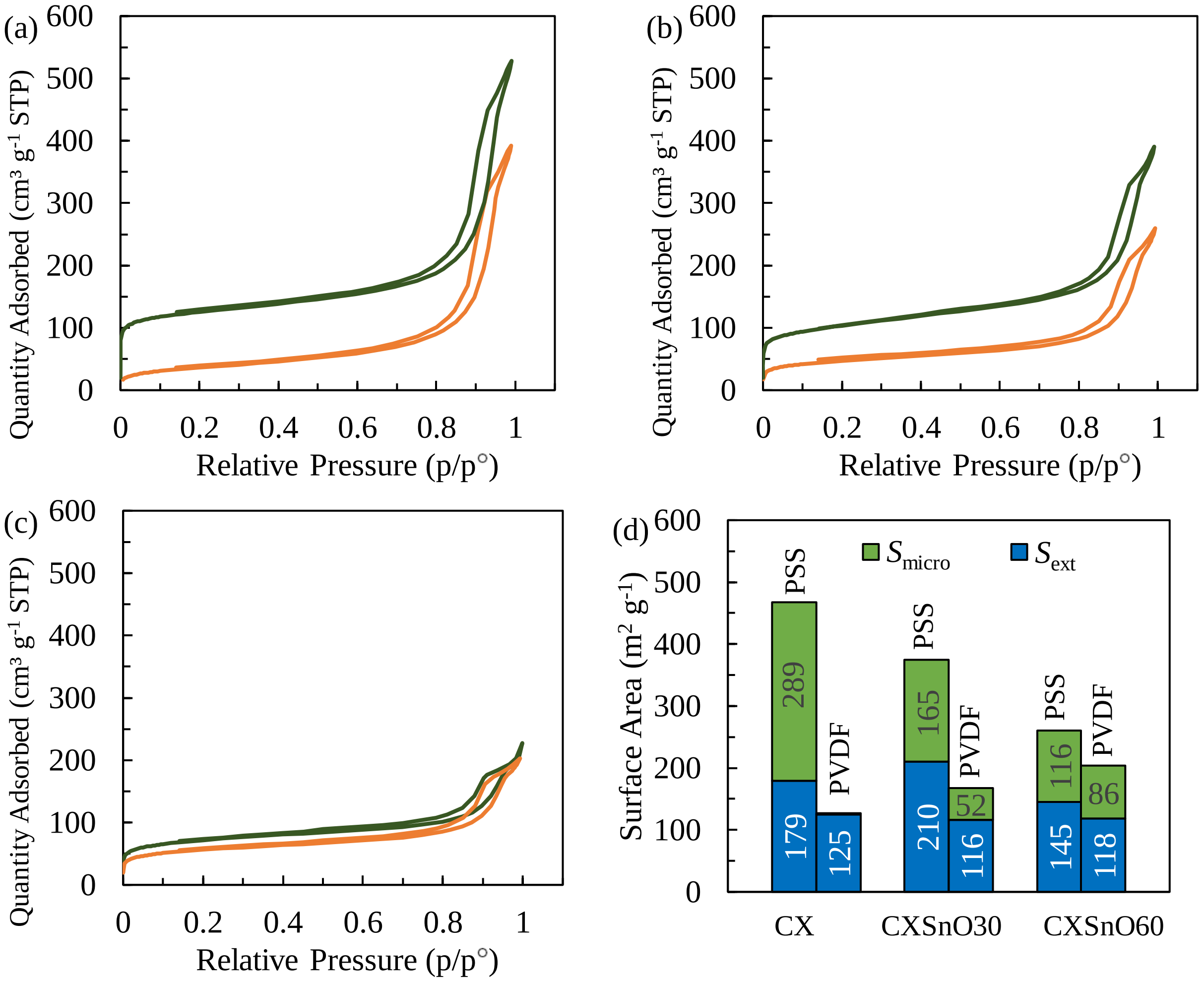

Figure 6.10 – N_2 adsorption-desorption isotherms for (a) the CX, (b) CXSnO30 sample and, (c) CXSnO60 sample with either (—) PVDF as a binder or (—) PSS as a binder (*i.e.* recovered after electrode preparation). (d) Corresponding specific surface areas (S_{BET}) divided into the constituent microporous surface area (S_{micro}) and meso/macroporous surface area (S_{ext}).

Table 6.3 – Nitrogen adsorption-desorption data for the CX, CXSnO30, and CXSnO60 composite samples with either PVDF or PSS as a binder.

	S_{BET} ($m^2\ g^{-1}$)		S_{ext} ($m^2\ g^{-1}$)		S_{micro} ($m^2\ g^{-1}$)	
	PVDF	**PSS**	**PVDF**	**PSS**	**PVDF**	**PSS**
CX	125	468	125	179	0	289
CXSnO30	168	375	116	210	52	165
CXSnO60	204	261	118	145	86	116

6.3.2 Electrochemical characterization

Cyclic voltammetry

Cyclic voltammetry of the CXSnO30 and CXSnO60 composite electrodes with either PVDF or PSS as a binder are shown in Figure 6.11 through Figure 6.14. These CV measurements were conducted up to either (a) 1 V or (b) 2 V *vs.* Li^+/Li to highlight any differences in the cycling stability and redox potentials. For all the composite electrodes, the pristine discharge exhibited two weak lithiation peaks at around 1 V and 0.5 V *vs.* Li^+/Li, which are likely related to the degradation of the electrolyte and formation of the solid-electrolyte interphase (SEI) [1-4]. These peaks can be compared with the SEI formation peak in the CX doped with tin oxide nanoparticles (SnONPs) in the previous chapter, which exhibited a single, stronger lithiation peak at 0.8 V *vs.* Li^+/Li. This difference may be a sign that the surface of the tin oxide in these samples are less exposed directly to the electrolyte and, therefore, only the response of the SEI formation on the CX and only some of the tin oxide surface is observed. The conversion reaction from tin oxide into tin occurs above 0.8 V *vs.* Li^+/Li along with the additional formation of Li_2O, as shown in Equation 5.1 in Chapter 5 [1-4]. The tin-lithium alloying reaction occurs below 0.8 V *vs.* Li^+/Li with a strong lithiation peak at 0.12 V *vs.* Li^+/Li.

For the 5th and 10th cycles, the composite electrodes cycled up to 2 V *vs.* Li^+/Li show the conversion reaction peaks at 1 V and 1.25 V *vs.* Li^+/Li, respectively, while the Li-Sn alloying reaction peaks occur at 0.12 V and 0.5 V *vs.* Li^+/Li, respectively. The composite electrodes cycled up to 1 V *vs.* Li^+/Li showed only the two Li-Sn alloying reaction lithiation/delithiation peaks. The CXSnO30 composite electrode with PVDF as a binder cycled up to 2 V *vs.* Li^+/Li (Figure 6.11b) showed more degradation (*i.e.* a decrease in the intensity of each respective peak) in both the alloying and conversion peaks for the 5th and 10th cycle as compared to the same composite electrode cycled up to only 1 V *vs.* Li^+/Li (Figure 6.11a). Similar responses were observed for the CXSnO30/60 composite electrodes with PSS as a binder (Figure 6.12 and Figure 6.14). The CXSnO60 composite electrode with PVDF as a binder showed the worst stability during cycling when cycled up to either 1 V (Figure 6.13a) or 2 V (Figure 6.13b) *vs.* Li^+/Li, as exhibited by the rapid loss of intensity of both the alloying and conversion peaks.

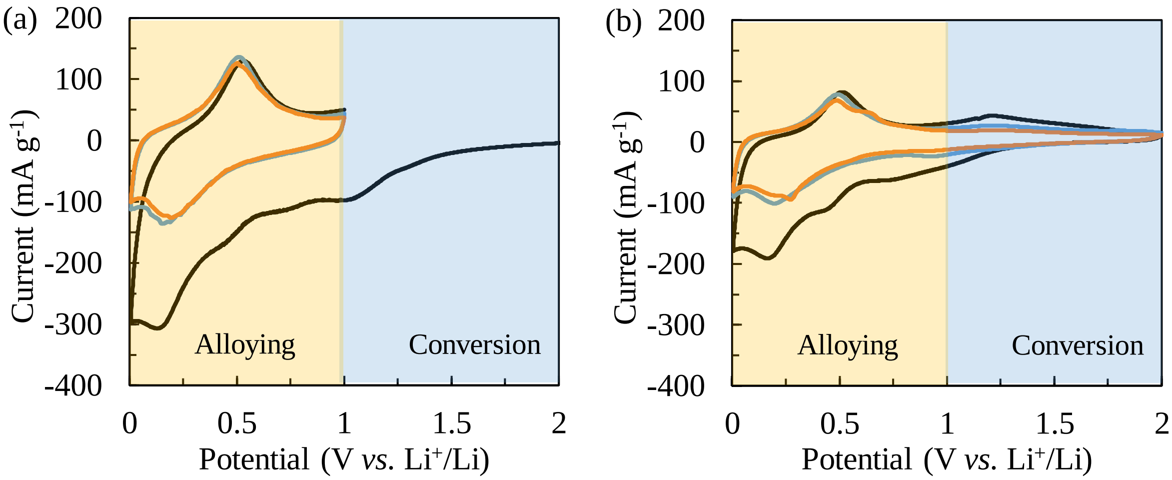

Figure 6.11 – Cyclic voltammetry between (a) 0.005 V and 1 V *vs.* Li$^+$/Li and (b) 0.005 V and 2 V *vs.* Li$^+$/Li of the CXSnO30 composite electrodes with PVDF as a binder. Shown for the (▬) pristine, (▬) 5th, and (▬) 10th cycle. The scan rate was 50 μV s^{-1}.

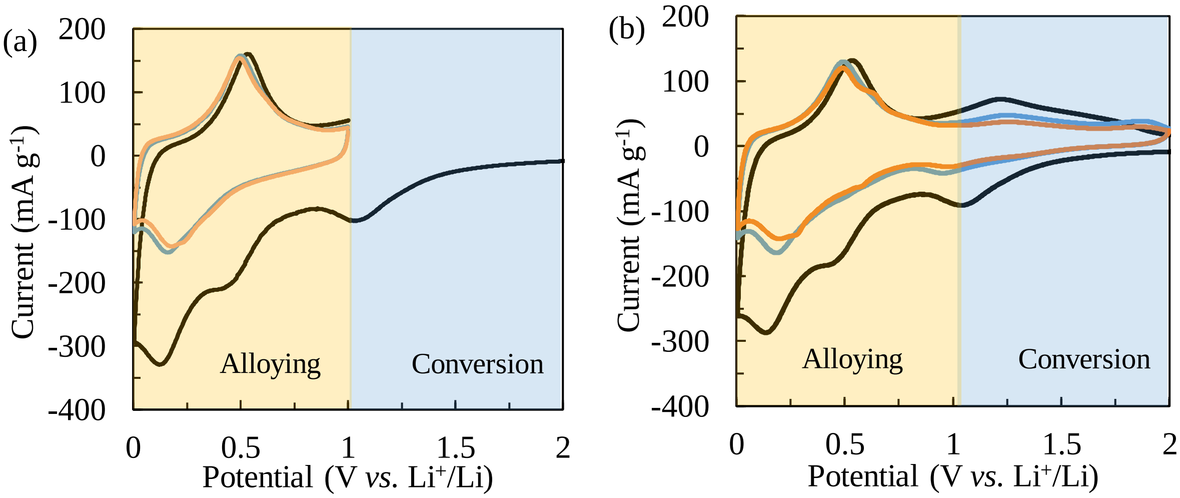

Figure 6.12 – Cyclic voltammetry between (a) 0.005 V and 1 V *vs.* Li$^+$/Li and (b) 0.005 V and 2 V *vs.* Li$^+$/Li of the CXSnO30 composite electrodes with PSS as a binder. Shown for the (▬) pristine, (▬) 5th, and (▬) 10th cycle. The scan rate was 50 μV s^{-1}.

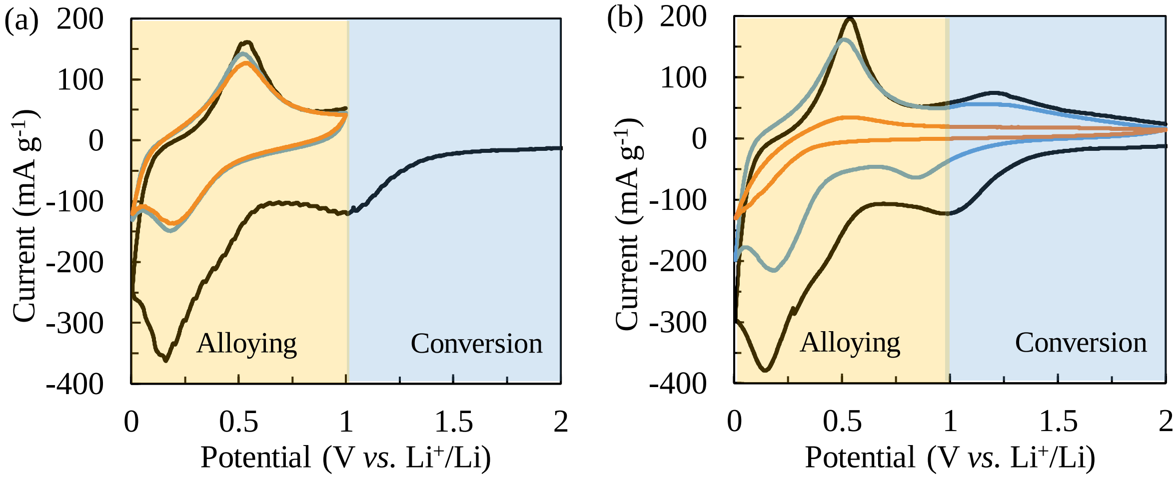

Figure 6.13 – Cyclic voltammetry between (a) 0.005 V and 1 V *vs.* Li$^+$/Li and (b) 0.005 V and 2 V *vs.* Li$^+$/Li of the CXSnO60 composite electrodes with PVDF as a binder. Shown for the (▬) pristine, (▬) 5th, and (▬) 10th cycle. The scan rate was 50 μV s^{-1}.

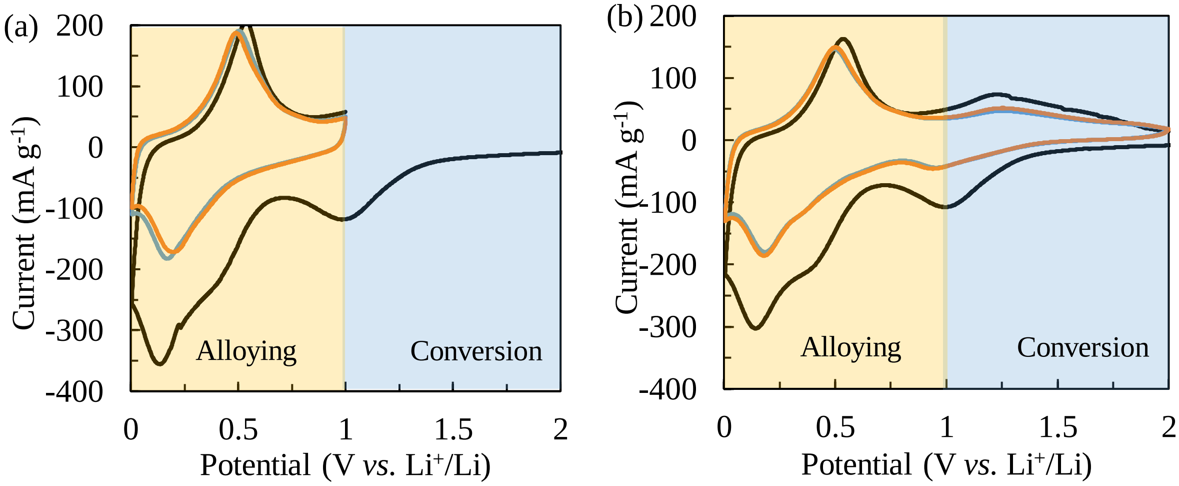

Figure 6.14 – Cyclic voltammetry between (a) 0.005 V and 1 V *vs.* Li$^+$/Li and (b) 0.005 V and 2 V *vs.* Li$^+$/Li of the CXSnO60 composite electrodes with PSS as a binder. Shown for the (▬) pristine, (▬) 5th, and (▬) 10th cycle. The scan rate was 50 μV s^{-1}.

Galvanostatic cycling

Galvanostatic cycling of the CXSnO30 and CXSnO60 composite electrodes further confirms both the irreversible and unstable nature of the conversion reaction as well as the reversibility of the Sn-Li alloying reaction. Figure 6.15and 6.15b show the galvanostatic cycling of the CXSnO30 composite electrode with either PVDF or PSS as a binder, respectively. The initial capacity of all the CXSnO30 composite electrodes reached their expected theoretical capacity. The CXSnO30 composite electrode with PSS as a binder cycled up to 1 V *vs.* Li$^+$/Li, *i.e.* only the Sn-Li alloying reaction, maintained more than 80% of the initial capacity after 78 cycles while the same composite electrode cycled up to 2 V *vs.* Li^{+}/Li maintained 80% of the initial capacity after only 11 cycles. The CXSnO30 composite electrode cycled up to 1 V *vs.* Li^{+}/Li was more stable with PSS as binder (Figure 6.15b) as compared to with PVDF as a binder (Figure 6.15a).

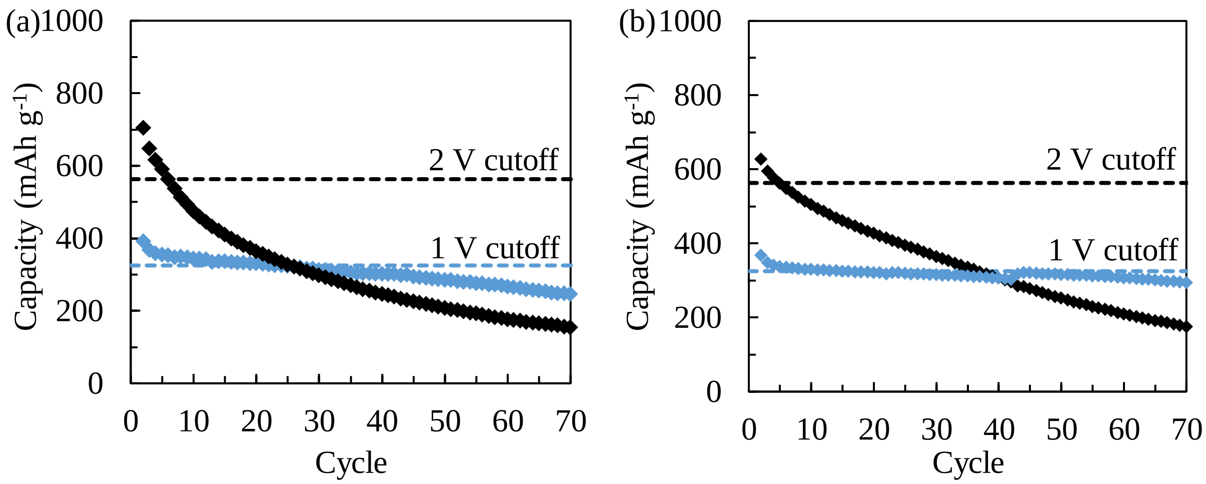

Figure 6.15 – Specific capacity during galvanostatic cycling of the CXSnO30 composite electrode with either (a) PVDF as a binder or (b) PSS as a binder. Cycling at a rate of C/10 up to (◆) 1 V *vs.* Li^{+}/Li or (◆) 2 V *vs.* Li^{+}/Li. Dotted lines represent the theoretical capacity for these composite electrodes cycled up to either (---) 1 V *vs.* Li^{+}/Li or (---) 2 V *vs.* Li^{+}/Li.

Figure 6.16a and b show the galvanostatic cycling of the CXSnO60 composite electrode with either PVDF or PSS as a binder, respectively. The initial capacity of all the CXSnO60 composite electrodes did not reach their expected theoretical capacity. Additionally, the cycling stability of all the CXSnO60 composite electrodes were less stable than their CXSnO30 composite electrode counterparts. The CXSnO60 composite electrode with PSS as a binder cycled up to 1 V *vs.* Li^{+}/Li, *i.e.* only the Sn-Li alloying reaction, maintained 80% of the initial capacity after 8 cycles while the same composite electrode cycled up to 2 V *vs.* Li^{+}/Li maintained 80% of the initial capacity after 11 cycles. The CXSnO60 composite electrode with PSS as a binder (Figure 6.16a) was more stable than the same electrode with PVDF as a binder (Figure 6.16b) when cycled up to 1 V *vs.* Li^{+}/Li, albeit less stable than all the CXSnO30 composite electrodes. A summary of the cycling stability of the CXSnO30/60 composite electrodes are shown in Figure 6.17.

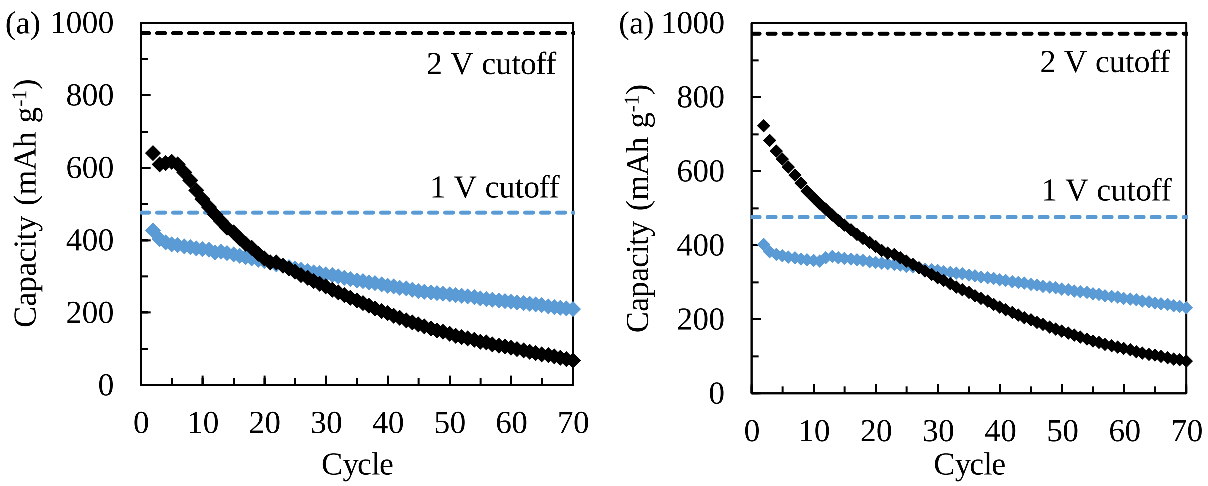

Figure 6.16 – Specific capacity during galvanostatic cycling of the CXSnO60 composite electrode with either (a) PVDF as a binder or (b) PSS as a binder. Cycling at a rate of C/10 up to (◆) 1 V *vs.* Li^+/Li or (◆) 2 V *vs.* Li^+/Li. Dotted lines represent the theoretical capacity for these composite electrodes cycled up to either (---) 1 V *vs.* Li^+/Li or (---) 2 V *vs.* Li^+/Li.

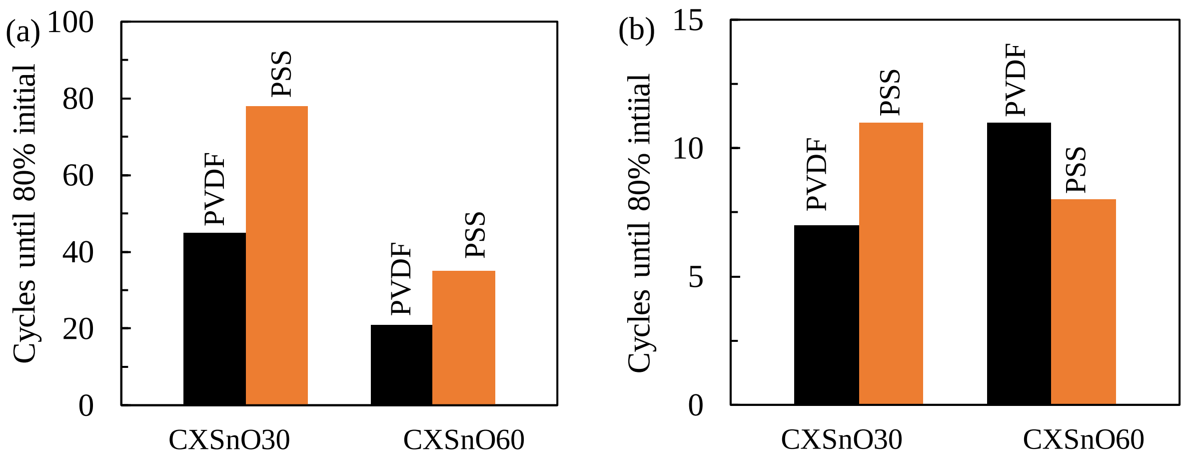

Figure 6.17 – Number of cycles before composite electrodes with either PVDF or PSS as a binder reached 80% initial capacity. Composite electrodes cycled up to either (a) 1 V or (b) 2 V *vs.* Li^+/Li.

Figure 6.18 shows the potential profile with respect to the capacity of the CXSnO30 composite electrodes with PSS as a binder with the regions corresponding to the tin oxide conversion reaction and Sn-Li alloying reaction denoted. For the composite electrode cycled up to 1 V *vs.* Li^+/Li, the reversibility of the Sn-Li alloying reaction appears fairly good, only showing a noticeable loss of capacity between the 20th and 50th cycles. (Figure 6.18a). However, when the composite electrode is cycled up to 2 V *vs.* Li^+/Li (Figure 6.18b), the alloying reaction, *i.e.* the capacity which occurs below 1 V *vs.* Li^+/Li, is less stable, as shown by the loss of capacity below 1 V *vs.* Li^+/Li occurring after only the 20th cycle. The loss of capacity due to the conversion reaction, *i.e.* above 2 V *vs.*

Li^+/Li, is also as rapid as or slightly more rapid than the loss of capacity of the alloying reaction. Similar trends were observed for the CXSnO30 composite electrode with PVDF as a binder (Figure S6.3) as well as the CXSnO60 composite electrodes with either PSS (Figure S6.4) and PVDF (Figure S6.5) as a binder.

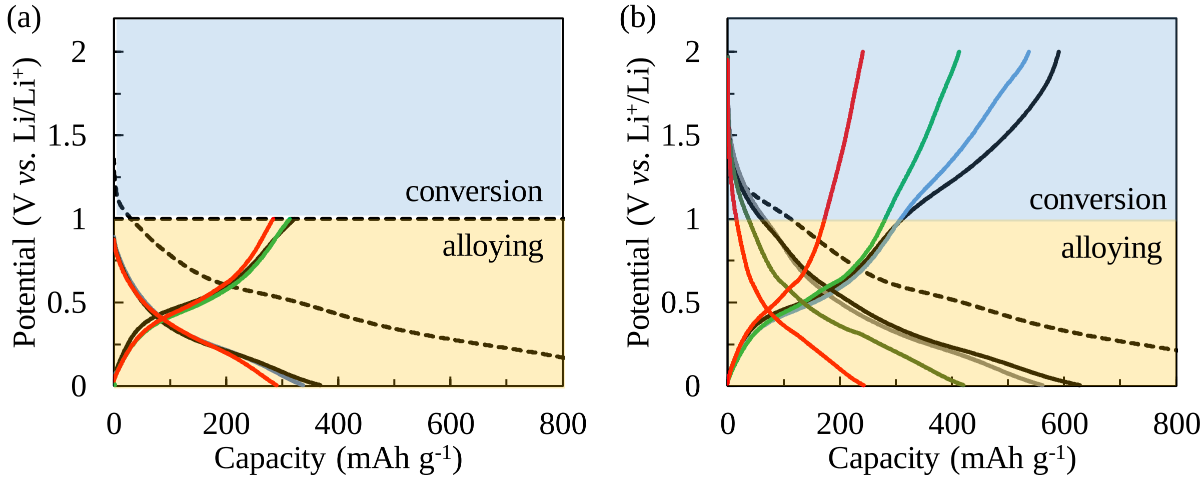

Figure 6.18 – Potential profiles for the CXSnO30 composite electrode with PSS as a binder. Cycling at a rate of C/10 up to (a) 1 V and (b) 2 V *vs.* Li^+/Li. Shown for the (---) 1st discharge, (▬) 1st cycle (▬) 5th cycle, (▬) 20th cycle, and (▬) 50th cycle.

Electrochemical impedance spectroscopy

EIS spectra for the CXSnO30 and CXSnO60 composite electrodes with either PVDF or PSS as a binder cycled up to 2 V *vs.* Li^+/Li are shown in Figure 6.20 through Figure 6.21. The Randles cell electrochemical model is shown in Annex 2 that outlines the pertinent electrochemical elements, such as the equivalent series resistance (ESR), charge transfer resistance (R_{ct}) and capacitance (C_d), and diffusion characteristics that should apply to these CX-based half cells.

The Nyquist plots and Bode diagrams of the CXSnO30 composite electrode with PVDF as a binder cycled up to 2 V *vs.* Li^+/Li are shown in Figure 6.19a and 6.19b, respectively. The Nyquist plots, shown in Figure 6.19a, exhibited a progressively increasing diameter of the charge transfer half circle between the pristine and 50th cycle. In the Bode diagram, this corresponds to a mid-frequency phase shift that no longer approaches 0°, but rather approaches -30° to -45°. The diffusion region response, which takes place at low frequency in the Bode diagram, shows a change in the phase shift from approaching -90° to approaching -45° between the pristine and 50th cycle, similar to the CXSnO30 composite electrode with PSS as a binder.

The ESR of this composite electrode also exhibits a similar stability during cycling as the CXSnO30 composite electrode with PSS as a binder. The ESR was maintained around 4 Ω to 5 Ω between the pristine and 50th cycle. The R_{ct} and C_d of this composite electrode, however, exhibit a notable different response than the CXSnO30 composite electrode with PSS as a binder. The R_{ct} progressively increased between the pristine and 50th cycle, from 100 Ω m^{-2} to 950 Ω m^{-2}. The increase in R_{ct} is a sign that charges are less easily transferred between the electrolyte and the active material. Similar to the CXSnO30 composite electrode with PSS as a binder, however, the C_d of the same composite electrode with PVDF as binder increased during the first 5 cycles; this was followed by a progressive decrease until the 50th cycle. This suggests that the active layer is at least as stable mechanically during cycling as the CXSnO30 composite electrode with PSS as a binder. Nevertheless, some transformation at the interface of the electrolyte and active material is still occurring. This is likely due to the pulverization of the active material and excessive SEI buildup, which is caused by the volume change of the tin oxide phase during lithiation/delithiation.

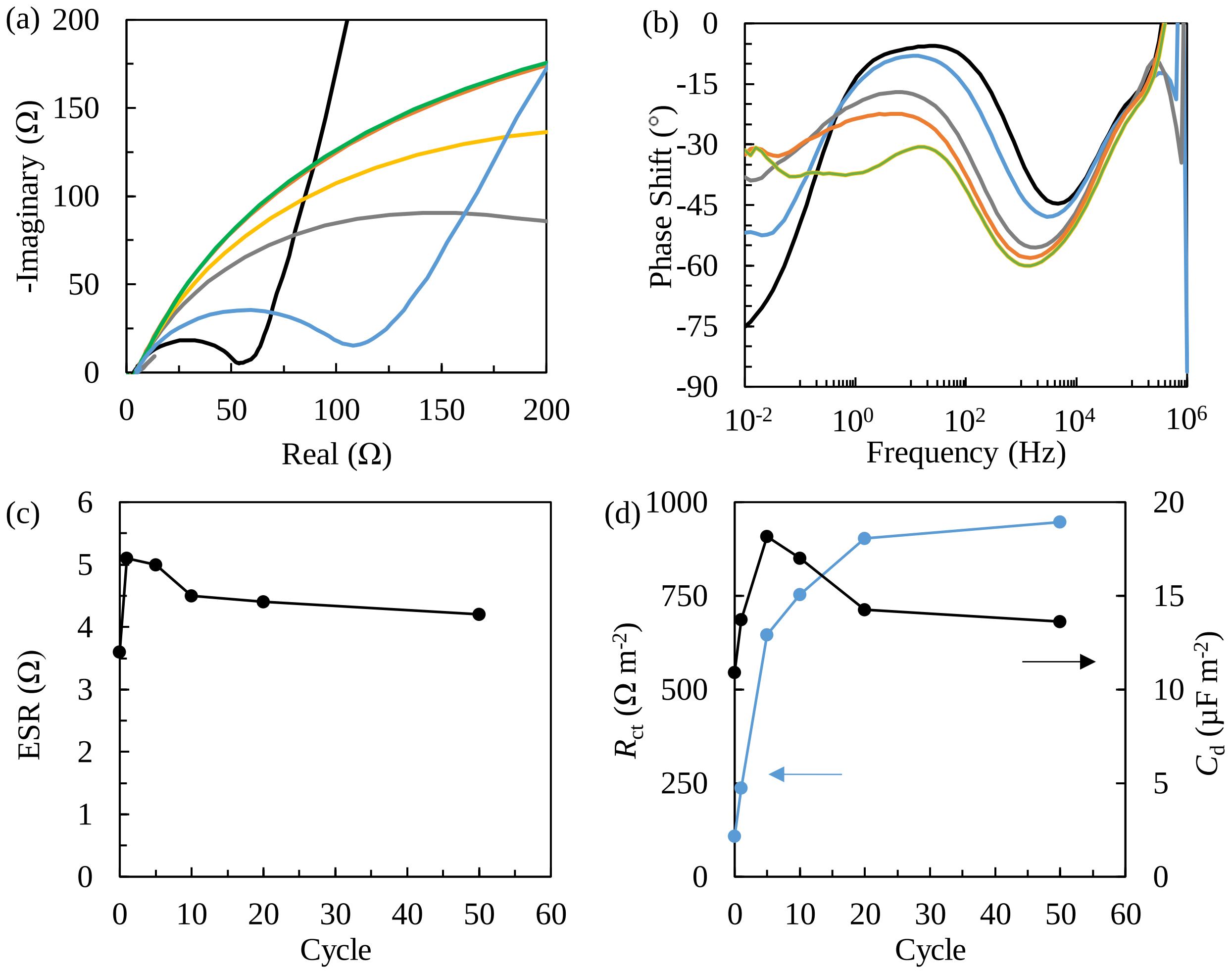

Figure 6.19 – EIS analysis of the CXSnO30 composite electrode with PVDF as a binder cycled between 0.005 V and 2 V *vs.* Li$^+$/Li. (a) Nyquist plot and (b) Bode diagram. (—) Pristine, (—) 1st, (—) 5th, (—) 10th, (—) 20th, and (—) 50th cycle. (c) ESR as a function of galvanostatic cycles. (d) Charge transfer resistance (R_{ct}) per specific surface area and charge transfer capacitance (C_d) per specific surface area as a function of galvanostatic cycles. Scan between 1 MHz and 100 mHz with 10 points per decade. Voltage amplitude of 10 mV.

The Nyquist plots and Bode diagrams of the CXSnO30 composite electrode with PSS as a binder cycled up to 2 V *vs.* Li$^+$/Li exhibited a notably different response than the CXSnO30 composite electrode with PVDF as binder. The Nyquist plot shows a continuously changing response during cycling. Notably, the diameter of the charge transfer half circle becomes smaller between the pristine and 1st cycle, followed by a continuously increasing diameter between the 1st and 50th cycle. In the Bode diagram, the diffusion region response, which takes place at low frequency, shows a change in the phase shift from approaching -90° to approaching -45° between the pristine and 50th cycle. As has been discussed in previous chapters, the formation of an SEI allows for the more facile transfer of Li$^+$ ions into the active material without causing further decomposition of the electrolyte [18]. This SEI layer therefore causes a change from a capacitive (phase shift = -90°) to diffusive response (phase shift = -45°) at low frequency.

The ESR, shown during cycling in Figure 6.20c, decreases from the pristine to the 1st cycle, followed by a gradual increase until 50th cycle from 3.5 Ω and 4.1 Ω. The evolution of R_{ct} during cycling is shown in Figure 6.20d: it decreased from 25 Ω m^{-2} to 10 Ω m^{-2} between the pristine and 1st cycle. Then between the 1st and 50th cycle, the R_{ct} increased gradually from 10 Ω m^{-2} to 25 Ω m^{-2}. This is evidence that the PSS facilitates the transfer of charge between the electrolyte and the active material. The C_d increased from 9 µF m^{-2} to 30 µF m^{-2} between the pristine and 1st cycle, followed by a gradual decrease of C_d to 20 µF m^{-2} for the 50th cycle. The relatively stable values of ESR, R_{ct}, and C_d after the pristine discharge of the CXSnO30 composite electrode with PSS as a binder as compared to the CXSnO30 composite electrode with PVDF as a binder are a sign that the morphology of the interface between the electrolyte and the active layer is relatively stable during cycling.

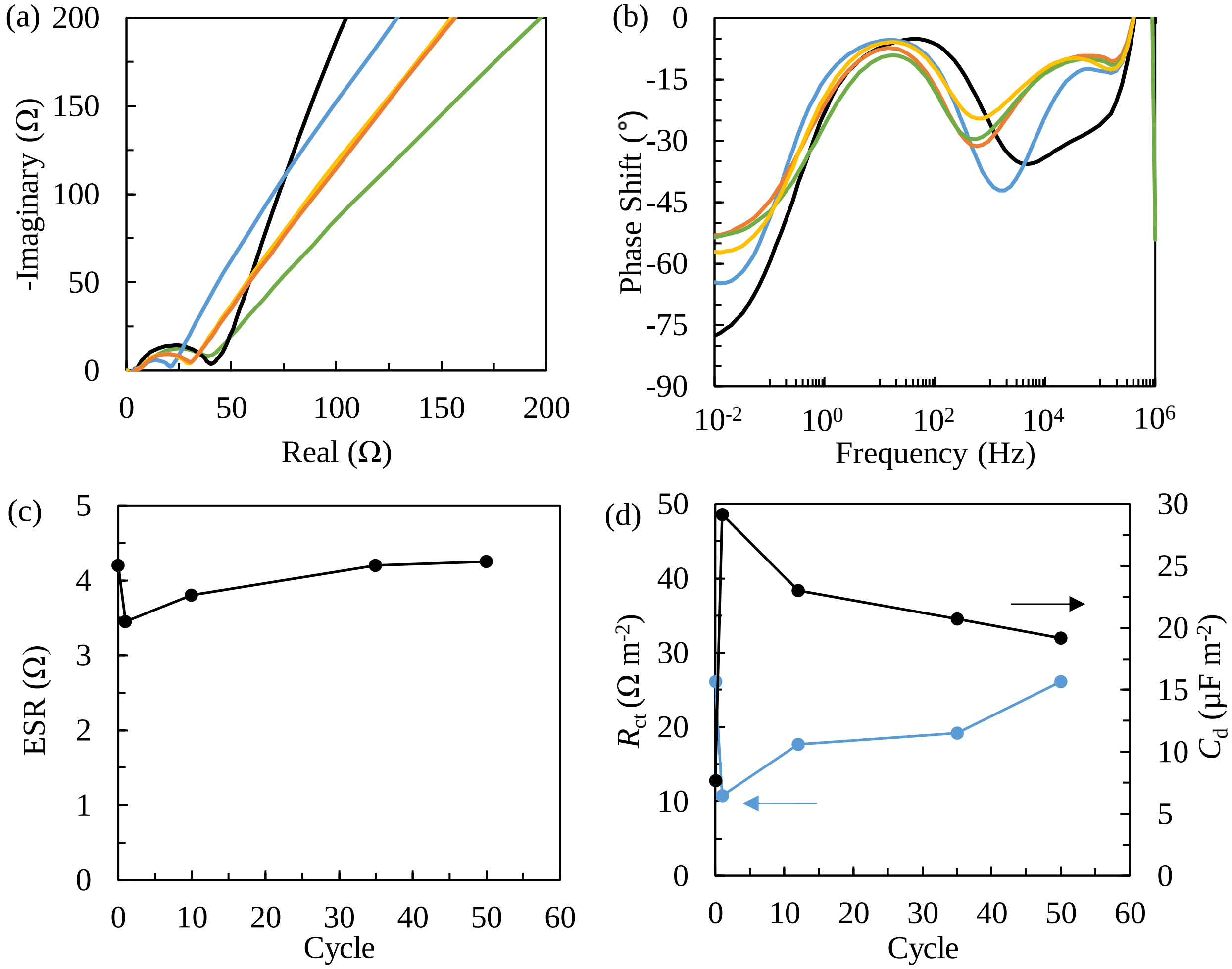

Figure 6.20 – EIS analysis of the CXSnO30 composite electrode with PSS as a binder cycled between 0.005 V and 2 V *vs.* Li^+/Li. (a) Nyquist plot and (b) Bode diagram. (▬) Pristine, (▬) 1st, (▬) 10th, (▬) 35th, and (▬) 50th cycle. (c) ESR as a function of galvanostatic cycles. (d) Charge transfer resistance (R_{ct}) per specific surface area and charge transfer capacitance (C_d) per specific surface area with binder as a function of galvanostatic cycles. Scan between 1 MHz and 100 mHz with 10 points per decade. Voltage amplitude of 10 mV.

The Nyquist plot and Bode diagrams of the CXSnO60 composite electrode with PVDF as a binder cycled up to 2 V *vs.* Li^+/Li are shown in Figure 6.21a and b, respectively. These electrodes were only cycled up to 25 cycles, however, given time restraints. The charge transfer half-circle initially increased in diameter between the pristine and 5th cycles, followed by a progressively decreasing diameter until the 25th cycle. The diffusion region response in the Bode diagram showed a change in the phase shift from approaching -90° to approaching -45° between the pristine and 25th cycle.

The ESR was stable at around 3.8 Ω between the pristine and 25th cycle. As shown by the charge transfer half-circle in the Nyquist plot, the R_{ct} sharply increased between the pristine and 5th cycle from 25 Ω m^{-2} to 500 Ω m^{-2}, followed by a progressive decrease to 200 Ω m^{-2} for the 25th cycle. The C_d exhibited a notably different response than all previous composite electrodes. The C_d initially slightly decreased between the pristine and 1st cycle followed by a progressive increase from 5 μF m^{-2} to 15 μF m^{-2} between the 1st cycle and 25th cycle. It is unclear, however, from where this instability arises. Although, it is likely due to a combination of (i) the high tin oxide loading of the CXSnO60 composite electrode, (ii) the use of PVDF as a binder, and (iii) the volume change during cycling of the tin oxide phase.

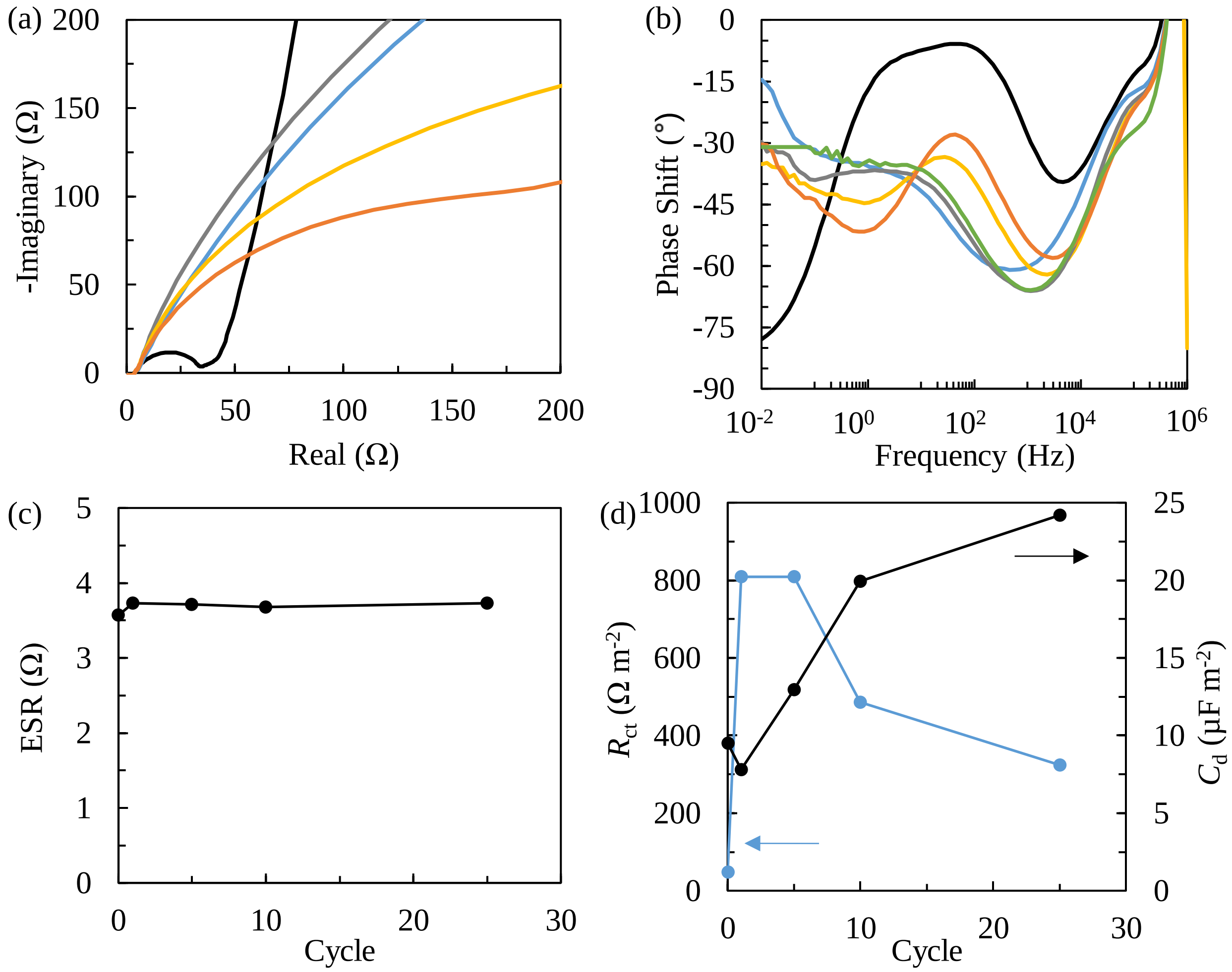

Figure 6.21 – EIS analysis of the CXSnO60 composite electrode with PVDF as a binder cycled between 0.005 V and 2 V *vs.* Li$^+$/Li. (a) Nyquist plot and (b) Bode diagram. (▬) Pristine, (▬) 1st, (▬) 5th, (▬) 10th, and (▬) 25th. (c) ESR as a function of galvanostatic cycles. (d) Charge transfer resistance (R_{ct}) per specific surface area and charge transfer capacitance (C_d) per specific surface area as a function of galvanostatic cycles. Scan between 1 MHz and 100 mHz with 10 points per decade. Voltage amplitude of 10 mV.

Finally, the Nyquist plot and Bode diagrams of the CXSnO60 composite electrode with PSS as a binder exhibited a similar response as the CXSnO30 composite electrode with PVDF as binder. These electrodes were only cycled up to 25 cycles, however, given time restraints. The Nyquist plot, shown in Figure 6.22a, exhibited a progressively increasing diameter of the charge transfer half circle between the pristine and 25th cycle. Similarly, the diffusion region response in the Bode diagram showed a change in the phase shift from approaching -90° to approaching -45° between the pristine and 25th cycle.

The ESR was stable, with values around 3.5 Ω between the pristine and 25th cycle. The R_{ct} and C_d of this composite electrode also exhibited a similar response as the CXSnO30 composite electrode with PVDF as a binder. The R_{ct} value progressively increased between the pristine and 25th cycle, from 50 Ω m^{-2} to 500 Ω m^{-2}. The C_d value also increased during the first 5 cycles; this increase was followed by a progressive decrease until the 25th cycle, approaching 1-2 µF m^{-2}.

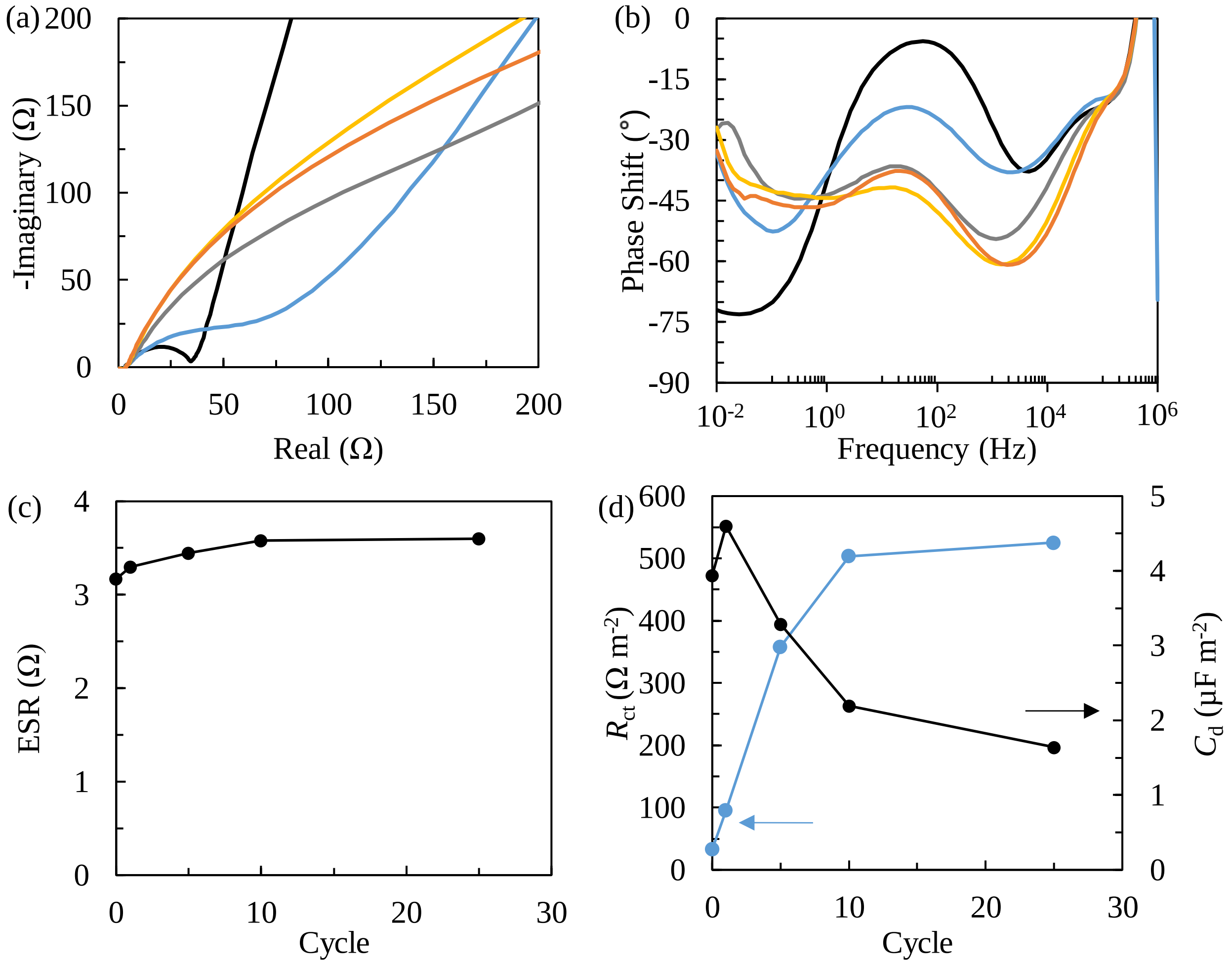

Figure 6.22 – EIS analysis of the CXSnO60 composite electrode with PSS as a binder cycled between 0.005 V and 2 V *vs.* Li$^+$/Li. (a) Nyquist plot and (b) Bode diagram. (▬) Pristine, (▬) 1st, (▬) 5th, (▬) 10th, and (▬) 25th. (c) ESR as a function of galvanostatic cycles. (d) Charge transfer resistance (R_{ct}) per specific surface area and charge transfer capacitance (C_d) per specific surface area as a function of galvanostatic cycles. Scan between 1 MHz and 100 mHz with 10 points per decade. Voltage amplitude of 10 mV.

In general, it seems that the composite electrodes that were comprised of the lower tin oxide content samples (*i.e.* CXSnO30) were more stable than the composite electrodes comprised of the higher tin oxide content samples (*i.e.* CXSnO60). Stability in this context included an ESR, charge transfer resistance (R_{ct}), and capacitance (C_d) that remained constant during cycling. The CXSnO30 composite electrodes with PSS as a binder clearly showed the most stable parameters among the four composite electrodes tested. Furthermore, the CXSnO30 composite electrode with PSS as a binder exhibited the lowest charge transfer resistance, which may be due to the use of PSS as an ionically conductive binder. However, the high R_{ct} of the CXSnO60 composite with PSS as a binder remains unexplained. It is possible that the high content of tin oxide in the CXSnO60 sample causes the high charge transfer resistance.

6.4 Conclusion

CX-SnO_2 active materials and composite electrodes were synthesized for use as negative electrodes in Li^+ ion batteries. These active materials consisted of either 30 wt% (CXSnO30) or 60 wt% (CXSnO60) tin oxide. They were synthesized by the impregnation and subsequent condensation, *via* a pH-controlled sol-gel reaction, of an aqueous solution of tin oxide precursor, sodium (IV) stannate trihydrate, into a previously synthesized CX. TEM micrographs of the synthesized CXSnO30/60 samples showed a relatively well-dispersed tin oxide phase throughout the CX particles as compared to the CX-SnONPs sample synthesized in the previous chapter (tin oxide phase confirmed *via* EDX analysis). The tin oxide phase did not exhibit the same faceted shape as was observed for the tin oxide nanoparticles in Chapter 5, but resembled more of the same morphology of the CX itself. X-ray diffraction of the CXSnO30 sample showed that the average crystallite size of the tin oxide phase was in the order of a few nanometers, determined *via* line broadening of the tin oxide diffraction peaks. Excessive line broadening caused many of the tin oxide diffraction peaks to overlap, which made the deconvolution of these diffraction peaks difficult. Nitrogen adsorption analysis of the CXSnO30/60 samples showed that some of the tin oxide precursor solution likely entered and deposited the tin oxide into the micropores of the CX given the progressive decrease in microporous surface as more tin oxide precursor was used during the synthesis.

Composite electrodes comprised of the CXSnO30 and CXSnO60 samples were prepared with either PVDF or PSS as a binder for electrochemical characterization. The reversible capacity retention of CXSnO30 and CXSnO60 composite electrodes was dependent on whether the electrodes were cycled up to 1 V or 2 V *vs.* Li^+/Li. If cycled up to only 1 V *vs.* Li^+/Li, the partially reversible conversion reaction between tin and tin oxide did not occur and the composite electrodes were able to maintain up to 300 mAh g^{-1} for more than 50 cycles, compared to 165 mAh g^{-1} for an undoped CX. The electrodes that were cycled up to 2 V *vs.* Li^+/Li, *i.e.* including both the alloying and conversion reactions, reached an initial specific capacity of around 600 mAh g^{-1} but were far less stable during cycling, gradually reaching 300 mAh g^{-1} after only 40 cycles. EIS measurements of the CXSnO30 and CXSnO60 composite electrodes that have been cycled up to 2 V *vs.* Li^+/Li were also conducted; these measurements showed that the CXSnO30 composite electrode with PSS as a binder was the most electrochemically stable during cycling.

The next steps for this synthesis technique would be to optimize the way the precursor is introduced into the CX. This includes the study of the impact of, *e.g.* dilution ratio of the sodium stannate trihydrate, type of solvent, pore size and distribution of the CX, as well as other variables of the sodium stannate trihydrate synthesis method (*i.e.* drying times, ageing, *etc.*). Changing the type of solvent may allow for the sodium stannate trihydrate to interact differently with the CX surfaces, and possibly allow the tin oxide to be deposited more intimately with the CX. The pore size distribution of the CX may also be important to maximize the support characteristics of the CX for tin oxide. Finally, altering the synthesis variables of the sodium stannate trihydrate sol-gel reaction may lead to other insights about the formation mechanism of tin oxide within the CX porosity. Other prospects include using surfactants or other functional additives to increase the compatibility of the sodium stannate trihydrate with the CX matrix to ensure that the sodium stannate trihydrate is best transformed into tin oxide within the CX particles. The composite electrodes with higher tin oxide content, like the CXSnO60 composite electrodes, should also be explored further to determine as to why they exhibited a lower than expected specific capacity.

6.5 References

[1] S.Y. Lee, K.Y. Park, W.S. Kim, S. Yoon, S.H. Hong, K. Kang, and M. Kim, Unveiling origin of additional capacity of SnO_2 anode in lithium-ion batteries by realistic *ex situ* TEM analysis. Nano Energy 19 (2016) 234-245.

[2] H. Liu, D. Long, X. Liu, W. Qiao, L. Zhan, and L. Ling, Facile synthesis and superior anodic performance of ultrafine SnO_2-containing nanocomposites. Electrochim. Acta. 54, 24 (2009) 5782-5788.

[3] F. Zoller, D. Bohm, T. Bein, and D. Fattakhova-Rohlfing, Tin oxide based nanomaterials and their application as anodes in lithium-ion batteries and beyond. ChemSusChem 12 (2019) 4140-4159.

[4] Y. Idota, T. Kubota, A. Matsufuji, Y. Maekawa, and T. Miyasaka, tin-based amorphous oxide: A high-capacity lithium-ion-storage material. Science 276, 5317 (1997) 1395-1397.

[5] M.G. Beier, C. Ziegler, K. Wegner, A. Benad, F. Simon, S. Kaskel, and A. Eychmüller, A fast route to obtain modified tin oxide aerogels using hydroxostannate precursors. Mater. Chem. Front. 2 (2018) 710-717.

[6] A. F. Hollemann, E. Wiberg and N. Wiberg, Lehrbuch der Anorganischen Chemie, 102nd ed. Walter de Gruyter & Co., Berlin, New York, 2007.

[7] K. Zhao, G. Du, G. Qin, Y. Liu, and H. Zhao, Facile synthesis of boscage-like SnO_2 nanorods by hydrothermal method. Mater. Lett. 141 (2015) 351-354.

[8] O. Lupan, L. Chow, G. Chai, H. Heinrich, S. Park, and A. Schulte, Synthesis of one-dimensional SnO_2 nanorods *via* a hydrothermal technique. Physica E 41, 4 (2009) 533-536.

[9] B. Kartick, S. K. Srivastava, and I. Srivastava, Green Synthesis of Graphene. J Nanosci. Nanotechno. 13 (2013) 4320-4324.

[10] G. Wang, J. Yang, J. Park, X. Gou, B. Wang, H. Liu, and J. Yao, Facile synthesis and characterization of graphene nanosheets. J. Phys. Chem. C112 (2008) 8192-8195.

[11] R. Siburian, H. Sihotang, S. Lumban Raja, M. Supeno, and C. Simanjuntak, New route to synthesize of graphene nano sheets. Orient. J. Chem. 34 (2018) 182-187.

[12] I.A. Courtney and J. R. Dahn, Electrochemical and in situ X-ray diffraction studies of the reaction of lithium with tin oxide composites. J. Electrochem. Soc. 144 (1997) 2045-2052.

[13] K.M. Lee, D.J. Lee and H. Ahn, XRD and TEM studies on tin oxide (II) nanoparticles prepared by inert gas condensation. Mater. Lett. 58, 25 (2004) 3122-3125,

[14] S. Gnanam and V. Rajendran, Synthesis of tin oxide nanoparticles by sol–gel process: effect of solvents on the optical properties. J. Sol-Gel Sci. Technol. 53 (2010) 555-559

[15] S. Enzo, G. Fagherazzi, A. Benedetti, and S. Polizzi, A profile-fitting procedure for analysis of broadened X-ray diffraction peaks: I. methodology. J. Appl. Cryst. 21 (1988) 536-542.

[16] S. Enzo, G. Fagherazzi, A. Benedetti, and S. Polizzi, A profile-fitting procedure for analysis of broadened X-ray diffraction peaks. II. Application and discussion of the methodology. J. Appl. Cryst. 21 (1988) 543-549.

[17] D. Balzar, N. Audebrand, R. Daymond, A. Fitch, A. Hewat, I. Langford, A. Le Bail, D. Louër, O. Masson, N. McCowan, C. Popa, W. Stephens, and B. H. Toby, Size–strain line-broadening analysis of the ceria round-robin sample. J. Appl. Cryst. 37 (2004) 911-924.

[18] S.J. An, J. Li, C. Daniel, D. Mohanty, S. Nagpure, and D.L. Wood, The state of understanding of the lithium-ion-battery graphite solid electrolyte interphase (SEI) and its relationship to formation cycling. Carbon 105 (2016) 52-76.

6.6 Supplemental information

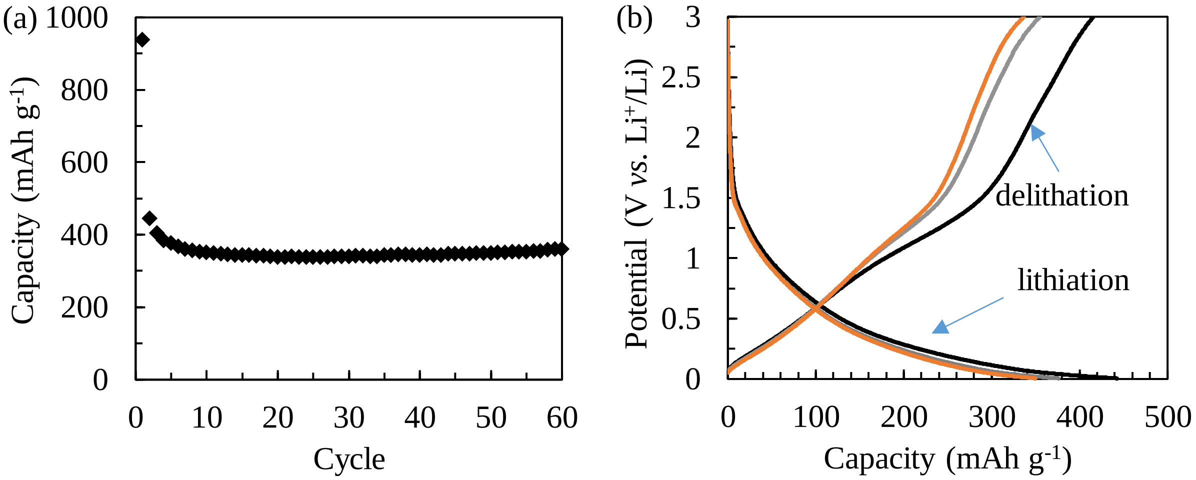

Figure S6.1 – (a) Capacity *vs.* cycling and corresponding (b) potential profiles of a CX composite electrode with PVDF as a binder cycled between 0.005 V and 3 V *vs.* Li^+/Li. (▬) 1st cycle, (▬) 5th cycle, and (▬) 10th cycle.

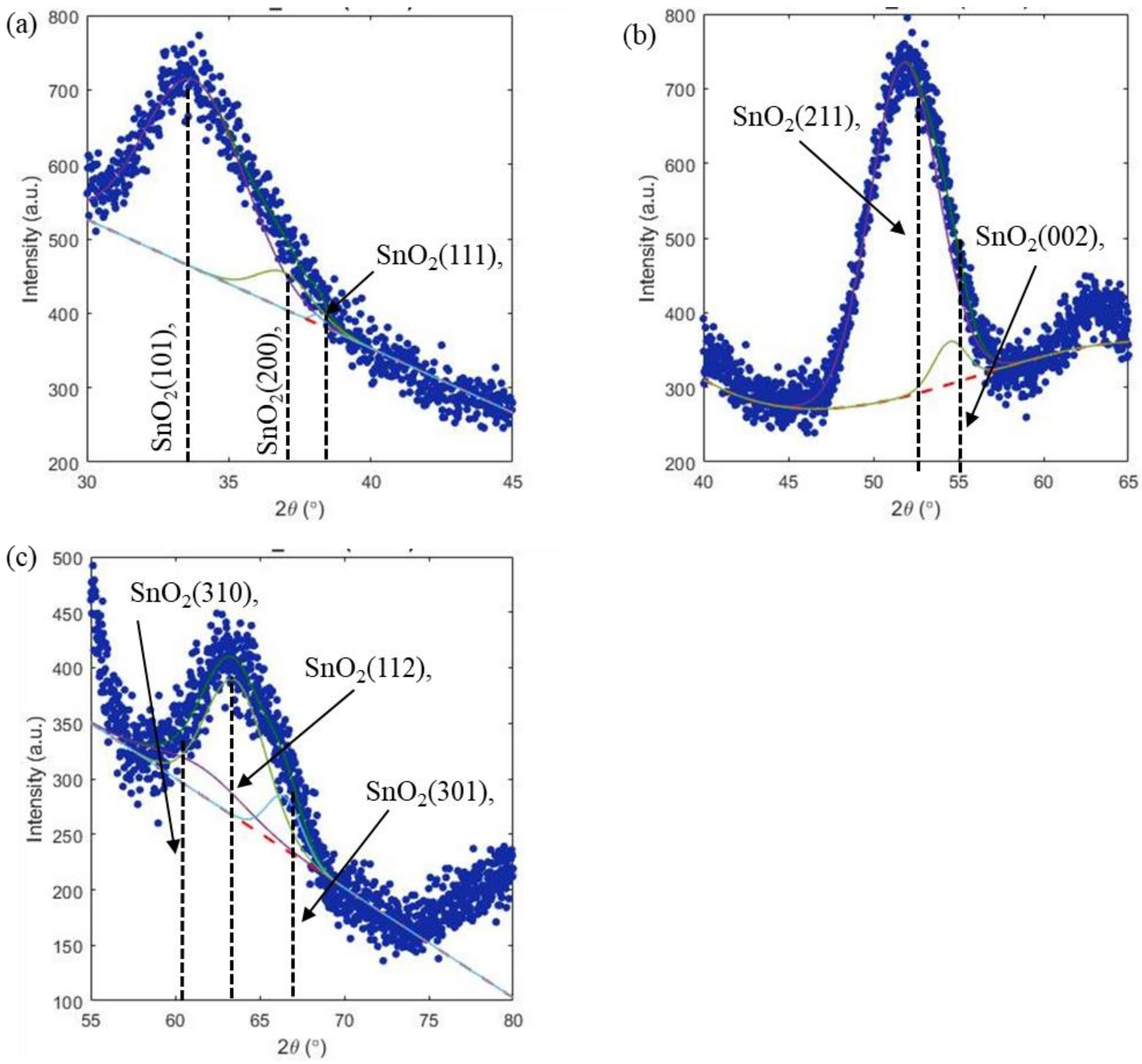

Figure S6.2 – Deconvolution of SnO_2 XRD diffraction peaks in the CX-SnO_2 composite. (a) SnO_2 diffraction peaks SnO_2(101), SnO_2(200), and SnO_2(111). (b) SnO_2 diffraction peaks SnO_2(211) and SnO_2(002). (c) SnO_2 diffraction peaks SnO_2(310), SnO_2(112), and SnO_2(301).

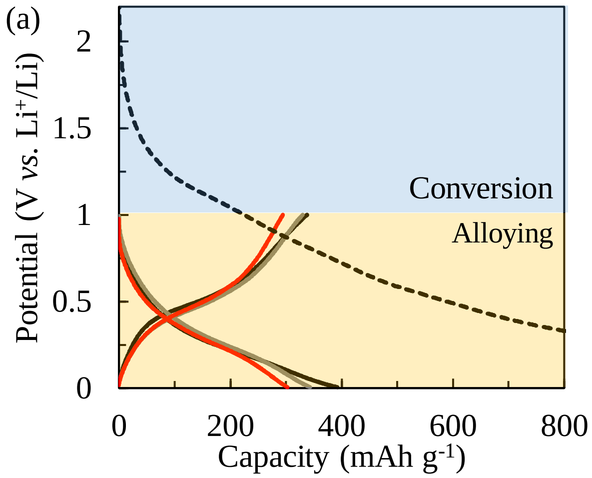

Figure S6.3 – Potential profiles for the CXSnO30 composite electrode with PVDF as a binder. Cycling at a rate of C/10 up to (a) 1 V and (b) 2 V *vs*. Li^+/Li. Shown for the (---) 1st discharge, (▬) 1st cycle (▬) 5th cycle, (▬) 20th cycle, and (▬) 50th cycle.

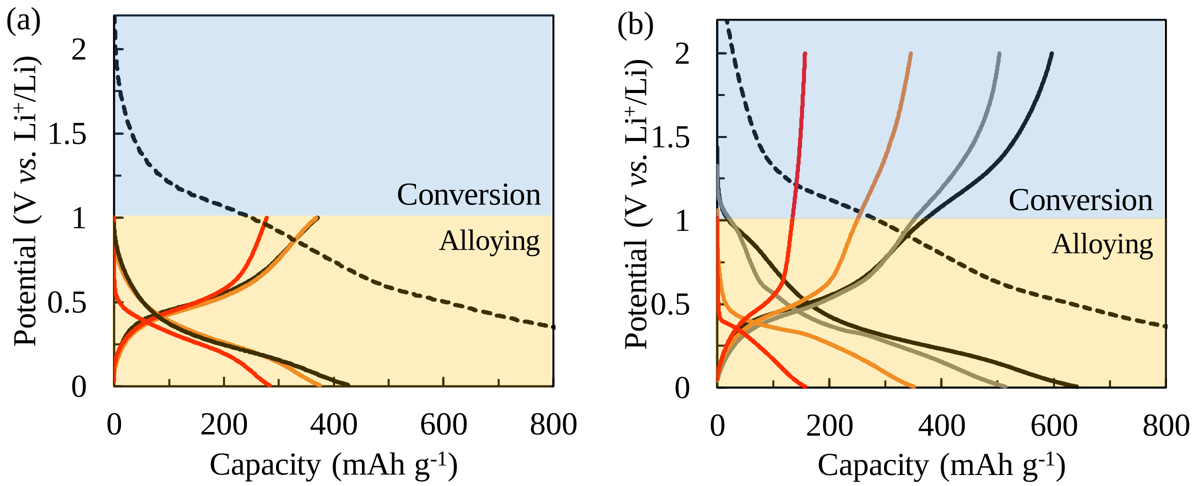

Figure S6.4 – Potential profiles for the CXSnO60 composite electrode with PVDF as a binder. Cycling at a rate of C/10 up to (a) 1 V and (b) 2V *vs*. Li^+/Li. Shown for the (---) 1st discharge, (▬) 1st cycle (▬) 5th cycle, (▬) 20th cycle, and (▬) 50th cycle.

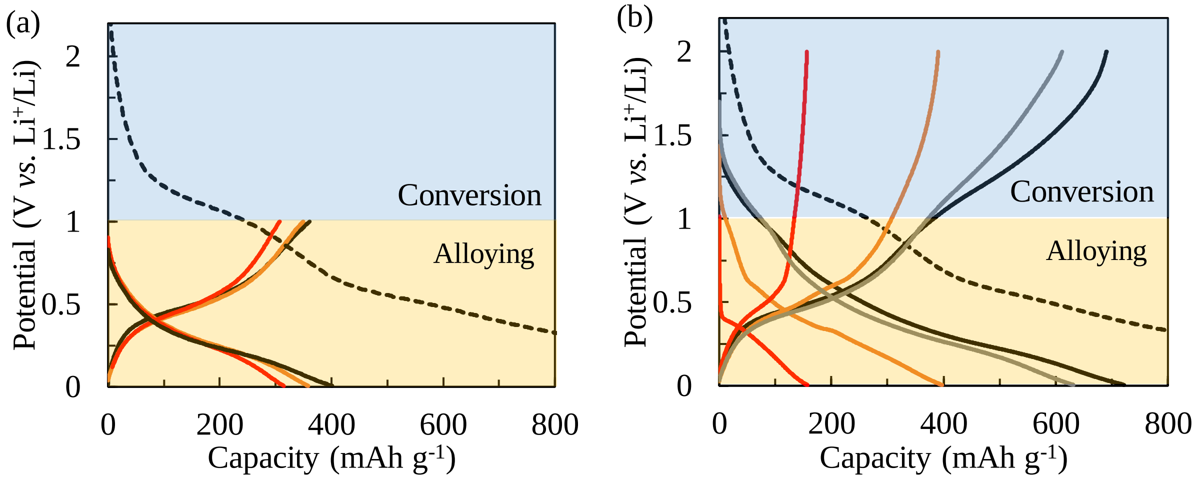

Figure S6.5 – Potential profiles for the CXSnO60 composite electrode with PSS as a binder. Cycling at a rate of C/10 up to (a) 1 V and (b) 2 V *vs*. Li^+/Li. Shown for the (---) 1st discharge, (▬) 1st cycle (▬) 5th cycle, (▬) 20th cycle, and (▬) 50th cycle.

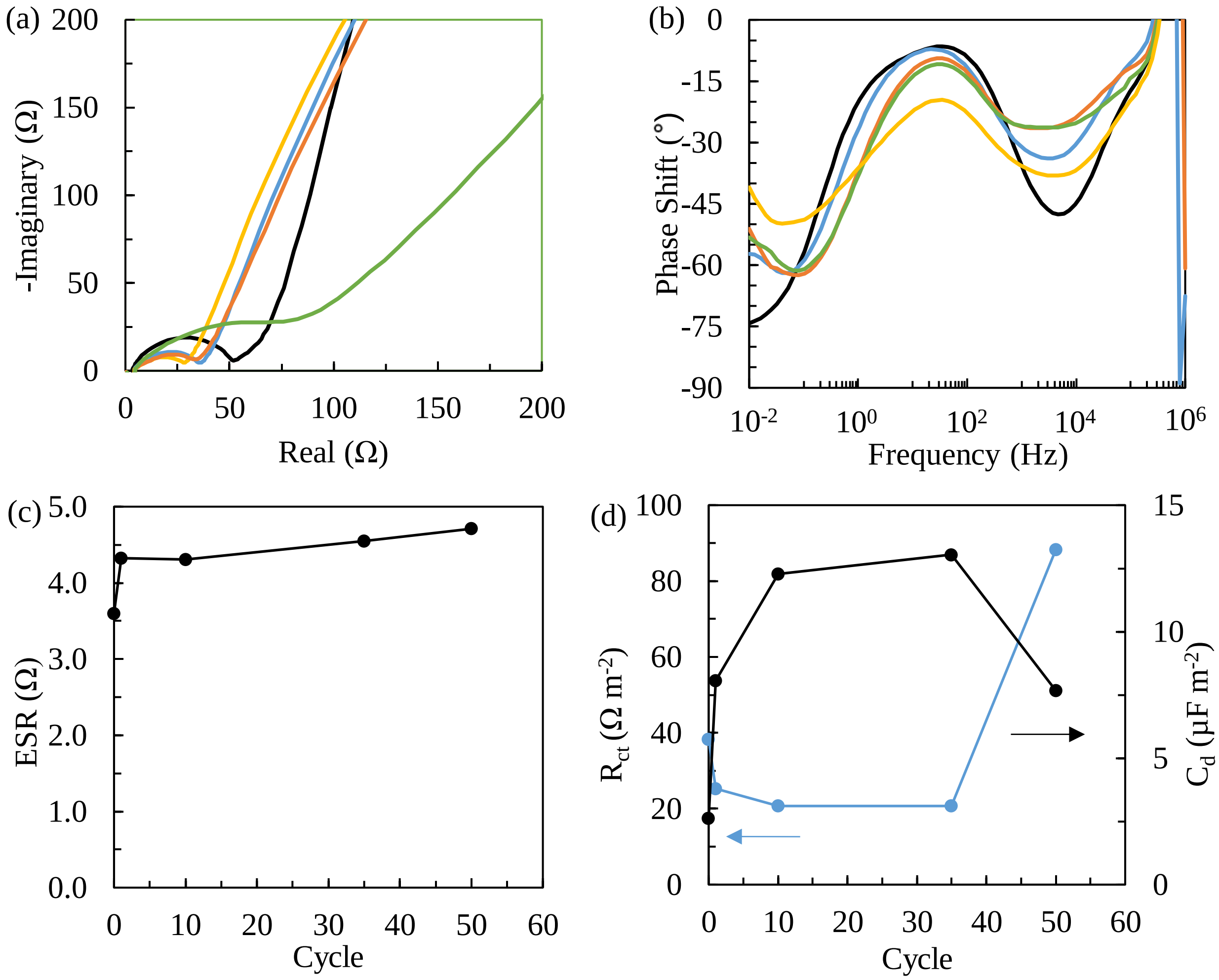

Figure S6.6 – EIS analysis of the CXSnO30 composite electrode with PSS as a binder cycled between 0.005 V and 1 V *vs.* Li^+/Li. (a) Nyquist plot and (b) Bode diagram. (▬) Pristine, (▬) 1st, (▬) 10th, and (▬) 35th, and (▬) 50th. (c) ESR as a function of galvanostatic cycles. (d) Charge transfer resistance (R_{ct}) per BET surface area and charge transfer capacitance (C_d) per BET surface area with binder as a function of galvanostatic cycles.

Conclusions and Outlook

Conclusions

In this thesis, a carbon xerogel (CX) was used as an electrically-conductive 3D support matrix for either silicon, an alloying-type active material, or tin oxide, a conversion-type and alloying-type active material, for use as a negative electrode in a Li^+ ion battery. As has been discussed throughout this thesis, both silicon and tin oxide undergo large volumetric changes during lithiation and delithiation that lead to the premature failure of composite electrodes synthesized with these materials. These large volumetric changes have two main consequences: (i) the unstable formation of the solid electrolyte interphase (SEI) and (ii) the pulverization of the active material particles. The former causes a loss of ionic conductivity and excessive consumption of the electrolyte and active material due to the repetitive formation of an SEI. The latter causes a loss of electrical contact with the current collector and, therefore, a loss of capacity. The strategies used to mitigate these problems in this thesis consisted primarily of (i) reducing the size of the silicon or tin oxide domains into nanoparticles or other nanosized structures, (ii) dispersing the silicon or tin oxide into the 3D CX matrix, and (iii) using a Li^+ ion conductive layer, such as PSS, as a protective element between the electrolyte and the active material. Reducing the domain size had been shown previously to help mitigate pulverization of silicon and tin oxide by reducing internal stresses within the material during the volumetric change. Dispersing the silicon or tin oxide into the 3D CX matrix would allow to keep good electrical contact between the silicon and tin oxide dopants and the current collector as well as serve as a support matrix for the silicon or tin oxide dopants while letting them expand and shrink upon cycling. Finally, the use of an ionically-conductive layer, such as a PSS, would serve to protect the active material from the electrolyte and avoid excessive (and repetitive) SEI formation while maintaining ionic conductivity.

This thesis aimed to understand not only the CX itself, but also how an active material comprised of a CX and these high specific capacity active materials can be synthesized, characterized, and optimized as discussed above. The thesis was, therefore, organized into three main sections: (i) the synthesis and characterization of the CX, and the modeling of its electrochemical behavior, (ii) synthesis and characterization of a silicon-doped CX, and (iii) synthesis and characterization of a tin oxide-doped CX.

Carbon xerogel synthesis, characterization, and modeling

In Chapter 1, the synthesis, characterization, and electrochemical modelling for a CX-based composite electrode were conducted by constructing supercapacitors rather than batteries. This was done in order to determine how the physico-chemical properties, such as the surface area, active layer thickness, density, affect the electrochemical properties of the composite electrodes. These composite electrodes were comprised of the CX with either a conventional poly(vinylidene difluoride) (PVDF) binder or an ionically-conductive polymer, poly(sodium 4-styrenesulfonate) (PSS), as a binder. PSS was used as a binder because of its protective properties for high energy density dopants, like silicon or tin oxide, as highlighted further in the thesis (see mainly Chapters 3 and 7). Besides, PSS is a water-soluble polymer and, therefore, allows for the synthesis of a composite electrode in an aqueous environment. This property was found to have an interesting effect on the electrochemical properties of the CX-based composite electrodes. The aqueous nature of the PSS allowed for some of the microporosity of the CX to be retained and, therefore, interact with the surrounding electrolyte in battery electrode configuration.

The main conclusions of this chapter were that, although the specific capacitance of a pore increases with decreasing diameter, the addition of a secondary diffuse region outside of the pore causes a net decrease in the specific capacitance per unit surface area. Other electrochemical properties, such as the charge transfer resistance (R_{ct}), charge transfer capacitance (C_d), and equivalent series resistance (ESR) were affected by the average pore size of the CX, the type of binder, and the thickness of the deposited active layer. Generally, a highly conductive (electronically and ionically) active layer with high density is preferable for Li^+ ion batteries or supercapacitors in order to maximize the volumetric and gravimetric energy and power density. It was found that the R_{ct} increased as the average pore size decreased. The R_{ct} also increased as the active layer thickness increased. The use of PSS as a binder, however, decreased the R_{ct}, likely as a result of the Li^+ conductivity of the PSS. Therefore, the ideal CX-based battery would likely consist of a thin CX active layer with a large average pore size and PSS as a binder.

Silicon-doped carbon xerogel

In Chapters 2 through 4, the synthesis and characterization of an active material comprised of silicon and CX were studied. In Chapter 2, the inclusion of previously synthesized silicon nanoparticles (SiNPs) was studied *via* impregnation at two different points in the CX synthesis: SiNPs were incorporated into the CX either (i) in the resorcinol-formaldehyde precursor solution before gelation (RF-SiNPs) or (ii) in the xerogel after gelation process but before pyrolysis (OX-SiNPs). It was found that, although the SiNPs were present in both samples (confirmed *via* XRD and thermogravimetric analysis), only the OX-SiNPs exhibited the silicon redox response in CV measurements and expected capacity in galvanostatic cycling. Therefore, it seems that either the morphology of the SiNPs within the CX or some other reaction occurred during the synthesis procedure that rendered the SiNPs inactive to lithiation. Further study should be done into this mechanism in order to understand it and come up with possible remedies.

In Chapter 3, poly(sodium 4-styrenesulfonate) (PSS) was used as an ionically-conductive binder or coating to further improve the cycling stability of the OX-SiNPs active material. As shown in Chapter 1, PSS is a water-soluble polymer and, therefore, allowed for the synthesis of a composite electrode active materials in an aqueous environment. PSS was able to infiltrate into the microporosity of the CX and maintain these microporous surfaces after deposition due to the water-soluble nature of PSS. Furthermore, since PSS is somewhat conductive for Li^+ ions, PSS was able to protect the dopant SiNPs and CX while maintaining ionic conductivity with the electrolyte. In this chapter, the protective properties of PSS led to increasing the cycling stability of composite electrodes comprised of the OX-SiNPs sample by up to 10 times compared to the same OX-SiNPs sample in a composite electrode using PVDF as a binder. Electrochemical impedance spectroscopy (EIS) showed evidence that PSS was able to (briefly) protect the active material from pulverization and excessive SEI formation. The mechanical fragility of PSS, however, likely caused the polymer to begin to fail after 20 cycles. The composite electrode with PSS as a binder showed a continuously increasing ESR during cycling, which can be related to the PSS detaching from the active material and poisoning the electrolyte. The charge transfer resistance, $R_{ct,}$ decreased over the first 20 cycles then began to increase, which can be related to the thinning of the PSS layer on the active material followed by unstable SEI formation, respectively.

Given that there was still room for improvement to the cycling stability of the CX doped with previously synthesized SiNPs, the goal of the work in Chapter 4 was to further reduce the negative effects caused by the volumetric change of the silicon during cycling by more intimately integrating silicon into the CX. A new synthesis technique, utilizing a silicon precursor and magnesiothermal reduction, was devised to more closely integrate silicon into the 3D matrix of the CX. Rather than impregnating previously-synthesized SiNPs into the CX, silica was introduced into the CX as a precursor and subsequently transformed into silicon *via* magnesiothermal reduction. NaCl was used as a heat scavenger during magnesiothermal reduction in order to maintain the reaction temperature below the melting point of silicon so that the parent silica nanostructure could be maintained in the silicon after magnesiothermal reduction. By using this technique, it was possible to use either silica nanoparticles or the silica precursor tetraethyl orthosilicate (TEOS) to impregnate the solid CX or organic xerogel (OX). This would lead to a CX/OX-silica material that had silica well dispersed throughout the porosity of the CX.

The active material that used silica nanoparticles as the silicon precursor exhibited the expected capacity during the pristine cycle; however, the capacity faded quickly during cycling. The active material that used TEOS as the silica and silicon precursor, however, did not seem to have been correctly transformed into silica or silicon during the synthesis procedure and exhibited a significantly reduced capacity during cycling. Further study into the best synthesis procedure for sample with the TEOS-derived silica is still needed in order to take advantage of this unique synthesis technique.

Tin oxide-doped carbon xerogel

In Chapters 5 and 6, the synthesis and characterization of an active material comprised of tin oxide and CX were studied. In Chapter 5, the inclusion of previously synthesized tin oxide nanoparticles

(SnONPs) was studied *via* impregnation into the CX after pyrolysis (CX-SnONPs). Tin oxide undergoes two different types of reactions during lithiation: (i) a conversion reaction from tin oxide to tin, which forms Li_2O as a byproduct and (ii) an alloying reaction between lithium and the tin product of the previous conversion reaction. It was found that the conversion reaction is only partially reversible while the alloying reaction is reversible but still undergoes a similar volume expansion as silicon, albeit to a lesser extent. The use of PSS as a protective binder also increased the cycling stability of these composite electrodes, although improvement remains necessary to achieve electrodes usable in common applications.

Therefore, a similar synthesis to the magnesiothermal reduction synthesis shown in Chapter 4 was studied in Chapter 6, but for tin oxide instead of silicon. Rather than impregnating previously-synthesized SnONPs into the CX, the tin oxide precursor, sodium stannate trihydrate, was impregnated into the CX and subsequently reduced into tin oxide *via* a simple sol-gel process. The CX-SnO_2 active materials synthesized with this technique still showed a similar cycling stability as the active materials synthesized with the SnONPs. Further study into how to properly infiltrate and reduce the tin oxide precursor into the CX and protect it from direct contact with the electrolyte is still needed. However, the results from this work are definitely promising, given the similar cycling stability observed as for the CX-SnONPs composite electrodes synthesized in Chapter 5.

Outlook

A carbon xerogel as a support material for high energy density dopants, like silicon or tin oxide, seems to be a promising research path to investigate. The unique tunable 3D pore structure of the carbon xerogel allows for the facile inclusion of these high energy dopants in a wide range of forms, *i.e.* as nanoparticles or *via* precursors, like has been shown in this thesis. The present work has shown that these techniques are feasible with a modest increase in the cycling stability of silicon/tin oxide-doped CX composite electrodes. Further research should be done, however, to optimize the inclusion of high energy density dopants into the CX pore structure either as previously-synthesized dopant nanoparticles or as a precursor.

As for the inclusion of dopant nanoparticles, the following areas should be considered. First, accurate tuning of the average pore size of the CX with the dopant nanoparticles should be explored. This includes preparing the dopant nanoparticles so that they are monodisperse, sufficiently small, and isolated from each other so that diffusion into the interior of the CX particles can occur. Furthermore, the exploration of a suitable surfactant that reduces the interactions with the CX surface should be done to further promote diffusion deep within the CX particles.

Regarding the use of a precursor to impregnate the CX, the following areas should be considered. First, the optimization of the precursor conversion into the final silicon or tin oxide should be explored independently. For silicon, this includes the TEOS hydrolyzation and condensation into silica and the magnesiothermal reduction of silica into silicon. Variables such as the TEOS dilution ratio, solvent type, temperature, pH, and ageing time should be explored. The magnesiothermal reduction procedure also needs to be fine-tuned in order to obtain improved and consistent results. The temperature of the reaction, the reaction time, the NaCl as a heat scavenger, and the interaction with the CX are a few of the things that should be studied further. For tin oxide, the sol-gel reaction of the sodium stannate trihydrate into tin oxide is the major unknown factor. The variables of this reaction (such as the reaction temperature, concentration, solvent type, *etc.*) should be explored more thoroughly in order to optimize the distribution of tin oxide through the CX particles.

Lastly, the use of the ionically-conducting and water-soluble polymer, PSS, as a protective binder or coating was shown to improve the cycling stability of these CX-based composite electrodes with high energy dopants. Although the specific capacity of these composite electrodes still decreases during cycling, the use of PSS was shown to be an interesting research path towards stability. Further research should therefore be done to optimize this system and to also look into other ionically-conductive and water-soluble polymers that could be used as a binder. The possibility to cross-link an ionically-conductive polymer like PSS seems like a very promising research area. An overview of some of the polymers that could be considered is given in Annex 3.

Annex 1

Physico-chemical and electrochemical characterization

Physico-chemical characterization

Mercury porosimetry

The pore size distribution of the CX-based powders after ball-milling and pyrolysis was measured by means of mercury porosimetry using a Thermo-Scientific Pascal 140/240. Measurements were performed between 0.01 MPa and 200 MPa. The mercury intrusion data obtained were analyzed to determine the size distribution of pores larger than 7.5 nm in diameter. The average pore size, d_{pore}, was calculated by using the Washburn equation:

$$d_{\text{pore}}\ (nm) = \frac{-4\gamma\, cos(\theta)}{P_{\text{Hg}}} \approx \frac{1500}{P_{\text{Hg}}} \qquad \text{(A1.1)}$$

where P_{Hg} is the mercury pressure (MPa), γ is the surface tension of mercury (mN m^{-1}), and θ is the contact angle between mercury and the carbon at 20°C [1]. The surface energy of mercury and the contact angle between mercury and carbon are 485 mN m^{-1} and 152.5°, respectively [2, 3]. The CX particle size can be estimated by assuming that the sample is represented by a hexagonal compact packing of ideal spherical particles. In this case, the volume between the ideal spheres is able to contain a theoretical volume seven times smaller than the diameter of the constituent ideal spheres. Since this central void volume is the volume probed by mercury porosimetry, the following alteration to the Washburn equation estimates the approximate diameter, d_{particle}, of the CX particles [4]:

$$d_{\text{particle}}(\text{nm}) = \frac{1500}{P_{\text{Hg}}} * 7 \qquad \text{(A1.2)}$$

Nitrogen adsorption-desorption

The CX-based powders after ball-milling and pyrolysis were characterized by performing nitrogen adsorption-desorption isotherm analysis at -196°C on a Micromeritics ASAP 2420 instrument. Prior to measurements, the samples were degassed overnight at 270°C under vacuum (133 Pa). The adsorption-desorption characterization yields the following quantities: (i) the total specific surface area (S_{BET}), which was calculated by applying the Brunauer-Emmett-Teller theory to the adsorption data obtained in the relative pressure range from 0.01 to 0.10 [5], (ii) the micropore surface area (S_{micro}), which is the cumulative surface area of all pores with a diameter less than 2 nm, and (iii) the external surface area (S_{ext}), *i.e.* the cumulative surface area of all pores with a diameter greater than 2 nm, which corresponds to the mesopores of the CX (2-50 nm) and any other surface areas of the CX particles. S_{micro} and S_{ext} were calculated *via* the t-plot method. The sum of S_{micro} and S_{ext} should approximately equal S_{BET}.

Transmission electron microscopy

Micrographs of the CX-based powders were obtained using a Philips CM100 Transmission Electron Microscope (TEM) operating at 80 kV. The samples were deposited onto Agar Scientific 200 mesh copper micro-grids covered with a PVDF film. To do so, the copper micro-grids were dipped into a dilute 1 g L^{-1} dispersion of the samples in ethanol. The copper micro-grids were subsequently dried in ambient conditions on the lab bench for at least 1 h before being introduced into the microscope.

Particle size distributions of dopant materials that were included in a CX or by themselves were calculated manually by measuring the diameter of at least 80 nanoparticles. A histogram of these particle sizes was then generated.

Scanning electron microscopy

SEM imaging was conducted on the six completed electrodes of the three CX with either PVDF or PSS as a binder. SEM analysis was performed using a Philips ESEM-XL30 at 7.5 kV under high vacuum. The samples were prepared by gently placing the electrodes against a small piece of glass side that had been coated with a double-sided conductive carbon tape. The glass side was then stuck on its edge with the same carbon tape to the SEM sample holder so that that edge of the electrode was facing perpendicular to the surface of the SEM sample holder. This orientation allowed for the imaging of the deposited active material as well as the thickness of the active material layer.

X-ray diffraction

X-ray diffraction (XRD) spectra on the CX-based powders after ball-milling and pyrolysis were collected to verify the presence of silicon in the CX host matrix. The spectra were collected on a Siemens D-5000 diffractometer (Cu K_α radiation, 40 kV, 40 mA) between 5° and 90° with a step size of 0.15° and 10 seconds per step. A Williamson-hall plot was calculated to determine how much the microstrain broadening, β_e, and size broadening, β_L, have on the total line broadening of the silicon or tin oxide in CX-based powders that contained these dopants [6-9]. Lattice microstrain is a measure of the distribution of lattice constants as a result of crystal imperfections, such as lattice dislocations, grain boundaries, or other stresses that may arise [6]. A distribution of lattice constants, both positive and negative, around the base lattice constant will, therefore, increase the FWHM of the diffraction peak accordingly [6]. In this analysis, the total line broadening can be considered as just the simple sum of the two components:

$$\beta_{\text{tot}} = \beta_{\text{e}} + \beta_{\text{L}} = C\varepsilon\, tan(\theta) + \frac{K\lambda}{Lcos\theta} \qquad \text{(A1.2)}$$

where ε is the internal microstrain and C is a constant. By considering that the strain is uniform in all crystallographic directions, *i.e.* a uniform deformation model (UDM), C has a value of 4. Then, by rearranging equation 1.3 the following relationship can be found:

$$\beta_{\text{tot}} cos\theta = 4\varepsilon\, sin(\theta) + \frac{K\lambda}{L} \rightarrow y = mx + b \qquad \text{(A1.3)}$$

A least square regression fit of each diffraction peak plotted on a Williamson-Hall plot (*i.e.* sinθ vs. β_{tot}cosθ) give that the y-axis intercept, *b,* is proportional to the size broadening, *L*, of the diffracted material, and the slope, *m*, is proportional to the microstrain broadening, ε, of the diffracted material [6-9].

The instrumental broadening was calculated using a LaB_6 standard. The following instrumental line broadening, shown in Figure A1.1 as a function of the 2θ angle was determined and fit with an exponential function.

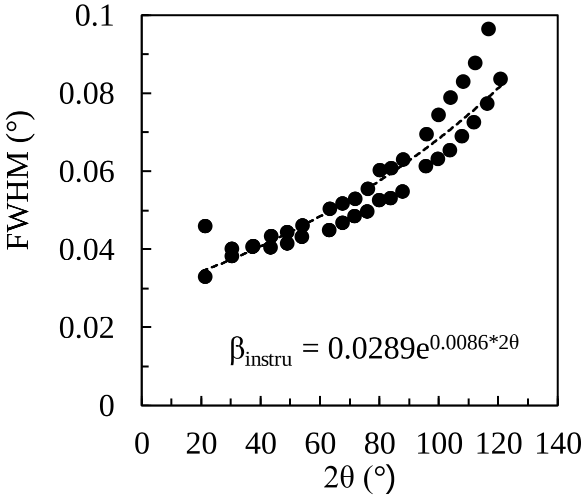

Figure A1.1 – Instrumental line broadening of a LaB_6 standard.

Then, by the following equation, the corrected line broadening can be calculated using the following equation:

$$\beta_{\text{tot}} = \sqrt{\beta^2_{\text{measured}} - \beta^2_{\text{instr}}} \qquad \text{(A1.4)}$$

where β_{measured} is the line broadening measured from the XRD patterns and β_{instru} is the instrumental line broadening at the corresponding 2θ angle. Line profile analysis of the Bragg diffractions peaks was conducted with the LIPRAS software. A pseudo-Voigt fit was used to fit the diffraction peaks and identify the line broadening of each sample as well as the LaB_6 standard.

Electrochemical characterization

Half-cells of the CX-based electrodes were assembled in CR2032 coin-cells with a lithium metal foil as the counter-electrode (Li-metal, MTI Corporation). In this half-cell configuration, the insertion of Li^+ ions into the active material corresponds to a decrease in potential, whereas the de-insertion corresponds to an increase in potential. This setup is opposite to that of a full-cell, where the composite electrodes would be the negative electrode and a metal oxide, such as $LiCoO_2$ for instance, would be the positive electrode. Two porous polyethylene separators (Celgard, 25 µm thickness, MTI Corporation) soaked with 80 µL of electrolyte (1 M $LiPF_6$ in a 1:1:1 ratio of ethylene carbonate: diethylene carbonate: dimethyl carbonate, Selectilyte LP71, Merck) were placed between the Li-metal disk and the electrode. The half-cells were assembled in an argon-filled glovebox (MBraun MB200B). Electrochemical measurements were conducted using CR2032 coin-cells. At least two coin-cells of each formulation were characterized under identical conditions in order to ensure the reproducibility of the results.

For Chapters 3 , 4, and 5, cyclic voltammetry (CV) measurements for were performed using a Biologic VMP3 multichannel potentiostat on each sample over a potential window of 0.005 V to 1.5 V, 2 V, or 3 V *vs.* Li^+/Li at a scan rate of 0.05 mV s^{-1} up to 10 cycles. Galvanostatic cycling was recorded using a Neware BST8-WA, 8 channel Battery Analyzer at a C-rate of approximately C/10 h^{-1} between 0.005 V and 1.5 V *vs.* Li^+/Li. C-rate is the rate at which a battery can be charged or discharged after one hour. Therefore, a rate of C/10 would mean that 1/10th of the battery would be charged or discharged after 1 hour. The specific capacities mention in these chapters refers to the discharge capacity (*i.e.* from high potential to low potential or during Li+ ion insertion into the active material). Electrochemical impedance spectroscopy (EIS) measurements were conducted in order to determine the electrochemical properties as outlined in the model presented in Annex 1. EIS measurements were conducted using a Biologic VMP3 multichannel potentiostat on each sample between 1 MHz and 10 mHz with a voltage amplitude of 10 mV and 10 data points per decade. EIS spectra were collected after various amounts of CV cycles for the electrodes cycled up to 1.5 V *vs.* Li^+/Li. The EIS measurements were recorded in the delithiated state (*i.e.* high potential, charged state). The coin-cells were kept inside a climate-controlled chamber at 25°C to ensure temperature stability for all electrochemical measurements.

For Chapters 6 and 7, cyclic voltammetry (CV) measurements for were performed using a Biologic VMP3 multichannel potentiostat on each sample over a potential window of 0.005 V to 1 V or 2 V *vs.* Li^+/Li at a scan rate of 0.05 mV s^{-1} up to 10 cycles. Galvanostatic cycling was recorded using a Neware BST8-WA, 8 channel Battery Analyzer at a C-rate of approximately C/10 h^{-1} between 0.005 V and 1 V or 2 V *vs.* Li^+/Li. The specific capacities mention in these chapters refers to the discharge capacity (*i.e.* from high potential to low potential or during Li+ ion insertion into the active material) Electrochemical Impedance Spectroscopy (EIS) measurements were conducted in order to determine the electrochemical properties as outlined in the model presented in Annex 1. EIS measurements were conducted using a Biologic VMP3 multichannel potentiostat on each sample between 1 MHz and 10 mHz with a voltage amplitude of 10 mV and 10 data points per decade. EIS spectra were collected after various amounts of CV cycles for the electrodes cycled up to 2 V *vs.* Li^+/Li. The EIS measurements were recorded in the delithiated state (*i.e.* high potential, charged state). The coin-cells were kept inside a climate-controlled chamber at 25°C to ensure temperature stability for all electrochemical measurements.

References

[1] E. Washburn, The dynamics of capillary flow, Phys. Rev. 17 (1921) 273–283.

[2] A. Awasthi, et al., Measurement of contact angle in systems involving liquid metals, Meas. Sci. Technol. 7 (1996) 753–757.

[3] M. Kernaghan, Surface tension of mercury, Phys. Rev. 37 (1931) 990–997.

[4] R. Pospech, P. Schneider, Powder particle sizes from mercury porosimetry, Powder Technol. 59 (1989) 163–171.

[5] S. Brunauer, P. H. Emmett, E. Teller, Adsorption of gases in multimolecular layers, J. Am. Chem. Soc. 60 (1938) 309–319.

[6] G.K Williamson and W.H Hall. Acta Metallurgica 1, 1 (1953) 22-31.

[7] http://pd.chem.ucl.ac.uk/pdnn/peaks/sizedet.htm

[8] B.D. Cullity & S.R. Stock, *Elements of X-Ray Diffraction*, 3rd Ed., Prentice-Hall Inc., (2001) 96-102

[9] T. Ida and K. Kimura, Flat-specimen effect as a convoluation in powder diffractometry with Bragg-Brentano geometry, J. Appl. Cryst. 32 (1999) 634.

[10] LIPRAS BSD License, Copyright (c) 2017, North Carolina State University. Line-Profile analysis Software (LIPRAS). G. Esteves, K. Ramos, C.M. Fancher, and J.L. Jones. https://sneakysnail.github.io/LIPRAS/

Annex 2

Electrochemical impedance model of a battery – Randles cell

A CX-based electrode, as discussed in Chapter 1, can be modelled by a set of discrete electrical components. For the electrodes used in a supercapacitor, we have modelled this behavior as shown in Figure 1.5. For batteries, however, the most commonly used model is the Randles cell, shown in Figure A2.1Figure A1.1 [1, 2]. This simple model consists of an equivalent series resistance (ESR), charge transfer resistance (R_{ct}) and capacitance (C_d), and a Warburg element.

The ESR is mainly a measure of the resistance of the bulk electrolyte and separator, the contact resistance between the active layer and the current collector, and any other ohmic resistances in the external circuit. Potential causes for an increase in the ESR may be a change in the concentration of ions in the electrolyte, poisoning of the electrolyte by inactive species, weakening contact between the active layer and the current collector, or pulverization of the active layer that causes less ohmic contact between the current collector and the active layer or between the particles within the active layer itself. Other elements of the active layer, such as the solid-electrolyte interphase (SEI) are not included in this quantity primarily because these interphases have a capacitive behavior and are not purely resistive in nature.

The elements that aim to model these interphases are the R_{ct} and C_d. These elements correspond to a migration current and a parallel displacement current, respectively. Both of these quantities have been more thoroughly explained in Chapter 1, but generally relate to the motion of charges and the formation of the capacitive layer of charge on the surface of the active material with the electrolyte [1, 2]. Potential causes for a change in the R_{ct} would be due to the ability for charge to be transferred from the electrolyte into the active material and vice versa. For example, the formation of a SEI generally allows for better change transfer between the electrolyte and the active material surface. Changes in the C_d is most likely caused by an increase in the surface area of the interphase in question or a change in the concentration of ions in the electrolyte.

The Warburg element is usually used to describe diffusive behavior of charged species throughout the active layer, and generally accounts for the ability of the active material to act as a battery since Li^+ ions are diffusing and migrating into the CX. This is in contrast with the work presented in Chapter 1, where the CX was acting as a supercapacitor, and therefore no Warburg element is present since diffusion of Li^+ ions into the CX does not occur or is limited. Although this model does not explicitly consider the unique porosity of the CX, it is sufficient to draw some conclusions about the electrochemical properties of these CX-based electrodes. Changes in the diffusive properties of the CX will have an effect on this element.

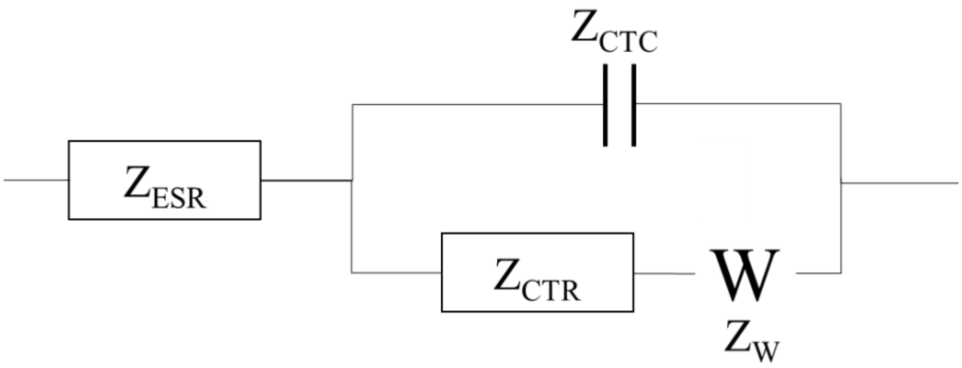

Figure A2.1 – Randles cell consisting of an equivalent series resistance (Z_{ESR}), charge transfer resistance (Z_{CTR}), charge transfer capacitance (Z_{CTC}), and Warburg element (Z_W).

The frequency dependent impedance response of the resistive elements, ESR and C_d, can be expressed as the following:

$$Z_{ESR} = R_{ESR} \tag{A2.1}$$

$$Z_{CTR} = R_{ct} \tag{A2.2}$$

Where Z is the impedance and R is the resistance. Since resistors exhibit no phase shift between the real and imaginary components, the impedance is simply the value of the resistance. The frequency dependent impedance response of the capacitive elements, C_d, however, is expressed as the following:

$$Z_d = -\frac{j}{\omega C_d} \tag{A2.3}$$

Where j is an imaginary number, ω is the angular frequency, and C_d is the value of the capacitance. This equation shows that purely capacitive elements exhibit a -90° phase shift between the real and imaginary components. The frequency dependent impedance response of the Warburg element is expressed as the following:

$$Z_W = \sigma\omega^{-\frac{1}{2}} - j\sigma\omega^{-\frac{1}{2}} \tag{A2.4}$$

Where σ is the Warburg coefficient. As can be seen by this equation, the phase shift of the Warburg element is 45°. The Warburg coefficient gives information about the diffusive behavior of the electroactive species and is defined as follows:

$$\sigma = \frac{RT}{n^2F^2A\sqrt{2}}\left[\frac{1}{\sqrt{D_O}C_{S,O}} + \frac{1}{\sqrt{D_R}C_{S,R}}\right] \tag{A2.5}$$

Where R is the universal gas constant, T is the absolute temperature, n is the number of electrons, A is the electrode surface area, D_O/D_R are the diffusion coefficient of oxidized and reduced species, and $C_{S,O}/C_{S,R}$ are surface concentrations of oxidized and reduced species. Then by combining these elements according to the model express in Figure A2.1, the total frequency dependent impedance response would be:

$$Z_{total} = \left((Z_W + Z_{CTR})^{-\frac{1}{2}} + (Z_{CTC})^{-\frac{1}{2}}\right)^{-1} + Z_{ESR} \tag{A2.6}$$

From this model, a comparison of the ohmic behavior, charge transfer characteristics, and diffusive characteristics of the active layers of different samples. Generally, the Nyquist diagram and Bode plot of the Randles cell should have resemble the example shown in Figure A2.2.

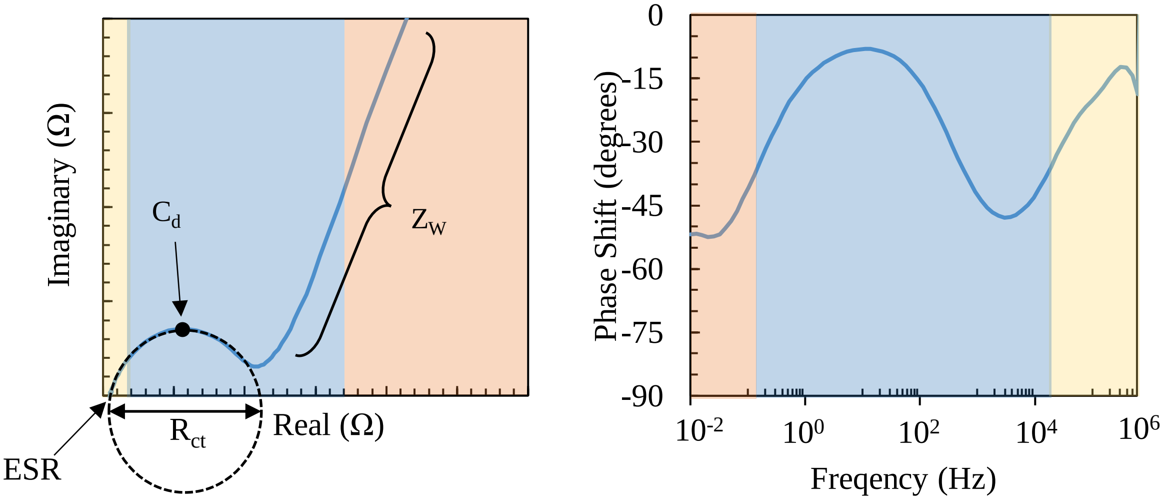

Figure A2.2 – Nyquist diagram and Bode plot of Randles Cell

References

[1] J. E. B. Randles, Discussions of the Faraday Society Kinetics of rapid electrode reactions Vol. 1 (1947).

[2] Gamry Inc, Common equivalent circuit models Available: https://www.gamry.com/assets/White-Papers/Gamry-Common-Equivalent-Circuit-Models.pdf. Accessed on: April 5, 2021.

Annex 3

Other polymers as a protective coating or binder

In this thesis, it was discovered that the use of a novel binder, poly(sodium 4-styrenesulfonate) (PSS), reduced the SEI instability and coating pulverization of silicon and tin oxide-based electrodes. The properties of ionic conductivity and water solubility of this unique binder likely contributed to its protective characteristics. Unfortunately, as has been discussed throughout this doctoral work, the stability of the PSS binder with silicon and tin-doped CX electrodes still leads to an eventual, albeit delayed, loss of capacity during cycling. Nevertheless, this discovery inspired further exploration of other novel binders that could be used as a protective element in the active layer of a lithium ion (Li^+ ion) battery electrode. Some of the possible formulations include forming a polymer blend of PSS with more elastic polymers, crosslinking PSS, or using other types of polymers, namely poly(dimethyl siloxane) (PDMS). The main goals of exploring these other polymers are to (i) increase the maximum tensile strain of the binder, *i.e.* how much the binder can be stretch before fracturing, (ii) include some degree of ionic conductivity, and (iii) add other functionality to the binder, such as better adhesion to the silicon or tin oxide dopants. These polymers would then be used either as a coating, similar to the PSS coating shown in Chapter 3, or as a binder. This annex explores some possibilities for other advanced binders as well as some preliminary experiments conducted on these ideas.

PSS/SBR blend as a binder

Styrene-butadiene rubber (SBR) and carboxymethylcellulose (CMC) blends are commonly used as an aqueous binders in Li^+ ion battery electrodes [1]. SBR is an elastic polymer composed of both styrene and butadiene monomers (see Figure A3.1). Therefore, it would be interesting to combine SBR with PSS to possibly form an ionically-conductive binder with higher elasticity. Given that both PSS and SBR are water soluble, the synthesis of this binder should be fairly straightforward to synthesize.

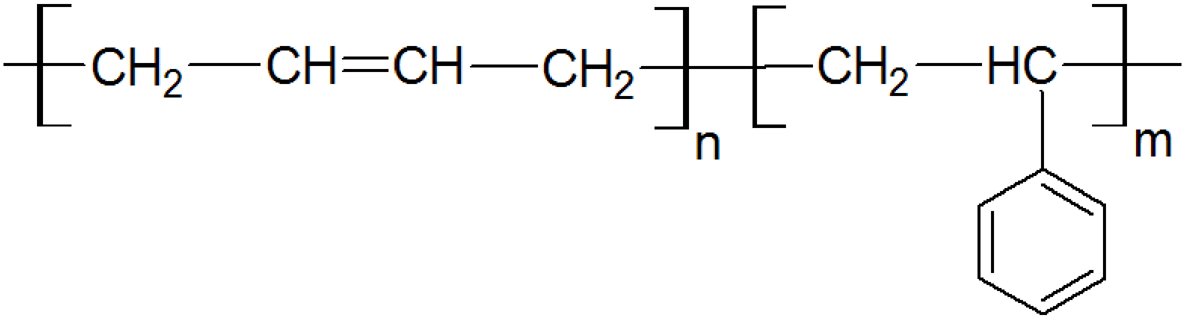

Figure A3.1 – Molecular diagram of styrene-butadiene rubber (SBR). Reprinted from [2].

A preliminary synthesis was conducted using the OX-15SiNPs sample from Chapter 3 as the active material. A similar synthesis to that explained in section 3.2.3 for the OX-15SiNPs composite electrodes with PSS as a binder was conducted. A 1:1 mixture by mass of SBR:PSS was dispersed into high purity water (*via* MilliQ process until R > 18 MΩ). The inks with SBR/PSS as a binder were prepared by mixing 90 wt% of the OX-15SiNPs sample and 10 wt% of SBR/PSS in high purity water (MilliQ, R > 18 MΩ) under magnetic stirring at 1000 rpm for 5 h. A solvent-to-solids mass ratio of 20:1 was used. The ink was sprayed onto stainless steel current collectors, similar to that explained in Chapter 3. Galvanostatic cycling of these electrodes (Figure A3.2) showed that, although the theoretical capacity of the material was reached (approximately 1000 mAh g^{-1}), the discharge capacity still decreased during the first 15 cycles, similar to that of the composite electrodes with PSS as a binder shown in Chapter 3.

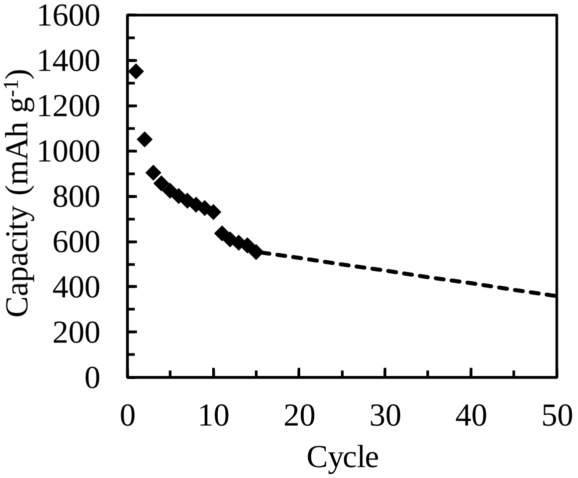

Figure A3.2 – Galvanostatic cycling of OX-15SiNPs composite electrodes with SBR/PSS as a binder at a current rate of C/10 between 0.005 V and 1.5 V *vs.* Li^+/Li. The dotted line is an extrapolation of the capacity after the 15th cycle.

Crosslinked PSS as a binder

Another way to increase the mechanical stability and elasticity of PSS is by crosslinking polymer chains. A crosslink connects one polymer chain to another via covalent or ionic bonds [3]. Crosslinking PSS should yield a more robust and durable material than PSS that has not been crosslinked. After crosslinking, the polymer should become less brittle and less prone to fracture [3]. This would be a useful characteristic for an advanced binder for silicon or tin oxide-based.

Ionically-bonded: poly(styrene sulfonic acid) and polyamine

One possible synthesis route would be to use poly(amine) as an ionic crosslinking agent with poly(styrene sulfonic acid). In this crosslinked material, the positively charged nitrogen in the poly(amine) would be ionically bonded to the negative sulfonate group in the poly(styrene sulfonic acid) (see Figure A3.3). Then, by carefully controlling the amount of poly(amine), the remaining sulfonate groups could be sodiated or lithiated, likely *via* the addition of NaOH or LiOH, respectively [4].

Although this procedure has not been carried out, it seems like a promising idea for an advanced binder for Li^+ ion battery electrodes. Difficulties may be encountered in the proper synthesis parameters of the binder, such as the quantity of each polymer, the lithiation of the polymer before or after crosslinking, as well as the stability of the binder with the electrolyte.

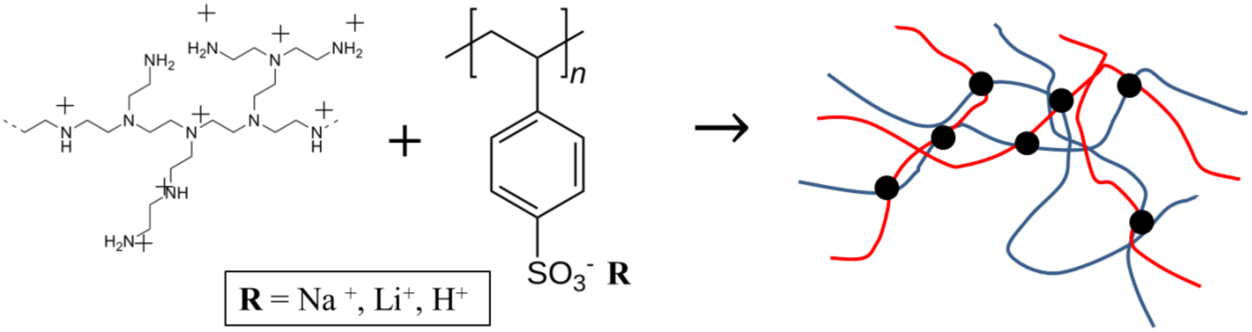

Figure A3.3 – Possible synthesis path for creating cross-linked poly(sodium/lithium 4-styrene sulfonate) using poly(amine) and poly(styrene sulfonic acid)-co-poly(Na/Li-4-styrenesulfonate). The red and blue lines represent the poly(amine) and poly(styrene sulfonic acid), respectively. The black dots in the figure represent the crosslink locations.

Covalently-bonded: crosslinked poly(sodium 4-styrene sulfonate) with EGDMA

Another possibility for creating crosslinked PSS would be *via* a covalently bonded crosslinking agent. In this theoretical procedure, ethylene glycol dimethyl acrylate (EGDMA) is used as a crosslinking agent with the monomer, sodium-4-styrene sulfonate [5]. Then, *via* 2,2′-Azobis(isobutyronitrile) (AIBN) as a radical initiator, the reaction shown in Figure A3.4 could possibly be carried out. In this specific reaction, the vinyl group present on the sodium-4-styrenesulfonate monomer would form the polymer backbone *via* free radical polymerization. The two methacrylate groups on the crosslinking agent would form the crosslinks between the polymer backbone and the growing polymer backbone [5]. Again, difficulties may be encountered in the proper synthesis parameters of the polymerization reaction as well as the application of the polymer on composite electrodes as either a coating or a binder during the crosslinking reaction. Nevertheless, this idea for a crosslinked binder seems like an interesting idea for an advanced electrode binder.

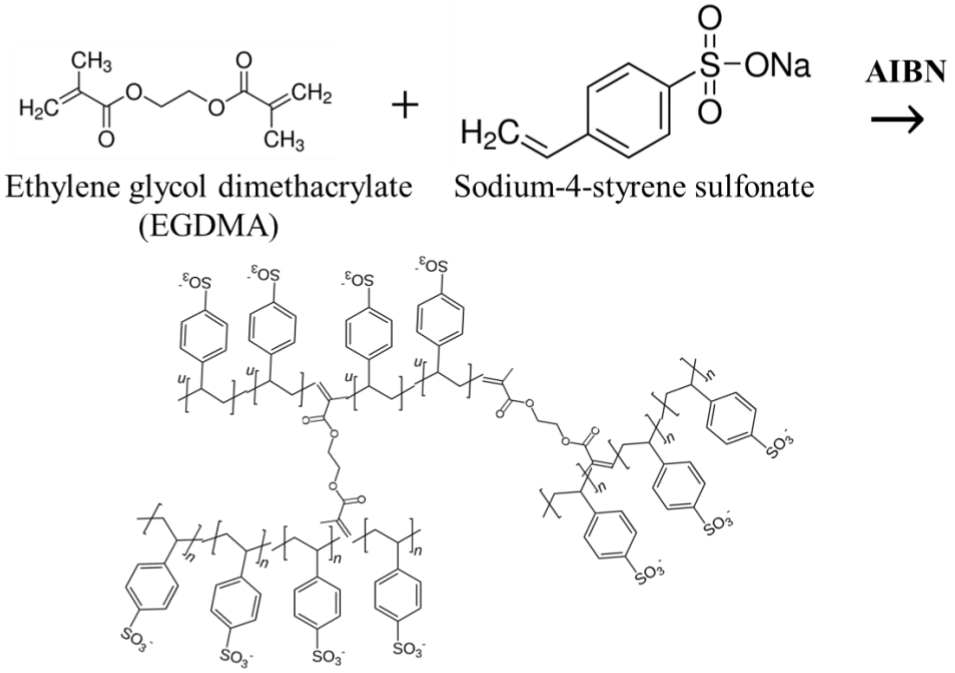

Figure A3.4 – Possible synthesis route for radical polymerization and crosslinking of EGDMA and sodium-4-styrene sulfonate via the radical initial AIBN.

Poly(dimethyl siloxane) as a binder or coating

Another possible polymer that may be an interesting candidate for an advanced binder for silicon or tin oxide-containing electrodes for Li^+ ion battery electrodes is poly(dimethyl siloxane) (PDMS). The most interesting characteristics of PDMS are its high elasticity, chemical stability, possibility for functionality, and various synthesis possibilities [6-9]. First, to determine how an unfunctionalized PDMS could act as a coating for a Li^+ ions battery electrode, the following synthesis was performed using silanol-terminated PDMS (M_w = 2750 g mol^{-1}, Gelest Inc.) and poly(methylhydrosiloxane) (PMHS, M_w = 2450 g mol^{-1}, Gelest Inc.), as shown in Figure A3.5. The electrodes that were used for the drop coating of the PDMS were the OX-10SiNPs composite electrodes with PVDF as a binder from Chapter 3.

The drop coating procedure was similar to the PSS drop coating procedure expressed in section 3.2.3 in Chapter 3. Two PDMS coatings with different dilution ratios were prepared by the hydrosilylation of a silanol-terminated PDMS with the crosslinking agent, PMHS. The first coating, referred to as PDMS1, consisted of 1.0 g of silanol-terminated PDMS with 1.5 g of PMHS dispersed in 2 g of hexamethyldisiloxane (HMDSO, XXXX). The second coating, referred to as PDMS2, consisted of 80 mg of silanol-terminated PDMS with 120 mg of PMHS, dispersed in 4.0 g of HMDSO. 20 µL of the catalyst, dibutyltin dilaurate (DBTDL, XXXX), was added to each solution just prior to the drop-coating on the surface of the electrode. The drop-coated electrodes were subsequently dried once more at 120°C at 2.5 kPa overnight.

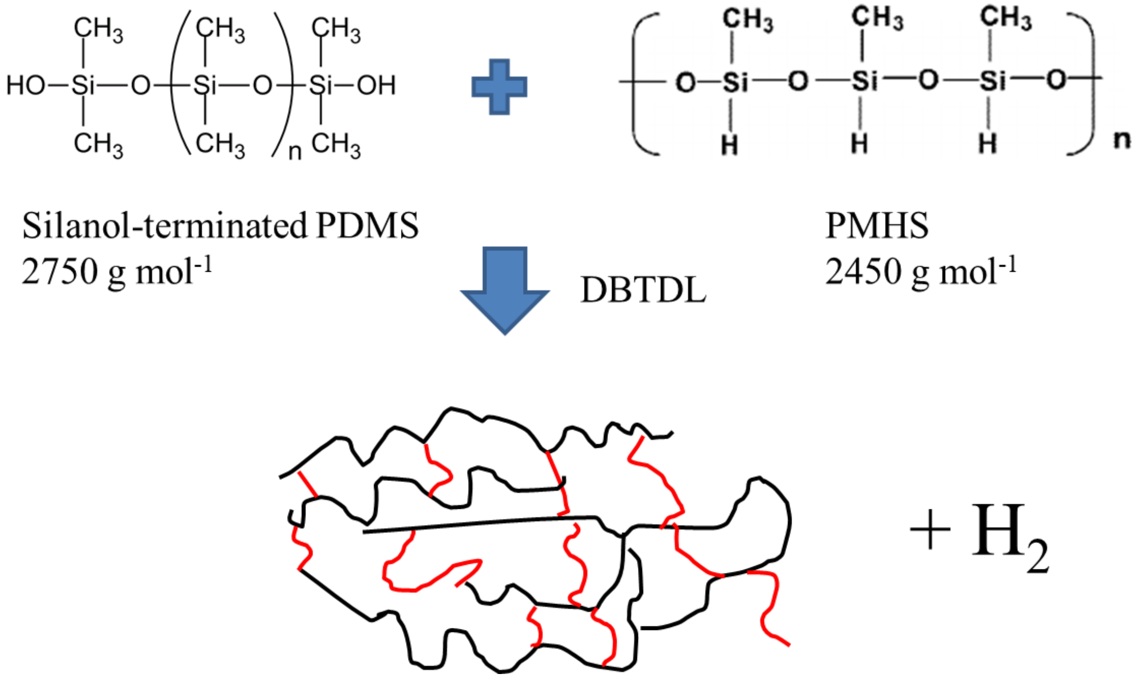

Figure A3.5 – PDMS synthesis using (▬) silanol-terminated PDMS and (▬) poly(methylhydrosiloxane) as a crosslinking agent, and dibutyltin dilaurate (DBTDL) as an initiator.

Galvanostatic cycling of the OX-10SiNPs composite electrode with PVDF as a binder either without a coating, with the PDMS1 coating, or with the PDMS2 coating is shown in Figure A3.6. The composite electrode with the PDMS1 coating shows a significantly reduced capacity as compared to the composite electrode without a coating. This can be likely explained by the excessive thickness of the coating applied on the surface of the active material, as exhibited by the SEM images shown in Figure A3.7. However, the composite electrode with the PDMS2 coating showed both the expected capacity as well as an increased cycling stability similar to the composite electrodes synthesized with PSS as a binder, as shown in Figure 3.11b in Chapter 3. SEM images of the composite electrode with the PDMS2 coating, which are shown in Figure A3.8 also exhibit a thinner layer of PDMS as compared to the active material shown in Figure A3.7.

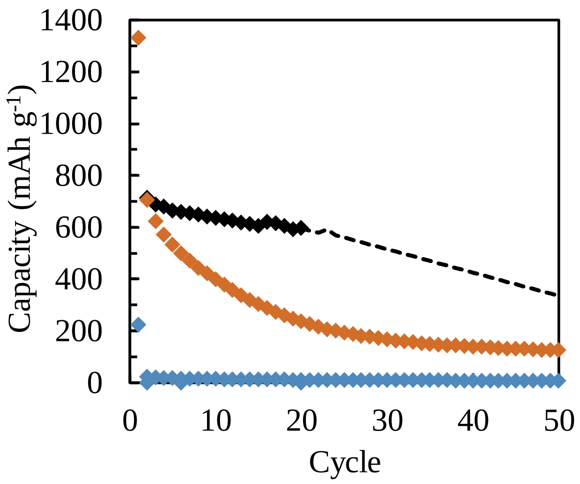

Figure A3.6 – Galvanostatic cycling for the OX-10SiNPs composite electrode with PVDF as a binder (◆) without a PDMS coating, (◆) PDMS1 as a coating, (◆) PDMS2 as a coating, and (---) extrapolated capacity of PDMS2 as a coating. The current rate was C/10 between 0.005 V and 1.5 V *vs*. Li^+/Li.

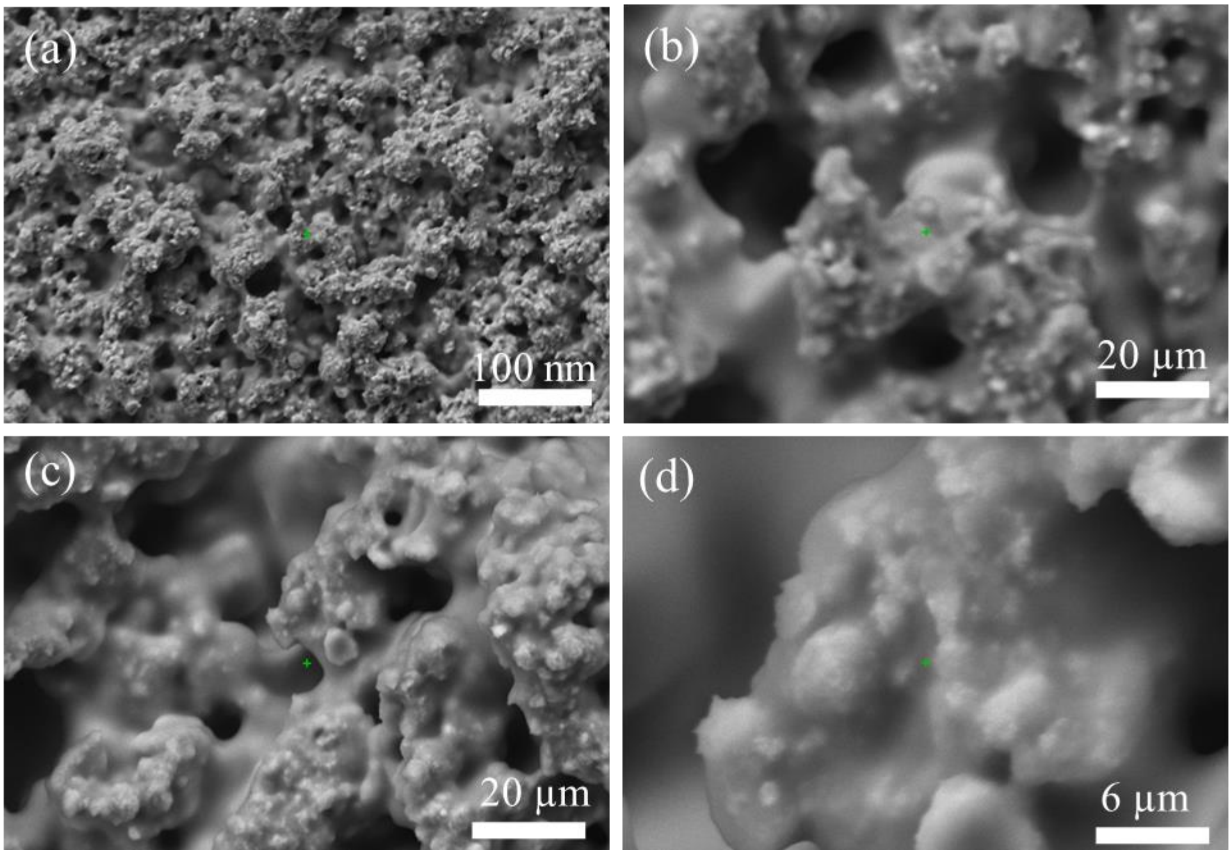

Figure A3.7 – SEM images of the OX-10SiNPs composite electrode with PVDF as a binder and PDMS1 as a coating at various magnifications.

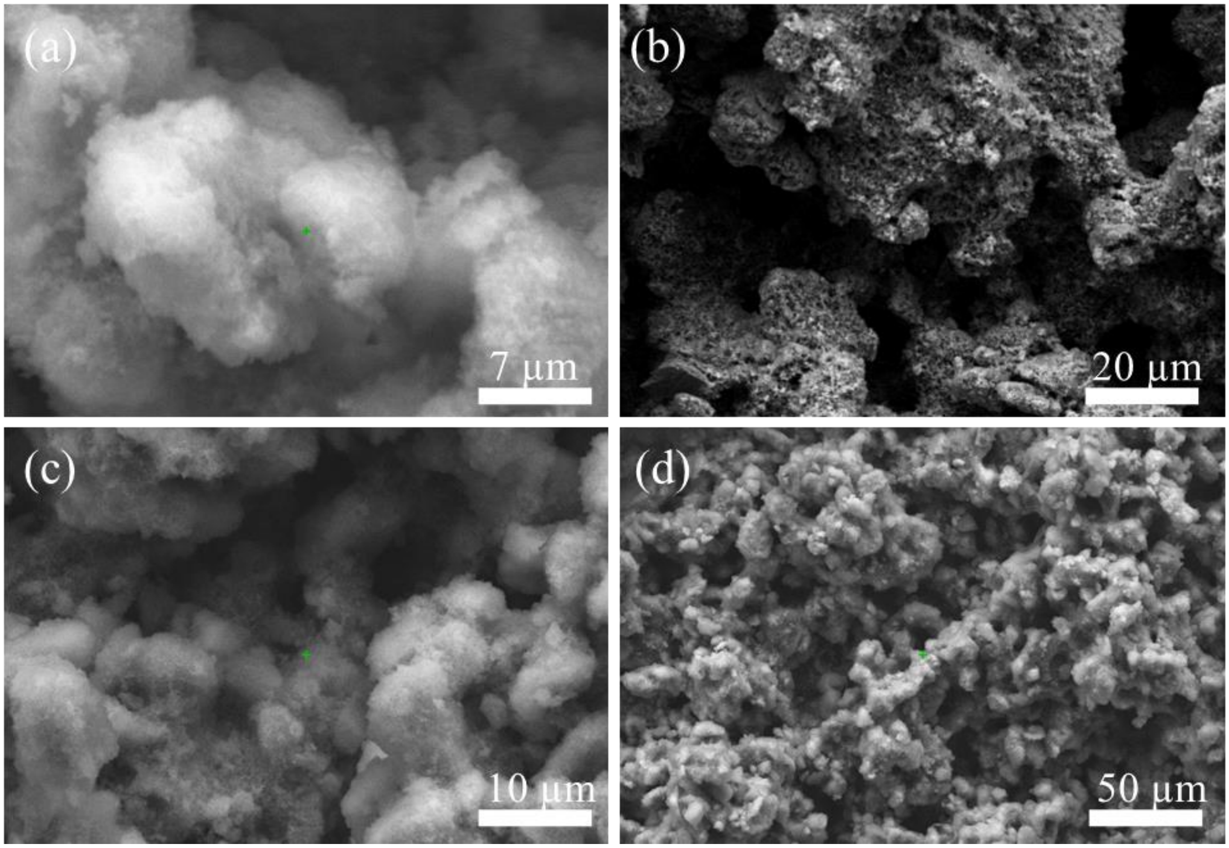

Figure A3.8 – SEM images of the OX-10SiNPs composite electrode with PVDF as a binder and PDMS2 as a coating at various magnifications.

Further research into PDMS as a binder should be focused on finding the correct dilution ratio of the PDMS, optimizing the molecular weight, and degree of crosslinking. Optimizing the dilution ratio of the PDMS would help determining both the minimum and maximum amount of PDMS that can be applied without affecting the electrochemical properties of the active material. Optimizing the molecular weight and degree of cross-linking of the PDMS would also help to form a durable, elastic, and strong polymer that would best mitigate the negative effects of the volumetric change of the silicon or tin oxide dopants.

PDMS with functional groups that could ionically or covalently bond to the silicon or tin oxide surface could also be explored; this would allow better protection against pulverization and SEI instability. For example, the hydrogen groups in PMHS could bond to the silanol group, Si–OH, on the surface of the silicon (see Figure A3.9) using a wide range of functionalized PDMS either functionally terminated or along the siloxane backbone. These PDMS with functional groups range from alkoxy, amine, acetoxy, and hydrides, to name a few, and can easily be bought commercially [9]. Furthermore, linking agents can be used, which consists of a functionally-terminated hydrocarbon [10]. The idea would be to form an extremely thin layer of PDMS on the surface of the silicon (or tin oxide) that would encase the high energy dopant and prevent pulverization and excessive SEI formation.

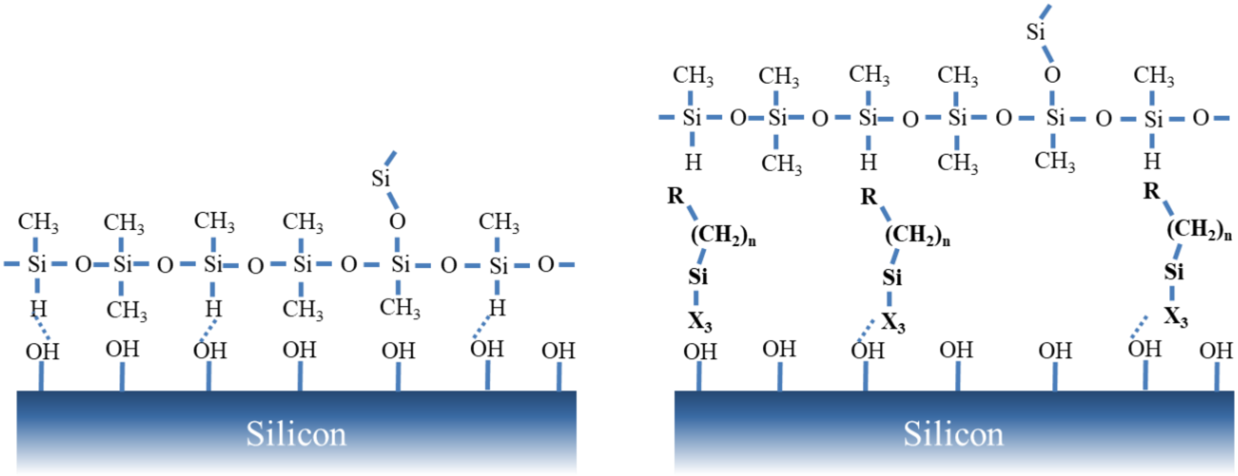

Figure A3.9 – Schematic of the bonding of PDMS on the surface of silicon nanoparticle either with direction silanol bonds with the hydride groups in PMHS or *via* functionally-terminated hydrocarbon linking agents which bond the hydride groups in the PMHS with the silanol groups on the silicon surface. Similar chemistry would be present for the surface of tin oxide.

Research into further functionalization of PDMS could be done that could offer ionic conductivity in addition to covalent bonds with the silicon or tin oxide surface. Functionalization of PDMS with ionically conductive functional groups, such as sulfonates, would hopefully yield similar positive effects as PSS explored in this thesis. A few possibilities for synthesizing these PDMS-based layers could be synthesized *via* the vinyl addition curing of vinyl-terminated PDMS with the free –H bonding sites commonly found on the surface of silicon (see Figure A3.10). Additionally, sodium 4-vinylbenzenesulfonate could possibly be used to form an ionically-conductive PDMS layer. The preparation of a sulfonated PDMS conducted by A. Neira-Carrillo *et al.* [6], for example, consisted of the vinyl addition curing of PMHS with styrene, followed by a subsequent sulfonation with sulfuric acid. It is therefore possible that these polymers can be reasonably synthesized and would be great candidates for an advanced binder for Li^+ ion batteries.

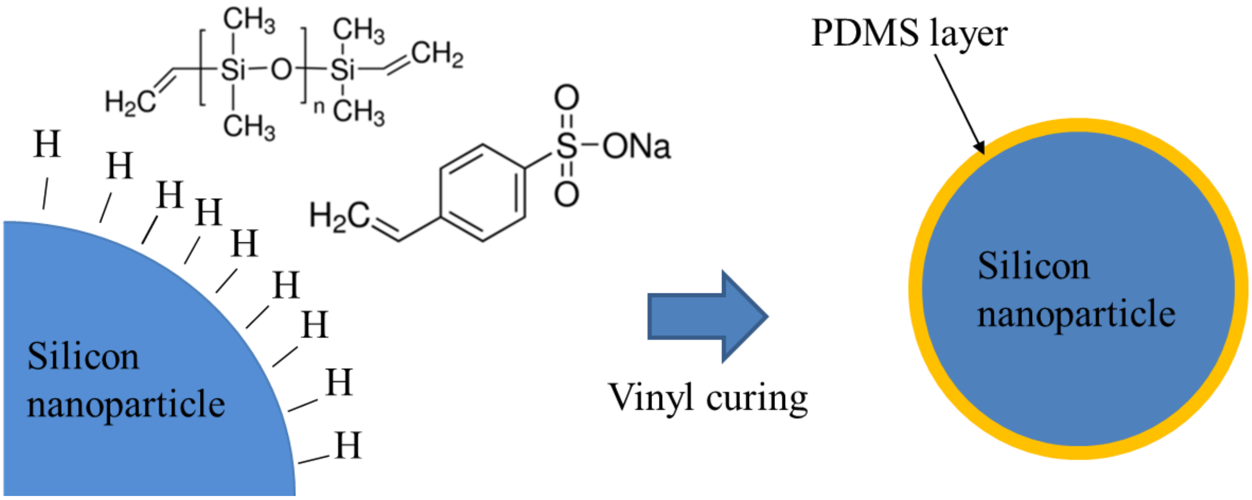

Figure A3.10 – Schematic of an ionically-conductive PDMS with sodium-3-styrenesulfonate as a conductive additive *via* vinyl curing on the surface of silicon nanoparticle.

References

[1] R. Wang, L. Feng, W. Yang, Y. Zhang, Y. Zhang, W. Bai, B. Liu, W. Zhang, Y. Chuan1, Z Zheng, and H. Guan. Nanoscale Research Letters 12 (2017) 575-586.

[2] Polymer Database. Elastomers, SBR. Available: https://polymerdatabase.com/Elastomers/SBR.html. Accessed on: April 4, 2021.

[3] J.-P. Pascault and R.J.J. Williams, Chapter 1 - Overview of thermosets: Present and future, Editor(s): Qipeng Guo, In: Thermosets (Second Edition), Elsevier, (2018) 3-34.

[4] N. Shubha, H. Zhu, M. Forsyth, and M. Srinivasan, Study of lithium conducting single ion conductor based on polystyrene sulfonate for lithium battery application. Polymer 99 (2016) 748-755.

[5] J.S. Song and M.A. Winnik, Cross-Linked, Monodisperse, Micron-Sized Polystyrene Particles by Two-Stage Dispersion Polymerization. Macromolecules 38, 20 (2005) 8300–8307.

[6] A. Neira-Carrillo, F. Luengo-Ponce, P. Vásquez-Quitral, M. Yazdani-Pedram, M. Soledad Fernández, H. Cölfen, J. Luis Arias, Sulfonated Polymethylsiloxane as an Additive for Selective Calcium Oxalate Crystallization. Eur. J. Inorg. Chem. (2015) 1167–1177.

[7] J. Ren, L. Wang, X. Han, J. Cheng, H. Lv, J. Wang, X. Jian, M. Zhao, and L. Jia, Organic silicone sol−gel polymer as a noncovalent carrier of receptor proteins for label-free optical biosensor application. Appl. Mater. Interfaces 5 (2013) 386−394.

[8] X. Yanga, T. Zhua, Z. Xub, H. Shanb, and J. Luoa, Significantly enhanced CH_4 permeability base on poly(styrene-b-butadieneb-styrene)-poly(dimethylsiloxane-co-methylhydrosiloxane) crosslinked membranes. React. Funct. Polym. 124 (2018) 48–54.

[9] Gelest Inc., Reactive silicones: Forging new polymer links. Available: https://www.gelest.com/wp-content/uploads/Reactive-SIlicones-No-Price-2016.pdf. Accessed: April 5, 2021.

[10] Gelest Inc., Silane coupling agents: Connecting across boundries. Available: https://www.gelest.com/wp-content/uploads/Silane_Coupling_Agents.pdf. Accessed: April 5, 2021.